Spacecraft Formation Flight on Quasi-periodic Invariant Tori

by

Nicola Baresi

B.S., Physics, University of Padua,

Padua, Italy, 2007

M.S., Physics, University of Padua,

Padua, Italy, 2011

M.S., Aerospace Engineering Sciences, University of Colorado Boulder,

Boulder, CO, 2015

A thesis submitted to the

Faculty of the Graduate School of the

University of Colorado in partial fulfillment

of the requirements for the degree of

Doctor of Philosophy

Department of Aerospace Engineering Sciences

2017

This thesis entitled:
Spacecraft Formation Flight on Quasi-periodic Invariant Tori
written by Nicola Baresi
has been approved for the Department of Aerospace Engineering Sciences

_____

Prof. Daniel J. Scheeres

_____

Prof. Natasha Bosanac

_____

Prof. Jay W. McMahon

_____

Prof. James D. Meiss

_____

Prof. Hanspeter Schaub

Date _____

The final copy of this thesis has been examined by the signatories, and we find that both the content and the form meet acceptable presentation standards of scholarly work in the above mentioned discipline.

Baresi, Nicola (Ph.D., Aerospace Engineering Sciences)

Spacecraft Formation Flight on Quasi-periodic Invariant Tori

Thesis directed by Prof. Daniel J. Scheeres

Since the successful rendezvous of the Gemini VI and VII spacecraft in 1965, spacecraft formation flying has attracted the interest of many researchers in the field. Yet, existing methodologies do not currently account for the oblateness of a central body when the distance between the satellites exceeds the reach of standard analytical techniques such as Brouwer-Lyddane theory and thereof.

In this dissertation, the problem of designing bounded relative orbits is approached with a dynamical systems theory perspective in order to overcome the limitations imposed by mean-to-osculating orbit element mappings and linearization errors. We find that the dynamics of satellites in the Earth zonal problem can be fundamentally described by three periods, whose averaged values can be accurately computed through numerical integration. To ensure long-term bounded relative motion between the satellites in a formation, at least two of their fundamental periods need to be matched on average. This condition is enforced by including additional constraints into existing techniques for calculating families of quasi-periodic invariant tori. The result is a numerical procedure that searches for the invariant curves of a stroboscopic mapping while changing the polar component of the angular momentum vector for each of the quasi-periodic tori within the family. Upon convergence, the algorithm outputs several curves that can be interpolated to obtain an entire surface of bounded relative motion. That is, by selecting arbitrary initial conditions on this surface, bounded relative motion can be established, regardless of the number of zonal harmonics terms that are included in the geopotential.

Given this encouraging result, we move beyond Earth's orbit and investigate the problem of designing bounded relative orbits about small irregular bodies. First, we consider the case of asteroid (4179) Toutatis, and build on previous research to identify periodic and quasi-periodic

orbits that ensure boundedness in spite of the complex shape and rotational state of the target asteroid. Next, we move to the Martian system and design spacecraft formations near Phobos. Once again, we aim at improving the realism of previous simulations found in the literature by modeling the nonspherical shape and nonzero eccentricity of the Martian moon. The resulting higher fidelity model causes entire families of periodic orbits to become quasi-periodic invariant tori that eventually serve as initial conditions for bounded spacecraft formations.

The last part of this thesis is dedicated to assessing the robustness of the relative trajectories computed throughout the manuscript. Although atmospheric drag and solar radiation pressure have catastrophic effects on the relative dynamics of satellites in LEO and near Toutatis, it is found that spacecraft formations in MEO, GEO, and about Phobos are quite resilient to mismodeled dynamics, making quasi-periodic invariant tori a robust option for flying satellite clusters in these complex dynamical environments.

To my parents, Alessandra and Fulvio,

and my little sis, Francesca.

Acknowledgements

Firstly, I would like to express my sincere gratitude to Prof. Scheeres for his continuous support throughout my doctoral studies. Dan is a phenomenal advisor, and I could have not asked for better guidance to fulfill my academic goals. Being one of his students will remain one of the greatest honors of my life and I will be certainly missing walking by his office every week to discuss research ideas and have all my doubts cleared in the time span of a meeting.

Besides my advisor, I would like to thank Prof. McMahon, Prof. Schaub, Prof. Meiss, and Prof. Bosanac for their invaluable feedbacks, career advice, and continuous encouragements throughout the years. Professors' schedules are extremely busy, and yet, I was always welcomed in their offices to debate on new approaches and different applications for my research. My sincere thanks also goes to Prof. Casotto for his friendship and for teaching me how to approach engineering problems with a physics mindset. Without him, I would have never discovered the beauty of orbital mechanics and the interesting challenges associated with distributed Space systems.

I also want to thank the Fulbright program for their support and assistance during my academic journey in Colorado. Becoming a Fulbrighter was an incredible gift and gave me the opportunity to meet remarkable people from all over the world. Among them, I am particularly grateful to my fellow CSMLers and CU grad students for their company and for keeping me sane over the last four years.

Last but not the least, I would like to thank my family and friends from Italy. Writing this thesis would have not been possible without their unconditional support and efforts to make me feel at Home regardless of the long distance.

Contents

Chapter

1 Introduction **2**

1.1 Spacecraft Formation Flying 2

1.2 The Bounded Relative Motion Problem 4

1.3 A Dynamical Systems Theory Approach 5

1.4 Organization 8

1.5 Contributions 10

1.6 Publications 11

2 Preliminaries **13**

2.1 The Hill Problem 13

2.2 Fixed Points 16

2.3 Periodic Orbits 18

2.3.1 Predictor 20

2.3.2 Corrector 21

2.4 Shooting vs Collocation techniques 23

2.5 Stability of Periodic Orbits 27

2.6 Quasi-periodic Invariant Tori 30

3 Numerical Computation of Quasi-periodic Invariant Tori **33**

3.1 Partial Differential Equation Solvers 34

3.1.1 The PDE(CD) algorithm . . . 39
3.1.2 The PDE(DFT) algorithm . . . 39
3.2 Two-Point Boundary Value Problem Solvers . . . 40
3.2.1 The KKG algorithm . . . 41
3.2.2 The GMOS algorithm . . . 46
3.3 Accuracy Test . . . 51
3.4 Further Remarks on GMOS and PDE(DFT) . . . 55
3.5 Collocation . . . 60
3.6 Stability of Quasi-periodic Invariant Tori . . . 64
3.7 Three-Dimensional Tori . . . 67
3.8 Conclusions . . . 73

4 Bounded Relative Trajectories about Axisymmetric Bodies 74

4.1 Equations of Motion . . . 75
4.2 Spacecraft Dynamics . . . 77
4.2.1 Pseudo-circular Orbits . . . 78
4.2.2 Pseudo-elliptic Trajectories . . . 83
4.3 Formation Flying . . . 87
4.4 GMOS revised . . . 94
4.5 1999 KW4α formations . . . 105
4.6 Conclusions . . . 108

5 Spacecraft Formation Flight about Small Bodies 110

5.1 Slowly Rotating Tri-axial Ellipsoids . . . 111
5.2 Slowly Rotating Constant Density Polyhedra . . . 115
5.3 Complex Rotators . . . 121
5.4 Formation Flight near Phobos . . . 126
5.5 Conclusions . . . 133

6 Robustness Analysis **135**

6.1 Dynamical Perturbations 135

6.1.1 Tesseral and Sectorial Harmonics 136

6.1.2 Third-body Attraction 138

6.1.3 Solar Radiation Pressure 138

6.1.4 Atmospheric Drag 139

6.2 LEO Formations 140

6.3 MEO & GEO Formations 140

6.4 (4179) Toutatis Formations 143

6.5 Phobos Formations 149

6.6 Conclusions 151

7 Conclusions and Future Work **152**

Bibliography **156**

Tables

Table

3.1 GMOS vs PDE(DFT) 59

3.2 Runtime of GMOS(C) 63

4.1 Legendre polynomials used for the simulations. 75

4.2 Earth's zonal harmonics coefficients up to the fifth order. 78

4.3 Nodal periods and RAAN drifts per nodal period 94

4.4 Chief and deputy initial conditions for bounded relative motion in MEO 105

4.5 Chief and deputy initial conditions for bounded relative motion in GEO 105

4.6 (66391) 1999 KW4α zonal harmonics coefficients 105

5.1 Monodromy matrix eigenvalues for the 1:1 direct orbit about (4179) Toutatis. 123

5.2 Chief and deputy initial conditions for bounded relative motion about M1 Phobos . 132

6.1 Unormalized Earth coefficients used for the simulations 137

Figures

Figure

1.1 Methods for calculating quasi-periodic invariant tori 7

2.1 Fixed point in the Hill Problem 16
2.2 Predictor-corrector scheme 20
2.3 Examples of Southern Halo orbits in the Hill problem 22
2.4 Branch of the Southern Halo family of the Hill Problem 23
2.5 Shooting VS collocation techniques 24
2.6 Manifolds emanating from a Southern Halo orbit 30
2.7 Quasi-periodic invariant tori 30
2.8 Torus function 31

3.1 Mesh of discretization points utilized by PDE solvers 36
3.2 Skeleton of a two-dimensional quasi-periodic invariant torus 36
3.3 KKG: invariant circles seen in different coordinate planes 43
3.4 KKG: first and last iterations 45
3.5 Conjugacy 46
3.6 GMOS: first and last iterations 50
3.7 Planar Circular Orbit (PCO) in both the ECEF and ECI frames. 51
3.8 Results of accuracy test 53
3.9 Eccentric trajectories in the ECEF and ECI frames 53

3.10 Sparsity of the Jacobian matrix for the PDE(CD) and PDE(DFT) algorithms 54
3.11 Example of DRO for the Earth-Moon system. 56
3.12 Members of the quasi-DRO family 57
3.13 GMOS error plot 58
3.14 PDE(DFT) error plot 59
3.15 Sparsity of the Jacobian matrix for the GMOS(C) algorithm 62
3.16 GMOS(C) error 64
3.17 Stable and Unstale manifolds of a HP L1 quasi-halo torus 66
3.18 Eigenvalues of $DS_{-\rho}$. 67
3.19 Quasi-halo three-dimensional torus 72

4.1 $\Delta\Omega_d$ and $\Delta\omega_d$ drifts due to zonal harmonics perturbations. 77
4.2 Example of pseudo-circular orbit about the Earth 81
4.3 Nodal, sidereal, and anomalistic Periods 81
4.4 Differerent brances of pseudo-circular families about the Earth 82
4.5 T_d and $\Delta\Omega_d$ contour plot 82
4.6 Evolution of the stability index with changes in r and H_z 83
4.7 GMOS invariant curves for a family of E Tori 85
4.8 Example of quasi-periodic E Torus about the Earth 86
4.9 Nodal, sidereal, and anomalistic Periods for a pseudo-ellitpical trajectory on a E torus 86
4.10 GMOS invariant curves for a family of P Tori 87
4.11 Example of a quasi-periodic P Torus about the Earth 88
4.12 Nodal, sidereal, and anomalistic Periods for a pseudo-ellitpical trajectory on the surface of a P torus 88
4.13 Relative motion between satellites on the surface of the same E torus 89
4.14 Relative motion between a satellite on the surface of a E torus and a pseudo-circular chief 90

4.15 Relative motion between a satellite on the surface of a P torus and a pseudo-circular chief . . . 91
4.16 Integration events for the trajectory of a sample solution point $\boldsymbol{y}_i$ in the revised GMOS algorithm. . . . 95
4.17 Revised GMOS invariant curves . . . 97
4.18 Example of a quasi-periodic HP Torus about the Earth . . . 97
4.19 Nodal, sidereal, and anomalistic Periods for a pseudo-ellitpical trajectory on the surface of a HP torus . . . 98
4.20 δE vs δH_z for two-hundred quasi-periodic HP tori computed with the revised GMOS algorithm. . . . 99
4.21 Relative motion between a satellite on the surface of a HP torus and a pseudo-circular chief . . . 100
4.22 Relative motion between two deputies being initialized on the surface of two different HP tori of the same family. . . . 100
4.23 Nodal periods and RAAN drifts per nodal period of two deputies being initialized on the surface of two different HP tori. . . . 101
4.24 Relative motion between a pseudo-circular chief and two pseudo-ellitpic satellites . . 101
4.25 Argument of perigee drift per nodal period for all of the HP tori computed with the revised GMOS algorithm . . . 102
4.26 Relative motion between a satellite on the surface of a HP torus and a pseudo-circular chief in MEO . . . 103
4.27 Relative motion between a satellite on the surface of a HP torus and a pseudo-circular chief in GEO . . . 104
4.28 Pseudo-circular orbit in a 5×0 gravity field about KW4α. $E = -0.4$, $H_z^2 = 0.5$ . . . 106
4.29 Revised GMOS invariant curves about 1999 KW4 α . . . 107
4.30 Relative motion between a pseudo-circular chief and a deputy on the surface of a HP torus in a 5×0 gravity field about KW4α . . . 107

4.31 Inter-satellite distance between a pseudo-circular chief and a deputy on the surface of a HP torus in a 5×0 gravity field about KW4α 108

5.1 First periodic orbit about a slowly rotating tri-axial ellipsoid 113

5.2 Family of periodic orbits about a slowly rotating tri-axial ellipsoid 113

5.3 Two-dimensional subtori projected onto the configuration space 114

5.4 In-plane relative orbit obtained for a constant density ellipsoidal gravity field. 115

5.5 Out-of-plane relative orbit obtained for a constant density ellipsoidal gravity field. . 116

5.6 Unit vectors for polyhedron gravity model 117

5.7 (4179) Toutatis shape model and reference frames. 118

5.8 Relative differences between the constant density polyhedron and ellipsoid gravity potentials 118

5.9 Family of periodic orbits about a slowly rotating constant density polyhedron 119

5.10 In-plane relative orbit obtained for a constant density polyhedron gravity field. . . . 120

5.11 Out-of-plane relative orbit obtained for a constant density polyhedron gravity field. . 121

5.12 1:1 direct periodic orbit as seen from Toutatis' body-fixed frame. 123

5.13 GMOS solution points for the first 3D quasi-periodic invariant torus. 125

5.14 Three-dimensional invariant torus about (4179) Toutatis 125

5.15 Relative motion between a chief on a 1:1 direct periodic orbit and a deputy on the surface of a three-dimensional torus about the complex rotator (4179) Toutatis . . . 126

5.16 Relative motion between satellites on the surface of the same torus about the complex rotator (4179) Toutatis 127

5.17 $\mathcal{S}$ and $\mathcal{B}$ reference frames as seen from the leading edge of Phobos. 129

5.18 Period vs positive x-crossing for the family of quasi-satellite orbits with $e = 0$. Only the periodic orbits whose period is resonant with $2\,\pi$ survive when $e \neq 0$. 130

5.19 Periodic VS Quasi-periodic trajectories about M1 Phobos 131

5.20 Bounded relative trajectory about Phobos 133

6.1 LEO formations pertubed by luni-solar attraction, atmospheric drag, SRP, and asymmetric Earth over one day 141
6.2 LEO formations: changes in the nodal and sidereal periods due to external perturbations 142
6.3 MEO formations pertubed by luni-solar attraction, SRP, and asymmetric Earth over one day 143
6.4 MEO formations: changes in the nodal and sidereal periods due to external perturbations 144
6.5 GEO formations pertubed by luni-solar attraction, SRP, and asymmetric Earth over one day 145
6.6 GEO formations: changes in the nodal and sidereal periods due to external perturbations 146
6.7 Perturbed relative dynamics between a chief on a 1:1 direct periodic orbit and a deputy on the surface of a three-dimensional torus about the complex rotator (4179) Toutatis 148
6.8 Perturbed relative dynamics between a chief and a deputy spacecraft near M1 Phobos 150

axisymmetric

Chapter 1

Introduction

1.1 Spacecraft Formation Flying

Groups of satellites that cooperate in space to fulfill their mission requirements are usually referred to as Distributed Space Systems (DSS) . This architecture is a relatively new concept in space mission design that offers several advantages over single satellite missions [1]. First, DSS can be designed to be cheaper and more practical than large monolithic spacecraft, as the tasks required for the mission are usually spread among a flock of smaller cost-effective satellites that can be manufactured with standard components and techniques. Accordingly, DSS are commonly acknowledged to be more robust than single-satellite missions due to the possibility of replacing faulty units with new pieces of technology that can be launched in space if needed. Even when unit replacement is prohibited by costs and engineering constraints, the geometry of the formation can sometimes be reconfigured to proceed with the mission objectives in spite of the loss of one or more vehicles. Finally, DSS enable space-based scientific investigations that cannot be performed with single satellites due to launch, budget, and physical restrictions. Examples of the latter include space-borne telescopes with long focal lengths or large-baseline Synthetic Aperture Radars (SAR) like the DLR's TanDEM-X, a SAR mission that started as soon as TerraSAR-X was joined by its twin satellite in order to deliver the most accurate and detailed digital elevation models of the Earth up to date [66].

The example of TanDEM-X is just one of several cases in which distributed space systems have contributed to improve our understanding and monitoring capabilities of the Earth environment.

Currently, NASA's GRACE is still measuring the inter-satellite distance between two twin satellites separated by a few hundreds of kilometers in order to capture the tiniest variations of the Earth's gravity field [106]. At much higher altitudes, the Magnetospheric Multiscale Mission (MMS) is studying the phenomenon of magnetic reconnection between the Sun's and Earth's magnetic fields based on the measurements of four identical satellites flying in a tetrahedral formation [54]. GRAIL just recently terminated its mission to the Moon after measuring the gravity field of our satellite with unprecedented accuracy [119], whereas PRISMA successfully tested new key technologies for upcoming DSS missions [26]. In the future, there is hope that ESA will commit to build the first space-based gravitational waves observatory by placing three satellites in a triangular configuration with separation distances on the order of millions of kilometers [10]. By then, the Asteroid Impact Mission (AIM) might have been the first spacecraft to ever establish an inter-satellite network about an asteroid with a mothercraft and two 3U Cubesats to be deployed upon arrival at (65803) Didymos [110].

A prerequisite for all of these ambitious missions to be successful is guaranteeing that the vehicles within the formations do not fly apart from each other. Yet, ensuing bounded relative motion is a nontrivial task considering all of the forces and sources of error that typically affect the motion of space vehicles. Fortunately, techniques from Dynamical Systems Theory (DST) can be leveraged to identify trajectories that mitigate the effects of perturbations and the need for corrective maneuvers. This search is hereby referred to as the Bounded Relative Motion Problem and is one of several focuses of Spacecraft Formation Flying (SFF), which is defined by NASA's Goddard Space Flight Center as *"the tracking or maintenance of a desired relative separation, orientation, or position between or among spacecraft"* [1]. In this thesis, we are primarily concerned with the maintenance aspect of a formation, as we will recurrently seek for initial conditions that guarantee bounded relative motion in spite of the complex dynamical environments being investigated.

1.2 The Bounded Relative Motion Problem

Since the pioneering work of Clohessy and Wiltshire [23], research on relative motion has addressed the reduction of the fuel requirements of a distributed spacecraft mission by identifying trajectories that minimize the relative drift between a reference spacecraft (the *chief*) and its companions (*deputies*). In the validity regime of the Clohessy-Wiltshire equations, such drift can be nullified if the initial relative velocity of the deputy in the along-track direction is equal to twice the initial displacement in the radial direction multiplied by the mean motion of the chief [95, 101]. This relationship between the component of the initial state vector ensures that the semi-major axes of the chief and deputy spacecraft are equivalent, a condition that guarantees bounded relative motion in the Keplerian case even when the trajectory of the chief is non-circular [46].

Unfortunately, straightforward analytical relationships between the initial conditions of the spacecraft are no longer valid when perturbations to the two-body dynamics are incorporated in the equations of motion. For spacecraft formations about the Earth, the main challenges are associated with the differential rates in the Right Ascension of the Ascending Node (RAAN), argument of perigee, and mean anomaly at epoch induced by the oblateness of the planet. Schaub and Alfriend realized this fact and developed first-order differential mean orbit element initial conditions that nullify the difference in RAAN and mean argument of latitude rates between two neighbouring orbits [94]. Specifically, the authors showed how differences in the mean semi-major axes, eccentricity, and inclination of two satellites can be applied to establish bounded relative motion over a few orbital revolutions. Similar results were also obtained by other authors using different orbit element rates [35, 107] and/or numerically corrected initial conditions [13, 93, 115] that ensure bounded relative motion over a few days in spite of the linearization and mean-to-osculating orbit element mapping errors that limit the size and accuracy of the computed relative orbits.

An alternate approach developed by Koon et al. studies the problem of the relative motion in a J_2-perturbed environment via Poincaré mappings, surfaces of section, and other tools imported from DST [64]. Their approach was based on the pioneering work of Broucke, who first

demonstrated that the majority of trajectories about an axisymmetric body are either periodic or quasi-periodic in the 2 DOF Routh Reduced System (RRS) derived from the Lagrangian of the Earth zonal problem [17]. There, satellites can be initialized on periodic and quasi-periodic orbits to achieve bounded relative motion over indefinite time spans. Although the strategy proposed by Koon and co-authors does not rely on either linearization or mean-to-osculating orbit element mappings, it no longer works as soon as the same initial conditions are translated to the full six-dimensional problem. Here, differences in the nodal periods and RAAN drifts per nodal period between the different satellites cause a natural drift that destroys the formation within a few days. Xu et al. [114] noted this fact and combined the dynamical system theory approach with a numerical searching method based on ergodic maps and contour plots to enforce a weaker version of the constraints originally derived by Martinusi and Gurfil [71]. This resulted in bounded relative trajectories that last for more than a year.

A similar searching method has also been adopted by Chu et al., who studied the J_2 bounded relative motion problem from a completely analytical point of view [22]. Albeit subject to some limiting assumptions, their method succeeds in generating bounded relative trajectories using Hamilton-Jacobi theory to calculate the natural frequencies of motion and matching the average of the nodal and sidereal periods of two satellites in different orbits. Unfortunately, the lack of numerical simulations that test the boundedness of their relative trajectories for extended periods of time prevents a rigorous comparison with previously discussed techniques, thereby leaving the Bounded Relative Motion Problem still open to debate.

1.3 A Dynamical Systems Theory Approach

In this thesis, the work of Koon and coauthors is leveraged to study the problem of bounded relative motion from a dynamical systems theory point of view. Differently from the majority of previous research, we design trajectories for spacecraft formations using the surface of quasi-periodic invariant tori that are *explicitly* calculated with numerical procedures imported from DST. This approach enables the investigation of the deployment of spacecraft formations in complex nonlinear

dynamical environments such as the Earth zonal problem or the vicinity of small irregular bodies without the need of the expensive grid searches proposed in Ref. [22] & [114].

The idea of using quasi-periodic invariant tori for spacecraft formation flying is not novel and was originally proposed by Barden & Howell in 1998 [5]. In their paper, the authors leveraged the knowledge of the center subspace of an unstable halo orbit to initialize a multitude of spacecraft and study their relative dynamics for planet-finding applications. Since then, many other authors have studied the possibility of using quasi-periodic tori to guarantee bounded relative motion between multiple vehicles, including [42] and [83]. However, it was not until recently that powerful numerical techniques to extend the computation of these dynamical structures beyond the center subspace became available.

Currently, numerical procedures for computing quasi-periodic invariant tori can be classified into two main categories: methods that compute invariant tori of flows, and methods that calculate invariant curves of maps (Fig. 1.1). Both strategies aim at calculating diffeomorphisms whose images are invariant for the considered dynamics. However, differences between these classes of methodologies arise when comparing the performance and limitations of these two approaches.

In the first case, invariant tori of flows are usually computed by translating the conditions for quasi-periodic motion into a set of Partial Differential Equations (PDE) that can be solved with standard procedures available in the literature. For instance, Schilder et al. propose to approximate the solution over an equally spaced grid of points while using Central Differences (CD) to replace partial derivatives with linear combinations of neighboring points [99]. This approach is hereby referred to as the PDE(CD) algorithm and produces a large system of nonlinear algebraic equations that can be solved via Newton's method to get a full parametrization of the torus whose accuracy depends on the spacing between consecutive mesh points. A finer mesh recovers a more accurate result at the expense of a higher computational cost. This increase in the computational time is particularly problematic for alternative formulations of the PDE approach, where central differences are substituted by more performing methods such as the Discrete Fourier Transform (DFT) (see PDE(DFT), Section 3.1.2).

In contrast with the previous strategies, methods that compute invariant curves of maps are less susceptible to the curse of dimensionality because they deal with objects of dimension one less. Gómez and Mondelo derived a numerical method for calculating the Fourier coefficients of Lissajous and halo orbits in the Circular Restricted Three-Body Problem (CRTBP) based upon the invarinat curves of a stroboscopic mapping [44]. Olikara and Scheeres modified this approach to operate directly on orbit states and to incorporate general-purpose constraints that generalize the algorithm to other systems and orbit families [86]. The resulting procedure, hereby referred to as GMOS, calculates families of quasi-periodic invariant tori by solving a Two-Point Boundary Value Problems (TPBVP) for the invariant curves of a stroboscopic mapping, and represents an alternative with respect to the methodology of Kolemen, Kasdin, and Gurfil (KKG), who built on similar ideas to calculate invariant curves of Poincaré maps [62].

Although both map strategies have been successfully tested in astrodynamics (see, e.g., [8, 15, 36]), it is unclear whether KKG or GMOS should be preferred for extensive studies as well as to establish bounded relative motion in complex dynamical environments. Furthermore, neither

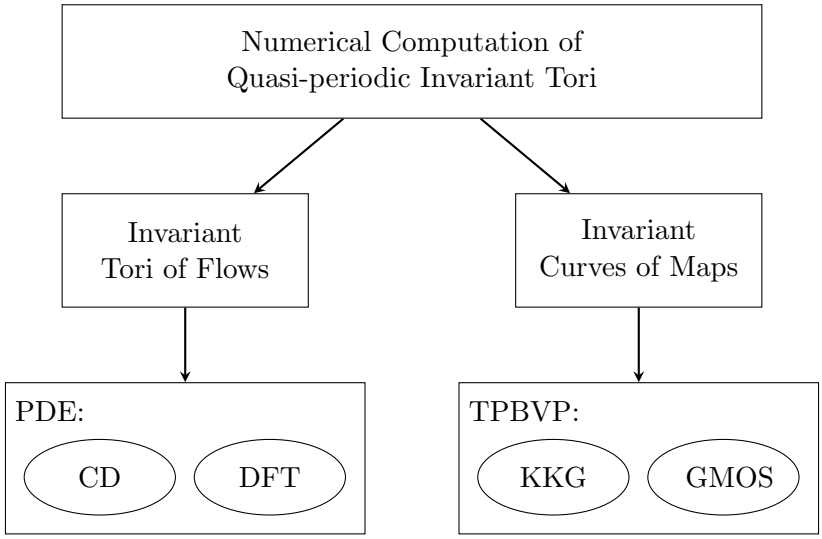

Figure 1.1: Methods for calculating quasi-periodic invariant tori. From left to right: Partial Differential Equation (PDE) solver based on Central Differences (CD), PDE solver based on Discrete Fourier Transform (DFT), Two-Point Boundary Value Problem (TPBVP) for invariant curves of Poincaré maps (KKG), and TPBVP for invariant curves of stroboscopic maps (GMOS).

of these methods has ever been compared with PDE approaches, which also succeed in generating families of quasi-periodic invariant tori in relevant astrodynamics problems [85].

For all these reasons, a comparison between different numerical procedures is first offered in this thesis. This will help us identify which of the proposed methodology should be preferred for formation flying purposes as well as to identify key features that proved to be useful for the remainder of this research. Next, we focus on the design of spacecraft formations starting from the zonal problem about axisymmetric bodies. This and other applications of quasi-periodic invariant tori are further discussed in the following research summary.

1.4 Organization

This thesis begins with a brief overview of dynamical systems theory techniques that are used for calculating low-dimensional invariant sets, i.e., fixed points and periodic orbits. This discussion allows us to introduce some of the notation and terminology used throughout the remainder of this work. For example, we review the predictor-corrector approach proposed by Seydel [100] to continue along family branches of periodic orbits, noting that a similar procedure can be also applied in the quasi-periodic case. We also discuss different approaches for solving Boundary Value Problem (BVP) as this may affect the implementation of some of the numerical procedures adopted for this research. Lastly, we introduce the definition of quasi-periodic invariant tori and highlight some of the fundamental features that may be relevant for our future analyses.

Chapter 3 of this thesis deals with the numerical procedures available in the literature for continuing families of quasi-periodic invariant tori. After reviewing the different methodologies, we propose a simple accuracy test so as to determine which of the candidate procedures should be preferred for practical studies of astrodynamics problems, including the establishment of bounded relative motion in complex dynamical environments. It is found that GMOS gives the most accurate results in the shortest amount of time, making it our preferred choice for our dynamical investigations. Additional benefits offered by this methodology are the possibility of carrying out stability analyses of quasi-periodic trajectories as well as the opportunity to calculate three-dimensional

invarinat tori.

Using these results, the GMOS algorithm is applied in the fourth chapter of this research to calculate quasi-periodic invariant tori in the zonal problem. It is demonstrated that modifications of the numerical procedure are necessary in order to mitigate the issues encountered by Koon et al. when trying to establish bounded relative motion about an axisymmetric model of the Earth [64]. Consequently, we adapt the GMOS algorithm for the numerical computation of entire families of bounded relative trajectories about stable periodic orbits of the RRS.

Moving beyond Earth orbit, Chapter 5 of this thesis explores the computation of bounded relative trajectories in highly perturbed dynamical environments such as the vicinity of asteroids and small planetary satellites. To start off, we consider the asymmetric case of a uniformly rotating tri-axial ellipsoid shaped as the slowly rotating asteroid (4179) Toutatis. The realism of our simulation is further enhanced in second part of this chapter by adding the irregular shape and tumbling motion of the chosen asteroid into our analysis. Lastly, we investigate the possibility of deploying spacecraft formations in the vicinity of Phobos, as this is probably one of the most challenging dynamical environments that are of interest to the astrodynamics community nowadays. It is found that quasi-periodic invariant tori may be extremely useful in understanding the dynamics in the proximity of the Martian moon, as quasi-periodic solutions are much more dominant in the system than resonant periodic orbits considered thus far in the literature.

Finally, Chapter 6 of this thesis deals with dynamical perturbations that have the potential to impact on the bounded relative trajectories identified throughout this thesis. We begin by demonstrating how satellites in LEO, MEO, and GEO formations tend to drift apart due to lunisolar attraction and radiation pressure (SRP). For spacecraft formations at low altitudes, we also model the nonconservative action of atmospheric drag and study the disruptive effects of this dynamical perturbation on the relative motion between two satellites. Lastly, we move beyond Earth's orbit and continue our robustness analysis for spacecraft formations about (4179) Toutatis and Phobos. It is found that countering the effects of SRP would be mandatory for distributed space systems near the complex rotator due to the impact of radiation pressure on the general dynamics

of massless spacecraft. In contrast, spacecraft formations about Phobos seem to be resilient to the oblateness of the Red planet and the eccentricity of the Martian moon, thereby suggesting that DSS could be flown in the vicinity of the small planetary satellite.

1.5 Contributions

The main contributions of this reaserch are divided by topic and summarized in the following list.

- *Numerical computation of quasi-periodic invariant tori:*
  - Comparison between several numerical procedures for computing quasi-periodic invariant tori;
  - Identify which of the existing methodologies should be preferred for practical studies of astrodynamics problems;
  - Adapt the GMOS algorithm for the calculation of three-dimensional tori;
- *Bounded relative motion about axisymmetric bodies:*
  - Understand the dynamics near rotationally symmetric bodies;
  - Modify existing procedures for QP tori to ensure bounded relative motion;
  - Design of spacecraft formations in the Earth's zonal problem;
- *Spacecraft Formation Flying in extreme dynamical environments:*
  - Studying quasi-periodic motion near small bodies;
  - Use quasi-periodic tori to establish bounded relative motion about uniformly rotating tri-axial ellipsoids, complex rotators, and small planetary satellites;
- *Robustness Analysis*
  - Include perturbations to evaluate the impact of unmodeled dynamics on the relative motion;

1.6 Publications

The following are the journal and conference papers resulting from the work completed during this thesis:

Journal Papers

- Baresi, N., Olikara, Z. P., and Scheeres, D. J., "Fully numerical methods for continuing families of quasi-periodic invariant tori in astrodynamics", Submitted to the Journal of Astronautical Sciences. Under Review;
- Baresi, N., and Scheeres, D. J., "Design of bounded relative trajectories in the Earth zonal problem", Journal of Guidance, Navigation, and Control, 2016 [*In Press*];
- Dell'Elce, L., Baresi, N., Naidu, S. P., Benner, L. A. M., and Scheeres, D. J., "Numerical investigation of the dynamical environment of 65803 Didymos", Advances in Space Research, Vol. **59**, No. 5, pp. 1304–1320, 2017;
- Baresi, N., and Scheeres, D. J., "Bounded relative motion under zonal harmonics perturbations", Celestial Mechanics and Dynamical Astronomy, Vol. **127**, No. 4, pp. 527–548, 2016;
- Baresi, N., Scheeres, D. J., and Schaub H., "Bounded relative motion about asteroids for formation flying and applications", Acta Astronautica, Vol. **123**, pp. 364–375, 2016;

Conference Papers

- Baresi, N., and Scheeres, D. J., "Design of bounded relative trajectories in the Earth zonal problem"", AAS/AIAA Space Flight Mechanics meeting, Feb 2017, San Antonio, TX;
- Baresi, N., Dell'Elce, L., and Scheeres, D. J., "The dynamical environment in the vicinity of (65803) Didymos: Applications to the Asteroid Impact & Deflection Assessment mission"", STARDUST final conference, Nov 2016, ESA-ESTEC, The Netherlands;

- Baresi, N., and Scheeres, D. J., "Quasi-periodic invariant tori for time-periodic dynamical systems: applications to small body exploration", 67th International Astronautical Congress, Sep 2016, Guadalajara, Mexico;

- Dell'Elce, L., Baresi, N., Kerschen, G., and Scheeres, D.J., "Robust mission design using invariant manifolds", 67th International Astronautical Congress, Sep 2016;

- Baresi, N., Olikara, Z. P., and Scheeres, D. J., "Survey of numerical methods for computing quasi-periodic invariant tori in astrodynamics", AAS/AIAA Space Flight Mechanics meeting, Feb 2016, Napa, CA;

- Baresi, N., Lubey, D. P., and Scheeres, D. J., "Model estimation using hovering satellites about asteroids", 66th International Astronautical Congress, Oct 2015, Jerusalem, Israel;

- McMahon, J. W., Baresi, N., and Scheeres, D. J., "On the projection of covariance ellipsoids onto non-planar surfaces for small body landing analysis", AAS/AIAA Astrodynamics Specialist conference, Aug 2015, Vail, CO;

- Baresi, N., Scheeres, D. J., and Schaub H., "Bounded relative motion about asteroids for formation flying and applications", 8th International Workshop on Satellite Constellations and Formation Flying, Jun 2015, Delft, The Netherlands;

- Baresi, N., and Scheeres, D. J., "Estimation of asteroid landing trajectories via Line-Of-Sight measurements", AAS/AIAA Astrodynamics Specialist conference, Aug 2014, San Diego, CA;

Chapter 2

Preliminaries

In order to better understand the methodologies implemented to calculate quasi-periodic invariant tori in this research, it is useful to briefly review standard techniques available in the literature to compute low-dimensional invariant sets, i.e., fixed points and periodic orbits. To support the discussion, examples of fixed points and periodic orbits in the Hill approximation of the CRTBP (also known as the Hill Problem (HP)) are shown. Accordingly, the chapter begins with a short discussion of the HP equations of motion along with key properties that are useful to interpret the plots displayed in the following pages. It is important to note, however, that the procedures hereby presented are general in nature and can be applied to a variety of astrodynamics problems with minor adjustments. Because of this, we will try to keep the discussion as more general as possible and without referring to the explicit form of the HP equations for the calculation of its equilibrium points and periodic orbits (Section 2.2 – 2.5). Section 2.6 finally introduces some of the key aspects of quasi-periodic invariant tori that prepare the ground for the numerical procedures of Chapter 3. A more rigorous discussion of tori in several classes of dynamical systems can be found in [14].

2.1 The Hill Problem

Let $\boldsymbol{x} \in \mathbb{R}^n$ be the state vector of a massless spacecraft with a dynamical evolution that is modeled by the smooth Hamiltonian vector field $\boldsymbol{f}(\boldsymbol{x}, \boldsymbol{p}, t) : \mathbb{R}^n \times \mathbb{R}^p \times \mathbb{R} \to \mathbb{R}^n$. Although $\boldsymbol{f}$ may depend explicitly on the independent variable t, it is assumed that $\boldsymbol{f}$ is actually autonomous and

does not depend on any external parameters $\boldsymbol{p}$. In this case, the system of first-order ordinary differential equations reduces to

$$\dot{\boldsymbol{x}} = \boldsymbol{f}(\boldsymbol{x}), \tag{2.1}$$

where $(\dot{-})$ denotes differentiation with respect to time.

A classical example in astrodynamics that falls into the category of problems represented by (2.1) is offered by the Hill approximation of the CRTBP. This approximation applies when the spacecraft is orbiting in the vicinity of a secondary body whose mass is significantly smaller than the mass of the primary, i.e., $(M_s/M_p) << 1$ [49, 50, 98]. In this case, the equations of the CRTBP can be conveniently rewritten in a rotating frame centered on the secondary and simplified in the dimensional formulae of the HP:

$$\begin{cases} \ddot{x} &= 2\,n_S\,\dot{y} + 3\,n_S^2\,x - \dfrac{\mu_S}{r^3}\,x, \\ \ddot{y} &= -2\,n_S\,\dot{x} - \dfrac{\mu_S}{r^3}\,y, \\ \ddot{z} &= -n_S^2\,z - \dfrac{\mu_S}{r^3}\,z, \end{cases} \tag{2.2}$$

where $r = \sqrt{x^2 + y^2 + z^2}$ is the distance from the origin of the coordinate frame, μ_S is the gravitational parameter of the secondary body, and n_S is its mean motion. By scaling the length and time units of the problem such that both n_S and $(\mu_S/n_S^2)^{(1/3)}$ are equal to 1, Eq. (2.2) eventually reduces to the classical form of Hill's equations:

$$\begin{cases} \ddot{x} &= 2\,\dot{y} + 3\,x - \dfrac{x}{r^3}, \\ \ddot{y} &= -2\,\dot{x} - \dfrac{y}{r^3}, \\ \ddot{z} &= -z - \dfrac{z}{r^3}. \end{cases} \tag{2.3}$$

As it can be seen, Eq. (2.3) does not depend on any external parameter and can be easily

rewritten in the form (2.1) via

$$\dot{\boldsymbol{x}} = \boldsymbol{f}(\boldsymbol{x}) = \begin{cases} \dot{x} &= v_x, \\ \dot{y} &= v_y, \\ \dot{z} &= v_z, \\ \dot{v}_x &= 2\,v_y + 3\,x - \dfrac{x}{r^3}, \\ \dot{v}_y &= -2\,v_x - \dfrac{y}{r^3}, \\ \dot{v}_z &= -z - \dfrac{z}{r^3}, \end{cases} \tag{2.4}$$

where $\boldsymbol{x} = \Big[x, \quad y, \quad z, \quad v_x, \quad v_y, \quad v_z,\Big]^T$.

It is worth noting that the system (2.4) admits one integral of motion known as the Jacobi constant:

$$C = T - V = \frac{1}{2}\left(v_x^2 + v_y^2 + v_z^2\right) - \frac{1}{2}\left(3\,x^2 - z^2\right) - \frac{1}{r} \tag{2.5}$$

where $T = \dfrac{1}{2}\left(v_x^2+v_y^2+v_z^2\right)$ represents the kinetic energy of the spacecraft and $V = \dfrac{1}{2}\left(3\,x^2-z^2\right)+\dfrac{1}{r}$ is referred to as the effective potential. Since kinetic energy is a positive-definite quantity, $C+V$ must also be positive, i.e., $V \geq -C$. This inequality defines zones of admissible motion for each specified value of the Jacobi constant. In particular, we are interested in the boundaries of these regions, i.e., the **zero-velocity** curves, as their study can immediately reveal the existence of trapping regions where the motion of massless particles is confined. For the HP, these trapping regions are typically found in the close proximity of the secondary body for low values of C (Fig. 2.1). As soon as the Jacobi constant is allowed to increase, the area and ellipticity of the zero-velocity curves tend to increment until the boundary is no longer close and the spacecraft is allowed to escape from the vicinity of the secondary body. The gates open up as soon as the Jacobi constant reach the "energy" value of the Lagrangian equilibrium points depicted in Fig. 2.1, thereby indicating that the study and analysis of these particular solutions may be beneficial for the understanding of the system dynamics. This situation is encountered in many other classes of dynamical problems, including the infamous CRTBP as well as the motion of spacecraft in the vicinity of uniformly rotating asteroids [96]. Accordingly, a brief overview of fixed points and their stability is first offered in the following

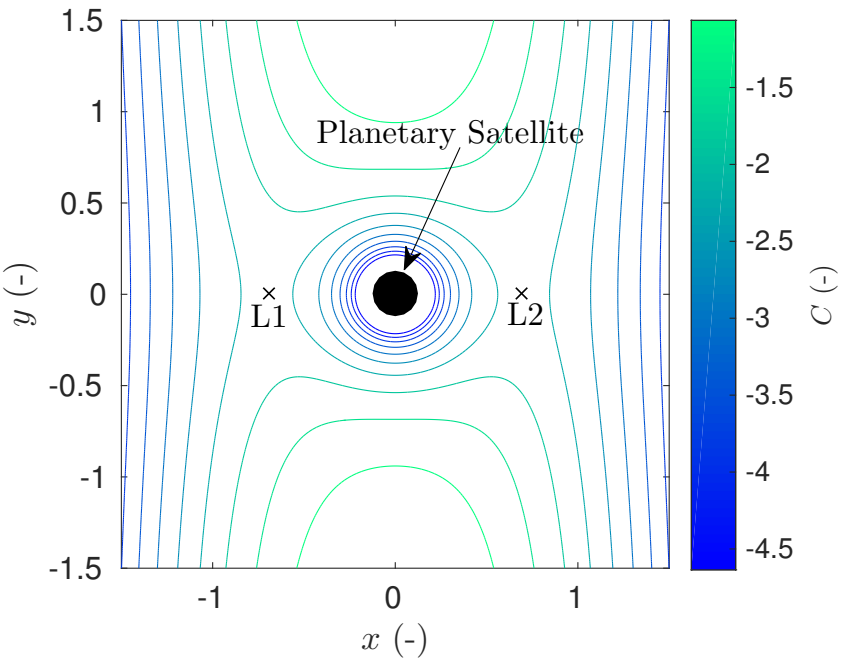

Figure 2.1: The two collinar points of the Hill problem in normalized units. The figure also shows zero-velocity curves defining zones of admissible motion and forbidden regions.

pages.

2.2 Fixed Points

By definition, fixed points $\boldsymbol{x}^*$ are states of the phase space where the dynamics is constantly equal to zero, i.e., $\boldsymbol{f}(\boldsymbol{x^*}) = \boldsymbol{0}$ [76]. Looking at the equations of the Hill problem, it is apparent that–in order for $\boldsymbol{f}(\boldsymbol{x^*}) = \boldsymbol{0}$ to be satisfied–y, z, v_x, v_y, and v_z must be equal to zero. The remaining equation for x reads as $3\,x - \dfrac{x}{|x|^3} = 0$ and gives the final expressions for the HP Lagrangian points: $\boldsymbol{x}^*_{L_1} = \left[-(1/3)^{1/3},\ \ 0,\ \ 0,\ \ 0,\ \ 0,\ \ 0\right]^T$; $\boldsymbol{x}^*_{L_2} = \left[(1/3)^{1/3},\ \ 0,\ \ 0,\ \ 0,\ \ 0,\ \ 0\right]^T$.

Next, we can address the stability of these equilibrium points by studying the dynamics of small perturbations about $\boldsymbol{x}^*$. If $\boldsymbol{x} = \boldsymbol{x}^* + \boldsymbol{w}$ is in a small neighborhood about $\boldsymbol{x}^*$, then

$$\dot{\boldsymbol{x}}^* + \dot{\boldsymbol{w}} = \boldsymbol{f}(\boldsymbol{x}^* + \boldsymbol{w}) \simeq \boldsymbol{f}(\boldsymbol{x}^*) + \left[\frac{\partial \boldsymbol{f}}{\partial \boldsymbol{x}}\right]^* \boldsymbol{w} + H.O.T. \tag{2.6}$$

Since $\dot{\boldsymbol{x}}^* = \boldsymbol{f}(\boldsymbol{x}^*) = 0$, neglecting the high order terms yields the linear system

$$\dot{\boldsymbol{w}} = \left[\frac{\partial \boldsymbol{f}}{\partial \boldsymbol{x}}\right]^* \boldsymbol{w} = A\,\boldsymbol{w}, \tag{2.7}$$

which can be solved using the State Transition Matrix (STM) $\Phi \in \mathbb{R}^{n\times n}$ given by the numerical integration of

$$\dot{\Phi}(t, t_0) = A\,\Phi(t, t_0), \qquad \Phi(t_0, t_0) = I_n, \tag{2.8}$$

where t and t_0 denote the current and initial times, respectively.

Using the STM, one can prove that $\boldsymbol{x}^*$ is stable whenever the real part of all the eigenvalues of A is negative. Conversely, if at least one of the eigenvalues of A has positive real part, the system is unstable as solutions along its associated eigenvector tend to escape from the vicinity of the equilibrium points. Both of these behaviors hold in the original nonlinear system too for as long as all of the eigenvalues of A have nonzero real part. Then, $\boldsymbol{x}^*$ is hyperbolic and Hartman-Grobman theorem can be applied to guarantee that the dynamics in the neighborhood of $\boldsymbol{x}^*$ is well represented by the linearization (2.7) [72]. A third option would be if some of the eigenvalues of A are purely imaginary, e.g., $\pm\mathrm{i}\,\nu$. If that is the case, linear analysis is inconclusive because linear centers have seen to become nonlinear center, stable spiral, or unstable spiral depending on the nonlinear terms appearing in the equations of motion (2.1). One could use nonlinear stability analysis to prove the true nature of the fixed point $\boldsymbol{x}^*$ [72, 76, 95]. However, if a system admits a non-degenerate integral of motion like (2.5) and the purely imaginary eigenvalues are not multiple of the other eigenvalues, then Lyapunov Center Theorem assures that there exists a one-parameter family of periodic orbits emanating from $\boldsymbol{x}^*$ with initial period $T \simeq 2\,\pi/\nu$ [77]. This is indeed observed for the collinear libration points of the Hill problem, as these turn out to be of the saddle $\times$ center $\times$ center type. In this case, for each pair of purely imaginary eigenvalues, there exist a one-parameter family of periodic orbits known as the Lyapunov and vertical periodic orbit families. These and other periodic orbit families may be calculated using the numerical procedures outlined in the next section.

2.3 Periodic Orbits

Periodic orbits are defined as those trajectories that repeat after a minimal period T. Defining the flow of the dynamical system (2.1) to be $\varphi_t(\boldsymbol{x}_0)$ for a generic time t and a generic initial condition $\boldsymbol{x}_0$, then periodic orbits must satisfy the relationship

$$\varphi_T(\boldsymbol{x}_0) - \boldsymbol{x}_0 = \boldsymbol{0}. \tag{2.9}$$

Together with (2.1), Eq. (2.9) defines a BVP that is better tackled as follows. To start off, let us define a new time variable τ such that $t = T\,\tau$ [33]. With this new independent variable, the dynamical system (2.1) reads as

$$\boldsymbol{x}' = T\,\boldsymbol{f}(\boldsymbol{x}), \tag{2.10}$$

where $(-)'$ denotes differentiation with respect to the nondimensional time τ. Since $t = T$ when $\tau = 1$, it is also easy to recast (2.9) as the boundary constraint

$$\boldsymbol{g}(\boldsymbol{x}_0, \boldsymbol{x}_1) := \boldsymbol{x}_1 - \boldsymbol{x}_0 = \boldsymbol{0} \tag{2.11}$$

where $\boldsymbol{x}_1 = \boldsymbol{x}(\tau = 1)$. This normalization limits the time domain of possible solutions on the interval $[0\,,\,1]$, thus enhancing the numerical robustness of the methodologies described in this thesis. Unfortunately, this change in the time scale of the problem still does not prevent the BVP to be ill-posed for a number of reasons.

First, note that, for autonomous systems such as (2.10), any point along the periodic orbit could be a solution of the BVP. Because of this, standard shooting techniques are prone to fail until extra constraints are included in the formulation of the problem. Doedel et al. [32] refer to these constraints as *phase conditions* and propose

$$p(\boldsymbol{x}_0) := \boldsymbol{f}(\tilde{\boldsymbol{x}}_0)^T\,(\boldsymbol{x}_0 - \tilde{\boldsymbol{x}}_0) = 0, \tag{2.12}$$

to anchor the initial conditions $\boldsymbol{x}_0$ in the plane perpendicular to $\boldsymbol{f}(\tilde{\boldsymbol{x}}_0)^T$. The same author refers to $\tilde{\boldsymbol{x}}_0$ as a *previously known solution* of the BVP, and, for the purpose of this dissertation, it can either be a linear approximation of the researched periodic orbit or a nearby periodic orbit previously

computed. Although other forms exist, this is also the equation that we generally refer to when talking about phase conditioning. Differences in the implementation of $p(\boldsymbol{x}_0)$ will be noted when opportune.

Second, observe that the period of the periodic orbit is generally not known a-priori and needs to be solved for by our numerical procedure. To find values of T, we leverage the family structure in which periodic orbits of autonomous systems are generally organized in. Consequently, instead of fixing the period directly, we allow for changes in $\boldsymbol{x}_0$ and T along the curve representing the periodic orbit family in the $(\boldsymbol{x}_0, T)$ plane, and that satisfy the *pseudo-arclength continuation* constraint:

$$s(\boldsymbol{x}_0, T) := \tilde{\boldsymbol{x}}_0'^T (\boldsymbol{x}_0 - \tilde{\boldsymbol{x}}_0) + \tilde{T}' (T - \tilde{T}) - \delta s = 0, \tag{2.13}$$

where $\boldsymbol{z}' = \begin{bmatrix} \tilde{\boldsymbol{x}}_0' & \tilde{T}' \end{bmatrix}^T$ denotes the *family tangent* computed in $(\tilde{\boldsymbol{x}}_0, \tilde{T})$, and δs represents the *continuation step-length* [34]. The constraint (2.13) has been advocated by many authors including [32, 61] for robustness and because local extrema such as the one portrayed in Fig. 2.4 are easily handled and overcome. Thus, it also represents our preferred choice moving forward.

Ultimately, the computation of several members of a periodic orbit family can be formulated as a BVP such that

$$\begin{cases} \boldsymbol{x}' &= T\, \boldsymbol{f}(\boldsymbol{x}), \\ T' &= 0, \end{cases} \tag{2.14}$$

subject to the boundary constraints

$$\boldsymbol{F}(\boldsymbol{x}_0, T) = \begin{bmatrix} \boldsymbol{g}(\boldsymbol{x}_0, \boldsymbol{x}_1) \\ p(\boldsymbol{x}_0) \\ s(\boldsymbol{x}_0, T) \end{bmatrix} = \boldsymbol{0}. \tag{2.15}$$

To find a unique solution of (2.14)–(2.15), consider the predictor-corrector scheme proposed by Seydel (Fig. 2.2, [100]) and outlined in the following subsections.

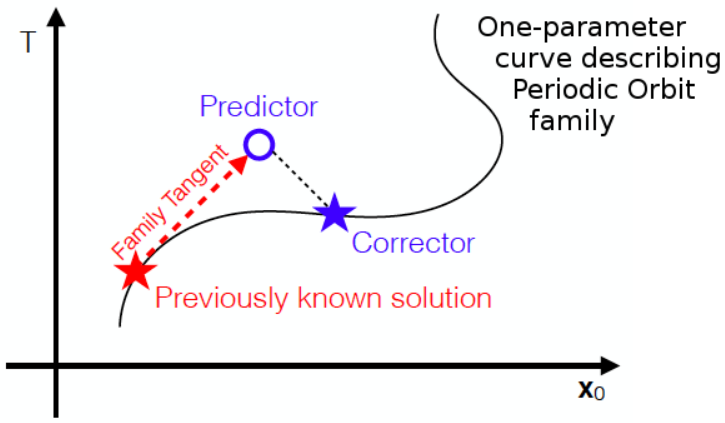

Figure 2.2: Predictor-corrector scheme for computing families of periodic orbits.

2.3.1 Predictor

First, assume a nearby periodic orbit $(\tilde{\boldsymbol{x}}_0, \tilde{T})$ of a one-parameter family is either given or initialized in the center subspace of an equilibrium point with $\tilde{T} \simeq 2\,\pi/\nu$ as specified by Lyapunov Center Theorem. In this case, one has that the periodicity constraint and the phase condition (2.12) must be approximately equal to zero:

$$\boldsymbol{h}(\tilde{\boldsymbol{x}}_0, \tilde{T}) = \begin{bmatrix} \tilde{\boldsymbol{x}}_1 - \tilde{\boldsymbol{x}}_0 \\ p(\tilde{\boldsymbol{x}}_0) \end{bmatrix} \simeq \boldsymbol{0}. \tag{2.16}$$

Now consider $\boldsymbol{h}(\tilde{\boldsymbol{x}}_0(s), \tilde{T}(s))$ to be a function of the arclength s, so that, by differentiation,

$$\left.\frac{\partial \boldsymbol{h}}{\partial \boldsymbol{x}}\right|_{(\tilde{\boldsymbol{x}}_0, \tilde{T})} \tilde{\boldsymbol{x}}_0' + \left.\frac{\partial \boldsymbol{h}}{\partial T}\right|_{(\tilde{\boldsymbol{x}}_0, \tilde{T})} \tilde{T}' = \begin{bmatrix} \boldsymbol{h}_{\boldsymbol{x}}(\tilde{\boldsymbol{x}}_0, \tilde{T}) & \boldsymbol{h}_T(\tilde{\boldsymbol{x}}_0, \tilde{T}) \end{bmatrix} \boldsymbol{z}' = [D\boldsymbol{h}]\,\boldsymbol{z}' = \boldsymbol{0}. \tag{2.17}$$

Eq. (2.17) shows that the family tangent $\boldsymbol{z}' \in \ker([D\boldsymbol{h}])$ with $\dim[\ker([D\boldsymbol{h}])] = 1$. Therefore, $\boldsymbol{z}'$ can be computed using, for instance, the single value decomposition of $[D\boldsymbol{h}]$. Accordingly, an initial guess for a new periodic orbit inside the family can be simply generated via

$$\begin{aligned} \boldsymbol{x}_0 &= \tilde{\boldsymbol{x}}_0 + \delta s\, \tilde{\boldsymbol{x}}_0', \\ T &= \tilde{T} + \delta s\, \tilde{T}', \end{aligned} \tag{2.18}$$

where δs is again the continuation step-length introduced in Eq. 2.13. These approximations give a reliable initial guess for the second part of the algorithm, which aims at refining the values of $(\boldsymbol{x}_0, T)$ until all of the boundary constraints (2.15) are met with satisfactory accuracy.

2.3.2 Corrector

Since $(\boldsymbol{x}_0, T)$ are only predicted values, it is unlikely that all of the constraints in Eq. (2.15) are immediately satisfied. Nevertheless, provided that $(\boldsymbol{x}_0, T)$ is sufficiently close to the true solution, Newton's method can be applied to update the initial guess until the L2-norm of (2.15) is zero within some tolerated margin: $\|\boldsymbol{F}(\boldsymbol{x}_0, T)\| \leq Tol$. To that end, consider expanding $\boldsymbol{F}(\boldsymbol{x}_0, T)$ to the first order in the vicinity of $(\boldsymbol{x}_0, T)$ such that

$$\boldsymbol{F}(\boldsymbol{x}_0 + \delta\boldsymbol{x}, T + \delta T) \simeq \boldsymbol{F}(\boldsymbol{x}_0, T) + [D\boldsymbol{F}] \begin{bmatrix} \delta\boldsymbol{x} \\ \delta T \end{bmatrix} + H.O.T., \tag{2.19}$$

where

$$[D\boldsymbol{F}] = \begin{bmatrix} \dfrac{\partial \boldsymbol{x}_1}{\partial \boldsymbol{x}_0} - I_n & \dfrac{\partial \boldsymbol{x}_1}{\partial T} \\ \dfrac{\partial p(\boldsymbol{x}_0)}{\partial \boldsymbol{x}_0} & 0 \\ \dfrac{\partial s(\boldsymbol{x}_0, T)}{\partial \boldsymbol{x}_0} & \dfrac{\partial s(\boldsymbol{x}_0, T)}{\partial T} \end{bmatrix} = \begin{bmatrix} M - I_n & \boldsymbol{f}(\boldsymbol{x}_1) \\ \boldsymbol{f}(\tilde{\boldsymbol{x}}_0)^T & 0 \\ \tilde{\boldsymbol{x}}_0'^T & \tilde{T}' \end{bmatrix}, \tag{2.20}$$

and I_n is the $n \times n$ identity matrix. Also notice that $\dfrac{\partial \boldsymbol{x}_1}{\partial \boldsymbol{x}_0}$ corresponds to the state transition matrix integrated over one orbital period. Such a matrix is known as the *monodromy matrix* M and turns out to be extremely useful in analyzing the stability of the periodic orbit (see Section 2.5). Similarly, $\dfrac{\partial \boldsymbol{x}_1}{\partial T}$ describes variations of the terminal state with respect to T and is equivalent to $\boldsymbol{f}(\boldsymbol{x}_1)$.

Now assume that $\boldsymbol{F}(\bar{\boldsymbol{x}}_0 + \delta\boldsymbol{x}, \bar{T} + \delta T) \simeq \boldsymbol{0}$, so that equation (2.19) can be rearranged and solved for in terms of $\begin{bmatrix} \delta\boldsymbol{x}^T & \delta T \end{bmatrix}^T$ via

$$\begin{bmatrix} \delta\boldsymbol{x} \\ \delta T \end{bmatrix} = -[D\boldsymbol{F}]^\dagger \, \boldsymbol{F}(\bar{\boldsymbol{x}}_0, \bar{T}), \tag{2.21}$$

where $[D\boldsymbol{F}]^\dagger$ is the left pseudo-inverse of the jacobian matrix $[D\boldsymbol{F}] \in \mathbb{R}^{(n+2)\times(n+1)}$. Iterating this process yields a recursive formula that shall be repeated until the norm of $\boldsymbol{F}(\boldsymbol{x}_0^{(k)}, T^{(k)})$ is below the chosen tolerance:

$$\begin{bmatrix} \boldsymbol{x}_0^{(k+1)} \\ T^{(k+1)} \end{bmatrix} = \begin{bmatrix} \boldsymbol{x}_0^{(k)} \\ T^{(k)} \end{bmatrix} - [D\boldsymbol{F}^{(k)}]^\dagger \, \boldsymbol{F}(\boldsymbol{x}_0^{(k)}, T^{(k)}). \tag{2.22}$$

Upon convergence, the algorithm produces a solution to the BVP that can be used to reinitialize the predictor-corrector scheme and march along the branch of the considered periodic orbit family. For continuing along the family, one needs to update the values of $(\tilde{\boldsymbol{x}}_0, \tilde{T})$ with the newly found solution and recompute the family tangent as discussed in Sec. 2.3.1. From there, predicted states can be generated and feed into the corrector part of the numerical procedure until a new periodic orbit is found. This solution can be given in input to the predictor part of the algorithm once again, and the process repeated until the entire family branch is calculated or the corrector stops converging. Fig. 2.3 shows an example of a periodic orbit family computed in the HP. Specifically, the plot displays several members of the L1 southern Halo family obtained with one single iteration

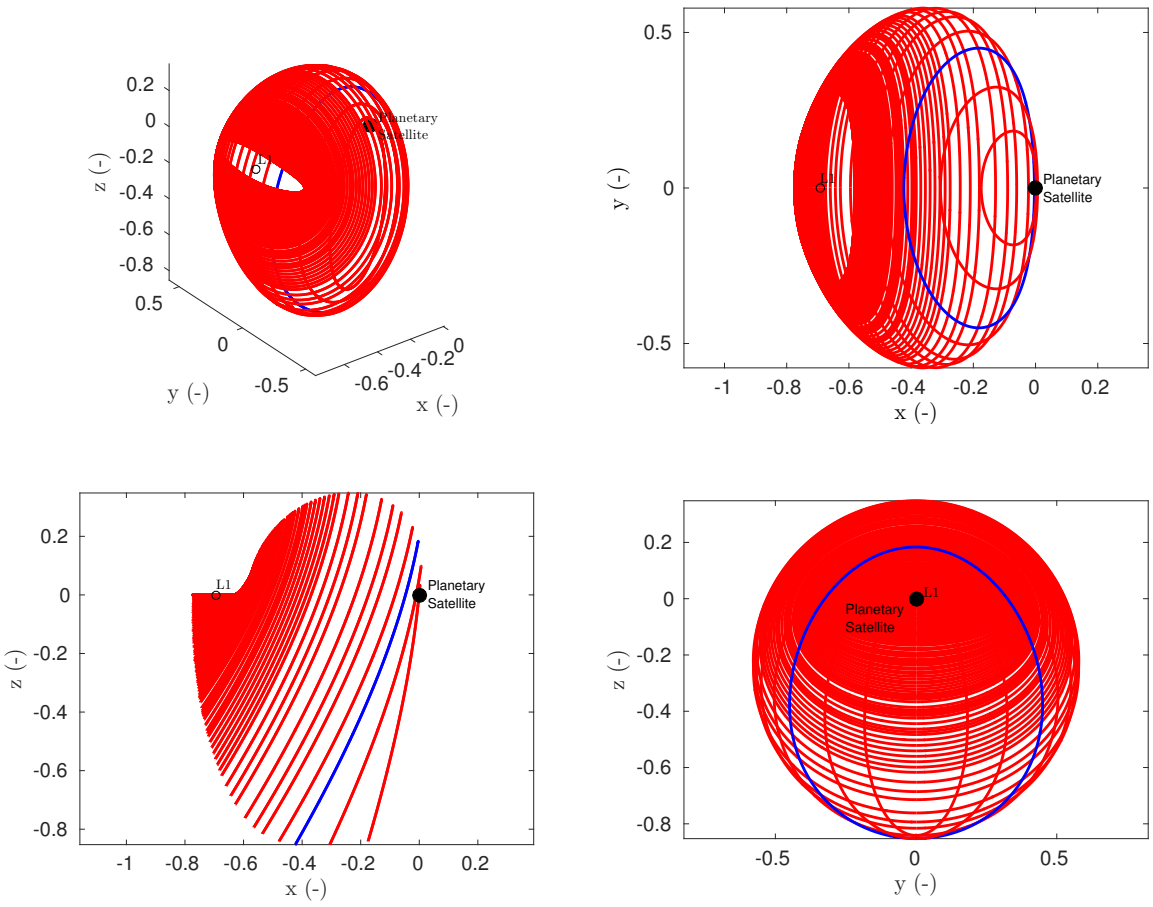

Figure 2.3: Examples of Southern Halo orbits about the first libration point of the Hill problem. The trajectories in red are unstable, whereas the trajectory in blue is stable. See 2.5 for details.

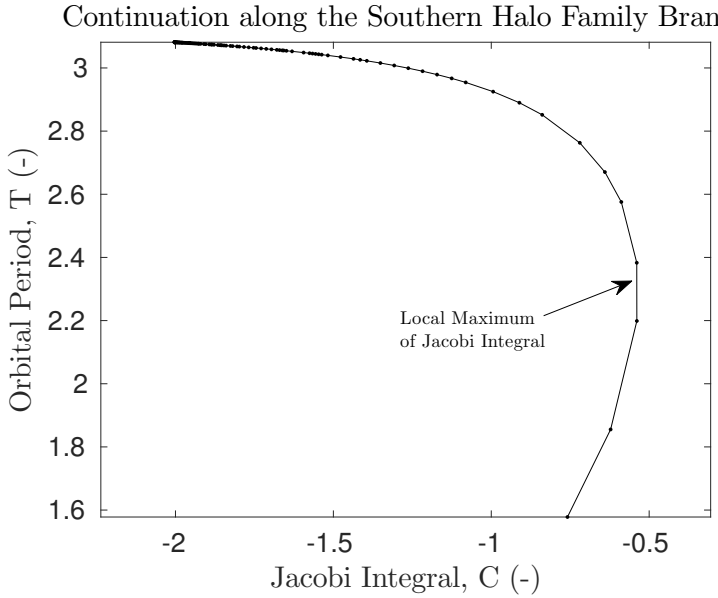

Figure 2.4: Continuation of the Southern Halo family branch.

of the algorithm. The same periodic orbits are finally organized in terms of orbital period and Jacobi integral to demonstrate the effectiveness of the proposed methodology in handling turning points and local extrema such as the one of Fig. 2.4.

2.4 Shooting vs Collocation techniques

Although representative of the numerical procedure considered in this thesis for computing periodic orbits, the algorithm outlined in the previous section is just one of several approaches that can be applied in order to solve BVPs. In that case, the equations of motion are integrated from $\boldsymbol{x}_0$, $\tau_0 = 0$ until $\tau = 1$ along with the variational equations

$$\dot{\Phi}(\tau, \tau_0) = A(\tau)\,\Phi(\tau, \tau_0), \qquad \Phi(\tau_0, \tau_0) = I_n, \tag{2.23}$$

so that $\boldsymbol{x}_1$ and M can be generated and plugged into $\boldsymbol{F}(\boldsymbol{x}_0, T)$ and $D\boldsymbol{F}(\boldsymbol{x}_0, T)$, respectively. Such a procedure is usually referred to as *single-shooting* (Figure 2.5(a)), and despite being attractive for its simplicity, it also suffers from stability issues when integrating trajectories near highly unstable regions.

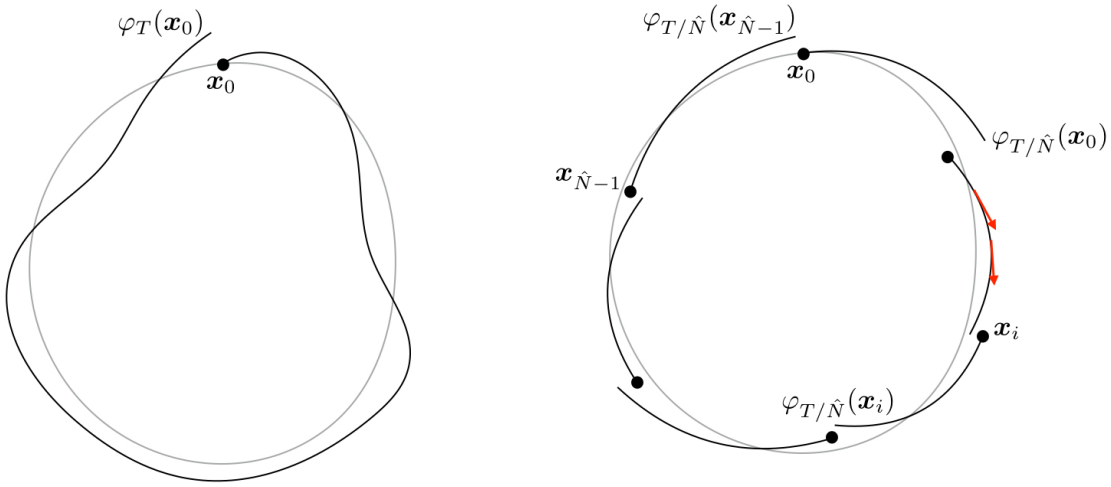

(a) Single-shooting

(b) Multiple-shooting

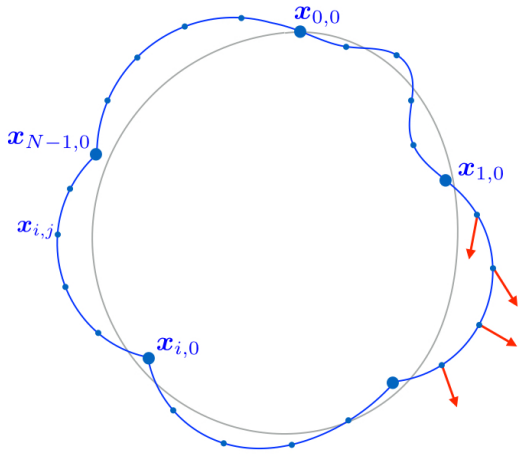

(c) Collocation

Figure 2.5: Shooting VS collocation techniques. The red arrows illustrate the direction of the force field at different points along the trajectory, showing that the equations of motion are readily satisfied in shooting approaches. Conversely, the vector field may not be necessarily tangent to collocation iterations until convergence.

A straightforward solution to this problem is to split the integration interval into $\hat{N}$ segments so as to limit the growth of the round-off error below some acceptable threshold. This approach is usually referred to as *multiple-shooting* (Figure 2.5(b)) and fall into the same category of Initial Value Problems (IVP) where trajectories need to be integrated by means of standard numerical integrators like Runge-Kutta or multistep methods [4].

Differently from the previous two approaches, collocation does not rely on any numerical integrator. Rather, the solution is approximated with a piece-wise continuous polynomial using a two-level discretization procedure (Figure 2.5(c)). First, the time domain is split in N subintervals $[\tau_i, \tau_{i+1}]$, $i = 0, \ldots, N-1$ for robustness and accuracy reasons. Second, the solution is evaluated in correspondence of the roots of a m-th degree Legendre polynomial over each of the N subintervals. Accordingly, let $\boldsymbol{x}_{i,j}$, $j = 0, \ldots, m-1$ be the *collocation points* for the i-th interval $[\tau_i, \tau_{i+1}]$, so that the solution over this entire subdomain may be approximated via Lagrange interpolation using

$$\boldsymbol{x}(\tau) = \sum_{j=0}^{m} \boldsymbol{x}_{i,j}\, L_j(\tau), \qquad \forall\, \tau \in [\tau_i, \tau_{i+1}] \tag{2.24}$$

with

$$L_j(\tau) = \prod_{\substack{k=0 \\ k \neq j}}^{m-1} \frac{\tau - \tau_k}{\tau_j - \tau_k}. \tag{2.25}$$

From (2.24), it also follows that

$$\boldsymbol{x}'(\tau) = \sum_{j=0}^{m} \boldsymbol{x}_{i,j}\, L'_j(\tau), \tag{2.26}$$

where

$$L'_j(\tau) = L_j(\tau) \sum_{\substack{k=0 \\ k \neq j}}^{m-1} \frac{1}{\tau - \tau_k}. \tag{2.27}$$

However, there is no guarantee that the interpolating polynomial is actually satisfying the equations of motion (2.1). To that end, one has to enforce the collocation constraints

$$\boldsymbol{x}'(\tau) = T\, \boldsymbol{f}(\boldsymbol{x}) \tag{2.28}$$

for all of the $N \times m$ collocation points $\boldsymbol{x}_{i,j}$, $i = 0, \cdots, N-1$, $j = 1, \ldots, m$. Furthermore, in order for the solution to be continuous, the following must be true:

$$\boldsymbol{x}(\tau_{i+1}) = \sum_{j=0}^{m} \boldsymbol{x}_{i,j}\, L_j(\tau_{i+1}). \tag{2.29}$$

Eq. (2.26), (2.28), and (2.29) form the total set of $[N\,(m+1)]\,n$ continuity and collocation

constraints that need to be appended to the error vector (2.15):

$$\begin{cases} c_c(\boldsymbol{X}) & := \quad \boldsymbol{x}_{i+1,0} - \sum_{j=0}^{m} \boldsymbol{x}_{i,j}\, L_j(\tau_{i+1}) = \boldsymbol{0}, & i = 0, \cdots, N-1 \\ c_d(\boldsymbol{X}, T) & := \quad T\, \boldsymbol{f}(\boldsymbol{x}_{i,j}) - \sum_{j=0}^{m} \boldsymbol{x}_{i,j}\, L_j'(\tau_j) = \boldsymbol{0}, & i = 0, \cdots, N-1; \quad j = 1, \cdots, m. \end{cases} \tag{2.30}$$

where $\boldsymbol{X} = \begin{bmatrix} \boldsymbol{x}_{0,0}, & \boldsymbol{x}_{0,1}, & \ldots, & \boldsymbol{x}_{N-1,m-1}, & \boldsymbol{x}_{N,0} \end{bmatrix}^T$ is the collection of all of the collocation points of a given periodic orbit, and n is the dimension of the state vector.

Typical values of N and m are between $50-100$ and $6-9$, respectively, illustrating the major drawback of collocation: Newton's method must be used to solve for $[N\,(m+1)]\,n+1$ variables, rather than either $n+1$ or $n\,\hat{N}+1$ as in the single-shooting and multiple-shooting cases.

Despite this increase in complexity, collocation techniques are still very attractive because of their stability and large basin of attraction. This follows from the fact that the solution is represented globally rather than through a set of a few discretized points, making it possible to consider integral constraints such as

$$p_{coll}(\boldsymbol{x}(\tau)) \quad := \quad \int_0^1 \boldsymbol{f}(\tilde{\boldsymbol{x}}(\tau))^T \left(\boldsymbol{x}(\tau) - \tilde{\boldsymbol{x}}(\tau)\right) \mathrm{d}\tau = 0, \tag{2.31}$$

$$s_{coll}(\boldsymbol{x}(\tau), T) \quad := \quad \int_0^1 \tilde{\boldsymbol{x}}(\tau)'^T \left(\boldsymbol{x}(\tau) - \tilde{\boldsymbol{x}}(\tau)\right) \mathrm{d}\tau + \tilde{T}' \left(T - \tilde{T}\right) - \delta s = 0 \tag{2.32}$$

that are found to be more robust than (2.12) and (2.13), respectively [33]. The reason for this being that both of the phase condition and pseudo-arclength continuation constraints are now evaluated over the entire trajectory rather than at a single point of the periodic orbit as in the single-shooting technique.

Following these improvements, one has the total set of constraints for the collocation method is given by

$$\boldsymbol{F}_{coll}(\boldsymbol{X}, T) = \begin{bmatrix} \boldsymbol{g}(\boldsymbol{x}_{0,0}, \boldsymbol{x}_{N,0}) \\ c_c(\boldsymbol{X}) \\ c_d(\boldsymbol{X}, T) \\ p_{coll}(\boldsymbol{X}) \\ s_{coll}(\boldsymbol{X}, T) \end{bmatrix}. \tag{2.33}$$

From (2.33), the monodromy matrix associated with the researched periodic orbit can be also inferred as a byproduct of the proposed methodology [83]. Specifically, if $\boldsymbol{F}_{coll}(\boldsymbol{X}, T) = \boldsymbol{0}$, the same must be true for the periodicity, continuation, and collocation constraints only. Let $\boldsymbol{G}(\boldsymbol{X}, T)$ be the collection of (2.11) and (2.30), such that $\boldsymbol{G}(\boldsymbol{X}, T) = \boldsymbol{0}$. By differentiation of this, one has that

$$\boldsymbol{G}_{\boldsymbol{X}}(\boldsymbol{X}, T)\,\delta\boldsymbol{X} + \boldsymbol{G}_{T}(\boldsymbol{X}, T)\,\delta T = \boldsymbol{0}, \tag{2.34}$$

which is also equivalent to

$$\boldsymbol{G}_{\boldsymbol{x}_{0,0}}(\boldsymbol{X}, T)\,\delta\boldsymbol{x}_{0,0} + \boldsymbol{G}_{\boldsymbol{x}_{0,1},\ldots,\boldsymbol{x}_{N,0}}(\boldsymbol{X}, T)\,\begin{bmatrix}\delta\boldsymbol{x}_{0,1}, & \ldots, & \delta\boldsymbol{x}_{N,0}\end{bmatrix}^{T} + \boldsymbol{G}_{T}(\boldsymbol{X}, T)\,\delta T = \boldsymbol{0} \tag{2.35}$$

according to our previous definition of $\boldsymbol{X}$.

Since $\delta\boldsymbol{x}_{0,0} = I_n\,\delta\boldsymbol{x}_{0,0}$, the latter may be also rewritten in matrix form as

$$\delta\boldsymbol{X} = \begin{bmatrix} I_n \\ -B^{\dagger}\,A \end{bmatrix}\delta\boldsymbol{x}_{0,0} + \begin{bmatrix} O_n \\ -B^{\dagger}\,C \end{bmatrix}\delta T, \tag{2.36}$$

which supplies a relationship between perturbations in $\delta\boldsymbol{x}_{0,0}$ and δT and state deviations at future instances of time. Of course, $A = \boldsymbol{G}_{\boldsymbol{x}_{0,0}} \in \mathbb{R}^{n\,[N\,(m+1)+1]\times n}$, $B = \boldsymbol{G}_{\boldsymbol{x}_{0,1},\ldots,\boldsymbol{x}_{N,0}} \in \mathbb{R}^{n\,[N\,(m+1)+1]\times n\,[N\,(m+1)]}$, $C = \boldsymbol{G}_{T}(\boldsymbol{X}, T) \in \mathbb{R}^{n\,[N\,(m+1)+1]}$, whereas I_n, O_n denote the $n \times n$ identity and zero matrices, respectively. Following this convention, one sees that the last n-th rows of $-B^{\dagger}\,A$ are responsible for mapping deviations in the initial state $\delta\boldsymbol{x}_{0,0}$ into deviations in the final state $\delta\boldsymbol{x}_{N,0}$, thus proving that the monodromy matrix of the periodic orbit can be also calculated without integrating the variational equations of the system. Such a matrix is fundamental in analyzing the stability of periodic solutions, which is why the fundamental properties of M are further discussed in the next section.

2.5 Stability of Periodic Orbits

The stability of periodic orbits is typically studied via the monodromy matrix M, i.e., the STM integrated over one orbital period. To prove this, consider small perturbations about the

initial state of the computed periodic orbit $\boldsymbol{x}_0$: $\boldsymbol{w}(t_0) = \delta\boldsymbol{x}_0$. Since the STM maps initial deviations forward in time, after k orbital periods

$$\boldsymbol{w}(T^k) = \Phi(T^k, t_0)\,\boldsymbol{w}(t_0) = \Phi(T^k, T^{k-1})\,\ldots\,\Phi(T, t_0)\,\boldsymbol{w}(t_0) = M^k\,\boldsymbol{w}(t_0) \tag{2.37}$$

Therefore, in order for the periodic orbit to be stable, all of the eigenvalues λ_i, $i = 1, \ldots, n$ of M should have magnitude less than one, i.e.,

$$|\lambda_i| \leq 1, \qquad \forall i = 1, \ldots, n. \tag{2.38}$$

Unfortunately, although applicable to different classes of dynamical systems, the latter condition turns out to be weak when dealing with the Hamiltonian systems that are often encountered in astrodynamics. In fact, according to the theory of Hamiltonian Dynamical Systems [98], for each $\lambda \in \mathbb{R}$, $1/\lambda$ is also an eigenvalue of M. Similarly, if $\lambda \in \mathbb{C}$, then $\bar{\lambda}$ and $1/\bar{\lambda}$ are both eigenvalues of M. This means that for any eigenvalue λ_i such that $|\lambda_i| < 1$, there exist a reciprocal eigenvalue with $|1/\lambda_i| > 1$, leaving us with the only possible conclusion that periodic orbits are stable if and only if all of the eigenvalues of M have unity magnitude.

To calculate these eigenvalues, it is worth noting that autonomous Hamiltonian systems like the HP offer additional advantages that can significantly reduce the computational burden of this procedure. For instance, if $\varphi_T(\boldsymbol{x}_0) = \boldsymbol{x}_0$ is a periodic solution of (2.1), then

$$\varphi_T(\boldsymbol{x}_0 + \boldsymbol{w}) \simeq \varphi_T(\boldsymbol{x}_0) + M\,\boldsymbol{w} + H.O.T. = \boldsymbol{x}_0 + \boldsymbol{w}. \tag{2.39}$$

Neglecting the high-order terms finally yields $(M - I_n)\,\boldsymbol{w} = \boldsymbol{0}$, thus proving that 1 is always an eigenvalue of M. If that is the case, a second eigenvalue must also be equal to unity, meaning that the characteristic polynomial of a 6-by-6 monodromy matrix can be further simplified in

$$\begin{aligned} \det(M - \lambda\, I_n) &= (\lambda - 1)^2\,(\lambda - \lambda_1)\,(\lambda - 1/\lambda_1)\,(\lambda - \lambda_2)\,(\lambda - 1/\lambda_2), \\ &= (\lambda - 1)^2\,(\lambda^2 + p\,\lambda + 1)\,(\lambda^2 + q\,\lambda + 1), \end{aligned} \tag{2.40}$$

where λ_1, $1/\lambda_1$, λ_2, $1/\lambda_2$ are the remaining non trivial eigenvalues, $p = -(\lambda_1 + 1/\lambda_1)$, and $q = -(\lambda_2 + 1/\lambda_2)$. Accordingly, in order for a periodic orbit to be stable, p and q must be real with

$k = \max(|\mathrm{Re}(p)|, |\mathrm{Re}(q)|) < 2$. The latter is referred to as the *stability index* and will be used throughout this thesis to assess the stability of periodic orbits [51].

Following Bray and Goumas [12], the value of p and q can be calculated via

$$p, q = \frac{\alpha \pm \sqrt{a^2 - 4\,\beta + 8}}{2}, \tag{2.41}$$

where $\alpha = 2 - \mathrm{trace}(M)$, and $\beta = \dfrac{\alpha^2 - \mathrm{trace}(M^2)}{2} + 1$. Furthermore,

$$1/\lambda_1, \lambda_1 = \frac{-p \pm \sqrt{p^2 - 4}}{2} \qquad 1/\lambda_2, \lambda_2 = \frac{-q \pm \sqrt{q^2 - 4}}{2}, \tag{2.42}$$

which provide the system dynamicist with a fast and reliable way to compute the eigenvalues of the monodromy matrix of any periodic orbit of a six-dimensional autonomous Hamiltonian system.

Of course, once the eigenvalues of M have been determined, one can also look at the corresponding eigenvectors to compute the invariant manifolds associated with the periodic orbit. For instance, except for the stable blue trajectory of Fig. 2.3, all of Southern Halo orbits about the HP L1 point have one pair of real reciprocal eigenvalues and one pair of complex conjugate eigenvalues with unitary magnitude (plus, of course, the unitary pair, which is usually neglected for stability analyses). By integrating perturbations along the stable or unstable eigenvectors for different locations along the periodic orbit backward and forward in time, one can trace out the two-dimensional stable and unstable manifolds emanating from each of the Southern Halo orbits (Fig. 2.6).

As for the eigenvectors associated with the complex conjugate eigenvalue pair, one can also integrate perturbations in this center subspace, thereby obtaining trajectories that not only never depart from the neighborhood of the periodic orbit, but also never repeat exactly after one orbital period.[1] As it turns out, these trajectories are only *quasi-periodic* and tend to cover the surface of a two-dimensional invariant torus as $t \to \infty$ (Fig. 2.7). These invariant manifolds are the real subject of this thesis and are formally introduced in the next section.

[1] In practice, this is difficult to see because of the numerical integration errors that build up exponentially, causing the integrated trajectory to leave along the unstable manifold

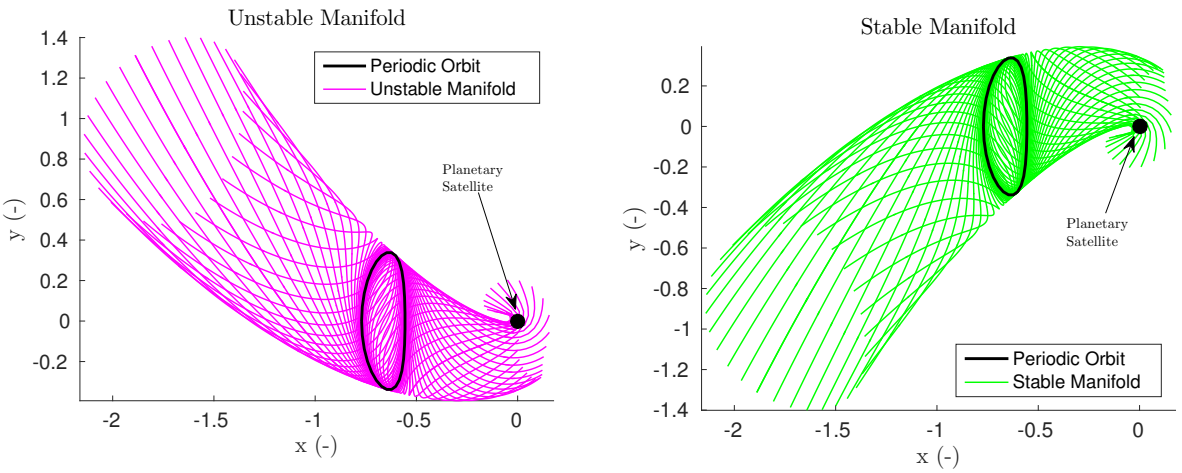

(a) (b)

Figure 2.6: Top view of the Unstable and Stable Invariant Manifolds emanating from a Southern Halo orbit about the L1 point of the Hill problem.

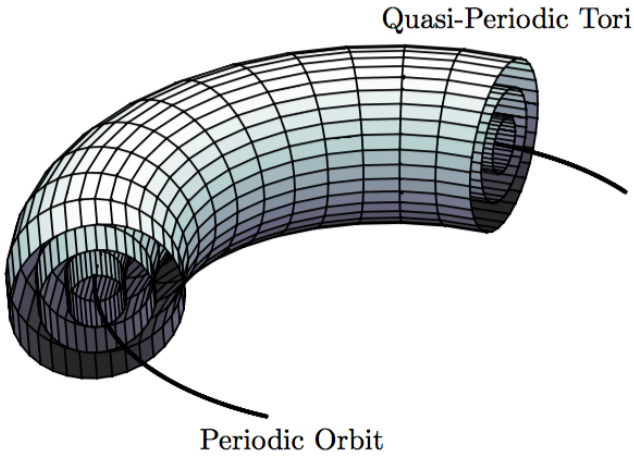

Figure 2.7: Quasi-periodic invariant tori in the center manifold of a periodic orbit

2.6 Quasi-periodic Invariant Tori

As observed in Section 2.5, quasi-periodic trajectories tend to cover the surface of a manifold whose topology resembles the one of a torus. Accordingly, in order to study quasi-periodic motion, consider the general case of a d-dimensional torus parametrized by d angular variables $\boldsymbol{\theta} = \begin{bmatrix} \theta_0, & \theta_1, & \dots & \theta_{d-1} \end{bmatrix}^T \in \mathbb{T}^d$. By definition, the vector field $\boldsymbol{f}$ induces *parallel motion* on $\mathcal{T} = \left\{ \boldsymbol{u}(\boldsymbol{\theta}) | \boldsymbol{\theta} \in \mathbb{T}^d \right\}$ if there exist a diffeomorphism $\boldsymbol{u}(\boldsymbol{\theta}) : \mathbb{T}^d \to \mathcal{T} \in \mathbb{R}^n$ such that the restriction

of the vector field to the set $\mathcal{T}$, namely $\boldsymbol{f}|_{\mathcal{T}}$, is mapped by the inverse of the differential map $D\boldsymbol{u}^{-1}$ into a constant vector field on the torus [14]:

$$\dot{\boldsymbol{\theta}} = \boldsymbol{\omega}. \tag{2.43}$$

If that is the case, trajectories initialized on the surface of the torus never depart from it, and the manifold is invariant for the dynamical system (2.1). $\boldsymbol{u}$ is sometimes referred to as the *torus function* (Fig. 2.8), whereas $\boldsymbol{\omega} = \begin{bmatrix} \omega_0, \ldots, \omega_{d-1} \end{bmatrix}^T \in \mathbb{R}^d$ is known as the *frequency vector* and, depending on its form, it determines the nature of the torus. For instance, if $\boldsymbol{k}$ is a vector of d integer numbers $\in \mathbb{Z}^d$, then $\mathcal{T}$ is a *quasi-periodic* or non-resonant torus if and only if $\boldsymbol{k} \cdot \boldsymbol{\omega} \neq 0, \forall \boldsymbol{k} \neq \boldsymbol{0}$. Conversely, if $\boldsymbol{k} \cdot \boldsymbol{\omega} = 0$ for some $\boldsymbol{k} \neq \boldsymbol{0}$, the torus is *resonant* and foliated by subtori of smaller dimension.

For the remaining of this thesis, we are going to tacitly assume that all of our invariant tori are actually non-resonant, i.e., they meet the non-resonant condition discussed above. Note that this is weaker than the *Diophantine* condition required by KAM theory for proving the existence and persistence of quasi-periodic invariant tori of integrable systems under small nonlinear perturbations [3, 28]. As such, we will not pursue the direct application of KAM theory to the classes of dynamical

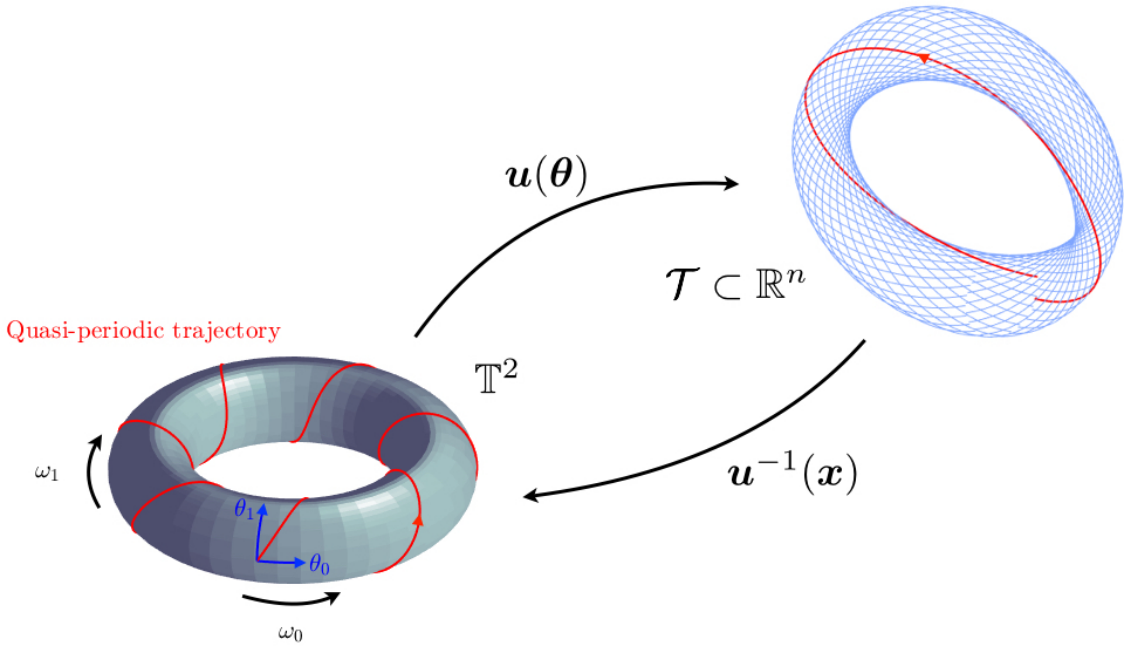

Figure 2.8: Illustration of a torus function for a two-dimensional quasi-periodic invariant torus.

problems being investigated in this manuscript. Nevertheless, some of the key results of KAM theory remain applicable to our discussion. For example, it is relevant for us that quasi-periodic invariant tori are generally organized in families that may be parametrized by Cantor sets of parameters. It is also found that the gaps in these Cantor sets are usually very small and do not prevent continuation scheme such as the predictor-corrector of Section 2.3 to be valid [42] & [83].

As for the number of parameters required to uniquely identify quasi-periodic tori within their families, Jorba and Villanueva [59] propose the following rule of thumb: generally speaking, d-dimensional quasi-periodic invariant tori of n-dimensional Hamiltonian systems that do not depend on any external parameters are organized in d-parameter families. Therefore, two-dimensional tori in the HP are organized in two-parameter families, three-dimensional tori in three-parameter families, and so on until $d = \bar{n}$, where $\bar{n}$ are the problem's degrees of freedom. The authors also discuss the non-autonomous case, which is relevant for some of the applications that are going to be investigated within this research. Specifically, if the vector field change periodically with time, it can be shown that one of the torus frequencies must be resonant with the forcing term of $\boldsymbol{f}$. This effectively reduces the number of external parameters by one, thereby implying that two-dimensional tori of time-periodic Hamiltonian systems are actually organized in 1-parameter families, three-dimensional tori in 2-parameter families, and so forth.

In the next chapter, we shall see how these external parameters can be identified by different numerical procedures without making any assumptions on the internal frequencies of the torus. After that, the application of quasi-periodic invariant tori to spacecraft formation flight is studied with the goal of developing systematic approaches for establishing bounded relative motion in practical astrodynamics problems.

Chapter 3

Numerical Computation of Quasi-periodic Invariant Tori

In this chapter, we review some of the methodologies developed throughout the last decades to compute quasi-periodic invariant tori in astrodynamics. Even though there exist analytical and semi-analytical methods [39, 43, 47, 57, 58, 92], we focus on fully numerical procedures that have been successfully tested in restricted three-body contexts [7, 62, 85, 86]. The algorithms were introduced in Section 1.3 and are more rigorously discussed in the following pages (Section 3.1–3.2). Furthermore, PDE solvers based on either CD or DFT are hereby compared with the KKG and GMOS algorithms in order to determine which of the different procedures should be preferred for the remainder of this thesis. As a case study, we consider the motion of a planar satellite in the co-rotating frame of the Earth (ECEF). Here, planar eccentric orbits wind around the surface of two-dimensional tori that can be explicitly calculated with the four different strategies (Sec. 3.3). Trajectories on the surface of these manifolds are generated and compared with the analytical solution of the two-body problem to assess the performance of the numerical approaches and evaluate their advantages and drawbacks. In the end, two of the considered methodologies turn out to significantly outperform the remaining strategies, thereby requiring for additional investigations. Because of this, Section 3.4 of this Chapter introduces the equations of motion of the Planar Circular Restricted Three-Body Problem (PCRTBP) and apply the most promising approaches in a more practical example. The results of this analysis show that GMOS should be our preferred choice moving forward because of accuracy and runtime considerations. Consequently, the last part of this chapter focuses on this procedure with the goal of highlighting some of the additional

advantages offered by this strategy. In particular, we review how the stability of quasi-periodic trajectories can be inferred as a byproduct of the method, and show how the numerical procedure can be adapted to calculate families of three-dimensional tori. These and other features appear consistently in the remainder of this research, making the flexibility and robustness of the GMOS algorithm part of the enabling factors in designing bounded relative trajectories about a variety of celestial bodies.

3.1 Partial Differential Equation Solvers

In this section, two methodologies that aim at calculating invariant tori of flows by solving a nonlinear system of PDE are summarized. Accordingly, let $\mathbb{T}^2$ be a two-dimensional torus parametrized by the two angular variables $\boldsymbol{\theta} = \begin{bmatrix} \theta_0, \theta_1 \end{bmatrix}^T \in [0, 2\,\pi)^2$, and let $\boldsymbol{u} : \mathbb{T}^2 \to T \subset \mathbb{R}^n$ be a torus function satisfying the properties outlined in Sec. 2.6. If this is the case, one can replace $\boldsymbol{x}$ with $\boldsymbol{u}(\boldsymbol{\theta})$ into the equations of motion (2.1), obtaining a system of partial differential equations for the unknown torus function $\boldsymbol{u}$ and frequencies $\boldsymbol{w} = \begin{bmatrix} \omega_0, & \omega_1 \end{bmatrix}^T$:

$$\sum_{i=0}^{1} \frac{\partial \boldsymbol{u}}{\partial \theta_i}\,\dot{\theta}_i = \frac{\partial \boldsymbol{u}}{\partial \theta_0}\,\omega_0 + \frac{\partial \boldsymbol{u}}{\partial \theta_1}\,\omega_1 = f(\boldsymbol{u}(\boldsymbol{\theta})), \tag{3.1}$$

subject to the boundary conditions

$$\begin{cases} \boldsymbol{u}(\theta_0, 0) &= \boldsymbol{u}(\theta_0, 2\,\pi), \quad \forall \theta_0 \in [0, 2\,\pi), \\ \boldsymbol{u}(0, \theta_1) &= \boldsymbol{u}(2\,\pi, \theta_1), \quad \forall \theta_1 \in [0, 2\,\pi). \end{cases} \tag{3.2}$$

There exist several techniques for solving nonlinear systems of PDE such as the one of (3.1). However, only few of these techniques have been successfully applied for the numerical continuation of quasi-periodic invariant tori in astrodynamics. For instance, Schielder et al. [99] propose to solve the nonlinear system arising from the evaluation of (3.1) over an evenly distributed grid of points using central differences. This approach is hereby referred to as the PDE(CD) technique, and is further discussed in Sec. 3.1.1. Alternatively, one can approximate the partial derivatives appearing in (3.1) using the DFT. This seems particularly suitable for our problem given the

periodic boundary conditions (3.2). As such, the PDE(DFT) approach is also included in our analysis and further discussed in Sec. 3.1.2. To the best of our knowledge, such a procedure is yet to be applied for the numerical continuation of quasi-periodic invariant tori in orbital mechanics applications.

With this goal in mind, observe that both the PDE(CD) and PDE(DFT) approaches require a reliable initial guess to be initialized. Hence, let $\boldsymbol{x}_0$ be the initial state of a periodic orbit whose monodromy matrix M admits one pair of unitary magnitude complex conjugate eigenvalues as in Sec. 2.5: $\lambda_1 = e^{\mathrm{i}\,\rho}$, $1/\lambda_1 = e^{-\mathrm{i}\,\rho}$. Given $M\,\boldsymbol{e} = e^{\mathrm{i}\rho}\,\boldsymbol{e}$, one can construct the one-dimensional curve

$$\boldsymbol{\varphi}(\theta_1) = K\,\left[\cos\left(\theta_1\right)\mathrm{Re}(\boldsymbol{e}) - \sin(\theta_1)\,\mathrm{Im}(\boldsymbol{e})\right], \tag{3.3}$$

where K is an arbitrary small scalar $<<1$. It is easy to demonstrate that $M\,\boldsymbol{\varphi}(\theta_1) = \boldsymbol{\varphi}(\theta_1 - \rho)$, thereby proving that (3.3) is indeed invariant under the application of the monodromy matrix M. Because of this, the circle $\boldsymbol{\varphi}(\theta_1)$ is also known as *invariant circle* of the monodromy map and considered as a good initial guess for initializing the grid of points utilized by the PDE methods (Fig. 3.1).

Specifically, for each $\boldsymbol{\varphi}^j = \boldsymbol{\varphi}(\theta_{1,j})$ with $\theta_{1,j} = 2\,\pi\,j/N_1$, $j = 0, \ldots, N_1 - 1$, one can map the perturbations forward in time using the state transition matrix, i.e.,

$$\boldsymbol{\varphi}_i^j = e^{-\mathrm{i}\,\rho\,t_i/T}\,\Phi(t_i, t_0)\,\boldsymbol{\varphi}^j, \tag{3.4}$$

where $t_i = i\,T/N_0$, $i = 0, \ldots, N_0 - 1$, and T is the orbital period of the underlying periodic orbit. The factor $e^{-\mathrm{i}\,\rho\,t_i/T}$ is introduced to undo the effects of the *winding* frequency ω_1, which acts in the latitudinal direction of the torus and shall not be confused with the *longitudinal* frequency of the torus ω_0 (Fig. 2.8). By adding each of these perturbations to the value of the periodic orbit at time t_i, namely $\varphi_{t_i}(\boldsymbol{x}_0) + \boldsymbol{\varphi}_i^j$, where φ_t is the solution flow of (2.1) up to time t, the **skeleton** of the manifold, i.e., its initial approximation, can be finally generated. Fig. 3.2 shows an example of this skeleton for a HP southern halo orbit with $N_0 = 25$, $N_1 = 25$.

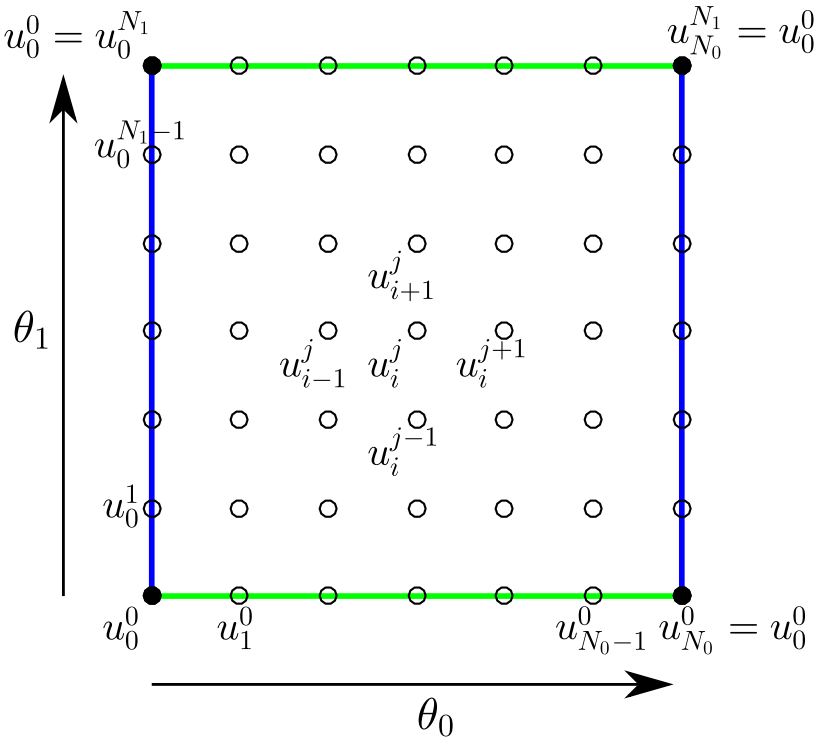

Figure 3.1: Mesh of discretization points utilized by PDE solvers. The blue and green lines illustrate the periodic boundary conditions (3.2).

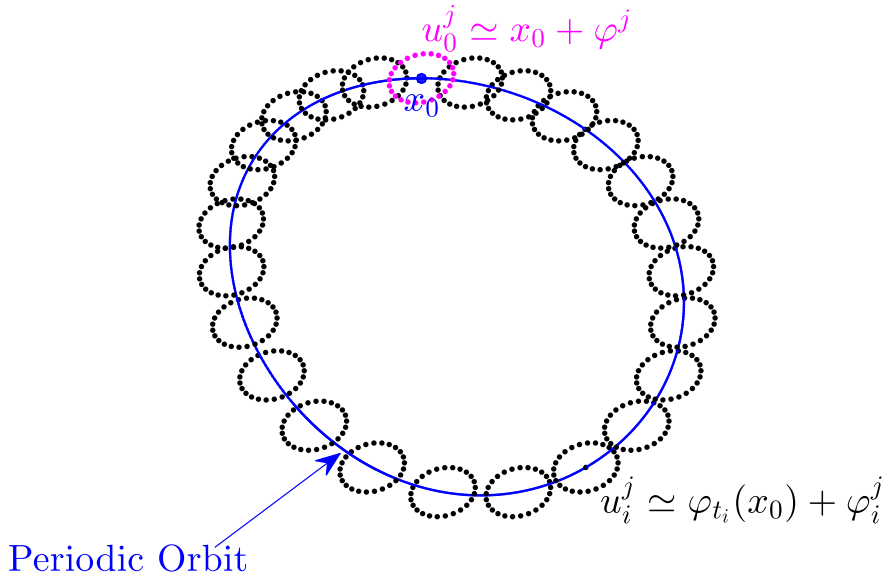

Figure 3.2: Skeleton of a two-dimensional quasi-periodic invariant torus. The black dots are used to initialized the numerical continuation scheme.

In order to be precisely on the surface of a quasi-periodic invariant torus, each of the mesh points $\boldsymbol{u}_i^j$ needs to satisfy (3.1). Accordingly, one has a set of $N_0 \times N_1$ vectorial relationships that can be used to update the initial approximations $\boldsymbol{u}_i^j \simeq \varphi_{t_i}(\boldsymbol{x}_0) + \boldsymbol{\varphi}_i^j$, $\omega_0 \simeq 2\,\pi/T$, $\omega_1 \simeq \rho/T$ via Newton's method. That is, given $\boldsymbol{z} = \left[\boldsymbol{u}_i^j\,,\,\boldsymbol{\omega}\right]^T$ and

$$\boxed{\boldsymbol{F}(\boldsymbol{z}) = \boldsymbol{f}(\boldsymbol{u}_i^j) - \frac{\partial \boldsymbol{u}_i^j}{\partial \theta_0}\,\omega_0 - \frac{\partial \boldsymbol{u}_i^j}{\partial \theta_1}\,\omega_1 = \boldsymbol{0},} \qquad \begin{array}{l} i = 0, \ldots, N_0 - 1, \\ j = 0, \ldots, N_1 - 1, \end{array} \tag{3.5}$$

then

$$\boldsymbol{z}^{(k+1)} = \boldsymbol{z}^{(k)} - D\boldsymbol{F}(\boldsymbol{z}^{(k)})^{\dagger}\,\boldsymbol{F}(\boldsymbol{z}^{(k)}), \tag{3.6}$$

where $D\boldsymbol{F}(\boldsymbol{z}^{(k)})^{\dagger}$ is the left pseudo-inverse of the Jacobian matrix of $\boldsymbol{F}$.

The system (3.5) is made of $(N_0 \times N_1)$ vectorial equations in $(N_0 \times N_1 + 2)$ unknowns that requires additional equations to be solved uniquely. This is very similar to what happens for periodic orbits, where one phase condition and pseudo-arclength continuation constraints are added to the list (2.15). In the quasi-periodic case, however, the choice of the mesh points is not unique in both the θ_0 and θ_1 directions. Thus, two phase conditions are attached to the error vector (3.5) in order to avoid these indeterminacies: one for each angular direction. Secondly, we now know that two-dimensional tori of Hamiltonian autonomous systems that do not depend on any parameter belong to two-parameter families. Therefore, differently from one-parameter families of periodic orbits, two *parametrizing* equations are actually needed. This implies that a total of four extra constraints are to be included in (3.5).

Schielder et al. [99] identify two of these equations with the phase conditions

$$p_0(\boldsymbol{u}_i^j) := < \boldsymbol{u}_i^j - \tilde{\boldsymbol{u}}_i^j, \frac{\partial \tilde{\boldsymbol{u}}_i^j}{\partial \theta_0} >= 0, \tag{3.7a}$$

$$p_1(\boldsymbol{u}_i^j) := < \boldsymbol{u}_i^j, \frac{\partial \tilde{\boldsymbol{u}}_i^j}{\partial \theta_1} >= 0, \tag{3.7b}$$

which help anchor the solution points once a previously found solution $\tilde{\boldsymbol{u}}_i^j$ is available. For the first family member, the latter is approximated with the skeleton of the torus itself. Also notice that the operator $< \boldsymbol{a}_i^j, \boldsymbol{b}_i^j >$ denotes the inner product $\dfrac{1}{N_0\,N_1}\,\sum_{i=0}^{N_0-1}\,\sum_{j=0}^{N_1-1}(\boldsymbol{a}_i^j)^T\,\boldsymbol{b}_i^j$.

As for the parametrizing equations, different choices are available. For instance, if the system (2.1) admits an integral of motion such as the Jacobi integral in the HP or CRTBP problems, one can require the quasi-periodic invariant torus to have the same energy level via

$$s_0(\boldsymbol{u}_i^j) := \frac{1}{N_0\, N_1} \left(\sum_{i=0}^{N_0-1} \sum_{j=0}^{N_1-1} \mathcal{C}(\boldsymbol{u}_i^j) \right) - C = \mathbf{0}, \tag{3.8}$$

where $\mathcal{C}(\boldsymbol{u}_i^j)$ is the Jacobi integral evaluated at the mesh point $\boldsymbol{u}_i^j$. Alternatively, one could also fix the value of a torus frequency, e.g.,

$$s_0(\omega_0) := \omega_0 - 2\,\pi/T = 0, \tag{3.9}$$

and obtain synchronous tori, i.e., tori of the same *period*.

Finally, the last equation $s_1(\boldsymbol{u}_i^j, \boldsymbol{\omega})$ may be covered by pseudo-arclength continuation as in Section 2.3:

$$s_1(\boldsymbol{z}) :=< \boldsymbol{u}_i^j - \tilde{\boldsymbol{u}}_i^j, \tilde{\boldsymbol{u}}'^j_i > + (\boldsymbol{\omega} - \tilde{\boldsymbol{\omega}})^T\, \boldsymbol{\omega}' - \delta s = 0, \tag{3.10}$$

where $\begin{bmatrix} \tilde{\boldsymbol{u}}'^j_i & \boldsymbol{\omega}' \end{bmatrix}^T$ is the family tangent evaluated at a previously known solution $(\tilde{\boldsymbol{u}}_i^j, \tilde{\boldsymbol{\omega}})$, and δs is again the continuation step-length.

The latter completes the set of constraints to be considered along with (3.5). Next, Newton's method can be applied to update the initial approximation of $\boldsymbol{u}_i^j$ and $\boldsymbol{\omega}$ until all of the constraints are satisfied within some small tolerance of choice. If desired, the computed solution can be used to replace the values of $\tilde{\boldsymbol{u}}_i^j$, $\tilde{\boldsymbol{\omega}}$, $\tilde{\boldsymbol{u}}'^j_i$, $\tilde{\boldsymbol{\omega}}'$, and rerun the code to continue through different members of the quasi-periodic invariant tori family. Following a predictor-corrector scheme such as the one of Chapter 2, the initial guess of the new family member would be given by

$$\begin{aligned} \boldsymbol{u}_i^j &= \tilde{\boldsymbol{u}}_i^j + \delta s\, \tilde{\boldsymbol{u}}'^j_i, \\ \boldsymbol{w} &= \tilde{\boldsymbol{\omega}} + \delta s\, \tilde{\boldsymbol{\omega}}'. \end{aligned} \tag{3.11}$$

3.1.1 The PDE(CD) algorithm

In the examples shown in the original paper by [99], the partial derivatives of $\boldsymbol{u}_i^j$ are approximated via second-order central differences [73]. In this case,

$$\begin{array}{rcl} \dfrac{\partial \boldsymbol{u}_i^j}{\partial \theta_0} & = & \dfrac{\boldsymbol{u}_{i-2}^j - 8\,\boldsymbol{u}_{i-1}^j + 8\,\boldsymbol{u}_{i+1}^j - \boldsymbol{u}_{i+2}^j}{12\,\Delta\theta_0}, \\ \dfrac{\partial \boldsymbol{u}_i^j}{\partial \theta_1} & = & \dfrac{\boldsymbol{u}_i^{j-2} - 8\,\boldsymbol{u}_i^{j-1} + 8\,\boldsymbol{u}_i^{j+1} - \boldsymbol{u}_i^{j+2}}{12\,\Delta\theta_1}, \end{array} \tag{3.12}$$

where $\Delta\theta_0 = 2\,\pi/N_0$, and $\Delta\theta_1 = 2\,\pi/N_1$. Note that the truncation error of such a local approximation is on the order of $O(\Delta\theta^4)$, and decrease with the fourth power of $1/N$.

3.1.2 The PDE(DFT) algorithm

Differently from the PDE(CD) method, in PDE(DFT) the partial derivatives appearing in (3.1) are approximated via the DFT. That is, given

$$A_k^j = \sum_{i=0}^{N_0-1} \boldsymbol{u}_i^j\, e^{\mathrm{i}\,2\,\pi\,k\,i/N_0}, \tag{3.13a}$$

$$B_i^l = \sum_{j=0}^{N_1-1} \boldsymbol{u}_i^j\, e^{\mathrm{i}\,2\,\pi\,l\,j/N_1}, \tag{3.13b}$$

then

$$\boldsymbol{u}^j(\theta_0) = \frac{1}{N_0} \sum_{k=-(N_0-1)/2}^{(N_0-1)/2} \boldsymbol{A}_k^j\, e^{\mathrm{i}\,k\,\theta_0}, \tag{3.14a}$$

$$\boldsymbol{u}_i(\theta_1) = \frac{1}{N_1} \sum_{l=-(N_1-1)/2}^{(N_1-1)/2} \boldsymbol{B}_i^l\, e^{\mathrm{i}\,l\,\theta_1}, \tag{3.14b}$$

so that

$$\frac{\partial \boldsymbol{u}_i^j}{\partial \theta_0} = \frac{1}{N_0} \sum_{k=-(N_0-1)/2}^{(N_0-1)/2} \mathrm{i}\,k\,\boldsymbol{A}_k^j\, e^{\mathrm{i}\,k\,(2\,\pi\,j/N_1)}, \tag{3.15a}$$

$$\frac{\partial \boldsymbol{u}_i^j}{\partial \theta_1} = \frac{1}{N_1} \sum_{l=-(N_1-1)/2}^{(N_1-1)/2} \mathrm{i}\,l\,\boldsymbol{B}_i^l\, e^{\mathrm{i}\,l\,(2\,\pi\,i/N_0)}. \tag{3.15b}$$

Numerical experiments show that the approximation error using the information from the *global* distribution of the mesh point is two-to-three orders of magnitude smaller than the truncation error of (3.12).

3.2 Two-Point Boundary Value Problem Solvers

Differently from the PDE approach, TPBVP occur whenever a solution of a system of ordinary differential equations (ODE) needs to satisfy boundary conditions at two different points in time. We have already seen an example of BVP when computing periodic orbits as in Sec. 2.3. The main idea of this Section is that both of the map strategies considered in this thesis, namely the KKG and GMOS algorithms, can be recast into this framework. Then, similar techniques to the ones illustrated in Chapter 2 may be applied to calculate entire families of quasi-periodic invariant tori.

First, let us recall the form of the system dynamics as a function of the dimensionless time $\tau = t/T$:

$$\boldsymbol{x}' = T\,\boldsymbol{f}(\boldsymbol{x}), \tag{3.16}$$

where $\boldsymbol{x}'$ denotes the first derivative of $\boldsymbol{x}$ with respect to the nondimensional time τ, and T is hereby referred to as the *reference* time.

Next, observe that the KKG and GMOS algorithms aim at calculating invariant curves of a Poincaré and stroboscopic mapping, respectively. Therefore, let $\boldsymbol{X} = \begin{bmatrix} \boldsymbol{x}_0^T, & \boldsymbol{x}_1^T, & \ldots, & \boldsymbol{x}_{N_1-1}^T \end{bmatrix}^T$ be the collection of N_1 evenly distributed points along one of these curves. Of course, $\boldsymbol{X} \in \mathbb{R}^{n\,N_1}$, where n is the dimension of the original Hamiltonian system (3.16). Furthermore, let $\mathbb{F}(\boldsymbol{X})$ be the $n\,N_1$-dimensional vector field given by

$$\mathbb{F}(\boldsymbol{X}, \boldsymbol{T}) = \begin{bmatrix} T_0\,\boldsymbol{f}(\boldsymbol{x}_0) \\ T_1\,\boldsymbol{f}(\boldsymbol{x}_1) \\ \cdots \\ T_{N_1-1}\,\boldsymbol{f}(\boldsymbol{x}_{N_1-1}) \end{bmatrix}, \tag{3.17}$$

where $\boldsymbol{T} = \begin{bmatrix} T_0, & T_1, & \ldots, & T_{N_1-1} \end{bmatrix}^T$ is a vector of constant reference times T_i, $i = 0, \ldots, N_1 - 1$.

Depending on the map strategy being considered, T_i is either the first return time of the i-th trajectory, or the stroboscopic time T. In the latter case, $T_i = T\ \forall i$, and the constant vector $\boldsymbol{T}$ may be reduced to a scalar parameter for the vector field (3.17).

Nevertheless, the augmented system

$$\boldsymbol{X}' = \mathbb{F}(\boldsymbol{X}, \boldsymbol{T}) \tag{3.18}$$

describes the dynamical evolution of a curve with respect to the non-dimensional time τ. In this case, a QP torus can be seen as a trajectory $\boldsymbol{X}(\tau)$, $\tau \in [0, 1]$ satisfying quasi-periodic boundary conditions $\boldsymbol{g}(\boldsymbol{X}_0, \boldsymbol{X}_1) = \boldsymbol{0}$, where $\boldsymbol{X}_0 = \boldsymbol{X}(\tau = 0)$, and $\boldsymbol{X}_1 = \boldsymbol{X}(\tau = 1)$.

Depending on the particular methodology being considered, different choices of boundary conditions emerge. Furthermore, phase conditions such as (3.7a)–(3.7b) may or may not be required in order to correctly identify quasi-periodic invariant tori within their families. To that end, two parametrizing equations are typically appended to the list of constraints that need to be satisfied by the BVP solver. The first of these equations is either provided by an integral of motion or by fixing one of the torus frequencies as in (3.9). Similarly, pseudo-arclength continuation may be used to complete the list of constraints and allow the user to step through different members of a quasi-peirodic invariant tori family as in Sec. 2.3 and 3.1. These and other implementation tips for both of the map strategies are further discussed in the next subsections.

3.2.1 The KKG algorithm

In their paper, Kolemen et al. [62] derive a numerical procedure to compute families of quasi-periodic invariant tori via invariant curves of a Poincaré map. Accordingly, consider the intersection of the quasi-periodic invariant torus of Fig. 3.2 with the equatorial plane $z = 0$ where the underlying periodic orbit is crossing from south to north. As described in Ref. [98], a Poincaré map takes a point $\boldsymbol{y}_0$ on the chosen surface of section and gives the corresponding state $\boldsymbol{y}_1$ at the next surface of section crossing. If $\boldsymbol{y}_1 = \boldsymbol{g}(\boldsymbol{y}_0)$ represents such mapping, one can linearize in the neighborhood of a periodic orbit $\boldsymbol{y}^* = \boldsymbol{g}(\boldsymbol{y}^*)$, obtaining the linearized Poincaré mapping:

$$\delta\boldsymbol{y}_1 = \left[\frac{\partial \boldsymbol{g}}{\partial \boldsymbol{y}}\right]^* \delta\boldsymbol{y}_0 = \Phi_{10}\, \delta\boldsymbol{y}_0, \tag{3.19}$$

where $\delta\boldsymbol{y} = \begin{bmatrix} \delta x, & \delta y, & \delta\dot{x}, & \delta\dot{y}, & \delta\dot{z} \end{bmatrix}^T$ represents deviations of the reduced state vector $\boldsymbol{y}$, and Φ_{10} is hereby referred to as the *reduced monodromy matrix*.

As soon as Φ_{10} is calculated, a linear approximation of an invariant curve of the Poincaré mapping g may be found. Specifically, if Φ_{10} admits at least one pair of complex conjugate eigenvalues, e.g., $\Phi_{10}\,\boldsymbol{e}_{10} = e^{\mathrm{i}\rho}\,\boldsymbol{e}_{10}$, then

$$\boldsymbol{\psi}(\phi) = K\,\left[\cos(\phi)\,\mathrm{Re}(\boldsymbol{e}_{10}) - \sin(\phi)\,\mathrm{Im}(\boldsymbol{e}_{10})\right], \tag{3.20}$$

is invariant with respect to Φ_{10}.

Now consider the N_1 perturbations $\delta\boldsymbol{x}_{0,i} = \boldsymbol{\psi}(\phi_i)$ found in correspondence of the N_1 angular values $\phi_i = 2\,\pi\,(i-1)/N_1$, $i = 1, \ldots, N_1$. Fig. 3.3 shows how this initial guess appears in different coordinate spaces for the example torus of Fig. 3.2. It can be seen that the projection of this curve in the x–y coordinate plane is actually the most circular and therefore the most suited to parametrize the intersection between the torus and the considered surface of section $\zeta(\boldsymbol{x}) := z = 0$, $\dot{z} > 0$ via Fourier analysis. Let $R = \sqrt{\delta x^2 + \delta y^2}$, and consider a DFT such that

$$\boldsymbol{X}_0 - \boldsymbol{X}^* = \delta\boldsymbol{X}_0 = \begin{bmatrix} \delta\boldsymbol{x}_{0,1} \\ \vdots \\ \delta\boldsymbol{x}_{0,N_1} \end{bmatrix} = A(\theta_0)\,\boldsymbol{Q}, \tag{3.21}$$

where $\boldsymbol{X}^*$ is the representation of the considered periodic orbit in the augmented system (3.17), $\delta\boldsymbol{x}_{0,i} = \begin{bmatrix} \delta x_{0,i}, & \delta y_{0,i}, & \delta z_{0,i} = 0, & \delta\dot{x}_{0,i}, & \delta\dot{y}_{0,i}, & \delta\dot{z}_{0,i} \end{bmatrix}^T$, and $\boldsymbol{Q} = \begin{bmatrix} \boldsymbol{Q}_R^T & \boldsymbol{Q}_{\dot{x}}^T & \boldsymbol{Q}_{\dot{y}}^T & \boldsymbol{Q}_{\dot{z}}^T \end{bmatrix}^T$ is the vector of Fourier coefficients obtained from (3.21)[1] . Furthermore, $A(\theta)$ is the matrix defined by

$$A(\theta_0) = \begin{bmatrix} A(\theta_{0,1}) \\ \vdots \\ A(\theta_{0,N_1}) \end{bmatrix}, \qquad A(\theta_{0,i}) = \begin{bmatrix} \cos(\theta_{0,i})\,\boldsymbol{S}(\theta_{0,i}) & 0 & 0 & 0 \\ \sin(\theta_{0,i})\,\boldsymbol{S}(\theta_{0,i}) & 0 & 0 & 0 \\ 0 & 0 & 0 & 0 \\ 0 & \boldsymbol{S}(\theta_{0,i}) & 0 & 0 \\ 0 & 0 & \boldsymbol{S}(\theta_{0,i}) & 0 \\ 0 & 0 & 0 & \boldsymbol{S}(\theta_{0,i}) \end{bmatrix}, \tag{3.22}$$

where

$$\boldsymbol{S}(\theta_{0,i}) = \begin{bmatrix} 1, & \cos(\theta_{0,i}), & \sin(\theta_{0,i}), & \ldots, & \cos(N_1\,\theta_{0,i}), & \sin(N_1\,\theta_{0,i}) \end{bmatrix}, \tag{3.23}$$

[1] since $z = 0$ on the surface of section, there is no need to compute the corresponding Fourier coefficients

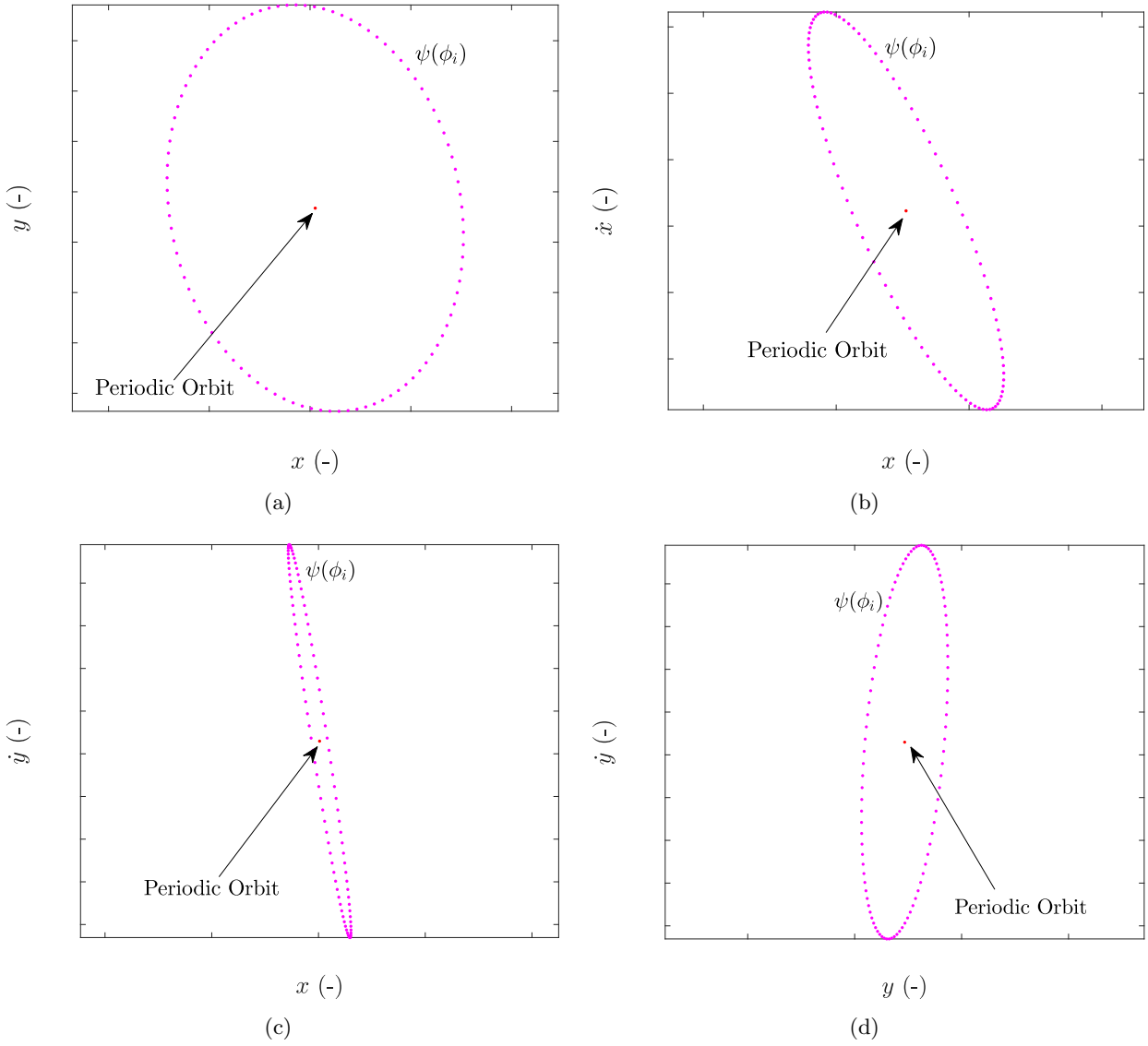

Figure 3.3: An invariant circle of the Poincaré map as seen in different coordinate planes.

and

$$\theta_{0,i} = \arctan\left(\frac{\delta y_{0,i}}{\delta x_{0,i}}\right), \qquad i = 1, \ldots, N_1. \tag{3.24}$$

It is now possible to propagate each of the N_1 points till the next surface of section crossing via (3.17), and obtain the corresponding angles in terms of the chosen coordinate variables at the next surface of section crossing:

$$\theta_{1,i} = \arctan\left(\frac{\delta y_{1,i}}{\delta x_{1,i}}\right). \tag{3.25}$$

If the $\delta \boldsymbol{X}_0$ points were initialized exactly on the surface of a QP invariant torus, the points obtained after one revolution, namely $\delta \boldsymbol{X}_1 = \boldsymbol{X}_1 - \boldsymbol{X}^*$, should satisfy the boundary conditions

$$\boxed{\boldsymbol{g}(\boldsymbol{X}_0, \boldsymbol{X}_1) := \delta \boldsymbol{X}_1 - A(\theta_1)\, \boldsymbol{Q}(\delta \boldsymbol{X}_0) = \boldsymbol{0}} \tag{3.26}$$

That is, the propagated points should end up on the same curve of the Poincaré map. Since this is not the case–at least for the very first iteration of the algorithm–consider updating the Fourier coefficients of $\boldsymbol{X}_0$ via Newton's method. The vectorial quantity to be nullified corresponds to

$$F(\boldsymbol{Q}) = \delta \boldsymbol{X}_1 - A(\theta_1)\, \boldsymbol{Q} = \boldsymbol{0}, \tag{3.27}$$

so that a Newton's update reads as

$$\boldsymbol{Q}^{(k+1)} = \boldsymbol{Q}^{(k)} - DF(\boldsymbol{Q}^{(k)})^{\dagger}\, F(\boldsymbol{Q}^{(k)}), \tag{3.28}$$

where $DF^{\dagger}$ is the left pseudo-inverse of the Jacobian matrix of $F(\boldsymbol{Q})$ (see [62] for details).

Also recall that phase conditions and parametrizing equations may or may not be needed in order to have a unique solution of the BVP. As it turns out, the KKG algorithms only needs two parametrizing equations to be appended to the error vector (3.27). This is because working with surfaces of section and projections in coordinate planes as in (3.24)–(3.25) effectively avoid the indeterminacies that would otherwise affect the Fourier representation of $\boldsymbol{X}_0$. Consequently, no phase constraints are needed, whereas the remaining two parametrizing equations are given by either

$$s_0(\boldsymbol{Q}) := \frac{1}{N_1}\left(\sum_{i=1}^{N_1} \mathcal{C}(A(\theta_{0,i})\, \boldsymbol{Q})\right) - C, \qquad \text{(Jacobi)} \tag{3.29}$$

or

$$s_0(\boldsymbol{Q}) := \frac{1}{N_1}\left(\sum_{i=1}^{N_1} \tau(A(\theta_{0,i})\,\boldsymbol{Q})\right) - T, \qquad \text{(Period)} \tag{3.30}$$

where $\tau(\boldsymbol{x})$ is the first return time for point $\boldsymbol{x}$, and

$$s_1(\boldsymbol{Q}) =< \boldsymbol{Q} - \tilde{\boldsymbol{Q}}, \tilde{\boldsymbol{Q}}' > -\delta s. \qquad \text{(Pseudo-arclength)} \tag{3.31}$$

By appending Eq, (3.31) and either Eq. (3.29) or (3.30) to the error vector (3.27), Newton's method can be correctly applied until convergence to the desired quasi-periodic torus. Specifically, the numerical procedure outputs invariant curves of the Poincaré mapping such as the one of Fig. 3.4(b), which proves the good agreement between the propagated points and their projection on the final estimate of the invariant curve. If desired, the KKG solution points can be finally integrated with the full nonlinear system of equations of motion to obtain a representation of the corresponding quasi-periodic invariant torus in the phase space.

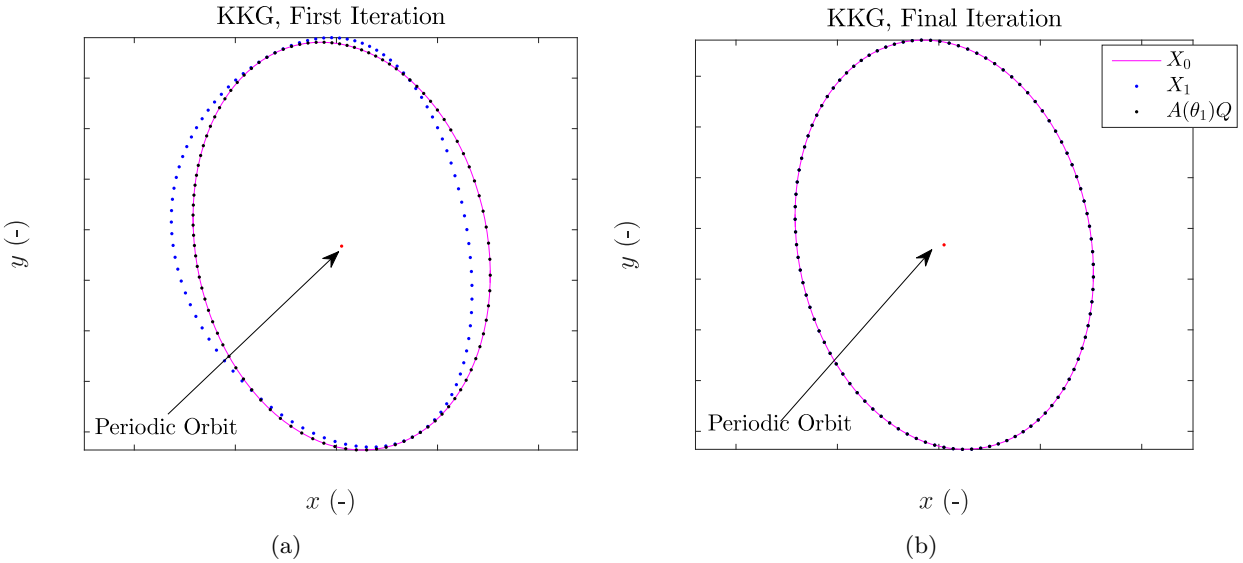

Figure 3.4: First (a) and last iteration (b) of the KKG algorithm. The propagated points are shown in blue, whereas the points projected on the current estimate of the invariant circle of the Poincaré map are shown in black.

3.2.2 The GMOS algorithm

In contrast to the KKG method, Gómez, Mondelo [44], Olikara, and Scheeres [86] (GMOS) compute families of QP tori via invariant curves of a stroboscopic map. To illustrate this methodology, recall that a torus function defines a diffeomorphism between the phase space and a torus space $\mathbb{T}^d$. Accordingly, one can integrate trajectories in $\mathbb{T}^d$ and use the conjugacy illustrated in Fig. 3.5 to obtain the final state vector in the original phase space. The advantage of this approach is that the dynamics in torus coordinates is indeed trivial and can be solved analytically without the need of numerical methods. For instance, the image of a T-stroboscopic mapping on a torus reads as $G_T(\boldsymbol{\theta}) = \bar{\boldsymbol{\theta}} = \boldsymbol{\theta} + \boldsymbol{\omega}\, T$, where $G_T : \mathbb{T}^d \to \mathbb{T}^d$, and $\boldsymbol{\omega}$ is the frequency vector introduced in Sec. 2.6. In the case of a two-dimensional torus with $T = 2\,\pi/\omega_0$, this corresponds to

$$\bar{\boldsymbol{\theta}} = \begin{cases} \theta_0 + 2\,\pi & = & \theta_0, \\ \theta_1 + 2\,\pi\,\dfrac{\omega_1}{\omega_0} & = & \theta_1 + \rho, \end{cases} \tag{3.32}$$

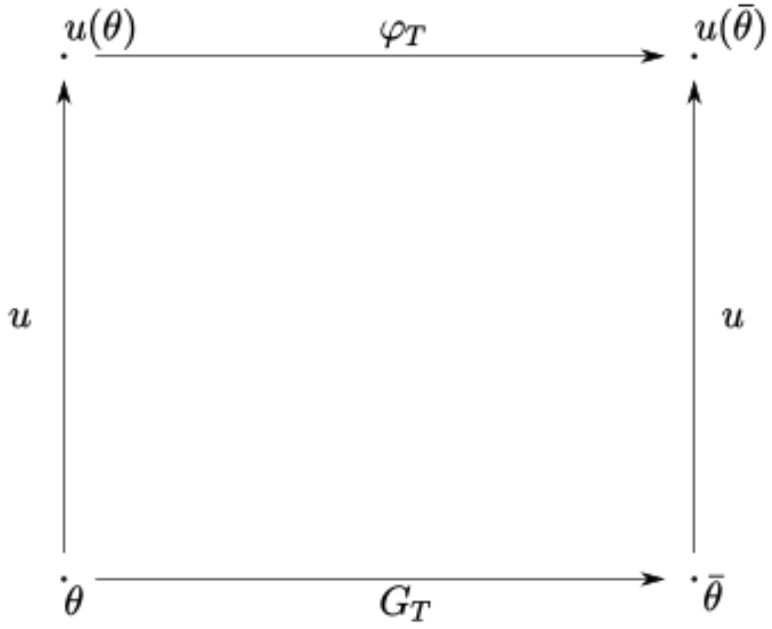

Figure 3.5: Conjugacy between G_T and φ_T

where $\rho = 2\,\pi\,\omega_1/\omega_0$ is known as the *rotation number* and is an intrinsic property of the manifold[60]. Furthermore, since $\boldsymbol{u} \circ G_T = \varphi_T \circ \boldsymbol{u}$, the following must be true for the images of a stroboscopic mapping φ_T in phase space:

$$\begin{aligned} \varphi_T(\boldsymbol{u}(\boldsymbol{\theta})) &= \boldsymbol{u}(G_T(\boldsymbol{\theta})), && \text{(3.33a)} \\ &= \boldsymbol{u}(\begin{bmatrix} \theta_0, & \theta_1 + \rho \end{bmatrix}^T). && \text{(3.33b)} \end{aligned}$$

Following Eq. (3.33), it is clear that for any given value of θ_0, $\boldsymbol{v}(\theta) = \boldsymbol{u}(\begin{bmatrix} \theta_0, & \theta \end{bmatrix}^T)$ must be an invariant curve of φ_T. To calculate this curve, observe that

$$\varphi_T(\boldsymbol{v}(\theta)) = \boldsymbol{v}(\theta + \rho) = \boldsymbol{v}(\bar{\theta}). \tag{3.34}$$

Therefore, by defining an operator $R_{-\rho}$ that acts on the space of the diffeomorphisms $\mathrm{V} = \{\boldsymbol{v}(\cdot) \,|\, \boldsymbol{v} : \mathbb{T}^1 \to \mathcal{T} \subset \mathbb{R}^6\}$ such that

$$(R_{-\rho} \circ \boldsymbol{v})(\theta) = \boldsymbol{v}(\theta - \rho), \tag{3.35}$$

one has the invariance relationship

$$R_{-\rho}[\varphi_T(\boldsymbol{v}(\theta))] - \boldsymbol{v}(\theta) = \boldsymbol{0}. \tag{3.36}$$

Eq. (3.36) establish a relationship between the unknowns $\boldsymbol{v}(\theta)$, T and ρ that may be used to refine these quantities via Newton's method once a reliable initial guess is provided.

It turns out that such an initial approximation can be provided by the invariant circle of the monodromy map as in Sec. 3.1. Consequently, assume a periodic orbit is given along with its monodromy matrix M admitting at least one pair of complex conjugate eigenvalues, i.e., $M\,\boldsymbol{e} = e^{\mathrm{i}\rho}\,\boldsymbol{e}$. It is easy to demonstrate that, after one orbital period T, the rotation number ρ should approximately be equal to the phase of the complex conjugate eigenvalue pair. This follows from the fact that $M\,\boldsymbol{\varphi}(\theta) = \boldsymbol{\varphi}(\theta - \rho)$ as in Eq. (3.3).

Next, consider N_1 points $\boldsymbol{v}(\theta_j)$, $j = 0, \ldots, N_1 - 1$ along $\boldsymbol{\varphi}(\theta)$ such that

$$\boldsymbol{X}_0 = \begin{bmatrix} \boldsymbol{v}(\theta_0)^T, & \boldsymbol{v}(\theta_1)^T, & \ldots, & \boldsymbol{v}(\theta_{N_1-1})^T \end{bmatrix}^T. \tag{3.37}$$

After propagating each of these points for one orbital period T, one obtains the image of the stroboscopic map $\boldsymbol{X}_1 = \left[\boldsymbol{v}(\bar{\theta}_0)^T = \varphi_T(\boldsymbol{v}(\theta_0))^T, \quad \boldsymbol{v}(\bar{\theta}_1)^T, \quad \ldots, \quad \boldsymbol{v}(\bar{\theta}_{N_1-1})^T\right]^T$. Furthermore, by means of the DFT of $\boldsymbol{X}_0$, i.e.,

$$\boldsymbol{c}_k = \sum_{j=1}^{N_1} \boldsymbol{v}(\bar{\theta}_j)\, e^{\mathrm{i}2\,\pi\,k\,(j-1)/N_1}, \tag{3.38}$$

a realization of $R_{-\rho}$ immediately follows: since

$$\boldsymbol{v}(\bar{\theta}_j) = \frac{1}{N_1} \sum_{k=-(N_1-1)/2}^{(N_1-1)/2} \boldsymbol{c}_k\, e^{\mathrm{i}\,k\,(2\,\pi\,(j-1)/N_1)}, \tag{3.39}$$

then

$$\begin{aligned} R_{-\rho}[\boldsymbol{v}(\bar{\theta}_j)] &= \frac{1}{N_1} \sum_{k=-(N_1-1)/2}^{(N_1-1)/2} \boldsymbol{c}_k\, e^{\mathrm{i}\,k\,(2\,\pi\,(j-1)/N_1-\rho)}, \\ &= \frac{1}{N_1} \sum_{k=-(N_1-1)/2}^{(N_1-1)/2} \boldsymbol{c}'_k\, e^{\mathrm{i}\,k\,2\,\pi\,(j-1)/N_1}. \end{aligned} \tag{3.40}$$

The invariance relationship (3.36) can be now translated into a set of $n\,N_1$ boundary conditions in the $(n\,N_1+2)$ unknowns $\boldsymbol{X}_0$, T, ρ:

$$\boxed{\boldsymbol{g}(\boldsymbol{X}_0, \boldsymbol{X}_1) = [D]^{-1}\,[R(-\rho)]\,[D]\,\boldsymbol{X}_1 - \boldsymbol{X}_0 = \boldsymbol{0},} \tag{3.41}$$

where $[D]$ and $[D]^{-1}$ are the DFT and inverse DFT operators rewritten in matrix form, and $[R(-\rho)]$ is the diagonal matrix that rotates the Fourier coefficients from $\boldsymbol{c}_k$ to $\boldsymbol{c}'_k = \boldsymbol{c}_k\, e^{-\mathrm{i}\,k\,\rho}$.

It is worth noting that the boundary conditions (3.41) would still be satisfied for all the possible choices of $\theta_0 = \phi \in [0,\, 2\,\pi]$. Besides, for each value of $\alpha \in [0,\, 2\,\pi]$, $\boldsymbol{v}(\theta+\alpha)$ would also be a solution of (3.36). To prevent these indeterminations to occur, two phase conditions are appended to the error vector (3.41). In particular, Olikara and Scheeres [86] define the phase condition for θ_1 by minimizing the distance between the researched curve $\boldsymbol{v}(\theta)$ and a previously found solution $\tilde{\boldsymbol{v}}(\theta)$. The distance between two solutions is defined as

$$\frac{1}{2\,\pi} \int_0^{2\,\pi} \|\boldsymbol{v}(\theta) - \tilde{\boldsymbol{v}}(\theta)\|^2\, \mathrm{d}\theta, \tag{3.42}$$

yielding

$$p_1(\boldsymbol{X}_0) :=< \boldsymbol{X}_0, \frac{\partial \tilde{\boldsymbol{X}}_0}{\partial \theta_1} >= \frac{1}{N_1} \sum_{j=1}^{N_1} \boldsymbol{v}(\theta_j)^T\, \frac{\partial \tilde{\boldsymbol{v}}(\theta_j)}{\partial \theta_1} = 0, \tag{3.43}$$

with

$$\frac{\partial \tilde{\boldsymbol{v}}(\theta_j)}{\partial \theta_1} = \frac{1}{N_1} \sum_{k=-(N_1-1)/2}^{(N_1-1)/2} \mathrm{i}\, k\, \boldsymbol{c}_k\, e^{\mathrm{i}\, k\, (2\,\pi\,(j-1)/N_1)} \tag{3.44}$$

as it follows from (3.39).

A similar formula, i.e.,

$$p_0(\boldsymbol{X}_0) :=< \boldsymbol{X}_0 - \tilde{\boldsymbol{X}}_0, \frac{\partial \tilde{\boldsymbol{X}}_0}{\partial \theta_0} >= \frac{1}{N_1} \sum_{j=1}^{N_1} [\boldsymbol{v}(\theta_j) - \tilde{\boldsymbol{v}}(\theta_j)]^T \; \frac{\partial \tilde{\boldsymbol{v}}(\theta_j)}{\partial \theta_0} = 0, \tag{3.45}$$

is also found for the phase condition of θ_0 recalling that, from (3.1),

$$\frac{\partial \tilde{\boldsymbol{v}}}{\partial \theta_0} = \frac{1}{\tilde{\omega}_0} \left[\boldsymbol{f}(\tilde{\boldsymbol{v}}(\theta)) - \tilde{\omega}_1 \frac{\partial \tilde{\boldsymbol{v}}}{\partial \theta_1} \right], \tag{3.46}$$

As for the parametrizing equations, one can either use the value of the Jacobi integral of the underlying periodic orbit C and seek for invariant tori that satisfy the relationship

$$s_0(\boldsymbol{X}_0) := \frac{1}{N_1} \sum_{j=1}^{N_1} \mathcal{C}(\boldsymbol{v}(\theta_j)) - C = 0, \tag{3.47}$$

or fix the stroboscopic time via

$$s_0(T) := T - \mathcal{P}, \tag{3.48}$$

where $\mathcal{P}$ is a user-defined value (usually corresponding to the period of the underlying periodic orbit). Lastly, pseudo-arclength continuation can be used to step through different family members:

$$s_1(\boldsymbol{z}) :=< \boldsymbol{X}_0 - \tilde{\boldsymbol{X}}_0, \tilde{\boldsymbol{X}}_0' > +(T - \tilde{T})\, T' + (\rho - \tilde{\rho})\, \rho' - \delta s = 0, \tag{3.49}$$

where $\tilde{\boldsymbol{z}}' = \left[\tilde{\boldsymbol{X}}_0', \quad T', \quad \rho' \right]^T$ is the family tangent evaluated in $\tilde{\boldsymbol{z}} = \left[\tilde{\boldsymbol{X}}_0, \tilde{T}, \tilde{\rho} \right]^T$.

In the end, the numerical calculation of a quasi-periodic invariant torus can be formulated as a BVP defined by

$$\begin{cases} \boldsymbol{X}' &= T\, \mathbb{F}(\boldsymbol{X}), \\ T' &= 0, \\ \rho' &= 0, \end{cases} \tag{3.50}$$

and subject to the boundary constraints

$$\boldsymbol{F}(\boldsymbol{z}) = \begin{bmatrix} g(\boldsymbol{X}_0, \boldsymbol{X}_1) \\ p_0(\boldsymbol{X}_0) \\ p_1(\boldsymbol{X}_0) \\ s_0(\boldsymbol{X}_0) \quad \text{or} \quad s_0(T) \\ s_1(\boldsymbol{z}) \end{bmatrix} = \boldsymbol{0}. \tag{3.51}$$

The combination of (3.50)–(3.51) forms a well posed BVP that can be solved with shooting techniques and Newton's method:

$$\boldsymbol{z}^{(k+1)} = \boldsymbol{z}^{(k)} - D\boldsymbol{F}(\boldsymbol{z}^{(k)})^{\dagger}\, \boldsymbol{F}(\boldsymbol{z}^{(k)}), \tag{3.52}$$

where $D\boldsymbol{F}(\boldsymbol{z})^{\dagger}$ denotes the left pseudo-inverse of the Jacobian of (3.51) (see Ref. [86] for details). Upon convergence, the GMOS algorithm outputs invariant curves of the stroboscopic map such as the one illustrated in Fig. 3.6(b). This curve can be used to reinitialize the algorithm and step through entire family branches by following the standard predictor-corrector scheme of Sec. 2.3.

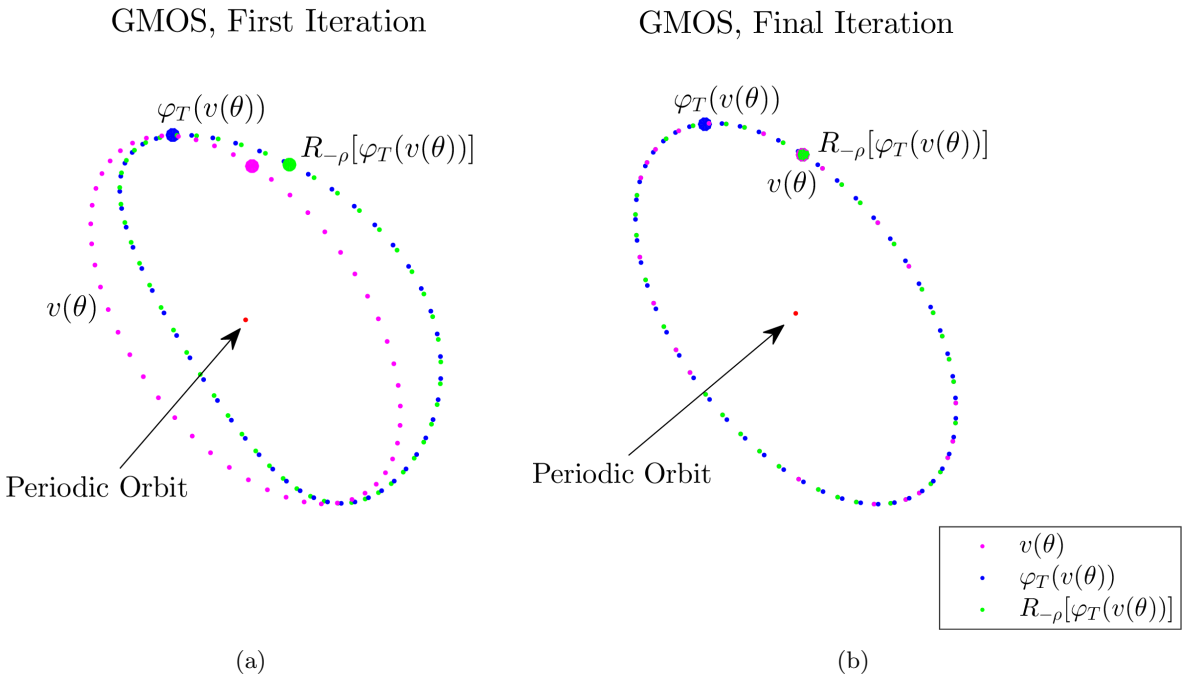

Figure 3.6: First (a) and last iteration (b) of GMOS.

3.3 Accuracy Test

In order to test the numerical procedures outlined in the previous sections, consider the equations of motion of the planar Earth problem in the co-rotating frame of the planet:

$$\begin{cases} \ddot{x} - 2\,\omega_\oplus\,\dot{y} &= -\dfrac{\mu_\oplus}{r^3}\,x + \omega_\oplus^2\,x, \\ \ddot{y} + 2\,\omega_\oplus\,\dot{x} &= -\dfrac{\mu_\oplus}{r^3}\,y + \omega_\oplus^2\,y, \end{cases} \tag{3.53}$$

where $\boldsymbol{x} = \begin{bmatrix} x, & y, & \dot{x}, & \dot{y} \end{bmatrix}^T$ is the state of a satellite with respect to the ECEF frame, $r = \sqrt{x^2 + y^2}$ is the norm of the spacecraft position vector, $\mu_\oplus = 398600.4418$ km^3/s^2 is the Earth gravitational parameter, and $\omega_\oplus = 7.2921 \times 10^{-5}$ rad/s is the Earth's spin rate . In what follows, we normalize the units of the problem such that the length and time units correspond to LU $= R_\oplus = 6378.137$ km and TU $= \sqrt{R_\oplus^3/\mu_\oplus} = 806.8111$ s, respectively. Following this convention, $\mu_\oplus = 1$, whereas $\omega_\oplus = 0.05883$.

Next, consider a Planar Circular Orbit (PCO) with semi-major axis $\bar{a} = 10000$ km $= 1.5679$ LU. As shown in Fig. 3.7, the trajectory is also periodic in the co-rotating frame of the Earth with period $T = 2\,\pi/(n - \omega_\oplus) = 13.9457$ TU, where $n = \sqrt{\mu_\oplus/\bar{a}^3}$ is the mean motion of the satellite. Moreover, computing the monodromy matrix and corresponding eigenvalues indicate that

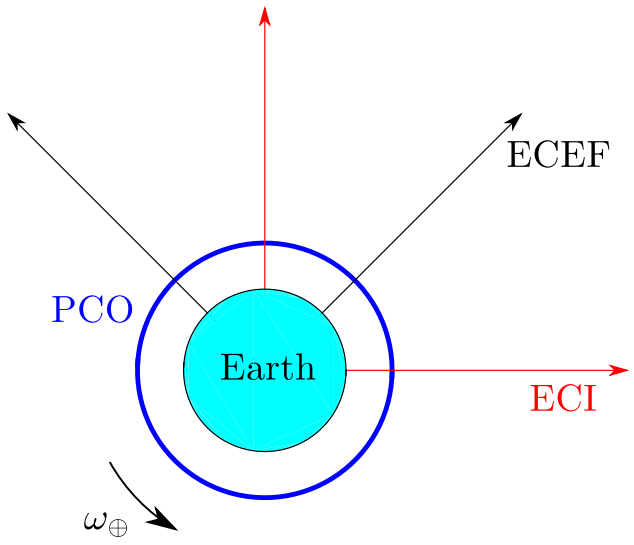

Figure 3.7: Planar Circular Orbit (PCO) in both the ECEF and ECI frames.

the periodic orbit is stable and surrounded by a family of two-dimensional tori.

Several members of the quasi-periodic invariant tori family can be then computed via the numerical procedures outlined in the previous sections. During this procedure, we fix the longitudinal frequency of the torus to match the period of the PCO via (3.9), (3.30), and (3.48), respectively. This selection ensures that the quasi-periodic trajectories initialized on the surface of the computed tori have, in principle, the same orbital period/semi-major axis of the planar circular trajectory. If differences occur, these are due to the approximations and accuracy limitations of the numerical procedures.

To estimate the accuracy of each method, we proceed in the following fashion. First, we rotate each of the solution points in the ECI frame and compute the corresponding Keplerian orbit elements. Next, we accumulate the differences between the semi-major axes and the nominal value before averaging over the number of points used by the considered methodology. For instance, if a quasi-periodic invariant torus has been computed with GMOS using N_1 points, the final error is given by $\sum_{i=0}^{N_1-1} |a_i - \bar{a}|/N_1$, where a_i are the semi-major axes obtained from each of the N_1 solution points. The outcome of our numerical investigation is illustrated in Fig. 3.8.

As it can be seen, the errors are shown as a function of the eccentricity e. This is possible because quasi-periodic trajectories in the ECEF frame are actually eccentric periodic orbits in the Earth-centered inertial frame (Fig. 3.9). What differs between trajectories on the surface of the same QP torus is just the phasing of the perigee with respect to the body-fixed frame of the Earth at epoch. Therefore, each QP torus can be related to a unique value of e and eventually compared with similar solutions produced with different algorithm. The inspection of the results indicates that GMOS and the PDE solver based on DFT (PDE(DFT)) significantly outperform the KKG and PDE(CD) algorithms.

Given that the DFT uses the full representation of either the torus or a curve on its surface, it is not surprising that the accuracy of PDE(DFT) and GMOS is considerably better than PDE(CD), which is rather based on the local approximation of the partial derivatives appearing in (3.5). That being said, it is still worth noting that the Jacobian matrix of $\boldsymbol{F}(\boldsymbol{z})$ in the PDE(CD) algorithm is

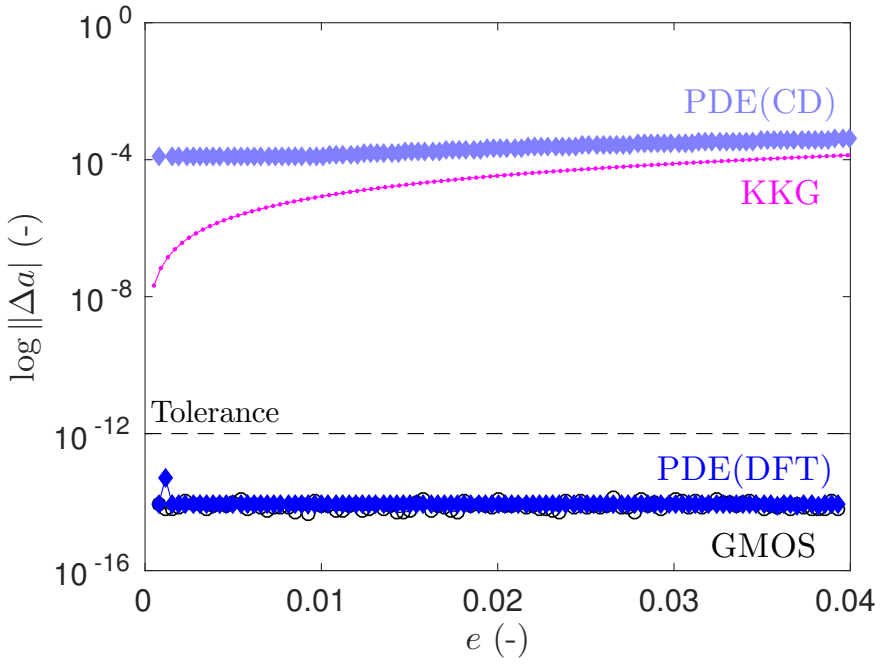

Figure 3.8: Accuracy test for several QP tori computed with the numerical procedures outlined in this Chapter. GMOS uses $N_1 = 25$ solution points, KKG uses $N_1 = 25$ with $N_{max} = 12$, whereas PDE(DFT) and PDE(CD) use an evenly distributed grid of $(N1 = 25) \times (N_0 = 25)$ points.

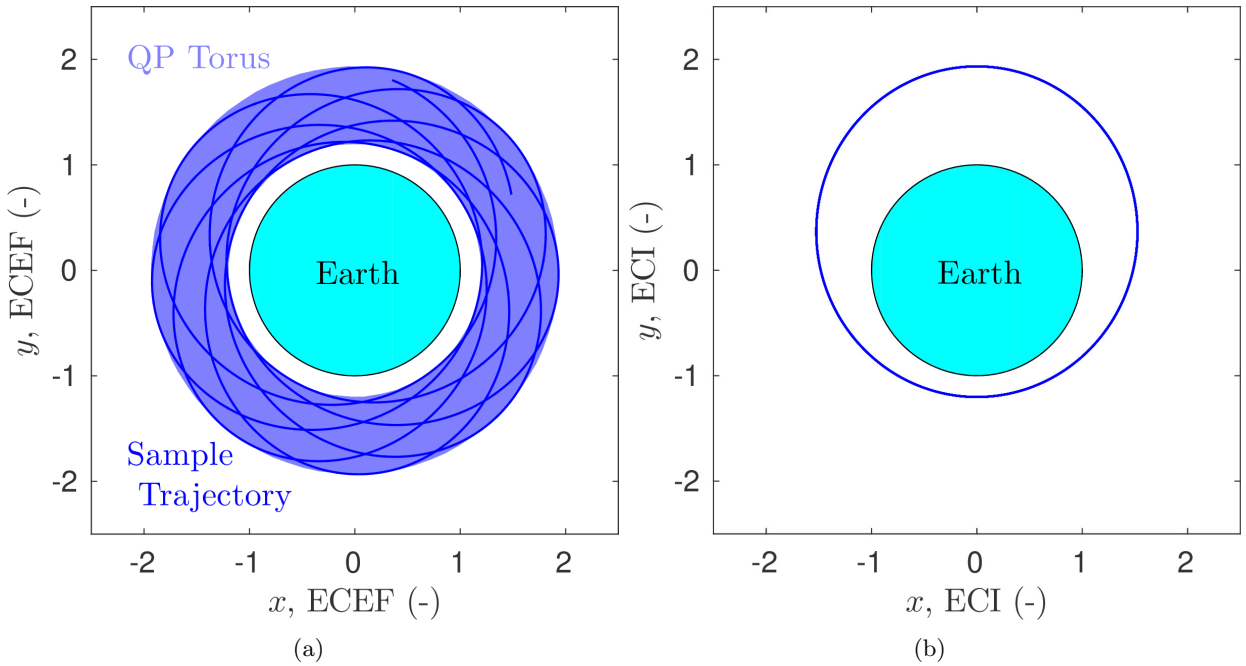

Figure 3.9: (a) Quasi-periodic invariant torus and sample trajectory in the ECEF frame of the Earth. (b) Sample trajectory as seen in the ECI frame. $e = 0.2334$.

still much sparser than the Jacobian matrix for the PDE(DFT) case (Fig. 3.10). With the proper implementation, this can save computational time when the number of solution points becomes significantly larger than the 25×25 grid used for the accuracy test.

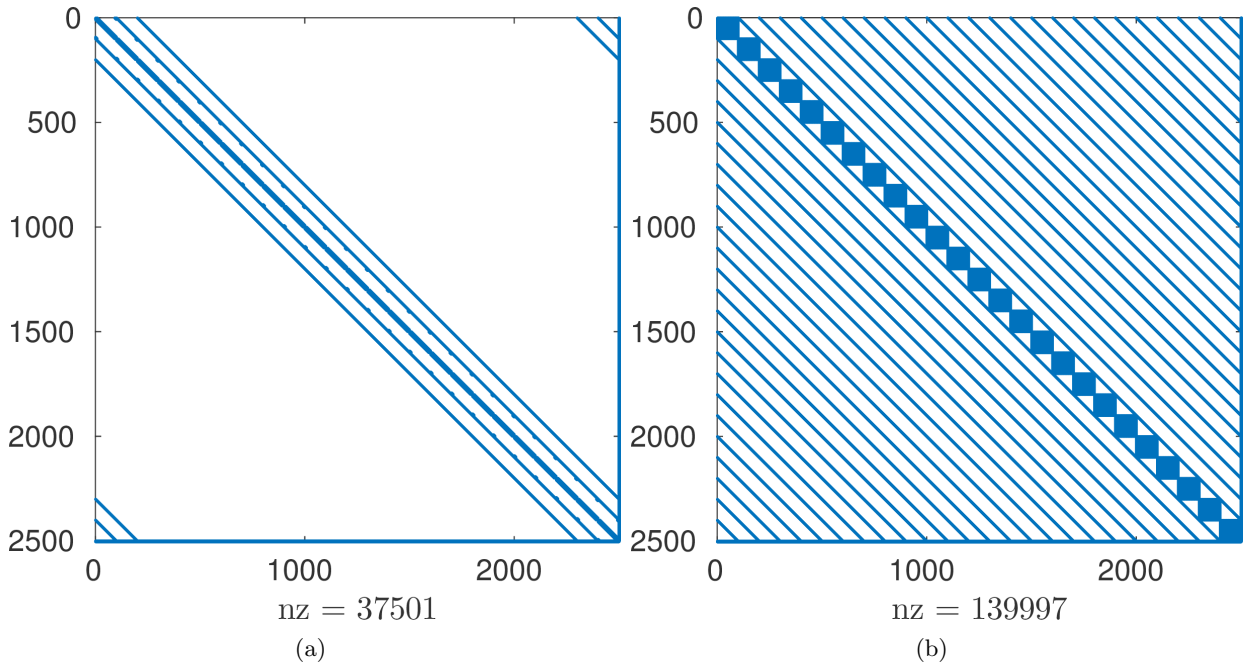

Figure 3.10: Sparsity of the Jacobian matrix for the PDE algorithms using central differences (a) and DFT (b). Both the matrices consist of $(n\,N_0\,N_1 + 4) \times (n\,N_0\,N_1 + 2) \simeq 6.26 \times 10^6$ entries.

As for the KKG method, it is fairly clear that the algorithm suffers from the lack of explicit dependency on the frequencies of the torus. Indeed, KKG is probably the least suitable method for computing families of QP tori with the same longitudinal frequency as the constraint (3.30) is certainly weaker than (3.9) and (3.48). A second disadvantage is that the algorithm works with the Fourier representation of the invariant curves of a Poincaré map rather than a finite set of satellite states. As it can be seen, this tends to decrease the accuracy of the solution points when the intersection of the torus with the surface of section becomes larger. Notably, such a trend is not observed in GMOS, probably because the DFT is applied to a set of n-dimensional states rather than on the projection of this curve onto a suitable coordinate plane. Speaking of this projection, it is also worth noting that the final choice of coordinates in the KKG algorithm is not unique

and ultimately depends on the topology of the QP tori family to be computed with the algorithm. Even different families of the same problem may require different coordinate choices, making the implementation of the KKG algorithm certainly more complicated and case dependent.

As far as GMOS and PDE(DFT) are concerned, it is difficult to distinguish between the performances of the two algorithms. Both of these strategies are well below the satisfactory tolerance used to check the convergence of Newton's method and none of them seem to decrease in accuracy when the eccentricity of the torus becomes larger. For all these reasons, we propose to further assess the accuracy and runtime of these methodology in a more practical astrodynamics problem such as the PCRTBP. The result of this analysis are summarized in the next sections, along with additional techniques that are relevant for the remainder of this thesis.

3.4 Further Remarks on GMOS and PDE(DFT)

Following the results of Fig. 3.8, it appears as GMOS and PDE(DFT) are the most accurate methodologies currently available in the astrodynamics literature. Therefore, it is interesting to further investigate these strategies in order to establish which of the candidate procedures should be preferred for practical studies of astrodynamics problems.

With this goal in mind, we now switch to the equations of motion of the PCRTBP with Earth-Moon masses [104, 103]:

$$\begin{cases} \ddot{x} - 2\,\dot{y} &= x - (1-\mu)\,\dfrac{(x+\mu)}{r_1^3} - \mu\,\dfrac{(x-1+\mu)}{r_2^3}, \\ \ddot{y} + 2\,\dot{x} &= y - (1-\mu)\,\dfrac{y}{r_1^3} - \mu\,\dfrac{y}{r_2^3}. \end{cases} \tag{3.54}$$

As usual, the mass, length, and time units of the problem are normalized such that total mass of the system, the mean motion of the secondary about the primary, and the total distance between the two are all equal to one. Furthermore, $\boldsymbol{x} = \begin{bmatrix} x, & y, & \dot{x}, & \dot{y} \end{bmatrix}^T$ is the state of a massless spacecraft in the co-rotating frame of the two primaries, r_1 is the distance from the larger body, r_2 is the distance from the secondary body, and $\mu = 0.01215$ is the mass ratio parameter.

Next, consider a distant retrograde orbit (DRO) such as the one of Fig. 3.11. As it is well

established in the literature [50], DROs are stable and surrounded by a family of two-dimensional quasi-periodic invariant tori. Therefore, fifty members of the family are computed using different combination of points with both the GMOS and PDE(DFT) algorithms (Figure 3.12).

Specifically, GMOS implementations based on multiple-shooting are hereby considered and compared with the single-shooting algorithm used for the results of Sec. 3.3. This should make the comparison more fair with the PDE(DFT) approach in terms of the size of the Jacobian matrix to be inverted via Newton's method. As for the PDE(DFT) methodology, the number of points in both the longitudinal and latitudinal directions is changed between $N_0 = 25$, 51, and $N_1 = 25$, 51, so as to verify the implications of using a finer mesh on the performance of the algorithm. For similar reasons, the number of GMOS points is also changed between 25 and 51.

The performance of the numerical procedures is assessed in terms of accuracy and runtime. For GMOS, the former is obtained by propagating a set of *midpoints* for one stroboscopic time and checking the invariant relationship (3.36). That is, once an invariant circle is calculated with the algorithm, a set of new initial conditions is obtained from the rotation of the solution points

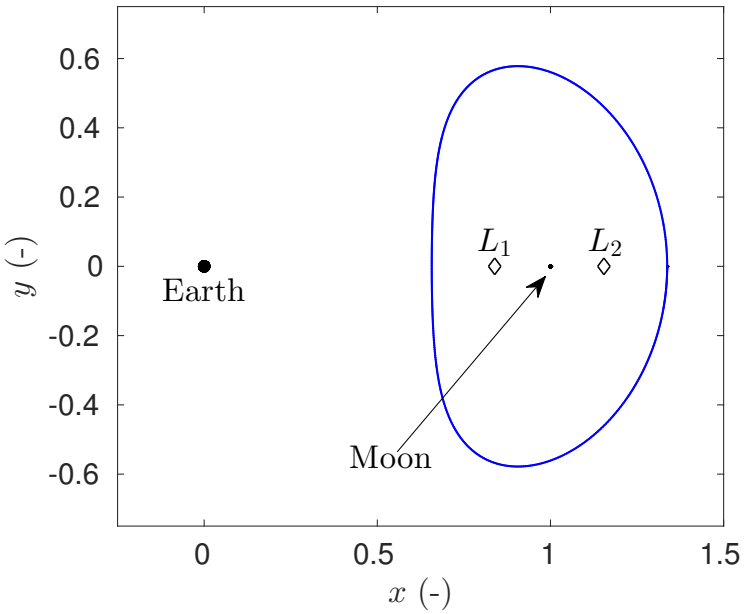

Figure 3.11: Example of DRO for the Earth-Moon system.

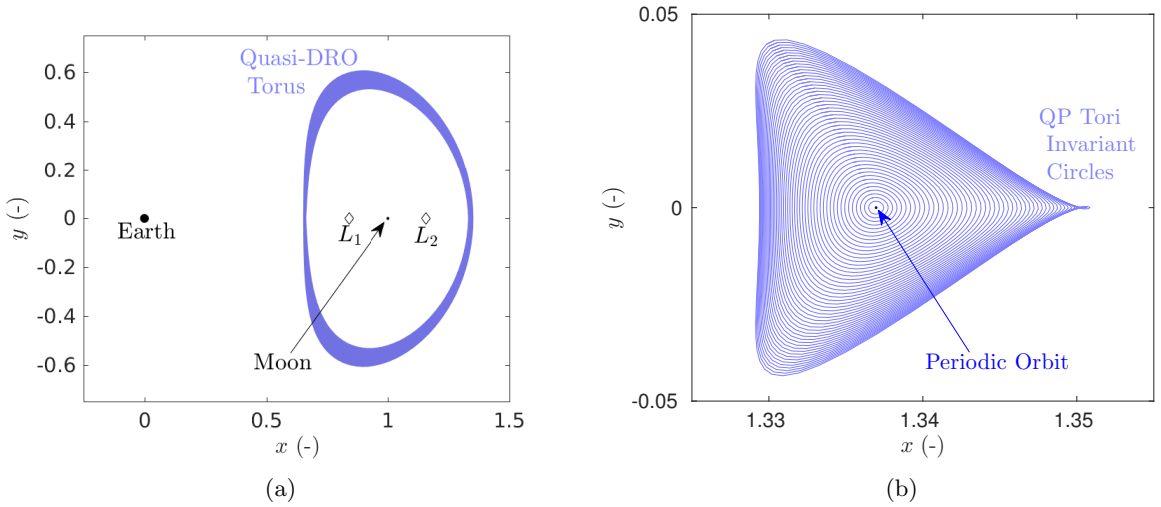

(a) (b)

Figure 3.12: (a) Fiftieth member of the quasi-DRO family of invariant tori computed with GMOS and PDE(DFT). (b) Fifty invariant circles of the stroboscopic mapping generated with the algorithms.

by an angle $\alpha = \pi/N_1$, where N_1 is the number of points used for the discretization of the curve. These midpoints are subsequently propagated forward in time using the equations of motion (3.54) until $T = 2\,\pi/\omega_0$, and eventually rotated backwards by an angle $\rho = \omega_1\,T$ via DFT. In theory, the rotated states should match the initial conditions generated for the accuracy test, whereas, in practice, discretization and numerical errors eventually start to degrade the quality of the computed solutions. This can be seen in the plot of Fig. 3.13, which illustrates the norm of the GMOS error vector normalized by the number of points for each of the different cases, i.e.,

$$E_{GMOS}(\boldsymbol{z}) = \sqrt{\sum_{i=0}^{N_1-1} \frac{\delta_i^2}{N_1}}, \tag{3.55}$$

where $\delta_i = \|R_{-\rho}\left[\boldsymbol{\varphi}_T(\boldsymbol{v}(\theta_i + \alpha))\right] - \boldsymbol{v}(\theta_i + \alpha)\|$.

Differently from the previous algorithm, PDE(DFT) does not compute invariant curves of stroboscopic maps. Therefore, the accuracy test proposed for GMOS cannot be applied to the PDE(DFT) approach. Instead, consider generating a set of midpoints along the first circle output by the algorithm, namely $\boldsymbol{u}(\theta_0 = 0, \theta_i + \beta)$, where $\beta = \pi/N_1$, and evaluate the force field in correspondence of this new set of points. Following the definition of quasi-periodic invariant tori

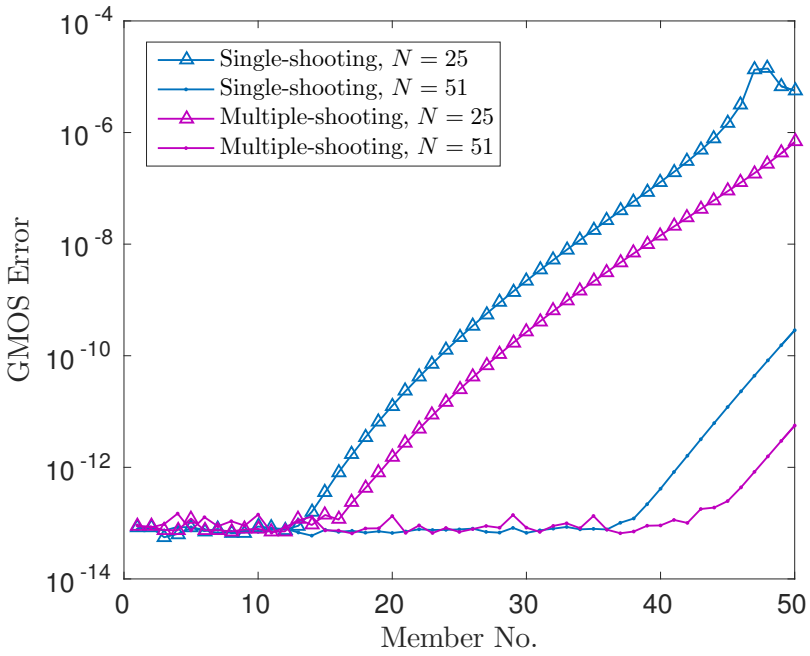

Figure 3.13: Norm of the error vector (3.55) computed from fifty GMOS solutions. It is worth noting that multiple-shooting trajectories have been generated using 5 segments.

(3.1), the force field should match the linear combination given by the partial derivatives of $\boldsymbol{u}(\theta_0 = 0, \theta_i + \beta)$ with respect to the parametrizing angles θ_0, θ_1, scaled by the torus frequencies ω_0 and ω_1.

Thus, let us define the error of the PDE(DFT) method as

$$E_{PDE}(\boldsymbol{z}) = \sqrt{\sum_{i=0}^{N_1-1} \frac{\epsilon_i^2}{N_1}}, \tag{3.56}$$

where

$$\epsilon_i = \left\| \boldsymbol{f}(\boldsymbol{u}(0, \theta_1 + \alpha_i)) - \omega_0 \left.\frac{\partial \boldsymbol{u}}{\partial \theta_0}\right|_{\theta_0=0,\theta_1=\theta_i+\alpha} - \omega_1 \left.\frac{\partial \boldsymbol{u}}{\partial \theta_1}\right|_{\theta_0=0,\theta_1=\theta_i+\alpha} \right\|. \tag{3.57}$$

The values of $E_{PDE}(\boldsymbol{z})$ are plotted in Fig. 3.14 for all of the fifty members of the quasi-DRO family obtained with different combinations of points, namely $(N_0 = 25) \times (N_1 = 25)$, 25×51, 51×25, and 51×51.

It turns out that GMOS is slightly more accurate than PDE(DFT). Not surprisingly, quasi-periodic trajectories obtained via multiple-shooting are also found to be more accurate than single-

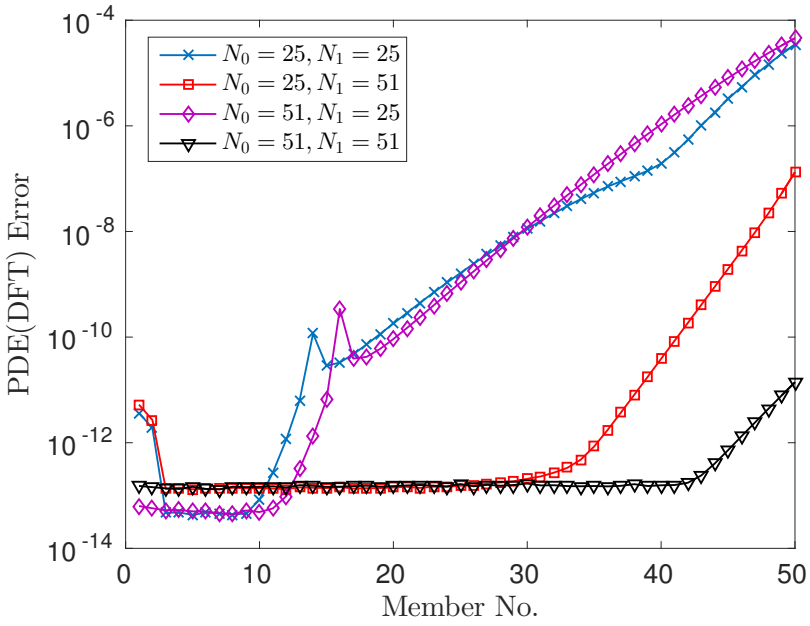

Figure 3.14: Norm of the PDE(DFT) error vector computed for fifty members of the quasi-DRO family with $(N_0 = 25) \times (N_1 = 25)$, 25×51, 51×25, and 51×51, respectively.

Table 3.1: Analysis of the runtime for the numerical computation of fifty quasi-DRO tori via GMOS and PDE(DFT). The data were collected for different combinations of N_1, N, and m using MATLAB's profiler on a System76 laptop running Ubuntu 15.04 with a quad-core i7-6700K CPU.

	Runtime		
	Total	ODE Integration	Newton's Update
GMOS, $N_1 = 25$	72.765 s	70.661 s	0.050 s
GMOS, $N_1 = 51$	135.263 s	132.958 s	0.189 s
GMOS(MS), $N_1 = 25$	138.493 s	137.284 s	0.615 s
GMOS(MS), $N_1 = 51$	647.153 s	642.978 s	3.027 s
PDE(DFT), $N_0 = 25$, $N_1 = 25$	67.682 s	N/A	49.671 s
PDE(DFT), $N_0 = 51$, $N_1 = 25$	453.530 s	N/A	405.130 s
PDE(DFT), $N_0 = 25$, $N_1 = 51$	459.413 s	N/A	411.188 s
PDE(DFT), $N_0 = 51$, $N_1 = 51$	3429.504 s	N/A	3324.771 s

shooting ones. Finally, doubling the number of discretization points significantly reduce the error up to the fortieth member of the family. Unfortunately, this also affects the runtime of the consider algorithms as observed in Table 3.1.

In Table 3.1, runtimes measured with MATLAB's profiler are summarized and compared

among each other. As it can be seen, PDE(DFT) turns out to be not only less accurate but also appreciably less efficient than GMOS. In particular, the algorithm spends $\simeq 90$ % of its time solving Newton's equation as no numerical integration is needed between different mesh points. Yet, the algorithm still comes out short as the total runtime is either comparable or greater than GMOS. In partial defense of the PDE(DFT) approach, it is worth noting that Newton's update is performed via MATLAB's backslash operator. For non-square matrices such as the Jacobians of the error vectors (3.5) and (3.41), this corresponds to a sparse QR-factorization based on Givens rotations that becomes particularly slow for large nonsparse matrices. Following [27], the speed of the algorithm could be significantly improved by making the Jacobian matrix square as in [83]. In the meantime, it should also be mentioned that the numerical integration of trajectories for the single-shooting and multiple-shooting GMOS cases has been performed using MATLAB's *ode113*. Appreciable speed-up is also expected by replacing this function with a pre-compiled numerical integrator, meaning that different implementations of the algorithms could hardly overthrow the outcome of our comparative analysis.

For all these reasons, it appears as the GMOS algorithm should be the method of investigation for the remainder of this thesis. Such a decision is also motivated by the possibility to carry out stability analyses on quasi-periodic trajectories and investigate novel design opportunities like ballistic lunar transfers [90] or formation deployment via quasi-periodic invariant manifolds. In addition to that, the algorithm is found to be applicable for calculating three-dimensional quasi-periodic invariant tori [7], as well as to be recast in collocation form for situations in which the instability of shooting techniques may become problematic. These and other advantages are further discussed in the following sections.

3.5 Collocation

As for all of the boundary value problems of the form (3.50)–(3.51), the GMOS algorithm can be also implemented with collocation. The benefit of this technique is that families of quasi-periodic invariant tori may be calculated even when poor initial guesses are available. This situation

is not uncommon and often occurs when dealing with time-periodic systems such as the Bicircular Problem (BCP) [24, 20, 42, 102] or the Elliptical Hill Problem (EHP) [40, 109] that is later discussed in this thesis. In addition to this, it is found that this particular implementation of GMOS allows for a very efficient solution of the system of algebraic equations arising from Newton's method. This makes the collocation version of GMOS particularly attractive and a valid alternative to the PDE(DFT) approach even when the global representation of a quasi-periodic invariant torus is needed.

To further investigate into this comparison, consider the boundary value problem given by (3.50) and subject to the boundary constraints

$$\boldsymbol{F}(\boldsymbol{z}) = \begin{bmatrix} g(\boldsymbol{X}_0, \boldsymbol{X}_1) \\ c_c(\boldsymbol{X}_0) \\ c_d(\boldsymbol{X}_0, T) \\ p_0(\boldsymbol{X}_0) \\ p_1(\boldsymbol{X}_0) \\ s_0(\boldsymbol{X}_0) \quad \text{or} \quad s_0(T) \\ s_1(\boldsymbol{z}) \end{bmatrix} = \boldsymbol{0}, \tag{3.58}$$

where $c_c(\boldsymbol{X}_0)$, $c_d(\boldsymbol{X}_0, T)$ are the continuity and collocation constraints defined in Eq. (2.30) adapted for the quasi-periodic case:

$$\begin{cases} c_c(\boldsymbol{X}_0) & := \quad \boldsymbol{X}_{i+1,0} - \sum_{j=0}^{m} \boldsymbol{X}_{i,j}\, L_j(\tau_{i+1}) = \boldsymbol{0}, & i = 0, \cdots, N-1 \\ c_d(\boldsymbol{X}_0, T) & := \quad T\, \mathbb{F}(\boldsymbol{X}_{i,j}) - \sum_{j=0}^{m} \boldsymbol{X}_{i,j}\, L_j'(\tau_j) = \boldsymbol{0}, & i = 0, \cdots, N-1; \quad j = 1, \cdots, m. \end{cases} \tag{3.59}$$

As it can be seen, the only difference with respect to (2.30) is that the states $\boldsymbol{X}_{i,j} \in \mathbb{R}^{n\,N_1}$ are now representative of a whole curve on the torus at the $N \times (m+1)$ collocation points defined in Sec. 2.4 rather than single samples of a periodic orbits at these instants. For the four-dimensional problem of Sec. 3.4, this means that the Jacobian matrix of (3.58) consists of, at least, 1×10^9 entries. This number assumes that an invariant curve of a stroboscopic mapping would be represented by $N_1 = 25$ discretization points, that the time domain would be split in $N = 50$ segments, and that

the solution $\boldsymbol{X}(\tau)$ would be evaluated in $m = 6$ collocation points on each of these subintervals. These are generally accepted as the minimum values for which the global error of the collocation method would be reasonable. However, depending on the application and accuracy requirements, it may be possible that the Jacobian matrix to be inverted via Eq. (3.52) could be even larger than this.

Fortunately, the sparsity of the Jacobian matrix portrayed in Fig. 3.15 is significantly better than the sparsity derived from the PDE(DFT) approach shown in Fig. 3.10(b). The consequences of this appear explictly in the numerical results of Table 3.2, where MATLAB's profiler has been applied to measure the performance of the collocation version of GMOS (GMOS(C)) with exactly the same setup of the previous section. In spite of the larger number of unknowns, GMOS(C) turns out to be quite efficient and fast, not only with respect to the PDE(DFT) approach, but also with respect to shooting versions of the same algorithm. The latter follows from the fact

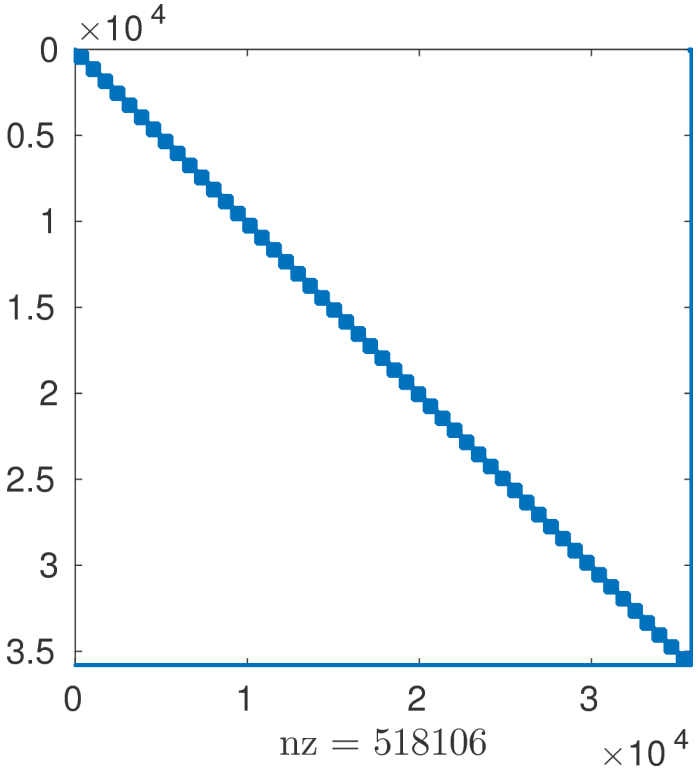

Figure 3.15: Jacobian matrix for the collocation version of GMOS. In this case, the GMOS(C) algorithm was launched with $N_1 = 25$ discretization points, $N = 51$ segments, and $m = 6$.

that the Jacobian matrix of (3.58) can be made squared by *unfolding the parameters* of a quasi-periodic invariant torus as advocated in Ref. [83]. Although a detailed discussion of this technique is beyond the scope of this manuscript, it is interesting to note that, in this case, MATLAB's backslash operator proceeds with a very efficient LU factorization that reduces the runtime of Newton's update by several factors [27]. For comparison, the application of Newton's method on a non-square Jacobian matrix in the GMOS(C) case with $N_1 = 25$, $N = 50$, $m = 6$ would take more than 3600 seconds to compute the same fifty members of the quasi-DRO family of Tables 3.1–3.2. Considering this appreciable speed-up, it goes without saying that the implementation strategy outlined in Ref. [83] should be preferred for thorough investigations of astrodynamics problems.

Moving forward, it is interesting to note that the accuracy of the GMOS(C) algorithm with $N_1 = 25$, $N = 50$, $m = 7$ remains within the tolerance of Newton's method (10^{-12}) for only several members of the quasi-DRO family. This is evident in the plot of Fig. 3.16, which displays the GMOS error of the collocation method in a similar fashion to Fig. 3.13. For future use of the GMOS(C), we will tacitly assume that the order of the Legendre polynomials used to interpolate the solution over each of the subintervals $[\tau_i, \tau_{i+1}]$ is $m = 7$. It also seems as $N = 50$ segments are enough to accurately represent a quasi-periodic solution in a class of dynamical problems that are as nonlinear as the PCRTBP. In particular, this configuration appears to be the best compromise between runtime and accuracy, even though the latter strongly depends on the number of solution points utilized for the discretization of the invariant curves. In this case, the plot of Fig. 3.16

Table 3.2: Analysis of the runtime for the numerical computation of fifty quasi-DRO tori via the collocation version of GMOS. The data were collected using MATLAB's profiler on a System76 laptop running Ubuntu 15.04 with a quad-core i7-6700K CPU.

	Runtime		
	Total	ODE Integration	Newton's Update
GMOS(C), $N_1 = 25$, $N = 50$, $m = 7$	104.038 s	N/A	66.758 s
GMOS(C), $N_1 = 35$, $N = 50$, $m = 7$	166.558 s	N/A	117.331 s
GMOS(C), $N_1 = 51$, $N = 50$, $m = 7$	311.413 s	N/A	232.662 s
GMOS(C), $N_1 = 51$, $N = 50$, $m = 9$	394.937 s	N/A	269.256 s
GMOS(C), $N_1 = 51$, $N = 100$, $m = 6$	650.574 s	N/A	527.149 s

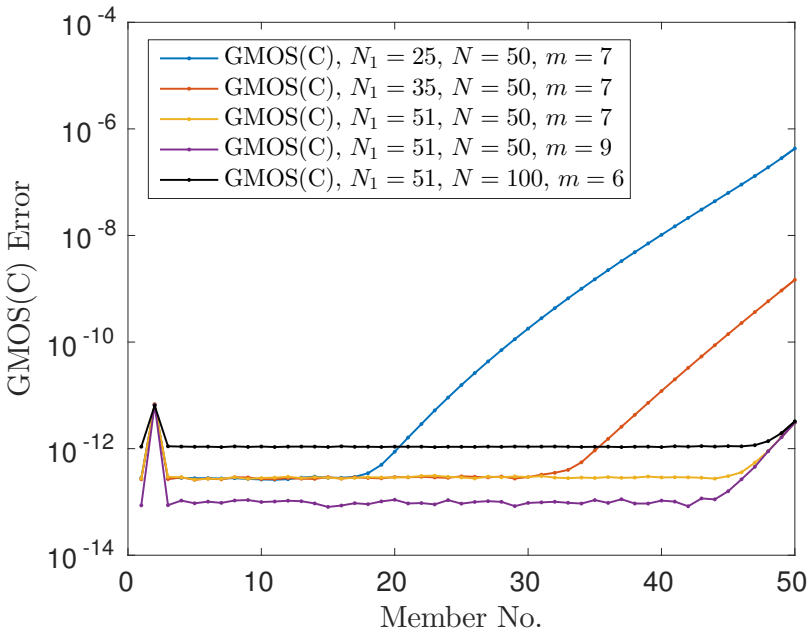

Figure 3.16: GMOS(C) error computed for fifty members of the quasi-DRO family with several combination of N_1, N, and m values.

suggests that more than $N_1 = 35$ points should be considered for accurate representations of several QP tori family members. Therefore, a value of $N_1 = 51$ is typically assumed for the numerical investigations presented in Sec. 5.4.

3.6 Stability of Quasi-periodic Invariant Tori

A second advantage offered by the GMOS algorithm is that the stability of quasi-periodic invariant tori can be calculated as a byproduct of the method. To support this claim, observe that if a solution of the BVP (3.50)–(3.51) is found, one has that the invariance relationship (3.36) is readily satisfied. Therefore, all of the GMOS solution points must be fixed points for the mapping $S_{-\rho} \equiv R_{-\rho} \circ \boldsymbol{\varphi}_T$. Following the latter, one might be tempted to infer the stability of a quasi-periodic torus from the differential map of $S_{-\rho}$ evaluated in $\boldsymbol{v}(\theta_j)$. However, if N solution points are used to approximate an invariant curve of the stroboscopic map $\boldsymbol{\varphi}_T$, the Jacobian of $S_{-\rho}$, namely $DS_{-\rho}(\boldsymbol{v}(\theta_j)) = R_{-\rho} \circ D\boldsymbol{\varphi}_T(\boldsymbol{v}(\theta_j))$, becomes a $n\,N \times n\,N$ matrix with $n\,N$ eigenvalues. In

order to identify which of the eigenvalues of $DS_{-\rho}$ are representative of the stability of torus, a criterion of selection needs to be established.

As explained in Ref. [56], such a criterion exists if the torus is *reducible*, i.e, if there is a coordinate transformation such that the differential of the stroboscopic map does not depend on the value of θ. To illustrate this statement, consider the linearization of (3.34) in the neighborhood of $\boldsymbol{v}(\theta)$, i.e.,

$$\delta\boldsymbol{v}(\theta+\rho) = D\boldsymbol{\varphi}_T(\boldsymbol{v}(\theta))\,\delta\boldsymbol{v}(\theta), \tag{3.60}$$

and let $\delta\boldsymbol{v}(\theta) = L(\theta)\,\boldsymbol{\gamma}(\theta)$ be a general coordinate transformation such that

$$\begin{aligned} L(\theta+\rho)\,\boldsymbol{\gamma}(\theta+\rho) &= D\boldsymbol{\varphi}_T(\boldsymbol{v}(\theta))\,L(\theta)\,\boldsymbol{\gamma}(\theta), \\ \boldsymbol{\gamma}(\theta+\rho) &= L(\theta+\rho)^{-1}\,D\boldsymbol{\varphi}_T(\boldsymbol{v}(\theta))\,L(\theta)\,\boldsymbol{\gamma}(\theta), \\ \boldsymbol{\gamma}(\theta+\rho) &= J(\theta)\,\boldsymbol{\gamma}(\theta). \end{aligned} \tag{3.61}$$

As it can be seen, if $L(\theta)$ is such that

$$J = L(\theta+\rho)^{-1}\,D\boldsymbol{\varphi}_T(\boldsymbol{v}(\theta))\,L(\theta) \tag{3.62}$$

no longer depends on θ, then J would be the same for all of the possible solution points $\boldsymbol{v}(\theta_j)$. This is of course ideal and in good agreement with the fact that the stability properties of the torus should be independent from the particular invariant curve being considered. This property is guaranteed by coordinate transformations based on the eigenfunctions $L_j(\theta)$ of the generalized eigenvalue problem

$$D\boldsymbol{\varphi}_T(\boldsymbol{v}(\theta))\,L_j(\theta) = \lambda_j\,R_\rho[L_j(\theta)]. \tag{3.63}$$

In this case, one also finds that the $n\,N$ eigenvalues μ_{jk} of $DS_{-\rho}$ can be immediately related to the n eigenvalues λ_j of J via

$$\mu_{jk} = \lambda_j\,e^{-\mathrm{i}\,k\,\rho} \tag{3.64}$$

where $k = 0, \cdots, N-1$. Consequently, the eigenvalues of $DS_{-\rho}$ lie on concentric circles of the complex plane, and each of these circles is representative of one eigenvalue λ_j, $j = 1, \cdots n$ of J.

It is worth noting that, due to the Hamiltonian structure of typical astrodynamics problems, concentric circles always come in pairs. That is, if one of the concentric circles has radius greater than one, say R_u, a second circle must exist with magnitude less than one, i.e., $R_s = 1/R_u$. Such a situation occurs when quasi-periodic invariant tori are hyperbolic. Then, global unstable and stable manifolds emanating from the torus can be generated via integration of quasi-periodic trajectories along any of the unstable and stable eigendirections found with this method. An example of these manifolds is disclosed in Fig. 3.17 along with the eigenvalues of a quasi-periodic invariant torus computed in the center manifold of HP L1 Halo orbit (Fig. 3.18). The interested reader may find additional applications of quasi-periodic invariant manifolds in Olikara's thesis [83] and [84].

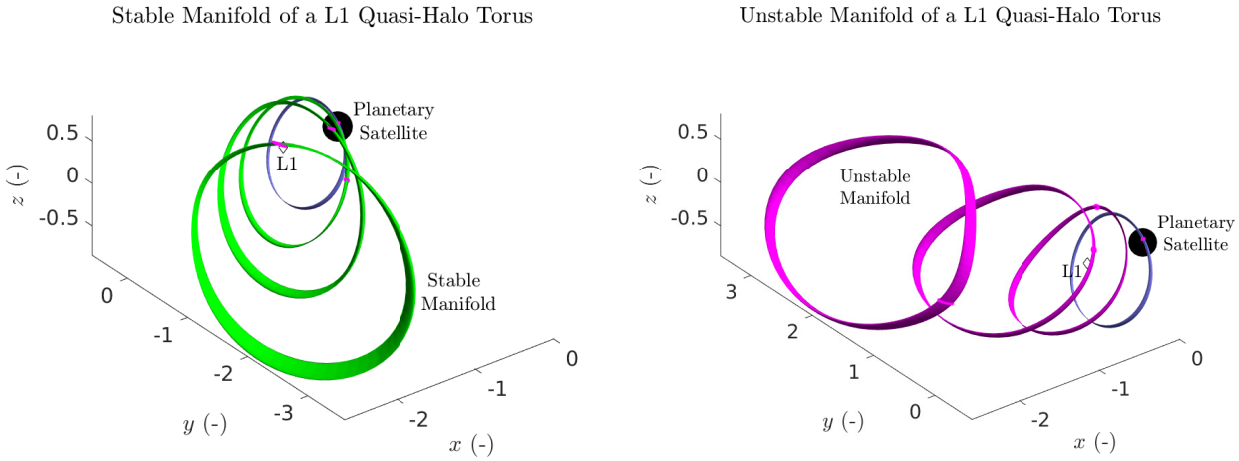

Figure 3.17: Stable (a) and Unstable manifolds (b) emanating from a L1 quasi-Halo invariant torus of the Hill problem.

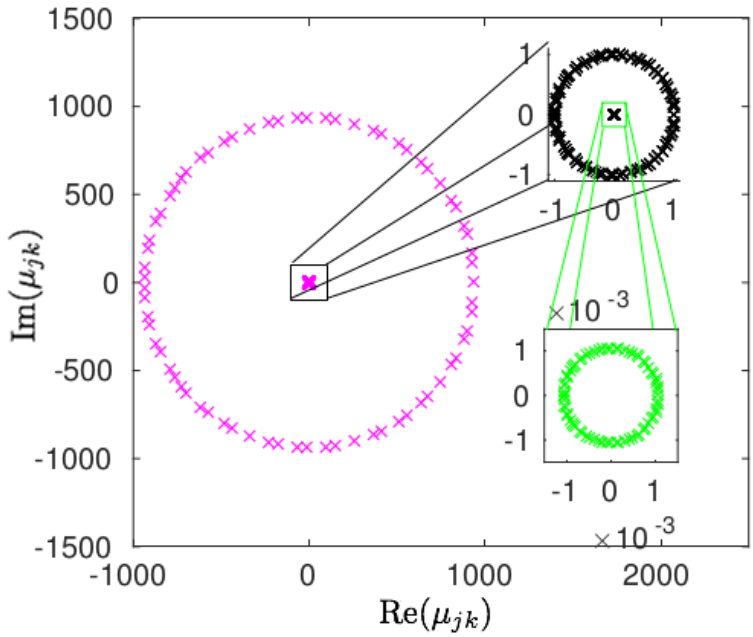

Figure 3.18: Eigenvalues of $DS_{-\rho}$.

3.7 Three-Dimensional Tori

As a final remark on the GMOS algorithm, it is worth mentioning that the numerical procedure can be easily adapted to compute quasi-periodic invariant tori of dimension three. These manifolds are usually found about stable periodic orbits of six-dimensional systems such as the HP or CRTBP problems, or in time-periodic systems such as the EHP discussed in Chapter 5. Therefore, it is relevant to briefly overview the changes in the GMOS algorithms needed to account for a third dimension. For instance, one finds that the output of the stroboscopic map after time T in torus coordinates corresponds to

$$\begin{aligned} \bar{\boldsymbol{\theta}} &= \begin{bmatrix} \theta_0 + \omega_0\, T, & \theta_1 + \omega_1\, T, & \theta_2 + \omega_2\, T \end{bmatrix}^T, \\ &= \begin{bmatrix} \theta_0, & \theta_1 + \rho, & \theta_2 + \nu \end{bmatrix}, \end{aligned} \tag{3.65}$$

where $\nu = 2\,\pi\,\omega_2/\omega_0$. Accordingly, let $\boldsymbol{\rho} = \begin{bmatrix} \rho, & \nu \end{bmatrix}^T$ be the *rotation vector* and consider the diffeomorphism $\boldsymbol{v} : \mathbb{T}^2 \to \mathbb{R}^n$ given by $\boldsymbol{v}(\boldsymbol{\psi}) = \boldsymbol{u}(\theta_0, \boldsymbol{\psi})$, where $\boldsymbol{\psi} = \begin{bmatrix} \theta_1, & \theta_2 \end{bmatrix}^T$.

From (3.34) it follows that

$$\boldsymbol{v}(\bar{\boldsymbol{\psi}}) = \boldsymbol{v}(\boldsymbol{\psi} + \boldsymbol{\rho}) = \boldsymbol{\varphi}_T(\boldsymbol{v}(\boldsymbol{\psi})), \tag{3.66}$$

so that a new set of algebraic equations can be found from the invariance relationships

$$R_{-\boldsymbol{\rho}}[\boldsymbol{\varphi}_T(\boldsymbol{v}(\boldsymbol{\psi}))] - \boldsymbol{v}(\boldsymbol{\psi}) = \mathbf{0}, \tag{3.67}$$

where $R_{-\boldsymbol{\rho}}$ is a new rotation operator, now acting on the space of the diffeomorphisms $\mathrm{V} = \{\boldsymbol{v}(\cdot) \,|\, \boldsymbol{v} : \mathbb{T}^2 \to \mathcal{T} \subset \mathbb{R}^6\}$.

Given the images of the stroboscopic map $\boldsymbol{v}(\bar{\boldsymbol{\psi}}_{j,k}) = \boldsymbol{v}(\theta_{1,j} + \rho, \theta_{2,k} + \nu)$ for the $N_1 \times N_2$ solution points $\boldsymbol{v}(\boldsymbol{\psi}_{j,k})$, one can apply the two-dimensional DFT [91]

$$\boldsymbol{c}_{l,m} = \sum_j \sum_k \boldsymbol{v}(\bar{\boldsymbol{\psi}}_{j,k})\, e^{\mathrm{i}\, l, \theta_{1,j}}\, e^{\mathrm{i}\, m, \theta_{2,k}}, \tag{3.68}$$

and obtain a realization of $R_{-\boldsymbol{\rho}}$ via

$$R_{-\boldsymbol{\rho}}[\boldsymbol{v}(\theta_{1,j}, \theta_{2,k})] = \frac{1}{N_1}\frac{1}{N_2} \sum_l \sum_m \boldsymbol{c}'_{l,m}\, e^{\mathrm{i}\, l\, \theta_1}\, e^{\mathrm{i}\, m\, \theta_2}, \tag{3.69}$$

where $\boldsymbol{c}'_{l,m} = e^{-\mathrm{i}\, l\, \rho}\, e^{-\mathrm{i}\, m\, \nu}\, \boldsymbol{c}_{l,m}$. Furthermore, if $\boldsymbol{X}_0 = \Big[\boldsymbol{v}(\boldsymbol{\psi}_{0,0}), \quad \boldsymbol{v}(\boldsymbol{\psi}_{0,1}), \quad \ldots, \quad \boldsymbol{v}(\boldsymbol{\psi})_{1,0}, \quad \ldots, \quad \boldsymbol{v}(\boldsymbol{\psi}_{N_1,N_2})\Big]^T$, and $\boldsymbol{X}_1 = \Big[\boldsymbol{v}(\bar{\boldsymbol{\psi}}_{0,0}), \quad \boldsymbol{v}(\bar{\boldsymbol{\psi}}_{0,1}), \quad \ldots, \quad \boldsymbol{v}(\bar{\boldsymbol{\psi}}_{N_1,N_2})\Big]$, the quasi-periodic boundary constraints become

$$\boxed{\boldsymbol{g}(\boldsymbol{X}_0, \boldsymbol{X}_1) := [\mathcal{D}]^{-1}\, [R(-\rho, -\nu)]\, [\mathcal{D}]\, \boldsymbol{X}_1 - \boldsymbol{X}_0 = \mathbf{0}} \tag{3.70}$$

where $\mathcal{D}$ is now the two-dimensional DFT operator written in matrix form, and $[R(-\rho, -\nu)]$ is the matrix that rotates the Fourier coefficients from $\boldsymbol{c}_{l,m}$ to $\boldsymbol{c}'_{l,m}$.

Of course, in order to find solution of the BVP given by (3.18)–(3.70), one has to update (3.70) via Newton's method. However, solutions are not unique until phase conditions and parametrization equations are added to the system of algebraic equations derived from (3.70). For three-dimensional tori of autonomous Hamiltonian system, it turns out that two phase conditions of the form (3.43) need to be included, namely

$$\begin{aligned} p_1(\boldsymbol{X}_0) \;&:= < \boldsymbol{X}_0, \frac{\partial \tilde{\boldsymbol{X}}_0}{\partial \theta_1} >, \\ &= \frac{1}{(2\,\pi)^2} \int_0^{2\,\pi} \int_0^{2\,\pi} \left[\boldsymbol{v}(\alpha, \beta)^T\, \frac{\partial \tilde{\boldsymbol{v}}(\alpha, \beta)}{\partial \theta_1}\right] \mathrm{d}\alpha\, \mathrm{d}\beta, \\ &\simeq \frac{1}{N_1\, N_2} \sum_j \sum_k \boldsymbol{v}(\boldsymbol{\psi}_{j,k})^T\, \frac{\partial \tilde{\boldsymbol{v}}(\boldsymbol{\psi}_{j,k})}{\partial \theta_1} = 0, \end{aligned} \tag{3.71}$$

and

$$\begin{aligned} p_2(\boldsymbol{X}_0) &:=< \boldsymbol{X}_0, \frac{\partial \tilde{\boldsymbol{X}}_0}{\partial \theta_2} >, \\ &\simeq \frac{1}{N_1\, N_2} \sum_j \sum_k \boldsymbol{v}(\boldsymbol{\psi}_{j,k})^T \frac{\partial \tilde{\boldsymbol{v}}(\boldsymbol{\psi}_{j,k})}{\partial \theta_2} = 0. \end{aligned} \tag{3.72}$$

Then, the last of the phase conditions can be given by

$$p_0(\boldsymbol{X}_0) :=< \boldsymbol{X}_0 - \tilde{\boldsymbol{X}}_0, \frac{\partial \tilde{\boldsymbol{X}}_0}{\partial \theta_0} >, \tag{3.73}$$

where

$$\frac{\partial \tilde{\boldsymbol{v}}}{\partial \theta_0} = \frac{1}{\tilde{\omega}_0} \left[\boldsymbol{f}(\tilde{\boldsymbol{v}}(\psi)) - \tilde{\omega}_1 \frac{\partial \tilde{\boldsymbol{v}}}{\partial \theta_1} - \tilde{\omega}_2 \frac{\partial \tilde{\boldsymbol{v}}}{\partial \theta_2} \right]. \tag{3.74}$$

As for the parametrization equations, recall that three-dimensional tori of autonomous Hamiltonian systems generally live in three-parameter families. Therefore, to identify unique members within a 3D tori family, three additional equations are needed, namely $s_0(\boldsymbol{X}_0, T, \boldsymbol{\rho})$, $s_1(\boldsymbol{X}_0, T, \boldsymbol{\rho})$, and $s_2(\boldsymbol{X}_0, T, \boldsymbol{\rho})$.

In the end, one has the BVP given by

$$\begin{cases} \boldsymbol{X}' &= T\, \mathbb{F}(\boldsymbol{X}), \\ T' &= 0, \\ \rho' &= 0, \\ \nu' &= 0, \end{cases} \tag{3.75}$$

and subject to the boundary constraints

$$\boldsymbol{F}(\boldsymbol{z}) = \begin{bmatrix} \boldsymbol{g}(\boldsymbol{X}_0, \boldsymbol{X}_1) \\ p_0(\boldsymbol{X}_0) \\ p_1(\boldsymbol{X}_0) \\ p_2(\boldsymbol{X}_0) \\ s_0(\boldsymbol{X}_0, T, \boldsymbol{\rho}) \\ s_1(\boldsymbol{X}_0, T, \boldsymbol{\rho}) \\ s_2(\boldsymbol{X}_0, T, \boldsymbol{\rho}) \end{bmatrix} = \boldsymbol{0}, \tag{3.76}$$

where $\boldsymbol{z}$ now corresponds to $\begin{bmatrix} \boldsymbol{X}_0, & T, & \boldsymbol{\rho} \end{bmatrix}^T$.

As usual, $s_0(\boldsymbol{X}_0, T, \boldsymbol{\rho})$ may be used to specify either the energy level of the torus, i.e.,

$$s_0(\boldsymbol{X}_0) := \frac{1}{N_1\, N_2} \sum_j \sum_k \mathcal{C}(\boldsymbol{w}_{j,k}) - C = 0 \tag{3.77}$$

or its *period*:

$$s_0(T) := T - \mathcal{P} = 0. \tag{3.78}$$

To find an expression for $s_1(\boldsymbol{X}_0, T, \boldsymbol{\rho})$ and $s_2(\boldsymbol{X}_0, T, \boldsymbol{\rho})$, consider the following generalized pseudo-arclength continuation approach [48]. First, assume $\tilde{\boldsymbol{z}}$ is a previously known solution of the BVP (3.75)–(3.76) such that

$$\boldsymbol{h}(\boldsymbol{z}) = \begin{bmatrix} \boldsymbol{g}(\boldsymbol{X}_0, \boldsymbol{X}_1) \\ p_0(\boldsymbol{X}_0) \\ p_1(\boldsymbol{X}_0) \\ p_2(\boldsymbol{X}_0) \end{bmatrix} \tag{3.79}$$

is also equal to $\mathbf{0}$. Also assume that such a solution is found in correspondence of the *unfolding* parameters r^* and s^*, i.e., $\boldsymbol{h}(\tilde{\boldsymbol{z}}) = \boldsymbol{h}(\boldsymbol{z}(r^*, s^*)) = \mathbf{0}$. Looking for nearby solutions in correspondence of $r^* + \delta r$ and $s^* + \delta s$, one finds that

$$\begin{aligned} \mathbf{0} &\simeq \boldsymbol{h}(\boldsymbol{z}(r^* + \delta r, s^* + \delta s)), \\ &\simeq \boldsymbol{h}(\boldsymbol{z}(r^*, s^*)) + D\boldsymbol{h}(\boldsymbol{z}(r^*, s^*))\, [\boldsymbol{z}'_r(r^*, s^*)\, \delta r + \boldsymbol{z}'_s(r^*, s^*)\, \delta s], \\ &= D\boldsymbol{h}(\tilde{\boldsymbol{z}})\, [\tilde{\boldsymbol{z}}'_r\, \delta r + \tilde{\boldsymbol{z}}'_s\, \delta s], \end{aligned} \tag{3.80}$$

where $\tilde{\boldsymbol{z}}'_r$ and $\tilde{\boldsymbol{z}}'_s$ denote the family tangent with respect to r and s, respectively, evaluated in (r^*, s^*). From Eq. (3.80), it follows that $\tilde{\boldsymbol{z}}'_r$ and $\tilde{\boldsymbol{z}}'_s$ form a basis for the kernel of $D\boldsymbol{h}(\tilde{\boldsymbol{z}})$. Therefore, $\tilde{\boldsymbol{z}}'_r$ and $\tilde{\boldsymbol{z}}'_s$ can be easily computed via the singular value decomposition of $D\boldsymbol{h}(\tilde{\boldsymbol{z}})$ or similar methods. In addition to that, observe that

$$\boldsymbol{z}(r^* + \delta r, s^* + \delta s) \simeq \tilde{\boldsymbol{z}} + \tilde{\boldsymbol{z}}'_r\, \delta r + \tilde{\boldsymbol{z}}'_s\, \delta s, \tag{3.81}$$

so that

$$(\boldsymbol{z} - \tilde{\boldsymbol{z}}) = \begin{bmatrix} \tilde{\boldsymbol{z}}'_r, & \tilde{\boldsymbol{z}}'_s \end{bmatrix} \begin{bmatrix} \delta r \\ \delta s \end{bmatrix} \tag{3.82}$$

also needs to be satisfied. Specifically,

$$\begin{bmatrix} \tilde{\boldsymbol{z}}_r'^T \\ \tilde{\boldsymbol{z}}_s'^T \end{bmatrix} (\boldsymbol{z} - \tilde{\boldsymbol{z}}) = \begin{bmatrix} \|\tilde{\boldsymbol{z}}_r'\|^2, & \tilde{\boldsymbol{z}}_r'^T \tilde{\boldsymbol{z}}_s' \\ \tilde{\boldsymbol{z}}_s'^T \tilde{\boldsymbol{z}}_r', & \|\tilde{\boldsymbol{z}}_s'\|^2 \end{bmatrix} \begin{bmatrix} \delta r \\ \delta s \end{bmatrix}, \tag{3.83}$$

yielding

$$s_1(\boldsymbol{z}) \;:=\; < \tilde{\boldsymbol{z}}_r' \,,\, \boldsymbol{z} - \tilde{\boldsymbol{z}} > -\delta r - \tilde{\boldsymbol{z}}_r'^T \tilde{\boldsymbol{z}}_s' \,\delta s = 0, \tag{3.84a}$$

$$s_2(\boldsymbol{z}) \;:=\; < \tilde{\boldsymbol{z}}_s' \,,\, \boldsymbol{z} - \tilde{\boldsymbol{z}} > -\tilde{\boldsymbol{z}}_s'^T \tilde{\boldsymbol{z}}_r' \,\delta r - \delta s = 0, \tag{3.84b}$$

when $\|\tilde{\boldsymbol{z}}_r'\|^2 = \|\tilde{\boldsymbol{z}}_s'\|^2 = 1$.

Eq. (3.84) completes the list of boundary constraints (3.76) to be satisfied with Newton's method once a reliable initial guess is provided. The latter is found via the eigenvalue and eigenvector pairs obtained from the monodromy matrix M of a periodic orbit such as the blue trajectory of Fig. 2.3. If $\boldsymbol{e}_{12}$ and $\boldsymbol{e}_{34}$ are the eigenvectors associated with $\lambda_{12} = e^{\pm \mathrm{i}\rho}$ and $\lambda_{34} = e^{\pm \mathrm{i}\nu}$, one can construct an *invariant torus* of the monodromy map:

$$\begin{aligned} \boldsymbol{\varphi}(\theta_1, \theta_2) =& K_{12} \,[\cos(\theta_1)\,\mathrm{Re}(\boldsymbol{e}_{12}) - \sin(\theta_1)\,\mathrm{Im}(\boldsymbol{e}_{12})] + \ldots \\ & K_{34} \,[\cos(\theta_2)\,\mathrm{Re}(\boldsymbol{e}_{34}) - \sin(\theta_2)\,\mathrm{Im}(\boldsymbol{e}_{34})]\,, \end{aligned} \tag{3.85}$$

where K_{12} and K_{34} are two arbitrary small scalars $<< 1$. Indeed, the torus (3.85) is invariant under the application of the monodromy matrix M as

$$M\,\boldsymbol{\varphi}(\theta_1, \theta_2) = \boldsymbol{\varphi}(\theta_1 + \rho, \theta_2 + \nu). \tag{3.86}$$

Therefore, consider taking $N_1 \times N_2$ points along the invariant torus of the monodromy map in correspondence of the $N_1 \times N_2$ angular values $(\theta_{1,j} = 2\,\pi\,j/N_1) \times (\theta_{2,k} = 2\,\pi\,k/N_2)$, $j = 0, 1, \ldots, N_1 - 1$, $k = 0, 1, \ldots, N_2 - 1$. Eq. (3.86) also suggests that the phases of the complex conjugate eigenvalues, namely ρ and ν, may be used to approximate the components of the rotation vector $\boldsymbol{\rho}$. For this to be true, the stroboscopic time T should be also initialized as the period of the underlying periodic orbit. This completes the initial guess $\tilde{\boldsymbol{z}} = (\tilde{\boldsymbol{X}}_0, \tilde{T}, \tilde{\boldsymbol{\rho}})$ since the points $\tilde{\boldsymbol{w}}(\theta_{1,j}, \theta_{2,k}) \simeq \boldsymbol{\varphi}(\theta_{1,j}, \theta_{2,k})$ can be also integrated and rotated to generate a reliable approximation of the family tangents $\tilde{\boldsymbol{z}}_r'$

and $\tilde{\boldsymbol{z}}_s^{'}$ via the singular value decomposition of $D\boldsymbol{h}(\tilde{\boldsymbol{z}})$. Then, Newton's method can be applied and embedded into a predictor-corrector scheme that allows to march along entire family branches. An example of this is shown in Fig. 3.19, which illustrates a three-dimensional quasi-halo torus belonging to the center manifold of the aforementioned stable periodic orbit.

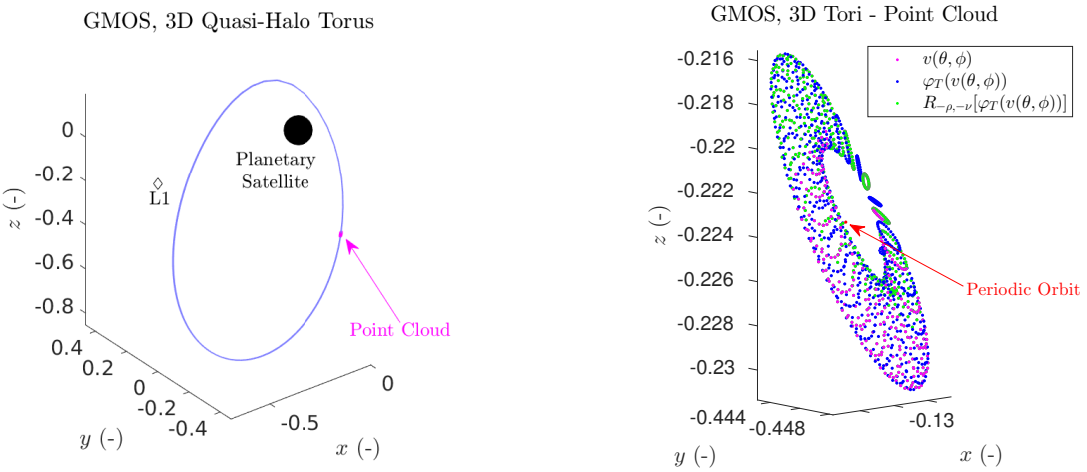

Figure 3.19: Quasi-Halo 3D torus(a) obtained by numerical integration of the invariant torus of the stroboscopic mapping shown in (b). The 3D version of GMOS was launched with $N_1 = 31$ and $N_2 = 21$ points, respectively.

Finally, observe that stability analysis can be also carried out as a byproduct of the algorithm in the three-dimensional case. The only difference with respect to the analysis of Sec. 3.6 is that the $n\,N_1\,N_2$ eigenvalues μ_{jkl} of $DS_{-\boldsymbol{\rho}}$ are now related to the n eigenvalues λ_j of J via

$$\mu_{jkl} = \lambda_j\, e^{-\mathrm{i}\,k\,\rho}\, e^{-\mathrm{i}\,l\,\nu} \tag{3.87}$$

where $k = 0, \ldots, N_1 - 1$, and $l = 0, \ldots, N_2 - 1$. As it can be seen, this does not change the fact that eigenvalues of $DS_{-\boldsymbol{\rho}}$ are still distributed along concentric circles of the complex plane, thereby proving the validity of the results of Sec. 3.6 for tori of arbitrary dimension.

3.8 Conclusions

This chapter has presented some of the numerical procedures involved with the astrodynamics applications of quasi-periodic invariant tori explored in the next chapters. Specifically, after reviewing the different methodologies available in the literature (Section 3.1–3.2), we have identified GMOS as our preferred approach for future studies. Such a conclusion was drawn after comparing the output of the code with the analytical solution of the Two-Body Problem (TBP) (Section 3.3), as well as by numerically investigating the accuracy of fifty quasi-DRO tori generated with the algorithm in the PCRTBP (Section 3.4). Remarkably, the strategy was also found to be solvable using collocation techniques, as well as to enable stability analysis and handle quasi-periodic invariant tori of dimension three (Section 3.5–3.7).

Starting from Chapter 4, we will see how the GMOS algorithm can be useful in space mission design contexts. This begins by studying how the stroboscopic mapping approach can be slightly modified to compute entire families of bounded relative trajectories about axisymmetric bodies.

Chapter 4

Bounded Relative Trajectories about Axisymmetric Bodies

In this chapter, we shall see how the GMOS algorithm can be adjusted to compute entire families of bounded relative orbits without the need for the numerically expensive grid searches proposed in Ref. [114] & [22]. We begin by reviewing the equation of motion for a mass particle subject to the gravitational attraction of an axisymmetric body and demonstrate how Routh reduction can be applied to lower the dimensionality of the problem (Sec. 4.1). Next, we discuss the dynamics of satellites in this force field and introduce three fundamental periods whose averaged values can be accurately computed through numerical integration. First is the nodal period, which is commonly defined as the time elapsed between two consecutive equatorial plane crossings at the ascending node. Next is the sidereal period, which is a function of the drift in the right ascension of the ascending node per nodal period. Lastly, there is the anomalistic period, which depends on the difference between the argument of pericenter of a satellite at consecutive equatorial plane crossings. To ensure bounded relative motion over long periods of time, at least two of these fundamental quantities need to be matched on average.

Based on this observation, we consider a formation of two satellites–a chief and a deputy spacecraft–and introduce a numerical procedure to ensure that the nodal and sidereal periods of the deputy match, on average, the values of the chief. The so-called revised GMOS algorithm is illustrated in Sec. 4.4 along with simulations showing that families of bounded relative trajectories can be generated once a stable periodic orbit of the Routh-reduced system is found. This holds at a range of altitude and inclination values, including MEO and geostationary orbits, as well as

beyond Earth orbit (Sec. 4.5). These and other remarks on the proposed numerical approach are finally summarized in Sec. 4.6.

4.1 Equations of Motion

Consider a spacecraft subject to the gravitational attraction of an axisymmetric body. As illustrated in Ref. [78], the zonal part of the gravitational potential is given by

$$U(R,\Theta) = \frac{\mu_\oplus}{R}\left[1 - \sum_{l=2}^{\infty} J_l \left(\frac{R_\oplus}{R}\right)^l P_l(\sin\Theta)\right], \tag{4.1}$$

where $\mu_\oplus$ denotes the gravitational parameter of the body, $R_\oplus$ is its reference radius, J_l are the zonal harmonics coefficients, and P_l are the Legendre's polynomials (Table 4.1). Furthermore, if $\boldsymbol{x} = \left[x, y, z, \dot{x}, \dot{y}, \dot{z}\right]^T$ represents the six-dimensional state of the satellite in a body-centered inertial frame (BCI) where $\hat{\boldsymbol{z}}$ is parallel to the body's spin axis, $\hat{\boldsymbol{x}}$ is directed towards the vernal equinox, and $\hat{\boldsymbol{y}} = \hat{\boldsymbol{z}} \times \hat{\boldsymbol{x}}$, then $R = \sqrt{x^2 + y^2 + z^2}$ is the distance from the gravity center to the spacecraft, $\Theta = \arcsin\left(\frac{z}{R}\right)$ is its latitude, and $\phi = \arctan^{-1}(y/x)$ is its longitude.

Following the latter convention, the Lagrangian of the system can be rewritten in spherical coordinates as

$$\mathcal{L}(R,\Theta,\dot{R},\dot{\Theta},\dot{\phi}) = \frac{1}{2}\left(\dot{R}^2 + R^2\,\dot{\Theta}^2 + R^2\,\dot{\phi}^2\,\cos\Theta^2\right) + U(R,\Theta), \tag{4.2}$$

thereby showing that $\mathcal{L}$ does not depend on the spacecraft longitude, i.e., ϕ is a cyclic variable. It is then possible to apply Routh reduction and simplify the dynamics in the four-dimensional RRS

Table 4.1: Legendre polynomials used for the simulations.

Legendre Polynomials	
$P_2(x)$	$\frac{1}{2}\left(3\,x^2 - 1\right)$
$P_3(x)$	$\frac{1}{2}\left(5\,x^3 - 3\,x\right)$
$P_4(x)$	$\frac{1}{8}\left(35\,x^4 - 15\,x^2 + 3\right)$
$P_5(x)$	$\frac{1}{8}\left(63\,x^5 - 70\,x^3 + 15\,x\right)$

discussed in Ref. [17]:

$$\dot{\boldsymbol{y}} = \boldsymbol{f}(\boldsymbol{y}, H_z) = \begin{cases} \dot{r}, \\ \dot{z}, \\ \dfrac{H_z^2}{r^3} + \dfrac{\partial U}{\partial r}, \\ \dfrac{\partial U}{\partial z}, \end{cases} \tag{4.3}$$

where $\boldsymbol{y} = \begin{bmatrix} r, & z, & \dot{r}, & \dot{z} \end{bmatrix}^T$ is the reduced state vector, and $(r, z) = (R\cos\Theta, R\sin\Theta)$ are the rectangular coordinates of the spacecraft.

Observe that the equations of motion (4.3) conserve the energy integral

$$\mathcal{E}(\boldsymbol{y}) = U - \frac{1}{2}\frac{H_z^2}{r^2} - \frac{1}{2}(\dot{r}^2 + \dot{z}^2) = E, \tag{4.4}$$

which is later used to distinguish between zones of admissible motion and forbidden regions as in Sec. 2.1. Furthermore, $H_z = \dfrac{\partial \mathcal{L}}{\partial \dot{\phi}} = R^2\cos^2\Theta\,\dot{\phi} = r^2\,\dot{\phi}$ =const is also conserved and corresponds to the third component of the angular momentum vector. Since H_z is constant, the quadrature

$$\phi(t) = \phi_0 + H_z \int_{t_0}^{t} \frac{1}{(r(t'))^2}\mathrm{d}t' \tag{4.5}$$

can be utilized to find the instantaneous longitude of the satellite at arbitrary times t, and generate a trajectory in BCI via

$$\begin{cases} x(t) &= r(t)\,\cos\phi(t), \\ y(t) &= r(t)\,\sin\phi(t), \\ z(t) &= z(t), \\ \dot{x}(t) &= \dot{r}(t)\,\cos\phi(t) - H_z\,\sin\phi(t)/r(t) \\ \dot{y}(t) &= \dot{r}(t)\,\sin\phi(t) + H_z\,\cos\phi(t)/r(t) \\ \dot{z}(t) &= \dot{z}(t). \end{cases} \tag{4.6}$$

ϕ_0 is the initial longitude of the spacecraft and its value does not affect the solution $(r(t), z(t))$ of the reduced system (4.3) nor the possibility of generating bounded relative trajectories in the full six-dimensional space. On the contrary, even though H_z is only a parameter for (4.3), its choice has remarkable impacts on the relative motion between two neighboring trajectories as demonstrated in the following sections.

4.2 Spacecraft Dynamics

As demonstrated by Chu et al. [22], the motion of a mass particle subject to the gravitational attraction of an axisymmetric body is characterized by three fundamental frequencies or periods: the nodal period, the sidereal period, and the anomalistic period. First is the nodal period T_d, which is conventionally defined as the time between two consecutive crossings of the equatorial plane from south to north [11]. If we define $\zeta(\boldsymbol{y}) := z = 0,\ \dot{z} > 0$ as the surface of section and $\boldsymbol{\varphi}_t$ as the solution flow of (4.3), then T_d is defined as the first return time such that $\boldsymbol{y}_2^* = \boldsymbol{\varphi}_{T_d}(\boldsymbol{y}_1^*)$, where $\boldsymbol{y}_1^*$ and $\boldsymbol{y}_2^*$ are the spacecraft reduced state vectors at the first and second intersection with $\zeta(\boldsymbol{y})$. By converting these states into osculating orbit elements, one can also infer the values of the sidereal and anomalistic periods as follow:

$$T_s = 2\,\pi\,T_d/(2\,\pi + \Delta\Omega_d), \qquad \text{and} \qquad T_a = 2\,\pi\,T_d/(2\,\pi - \Delta\varpi_d), \tag{4.7}$$

where $\Delta\Omega_d = \Omega_2 - \Omega_1$ and $\Delta\varpi_d = \varpi_2 - \varpi_1$ are the differences in RAAN and argument of perigee at consecutive $\zeta(\boldsymbol{y})$ crossings. Consequently, the sidereal period is related to the RAAN drift per nodal period caused by the non-spherical shape of the central body, whereas the anomalistic period

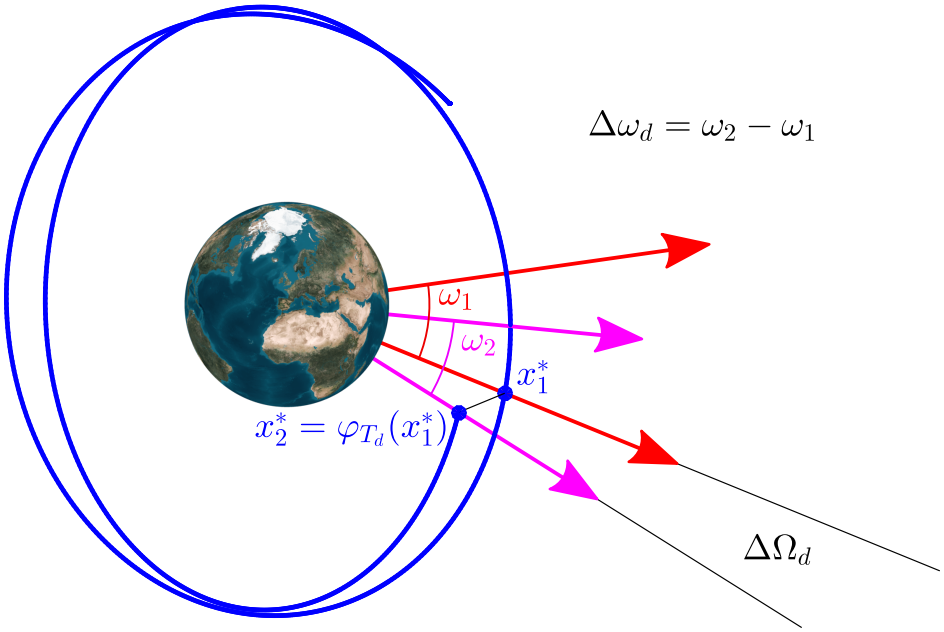

Figure 4.1: $\Delta\Omega_d$ and $\Delta\omega_d$ drifts due to zonal harmonics perturbations.

T_a is related to the pericenter drift per nodal period due to the same perturbations. Knowing this fact, one can numerically integrate any arbitrary trajectory and obtain the time histories of the fundamental periods over multiple revolutions about the central body. In particular, we will focus on the time histories of $\Delta\Omega_d$, $\Delta\varpi_d$ as these are directly related to T_s and T_a through (4.7).

Fig. 4.1 shows the described methodology for a spacecraft in orbit about an Earth-like spheroid. In this case and aside from orbits at critical inclinations[1] [65],the periods are either constants of motion or exhibit oscillations about their time averaged value. The first case is typical of trajectories that are periodic in the Routh-reduced system (4.3), whereas the second case is representative of quasi-periodic trajectories that populate the center manifolds about RRS periodic orbits. Following the nomenclature of Broucke [17], the latter are referred to as *pseudo-elliptic* trajectories, whereas the former are referred to as *pseudo-circular* orbits and can be calculated as illustrated in the following subsection.

4.2.1 Pseudo-circular Orbits

For the sake of illustration, consider the motion of a mass particle about an Earth-like axisymmetric body. In this case, $\mu_\oplus = 398600.4418$ km^3/s^2, $R_\oplus = 6378.1374$ km, and the zonal harmonics coefficients up to the fifth order are given as in Table 4.2. It is also possible to normalized the length and time units of the problem such that the reference radius $R_\oplus$ and $\sqrt{R_\oplus^3/\mu_\oplus}$ are equal to 1. For an Earth-like planet, this corresponds to $LU = 6378.137$ km and $TU = 806.11$ s, respectively.

Table 4.2: Earth's zonal harmonics coefficients up to the fifth order.

Zonal Coefficients	
J_2	1.08263×10^{-3}
J_3	-2.53241×10^{-6}
J_4	$-1.6198976 \times 10^{-6}$
J_5	$-0.22775359 \times 10^{-6}$

Next, observe that by fixing the value of H_z, the system (4.3) becomes an autonomous

[1] The inclination of a satellite is considered critical when $\cos^2 i \simeq 1/5$

Hamiltonian system that does not depend on any external parameter. In this case, one can proceed to specify a phase condition and a parametrizing constraint as in Sec. 2.3, and formulate a well-posed boundary value problem to look for periodic solutions of the RRS, i.e., pseudo-circular trajectories. The BVP reads as

$$\begin{cases} \boldsymbol{y}' &= T\,\boldsymbol{f}(\boldsymbol{y}, H_z), \\ T' &= 0, \end{cases} \tag{4.8}$$

subject to the boundary constraints

$$\boldsymbol{F}(\boldsymbol{y}_0, T) = \begin{bmatrix} \boldsymbol{g}(\boldsymbol{y}_0, \boldsymbol{y}_1) \\ p(\boldsymbol{y}_0) \\ s(\boldsymbol{y}_0, T) \end{bmatrix} = \boldsymbol{0}, \tag{4.9}$$

where $\boldsymbol{y}_0 = \begin{bmatrix} r_0, & z_0, & \dot{r}_0, & \dot{z}_0 \end{bmatrix}^T$, $\boldsymbol{y}_1$ is the terminal state of the satellite, and T is the period of the pseudo-circular orbit.

Because of (4.7), we are interested in finding periodic orbits on the surface of section $\zeta(\boldsymbol{y})$. This constraint is enforced by replacing (2.12) with the phase condition:

$$p(\boldsymbol{y}_0) := z_0 = 0, \tag{4.10}$$

which guarantees that the initial state of our periodic orbit would lie on the equatorial plane of the central body. Furthermore, as no information on the family tangent is currently available, it is better to initially replace the pseudo-arclength continuation constraint with

$$s(\boldsymbol{y}_0) := \mathcal{E}(\boldsymbol{y}) - E = 0, \tag{4.11}$$

where $\mathcal{E}(\boldsymbol{y})$ is defined as in (4.4). In this case, one can initialize the predictor-corrector scheme of Sec. 2.3 by picking any arbitrary circular two-body trajectory defining the constant values of H_z and E and using Newton's method to converge on the first family member.

Figure 4.2 shows an example of a pseudo-circular orbit obtained after initializing the BVP solver with a two-body trajectory defined by the Keplerian orbit elements $a = 1.1$ LU, $e = 0.0$, $i = 28.5$ deg, $\Omega = \varpi = M = 0$ deg, and providing the constant values of $H_z = 0.9217$,

$E = 0.4549$. After a few iterations, the algorithm converges on a periodic-orbit with $\boldsymbol{y}_0 = \begin{bmatrix} 1.0987, & 0 & -4.4411 \times 10^{-4}, & 0.4554 \end{bmatrix}^T$, $T = 7.2252$ TU, and characterized by the constant nodal, sidereal, and anomalistic periods disclosed in Fig. 4.3.

First, observe that $\Delta\omega_d$ is expected to be zero such that $T_a = T_d$. If this was not the case, then $\boldsymbol{y}(t)$ would cease to be periodic even in the RRS and violate the boundary constraint $\boldsymbol{g}(\boldsymbol{y}_0, \boldsymbol{y}_1) := \boldsymbol{y}_1 - \boldsymbol{y}_0 = 0$. Such a constraint does not prevent the longitude of the satellites to change in the full six-dimensional problem, which is why the RAAN drift per nodal period are allowed to be nonzero (Fig. 4.3).

A second thing to note is that, upon convergence, the family tangent can be evaluated in $(\boldsymbol{y}_0, T)$ to produce a reliable initial guess for a different pseudo-circular trajectory at the same H_z level. By iterating this process, one obtains entire family branches such as the ones of Fig. 4.4. The figure shows several family members obtained with the algorithm after replacing the parametrizing equations (4.11) with (2.13). The colors correspond to the different values of energy calculated in correspondence of the different periodic orbits, whereas the lines represent different families of pseudo-circular trajectories obtained after repeating the whole procedure for different values of H_z.

Differently from the previous chart, Fig. 4.5 shows the nodal and sidereal periods found for a range of E and H_z values. This is a useful plot for the purpose of designing pseudo-circular orbits with specified input values of T_d and T_s–namely $\bar{T}_d$ and $\Delta\bar{\Omega}_d$–even though arbitrary combinations of these quantities may not admit valid pseudo-circular trajectories. This is evident from the figure as not all of the different contours of $\bar{T}_d$ and $\Delta\bar{\Omega}_d$ overlap in one point.

Finally, Fig. 4.6 shows the evolution of the stability index[2] of several pseudo-circular families with changes in r and third component of the angular momentum vector. As it can be seen, the closer we are to critical inclinations, the closer we get to the instability limit of $k = 2$. Nevertheless, all of the computed pseudo-circular trajectories are stable and surrounded by a two-parameter family of quasi-periodic invariant tori [17]. These tori are filled by pseudo-elliptical trajectories, which are further discussed in the next subsection.

[2] see Section 2.5 for details

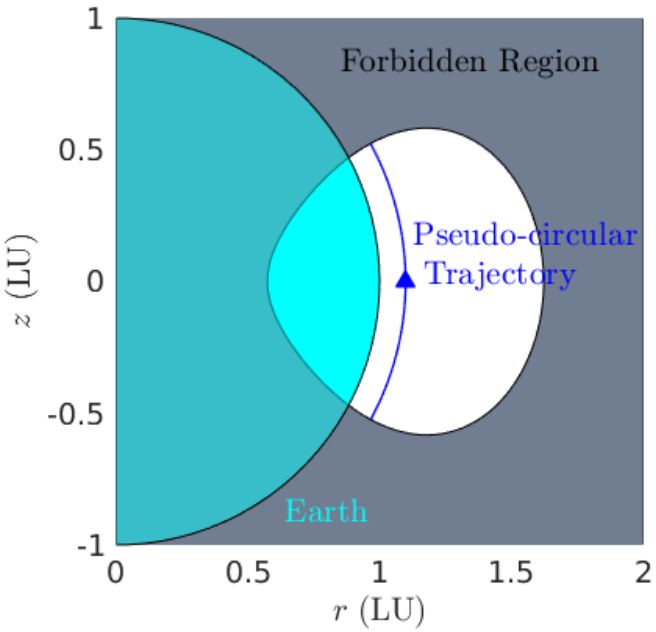

Figure 4.2: Pseudo-circular orbit about the Earth for the case $E = -0.4549$, $H_z = 0.9217$. Starting from the equatorial plane, the spacecraft moves upwards until it touches the zero-velocity curves. Then, it turns around and move downwards passing through the equatorial plane from north to south, and finally completes its revolution around the planet in $T = 7.2252$ TU.

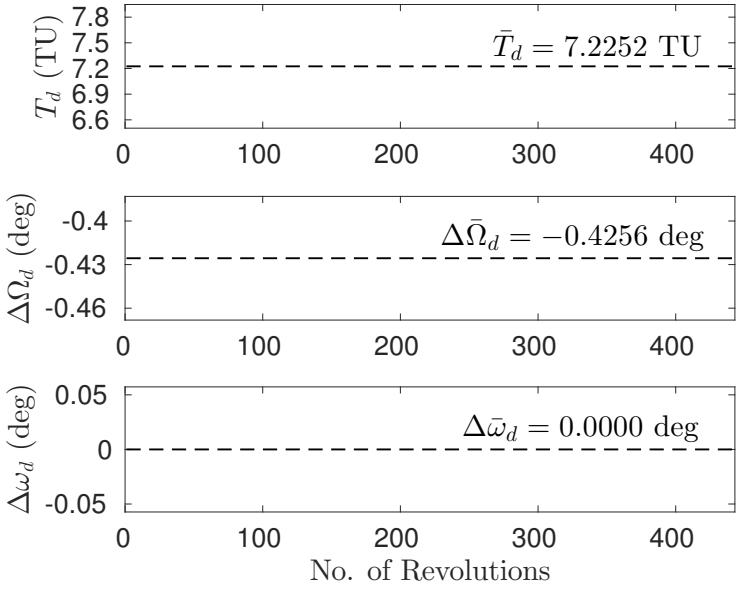

Figure 4.3: Nodal, sidereal, and anomalistic Periods for a pseudo-circular orbit about the Earth for the case $E = -0.4549$, $H_z = 0.9217$.

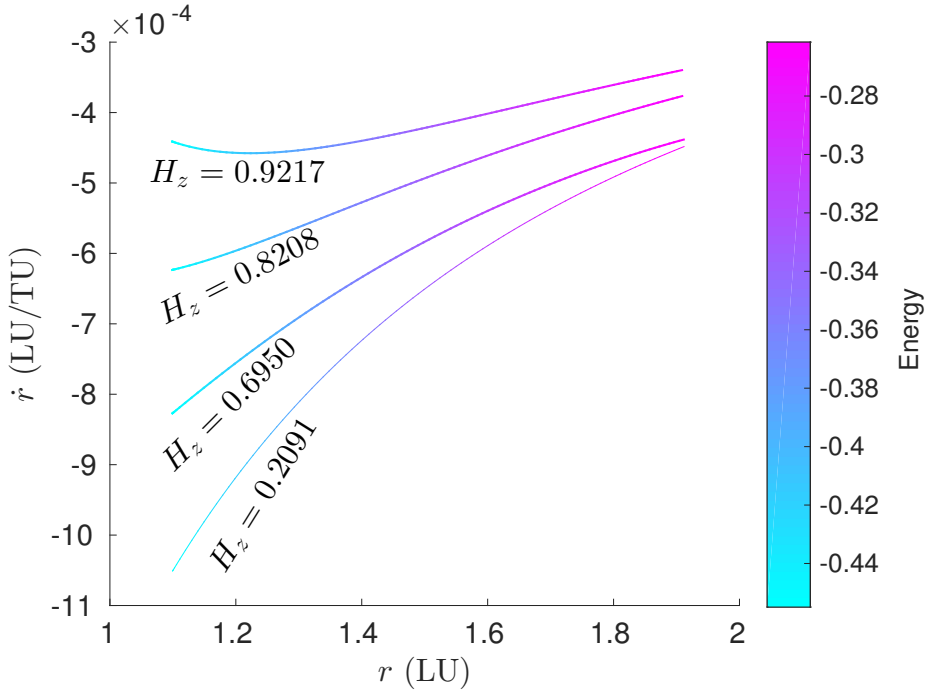

Figure 4.4: Differerent brances of pseudo-circular families about the Earth.

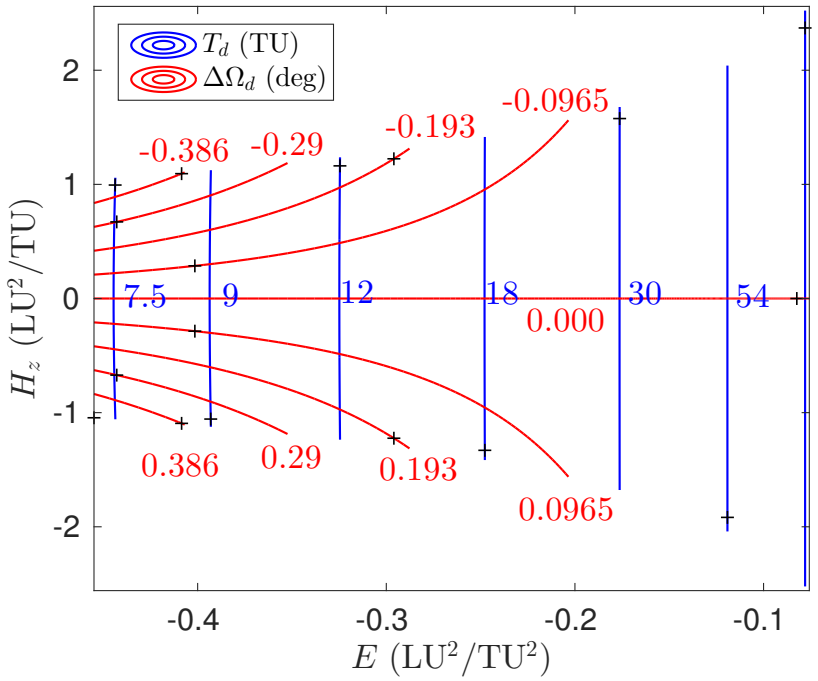

Figure 4.5: Nodal period and RAAN drift per nodal period computed for the families of pseudo-circular orbits displayed above.

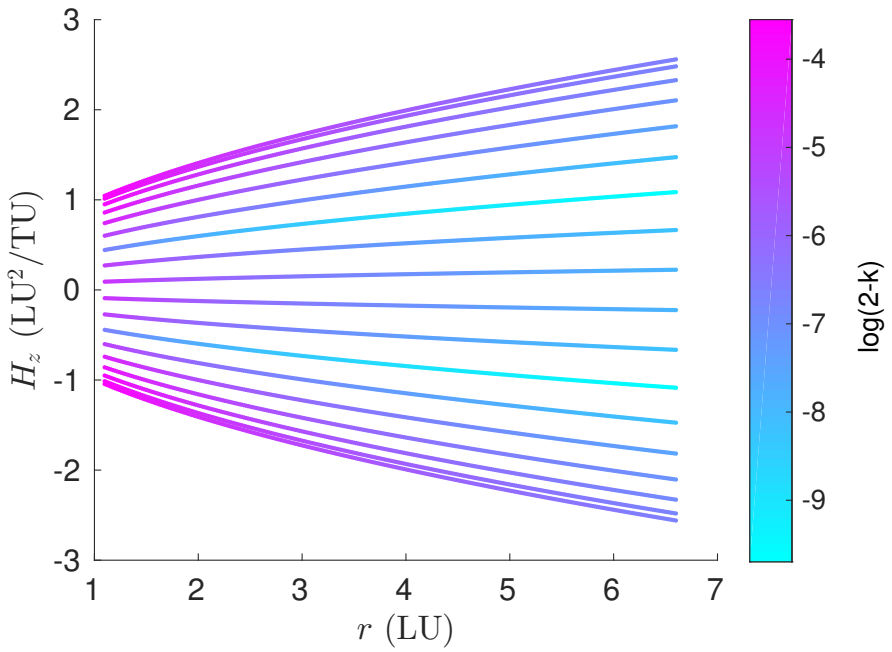

Figure 4.6: Evolution of the stability index with changes in r and H_z.

4.2.2 Pseudo-elliptic Trajectories

As predicted by Broucke, periodic orbits of the RRS are stable everywhere except at critical inclinations [17]. Since this is not the case for the periodic orbit of Fig. 4.2, consider the monodromy matrix M obtained from the numerical integration of the variational equations of (4.3). As expected, the monodromy matrix admits one pair of complex conjugate eigenvalues with unitary magnitude, meaning that the periodic orbit is surrounded by a two-parameter family of two-dimensional invariant tori.

To compute these manifolds, consider the BVP developed in Sec. 3.4

$$\begin{cases} \boldsymbol{Y}' &= T\,\mathbb{F}(\boldsymbol{Y}, H_z), \\ T' &= 0, \\ \rho' &= 0, \end{cases} \tag{4.12}$$

and subject to the terminal constraints

$$\boldsymbol{F}(\boldsymbol{z}) = \begin{bmatrix} \boldsymbol{g}(\boldsymbol{Y}_0, \boldsymbol{Y}_1) \\ p_0(\boldsymbol{Y}_0) \\ p_1(\boldsymbol{Y}_0) \\ s_0(\boldsymbol{Y}_0) \quad \text{or} \quad s_0(T) \\ s_1(\boldsymbol{z}) \end{bmatrix} = \boldsymbol{0}, \tag{4.13}$$

where $\boldsymbol{z} = \begin{bmatrix} \boldsymbol{Y}_0, & T, & \rho \end{bmatrix}^T$, $\boldsymbol{Y} = \begin{bmatrix} \boldsymbol{y}_0^T, & \boldsymbol{y}_1^T, & \ldots, & \boldsymbol{y}_{N_1-1}^T \end{bmatrix}^T$ is the $n\,N_1$-dimensional vector derived from the discretization of the invariant curve of the stroboscopic mapping $\boldsymbol{\varphi}_{T_d} : \mathbb{R}^4 \to \mathbb{R}^4$ in N_1 solution points, and $\mathbb{F}(\boldsymbol{Y}, T)$ is the $n\,N_1$-dimensional vector field given by

$$\mathbb{F}(\boldsymbol{Y}, T) = T \begin{bmatrix} \boldsymbol{f}(\boldsymbol{y}_0, H_z) \\ \boldsymbol{f}(\boldsymbol{y}_1, H_z) \\ \cdots \\ \boldsymbol{f}(\boldsymbol{y}_{N_1-1}, H_z) \end{bmatrix}, \tag{4.14}$$

with $\boldsymbol{f}(\boldsymbol{y}, H_z)$ as in (4.3). $p_0(\boldsymbol{Y}_0)$, $p_1(\boldsymbol{Y}_0)$, and $s_1(\boldsymbol{z})$ are given as in (3.45), (3.43), and (3.49), respectively. However, depending on the choice of s_0, the numerical procedure produces quasi-periodic invariant tori of either the same energy (E Tori) or the same "period" (P Tori). As described in Sec. 4.3, this leads to different relative motion behaviors when a formation of two satellite with a chief on the pseudo-circular trajectory of Fig. 4.2 and a deputy on one of these quasi-periodic trajectories is considered. Therefore, it is important to distinguish between the two different cases as follows.

4.2.2.1 E Tori

In the first case, one has that

$$s_0(\boldsymbol{Y}_0) := \sum_{i=0}^{N_1-1} \mathcal{E}(\boldsymbol{y}_i) - E = 0, \tag{4.15}$$

which ensures that all of the computed quasi-periodic invariant tori have the same value of energy E of the underlying pseudo-circular trajectory (E Tori). This leads to the invariant curves of the

stroboscopic map $\boldsymbol{\varphi}_{T_d}$ shown in Fig. 4.7(a), and obtained with the GMOS algorithm of Sec. 3.2.2. Each of these solutions can be propagated till the first surface of section crossing to produce the meaningful plot of Fig. 4.7(b) where pairs $(r, \dot{r})$ completely specify the states of the satellites. The bold curve correspond to the quasi-periodic invariant torus of Fig. 4.8, illustrating a collection of $N_1 = 51$ pseudo-elliptical trajectories being initialized on the surface of this manifold. Finally, the nodal, sidereal, and anomalistic periods change periodically over time as disclosed in Fig. 4.9.

4.2.2.2 P Tori

Alternatively, one can compute tori of the same period by setting the stroboscopic time to

$$s_0(T) = T - \mathcal{P} = 0. \tag{4.16}$$

$\mathcal{P}$ is the desired periodicity and may be conveniently set to the nodal period of the underlying pseudo-circular trajectory, i.e., $\mathcal{P} = T_{d,c}$. Fig. 4.10(a) displays the invariant curves of the stroboscopic mapping obtained with the former selection, whereas Fig. 4.10(b) shows the same invariant curves after propagating each of the GMOS solutions points till the first crossing with the surface of section $\zeta(\boldsymbol{y})$. Perhaps, the most evident difference with respect to the E tori case is that we are

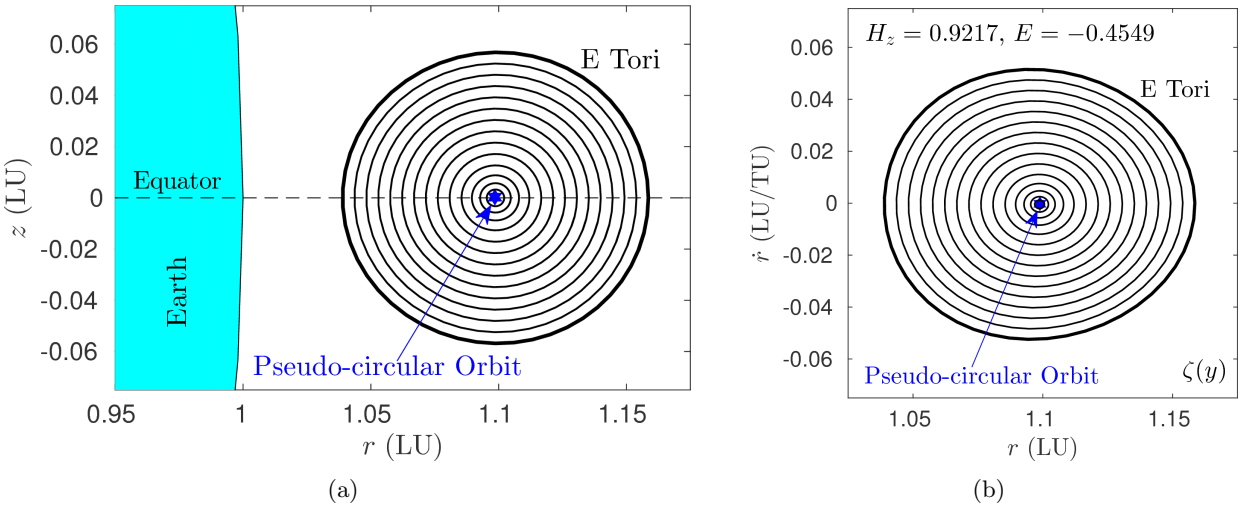

Figure 4.7: GMOS invariant curves as seen in configuration space (a) and on the surface of section $\zeta(\boldsymbol{y})$ (b). The bold curve corresponds to the quasi-periodic invariant torus shown below.

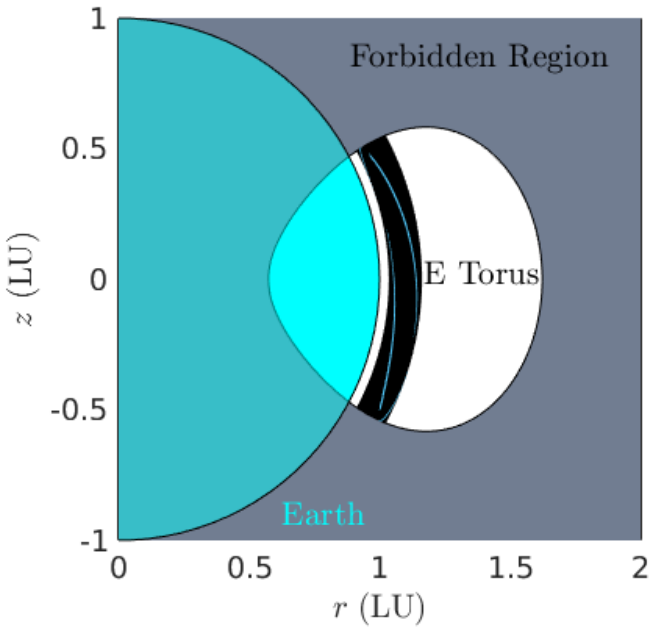

Figure 4.8: Pseudo-elliptical trajectories about the Earth being initialized on the surface of a quasi-periodic E Torus with $E = -0.4549$, $H_z = 0.9217$.

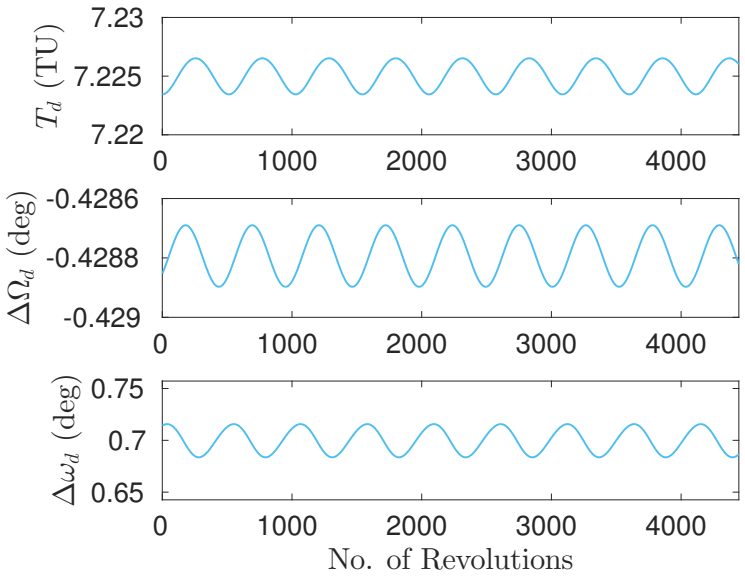

Figure 4.9: Nodal, sideral, and anomalistic Periods for a pseudo-ellitpical trajectory on the surface of a E torus about the Earth with $E = -0.4549$, $H_z = 0.9217$.

no longer allowed to represent the entire state of a spacecraft on a two-dimensional plot like Fig. 4.7(b). The reason for this being that the energy of the pseudo-elliptical trajectories is no longer conserved throughout the family, but slowly increases the farther we move from the pseudo-circular orbit. Next is an example of a quasi-periodic invariant P torus corresponding to the bold curve of Fig. 4.10(a) and 4.10(b). By selecting a pseudo-elliptical trajectory on the surface of this manifold, it is found that the nodal, sidereal, and anomalistic periods vary over time as disclosed in Fig. 4.12. This matches the observations of Xu et al. [114], who also noted that the time averages of T_d and $\Delta\Omega_d$ do not necessarily match with the nodal and sidereal periods of the pseudo-circular orbit. This may lead to unbounded relative motion as observed in the next section.

4.3 Formation Flying

The goal of this section is to study the relative motion between two or more spacecraft being initialized on either pseudo-circular or pseudo-elliptical trajectories. To that end, we integrate the equations of motion (4.3) for all of the satellites, convert into BCI coordinates via (4.5) & (4.6), and rotate the relative states in the LVLH frame of the reference spacecraft, i.e., the chief.

As a first example, we consider the relative motion between a chief and a deputy being initialized on the surface of the same quasi-periodic invariant E torus. Fig. 4.13 displays the

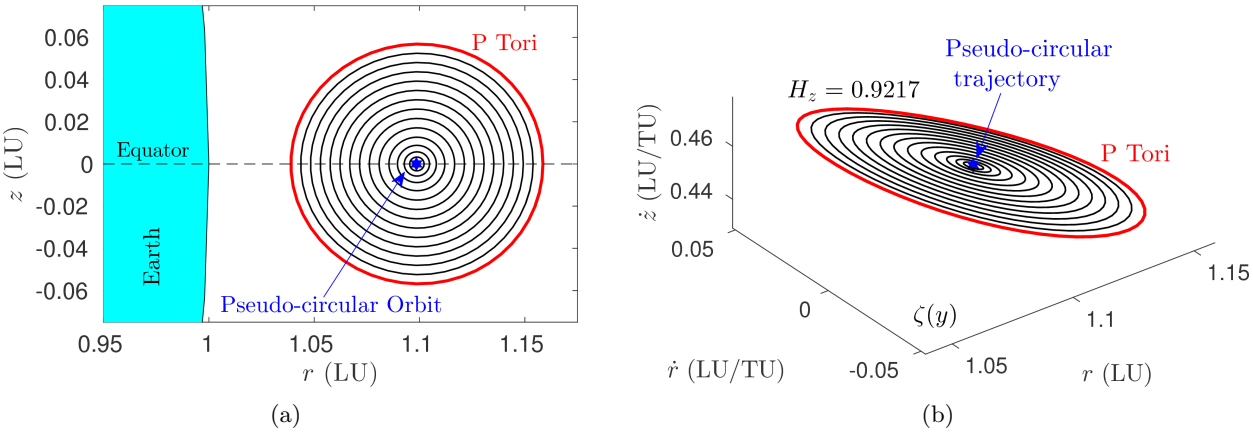

Figure 4.10: GMOS invariant curves as seen in configuration space (a) and on the surface of section $\zeta(\boldsymbol{y})$ (b). The bold red curve corresponds to the quasi-periodic invariant torus shown below.

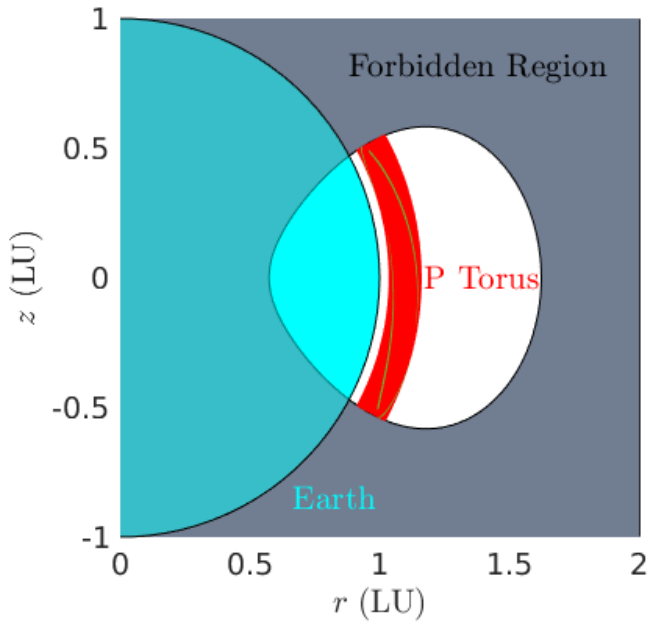

Figure 4.11: Pseudo-elliptical trajectories about the Earth being initialized on the surface of a quasi-periodic P Torus with $H_z = 0.9217$.

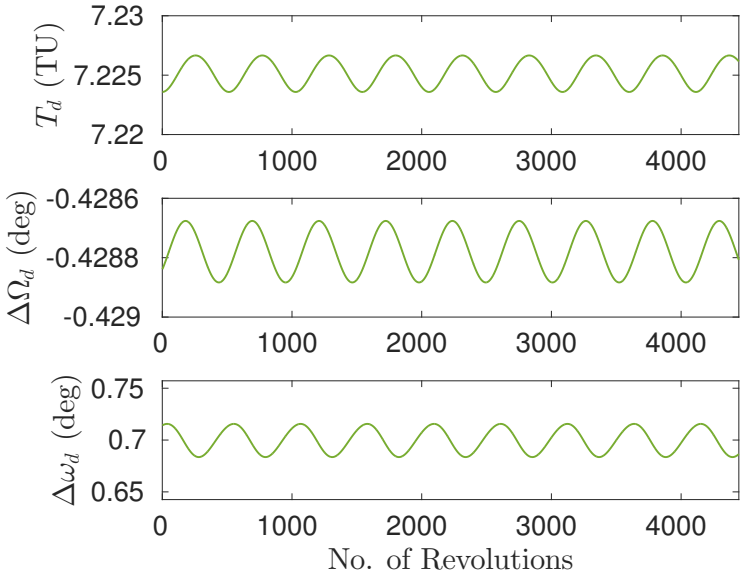

Figure 4.12: Nodal, sidereal, and anomalistic Periods for a pseudo-ellitpical trajectory on the surface of a P torus about the Earth with $H_z = 0.9217$.

relative motion in the LVLH frame of the chief, as well as the inter-satellite distance between the two vehicles. Despite some oscillations in the relative distance, the deputy remains within 350 km from the chief for more than a year, thus proving that quasi-periodic invariant tori can be successfully utilized for establishing bounded relative motion over long intervals of time. Indeed, the same occurs whenever the two satellites are initialized on the surface of the same P torus, which leaves us with the more interesting question of what happens whenever the deputy and the chief are no longer placed on the surface of the same manifolds.

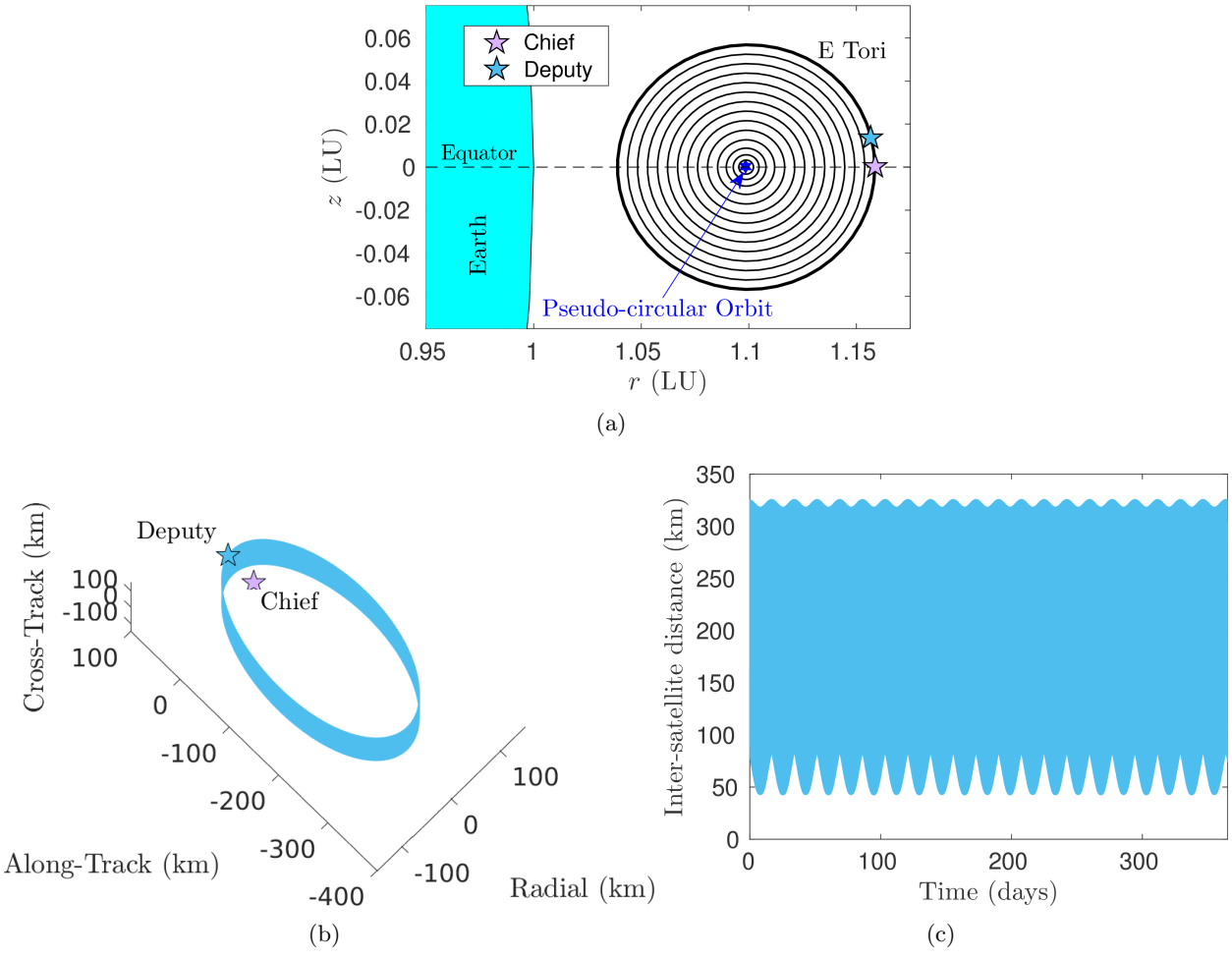

Figure 4.13: Relative motion between a chief and a deputy spacecraft on the surface of the same E torus. a) Initial conditions in configuration space. b) Relative trajectory in the LVLH frame of the chief. c) Inter-satellite distance over one year.

Fig. 4.14 portrays the relative motion between a chief on the pseudo-circular orbit of Fig. 4.2 and a deputy on the cyan pseudo-elliptical trajectory of Fig. 4.8. The initial conditions of the two satellites correspond to $r_c = 1.09874650952774$, $z_c = 0$, $\dot{r}_c = -0.000441104004566637$, $\dot{z}_c = 0.455473605978406$, and $r_d^{(E)} = 1.15685184543499$, $z_d^{(E)} = 0.0137239525985908$, $\dot{r}_d^{(E)} = 0.00588501453123112$, $\dot{z}_d^{(E)} = 0.429734647361727$ respectively, and yield the inter-satellite distance of Fig. 4.14(c). As it can be seen, the satellites seem to be no longer bounded to each other, and tend to slowly drift apart mostly in the along-track and cross-track directions.

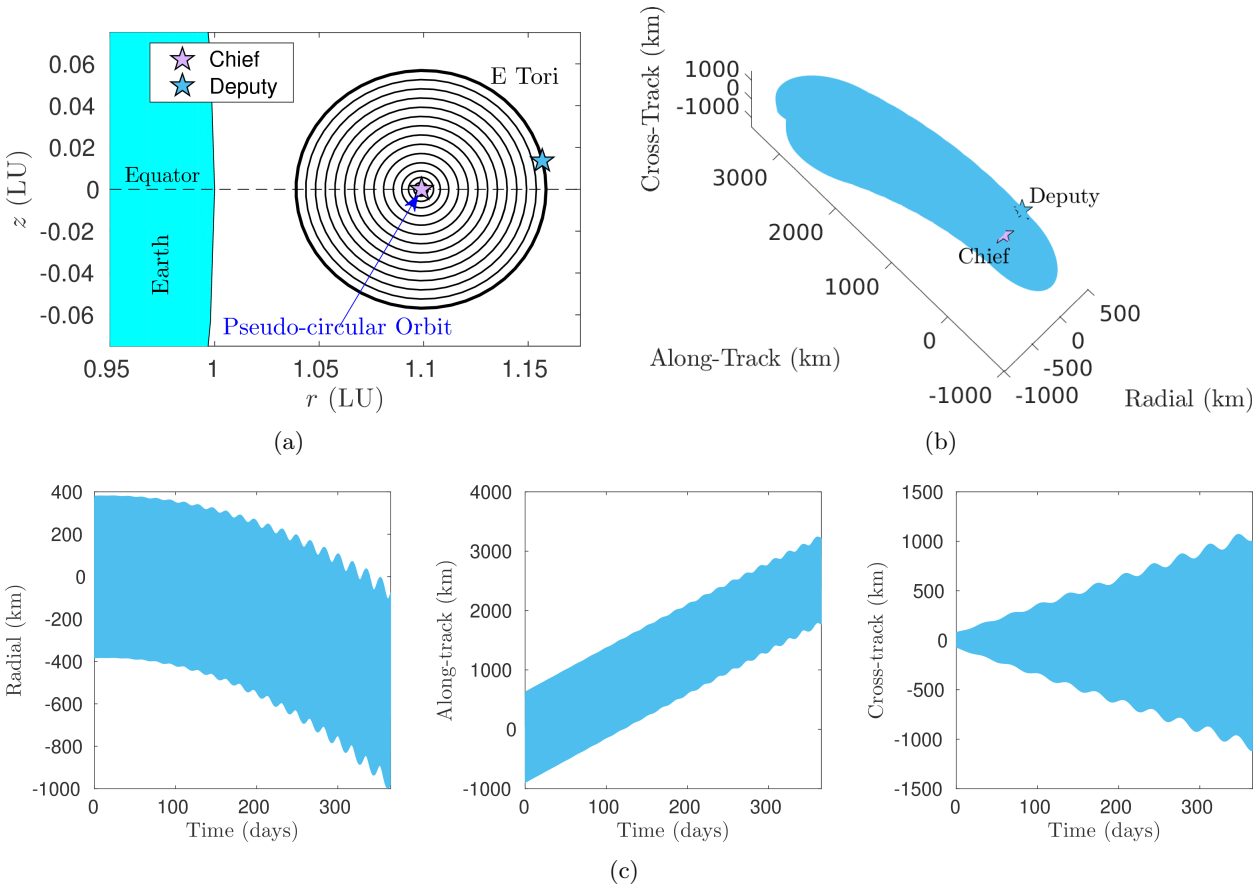

Figure 4.14: Relative motion between a satellite on the surface of a E torus and a pseudo-circular chief. a) Initial conditions in configuration space. b) Relative trajectory in the LVLH frame of the chief. c) Inter-satellite distance over one year.

Similarly, Fig. 4.15 shows the relative motion between the same chief and a deputy on the green pseudo-elliptic orbit of Fig. 4.11. In this case, $r_d^{(P)} = 1.15686604307968$, $z_d^{(P)} = 0.0137242998088076$, $\dot{r}_d^{(P)} = 0.00588468477904195$, $\dot{z}_d^{(P)} = 0.429741583983593$, and the relative motion exhibits less drift in the along-track direction, but still fails to remain bounded over time.

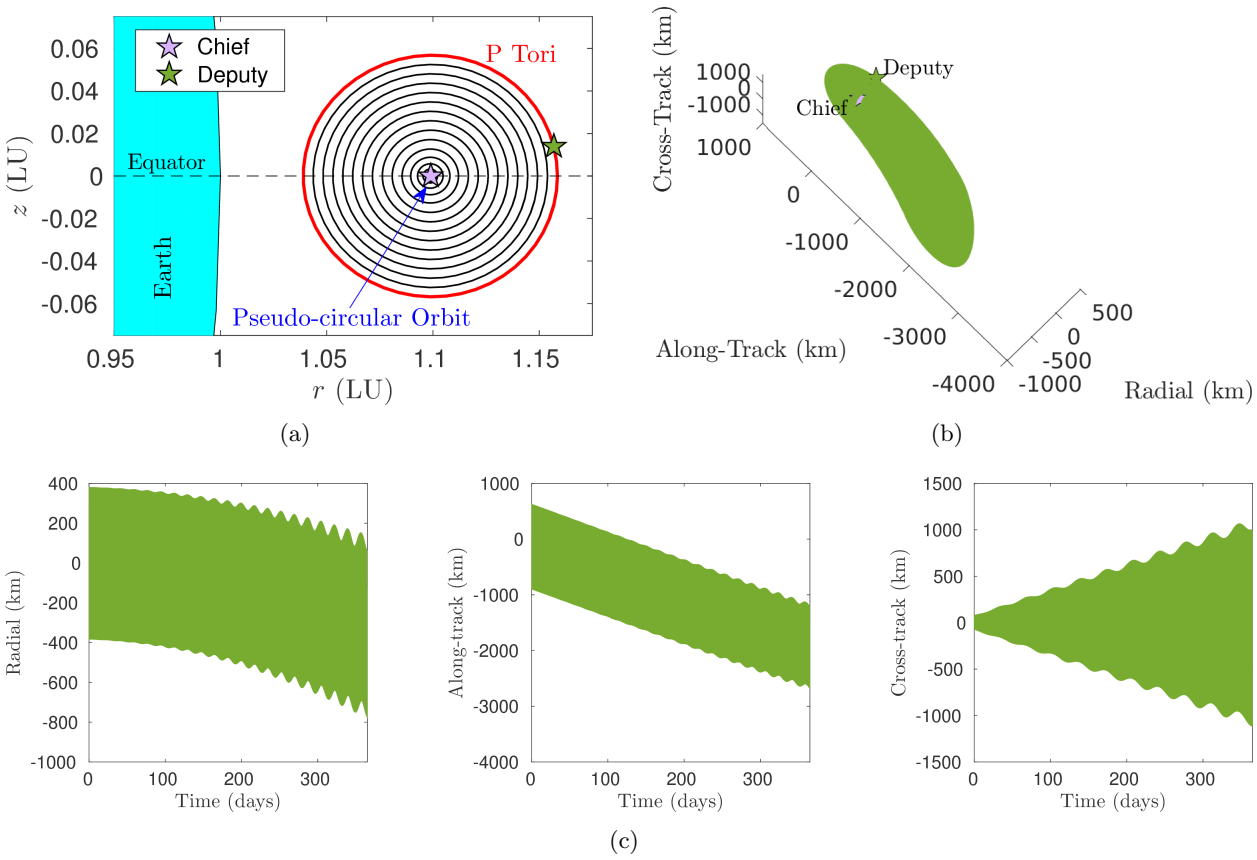

Figure 4.15: Relative motion between a satellite on the surface of a P torus and a pseudo-circular chief. a) Initial conditions in configuration space. b) Relative trajectory in the LVLH frame of the chief. c) Inter-satellite distance over one year.

Considering that the evolution of *any* spacecraft subject to the gravitational attraction of an axisymmetric bodies can be characterized by the three fundamental periods identified in Section 4.2, the cause for this drifting has to be researched in the time averaged value of these quantities. From this point of view, it is straightforward to demonstrate that if the satellites within the formation have the same values of T_d, T_s, and T_a, then bounded relative motion is achieved. This is indeed the situation of Fig. 4.13 as the frequencies of a torus (and therefore its periods) are fundamentally

defined for each state on the manifold and do not vary with the location of the satellites on its surface.

Conversely, if the chief and the deputy satellites are placed on different quasi-periodic invariant tori, it is no longer guaranteed that the values of the nodal, sidereal, and anomalistic periods are actually conserved within the formation. In order to establish bounded relative motion, however, at least two of the three fundamental frequencies need to be shared on average. The final choice falls on the nodal and sidereal periods as this is the only combination where the inter-satellite distance remains within reasonable ranges. In fact, bounded relative motion is technically achieved even when two satellites share either the nodal and anomalistic periods or the sidereal and anomalistic ones. However, in these cases, the inter-satellite distance can grow as large as twice the mean semi-major axis of the formation, thereby nullifying the utility of these relative trajectories for formation flying applications. It is also worth noting that the average values of the nodal and sidereal periods roughly correspond to

$$\bar{T}_d = \frac{2\,\pi}{\dot{\theta}_M} = \frac{2\,\pi}{\dot{\omega} + \dot{M}}, \qquad \Delta\bar{\Omega}_d = \dot{\Omega}\,\bar{T}_d = 2\,\pi\,\frac{\dot{\Omega}}{\dot{\omega} + \dot{M}}, \tag{4.17}$$

where $\theta_M = \omega + M$ is the mean argument of latitude, and $\dot{\Omega}$, $\dot{\omega}$, and $\dot{M}$ are the secular drift in the mean RAAN, argument of perigee, and mean anomaly due to the zonal perturbations [18, 95]. Accordingly, requiring that $\bar{T}_d$ and $\Delta\bar{\Omega}_d$ are shared among the chief and deputy vehicles essentially implies that the secular rates in θ_M and Ω must be the same for all of the satellites in the formation. Such a condition is not novel and can be considered as a stronger version of the J_2-invariant relative orbit constraints [94], which successfully yield bounded relative motion in the linear regime about the chief.

Moving beyond this validity region, let us focus on the time average of T_d and $\Delta\Omega_d$ as these are the actual key parameters that yield bounded relative motion over long intervals of time [6, 22, 114]. By definition, the averaged values of $T_d(k)$ and $\Delta\Omega_d(k)$ would be given by

$$\bar{T}_d = \lim_{N\to\infty} \frac{1}{N} \sum_{k=0}^{N} T_d(k), \qquad \Delta\bar{\Omega}_d = \lim_{N\to\infty} \frac{1}{N} \sum_{k=0}^{N} \Delta\Omega_d(k), \tag{4.18}$$

meaning that spacecraft trajectories should be integrated for a very large number of orbital revolutions in order to correctly predict the means of the nodal and sidereal period. This is, of course, impractical due to the accumulation of the truncation and round-off error that limit the accuracy of our results over long intervals of time.

Alternatively, since trajectories on the surface of a quasi-periodic torus are ergodic Fig. 4.10(a), i.e., fill the whol [14], the expressions (4.18) can be replaced by the spatial average of $T_d(k)$ and $\Delta\Omega_d(k)$ over one cycle [2]:

$$\bar{T}_d = \frac{1}{2\,\pi}\int_0^{2\,\pi} T_d(\xi)\,\mathrm{d}\xi, \qquad\qquad \Delta\bar{\Omega}_d = \frac{1}{2\,\pi}\int_0^{2\,\pi} \Delta\Omega_d(\chi)\,\mathrm{d}\chi. \tag{4.19}$$

This requires us to compute the number of orbital revolutions N_T and N_Ω such that $T_d(k) = T_d(k+N_T)$ and $\Delta\Omega_d(k) = \Delta\Omega_d(k+N_\Omega)$. To that end, we can pick the values of T_d and $\Delta\Omega_d$ at the first surface of section crossing, namely $T_d(1)$, $\Delta\Omega_d(1)$, and subtract them from the time histories of the nodal period and RAAN drift per nodal period. This yields two sinusoidal functions that pierce the zero axis at multiple locations. Therefore, by interpolating between neighboring data points in the vicinity of the first zero crossing, one obtains a numerical approximation of the desired values:

$$N_T = k^* + \frac{T_d(1) - T_d(k^*)}{T_d(k^*+1) - T_d(k^*)}, \qquad\qquad N_\Omega = j^* + \frac{\Delta\Omega_d(1) - \Delta\Omega_d(j^*)}{\Delta\Omega_d(j^*+1) - \Delta\Omega_d(j^*)}, \tag{4.20}$$

where k^* and j^* represent the number of orbital revolutions before the first zero crossings in $T_d(k) - T_d(1)$ and $\Delta\Omega_d(k) - \Delta\Omega_d(1)$, respectively. Next, the time averaged values of T_d and $\Delta\Omega_d$ may be calculated with a trapezoidal rule as

$$\bar{T}_d =\simeq \frac{1}{2\,\pi}\left\{\frac{1}{2}\left[2\,\pi - \xi(k^*-1)\right]\left[T_d(1) + T_d(k^*)\right] + \sum_{k=2}^{k^*-1}\left[\xi(k) - \xi(k-1)\right]T_d(k)\right\}, \tag{4.21}$$

$$\Delta\bar{\Omega}_d =\simeq \frac{1}{2\,\pi}\left\{\frac{1}{2}\left[2\,\pi - \chi(j^*-1)\right]\left[\Delta\Omega_d(1) + \Delta\Omega_d(j^*)\right] + \sum_{j=2}^{j^*-1}\left[\chi(j) - \chi(j-1)\right]\Delta\Omega_d(j)\right\}, \tag{4.22}$$

where $\xi(k) = 2\,\pi\,(k-1)/(N_T-1)$, and $\chi(j) = 2\,\pi\,(j-1)/(N_\Omega-1)$.

Table 4.3 summarizes the averaged values of T_d and $\Delta\Omega_d$ measured from the trajectories of Fig. 4.2, 4.8, and 4.11, thereby proving that the $\bar{T}_d$ and $\Delta\bar{\Omega}_d$ values for the deputy satellites of Fig.

Table 4.3: Nodal periods and RAAN drifts per nodal period of a pseudo-circular chief, a pseudo-elliptic deputy on the surface of a E torus, and a pseudo-ellitpic deputy on the surface of a P torus.

	$\bar{T}_d$ (TU)	$\Delta\bar{\Omega}_d$ (deg)
Pseudo-circular Chief	7.22518505463333	−0.42562399818902
Pseudo-elliptic Deputy (E Torus)	7.22504604288588	−0.428793535175085
Pseudo-elliptic Deputy (P Torus)	7.22518506976361	−0.42877978243654

4.14 & 4.15 are actually different from the constant periods of the pseudo-circular chief observed in Fig. 4.3. This is particularly true for the deputy spacecraft on the surface of the E torus as both of $\bar{T}_d$ and $\Delta\bar{\Omega}_d$ do not seem to match the desired values. In contrast, the deputy on the surface of a P torus shares the value of the nodal period within the numerical precision of both GMOS and (4.21), thereby explaining the better performance observed in Fig. 4.15. This improvement indicates a possible path to establish bounded relative motion about axisymmetric bodies, even though more work needs to be done in order to correct for the difference in $\Delta\bar{\Omega}_d$. This final step is accomplished in the next section by reformulating the boundary value problem of the GMOS algorithm to accommodate extra constraints that fix the time average of the RAAN drift per nodal period in addition to (4.16).

4.4 GMOS revised

Although H_z rules the evolution of the spacecraft longitude ϕ, its value has never been changed throughout the computation of the P and E quasi-periodic invariant tori illustrated in the previous sections. Yet, changing the value of H_z does affect the average value of the RAAN drift per nodal period, thus creating the possibility to match the value of the chief. This condition is achieved by appending the H_z parameter to the boundary value problem (4.12)–(4.13), along with the extra constraint

$$l(\boldsymbol{Y}_0, H_z) := \frac{1}{N_1}\sum_{i=0}^{N_1-1}\Delta\,\Omega_i - \Delta\Omega_d = 0, \tag{4.23}$$

where $\Delta\,\Omega_i$ denotes the RAAN drift per nodal period of the i-th GMOS solution point.

To compute the values of $\Delta\,\Omega_i$, consider the augmented system

$$\boldsymbol{y}'_\phi = \boldsymbol{f}_\phi(\boldsymbol{y}_\phi, H_z) = \begin{cases} \boldsymbol{y}' &= \boldsymbol{f}(\boldsymbol{y}, H_z), \\ \phi' &= \dfrac{H_z}{r^2} \end{cases} \tag{4.24}$$

where $\boldsymbol{y}_\phi = \begin{bmatrix} r & z & \dot{r} & \dot{z} & \phi \end{bmatrix}^T$, $\boldsymbol{f}(\boldsymbol{y}, Hz)$ is given by (4.3), and ϕ is the longitude of the i-th GMOS solution point. Assuming that the initial longitude of the N_1 solution points is always equal to zero, one can integrate the system (4.24) for each of the sample trajectories and record the values of $\boldsymbol{y}_\phi$ at three different points in time. These instants are shown in Fig. 4.16 and identified as

A) when the trajectory first crosses the equatorial plane from south to north and $t > T/2$;

B) at $t = T$ for storing the output of the stroboscopic map φ_T;

C) when the trajectory recrosses the equatorial plane from south to north after event A;

Eventually, the values of $\Delta\Omega_i$ are computed as the difference between the longitude in C and the longitude in A of the i-th trajectory, i.e., $\Delta\Omega_i = \phi_{C,i} - \phi_{A,i}$.

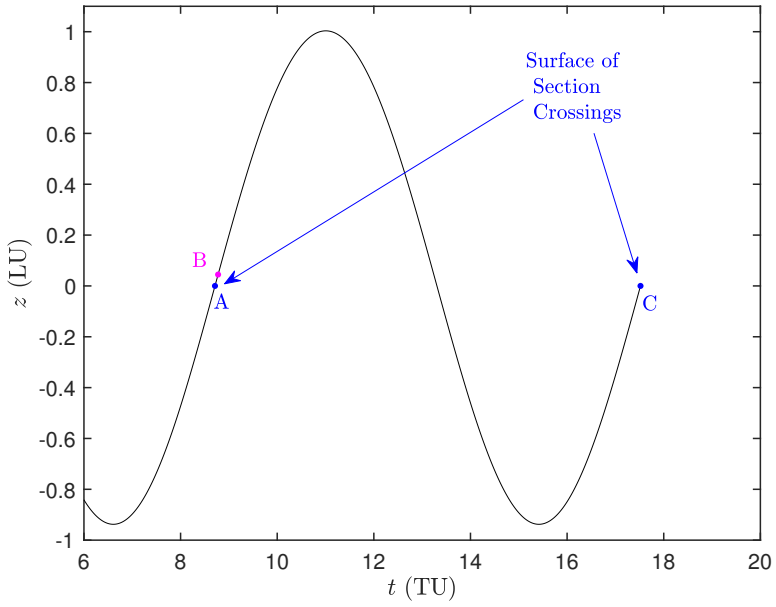

Figure 4.16: Integration events for the trajectory of a sample solution point $\boldsymbol{y}_i$ in the revised GMOS algorithm.

The evaluation of Eq. (4.23) completes the revised GMOS BVP, which reads as

$$\begin{cases} \boldsymbol{Y}' &= T\,\mathbb{F}(\boldsymbol{Y}, H_z), \\ T' &= 0, \\ \rho' &= 0, \\ H_z' &= 0, \end{cases} \tag{4.25}$$

subject to the boundary constraints

$$\boldsymbol{F}(\boldsymbol{Z}) = \begin{bmatrix} \boldsymbol{g}(\boldsymbol{Y}_0, \boldsymbol{Y}_1) \\ l(\boldsymbol{Y}_0, H_z) \\ p_0(\boldsymbol{Y}_0) \\ p_1(\boldsymbol{Y}_0) \\ s_0(T) \\ s_1(\boldsymbol{Z}) \end{bmatrix} = \boldsymbol{0}, \tag{4.26}$$

with $\boldsymbol{Z} = \begin{bmatrix} \boldsymbol{Y}_0 & T & \rho & H_z \end{bmatrix}^T$.

As usual, once a reliable initial guess is given, the solution of the BVP can be found via Newton's method. Specifically, one has to iterate

$$\boldsymbol{Z}^{(k+1)} = \boldsymbol{Z}^{(k)} - \left[D\mathcal{F}(\boldsymbol{Z}^{(k)})\right]^{\dagger}\,\mathcal{F}(\boldsymbol{Z}^{(k)}) \tag{4.27}$$

until the L2-norm of $\boldsymbol{F}(\boldsymbol{Z})$ is below some user-defined tolerance (typically 10^{-10} for the normalized problem). Note that $D\mathcal{F}(\boldsymbol{Z}^{(k)})$ represents the Jacobian matrix of (4.26) and is calculated as in Ref. [6].

Upon convergence, the numerical procedure recovers invariant curves of the stroboscopic mapping such as the ones illustrated in Fig. 4.17. The different colors of the invariant curves correspond to the different values of H_z that guarantee that the average of the RAAN drift over one nodal period matches the value of the chief. Accordingly, points on different curves have different values of energy and H_z, and yet they are all guaranteed to remain bounded over indefinite time spans.

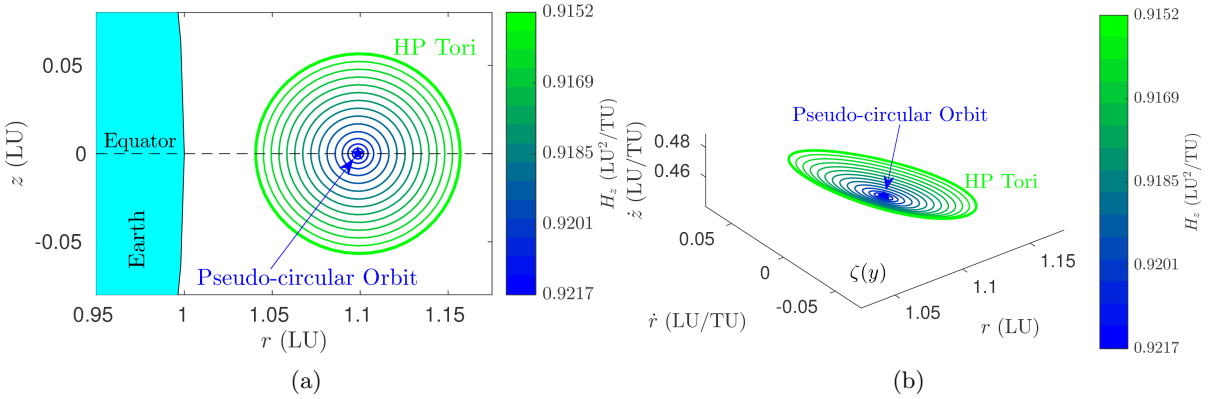

Figure 4.17: Invariant curves output by the revised GMOS algorithm and projected onto the configuration space (a) and on the surface of section $\zeta(\boldsymbol{y})$ (b). The bold green curve corresponds to the quasi-periodic invariant torus shown below.

To distinguish between previous solutions, we denote these new family of quasi-periodic invariant tori as "HP" and display a random family member in Fig. 4.18 & 4.19). Observe that the evolution of the nodal and sidereal periods effectively match, on average, the target values derived from the chief.

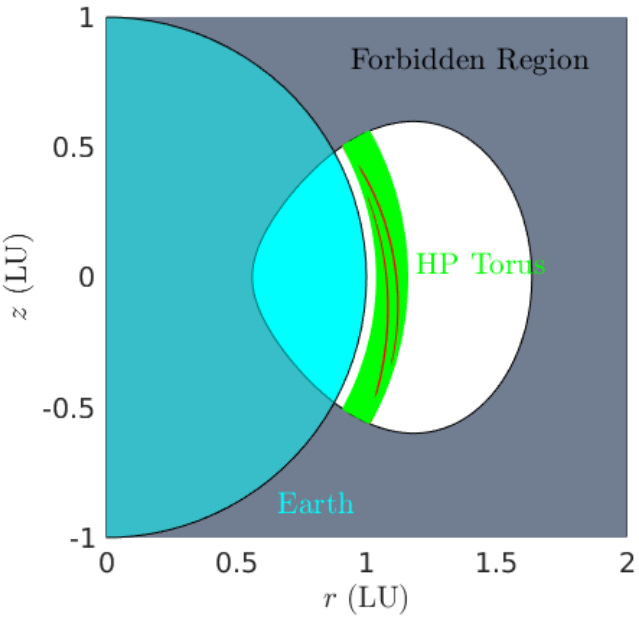

Figure 4.18: Pseudo-elliptical trajectories about the Earth being initialized on the surface of a quasi-periodic HP Torus.

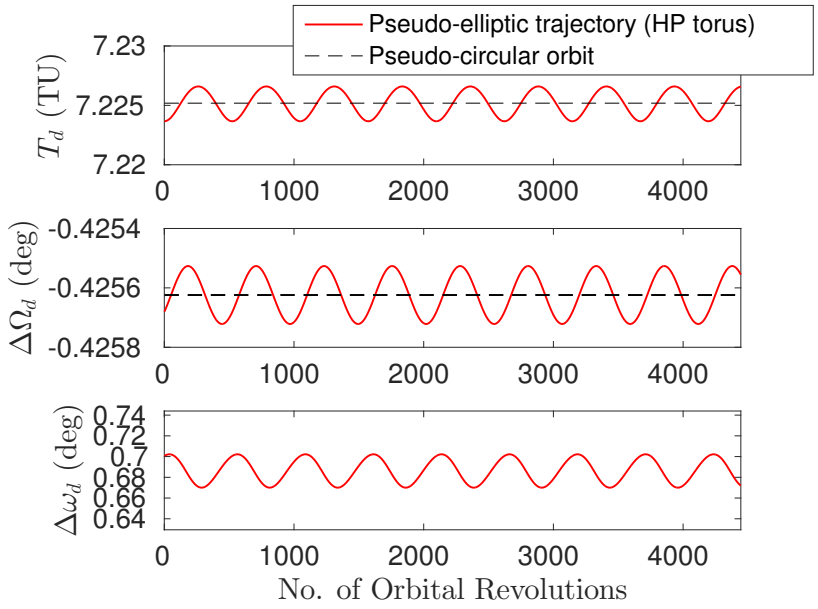

Figure 4.19: Nodal, sidereal, and anomalistic Periods for a pseudo-ellitpical trajectory on the surface of a HP torus about the Earth.

It is also worth noting that the differences in energy and polar component of the angular momentum vector of this and other tori within the family are found to be in good agreement with the first-order analytical relationship derived in Ref. [94] & [107] for J_2 formations:

$$\delta E = \frac{J_2}{5} \frac{(1 + 5\cos^2 \bar{i})}{\bar{a}^3 (1 - \bar{e}^2)^2 H_{z,c}} \delta H_z, \tag{4.28}$$

where $\bar{a}$, $\bar{e}$, $\bar{i}$ are the mean semi-major axis, eccentricity, and inclination of the chief in normalized units [18], and $H_{z,c}$ is the polar component of its angular momentum vector. The agreement is demonstrated with the plot of Fig. 4.20, which compares the analytical expression of Eq. (4.28) with the δE and δH_z values obtained with the revised GMOS algorithm. The overlap suggests that all of the pseudo-elliptical trajectories generated via the revised GMOS algorithm shown in Fig. 4.17 belong to a family of J_5-invariant relative orbits that guarantee bounded relative motion with the selected pseudo-circular chief.

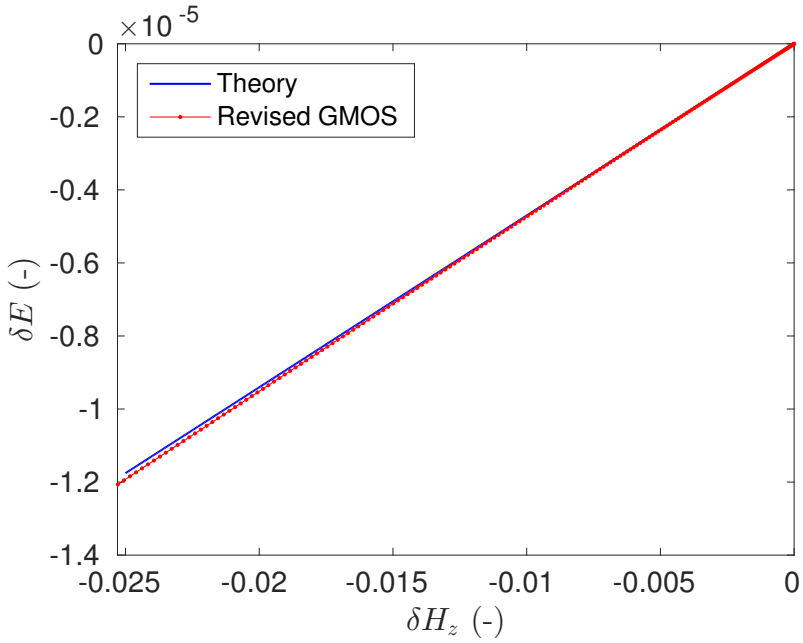

Figure 4.20: δE vs δH_z for two-hundred quasi-periodic HP tori computed with the revised GMOS algorithm.

To support this claim, consider the plots of Fig. 4.21, which portrays the relative motion between a chief on the pseudo-circular orbit of Fig. 4.2 and the red pseudo-elliptic trajectory of Fig. 4.18–4.19. In this case, the ICs of the deputy spacecraft are given by $r_d^{(HP)} = 1.1552645635828$, $z_d^{(HP)} = 0.0136692999855168$, $\dot{r}_d^{(HP)} = 0.0054772484569905$, $\dot{z}_d^{(HP)} = 0.440673756862056$ and yield a relative trajectory with an in-plane ellipse of size 800×1200 km, i.e., well beyond the reach of standard analytical methods based on linearization (e.g., [94], [35]). Nevertheless, the deputy remains in the vicinity of the chief for more than one year without any sign of secular drifts in both the along track and cross-track directions (Fig. 4.21(c)).

The same outcome is achieved for any formation of two or more satellites being randomly initialized on the invariant curves of Fig. 4.17. For example, consider the plots of Fig. 4.22–4.23, which displays the relative trajectory between two deputies on two different quasi-periodic invariant tori of the same HP family. In spite of the fact that the spacecraft are no longer on the surface of the same quasi-periodic torus, it is still found that the inter-satellite distance between the two remains bounded. This is clearly visible from the plots of the relative motion between the same

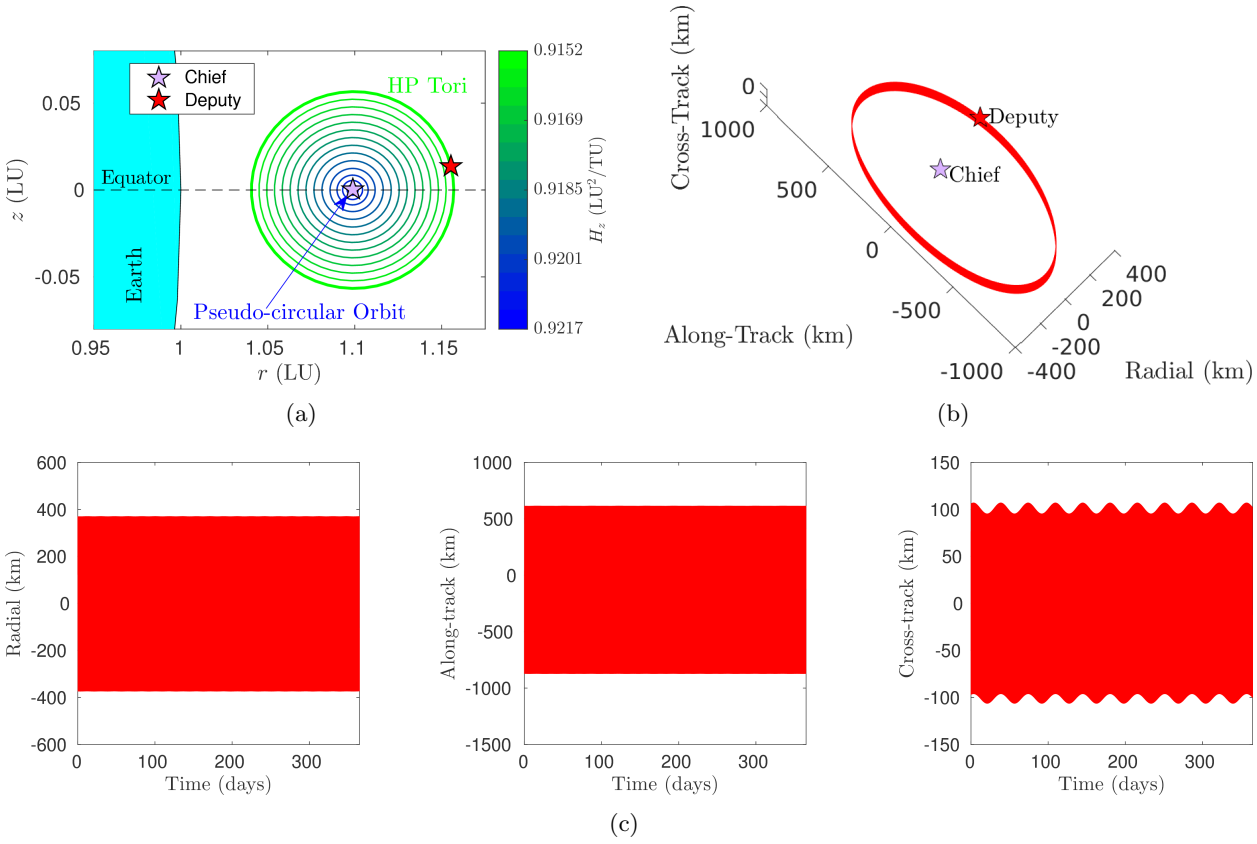

Figure 4.21: Relative motion between a satellite on the surface of a HP torus and a pseudo-circular chief. a) Initial conditions in configuration space. b) Relative trajectory in the LVLH frame of the chief. c) Inter-satellite distance over one year.

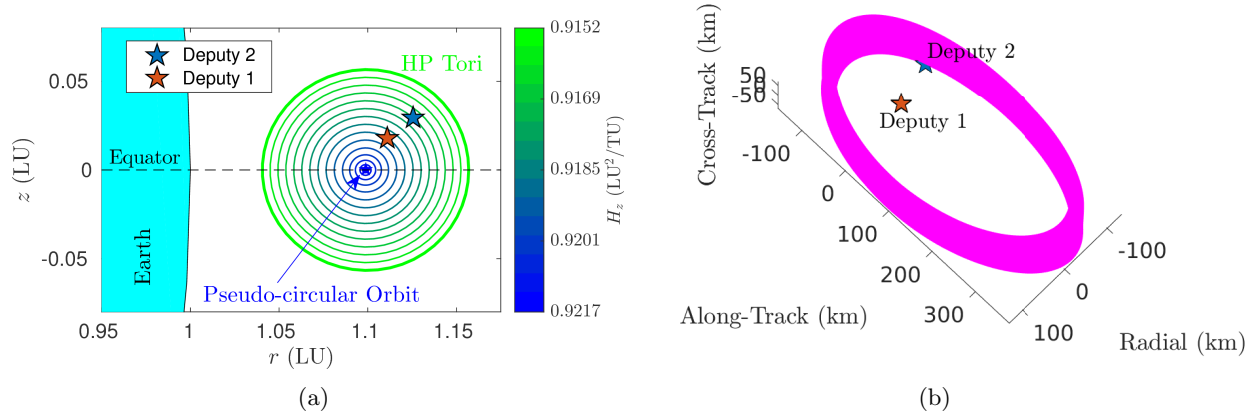

Figure 4.22: Relative motion between two deputies being initialized on the surface of two different HP tori of the same family.

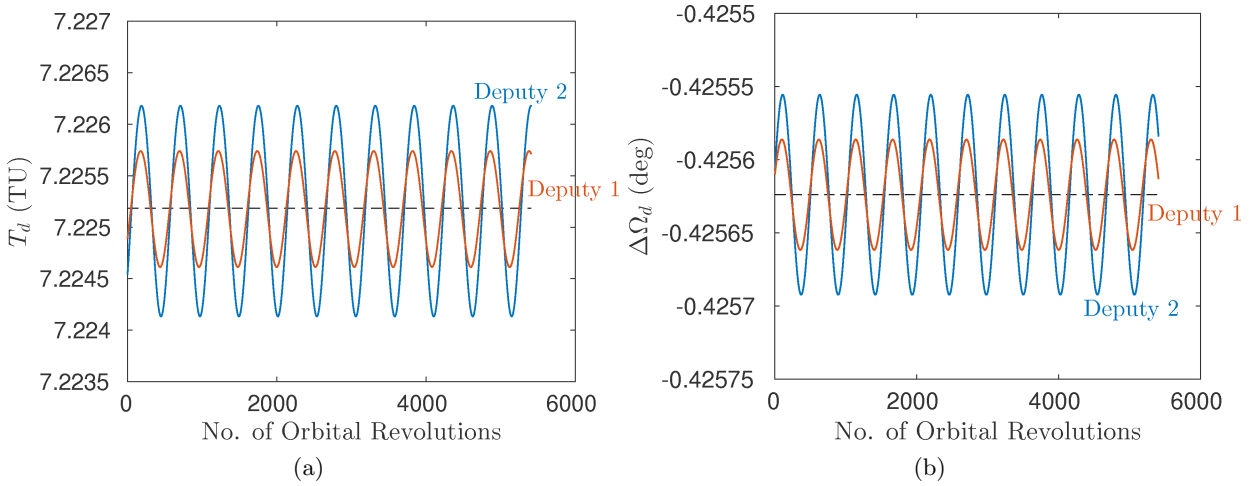

Figure 4.23: Nodal periods and RAAN drifts per nodal period of two deputies being initialized on the surface of two different HP tori.

deputies and a chief on the pseudo-circular trajectory disclosed in Fig. 4.24. What differs from the previous simulation scenarios is that the mutual distance between Deputy 1 and 2 now exhibits long-periodic oscillations due to the incommensurate winding frequencies at which the two satellites evolve around their corresponding HP tori, i.e., their anomalistic period (Fig. 4.25). Because of that, the two spacecraft are never in the same configuration with respect to the pseudo-circular

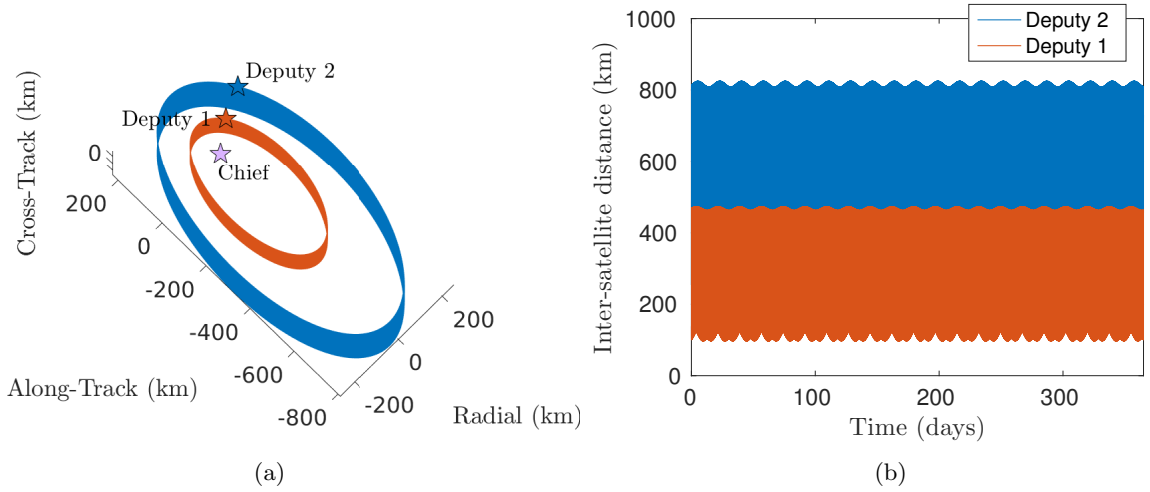

Figure 4.24: Relative motion in the LHLV frame of the pseudo-circular chief (a) and inter-satellite distances (b) over 365 days.

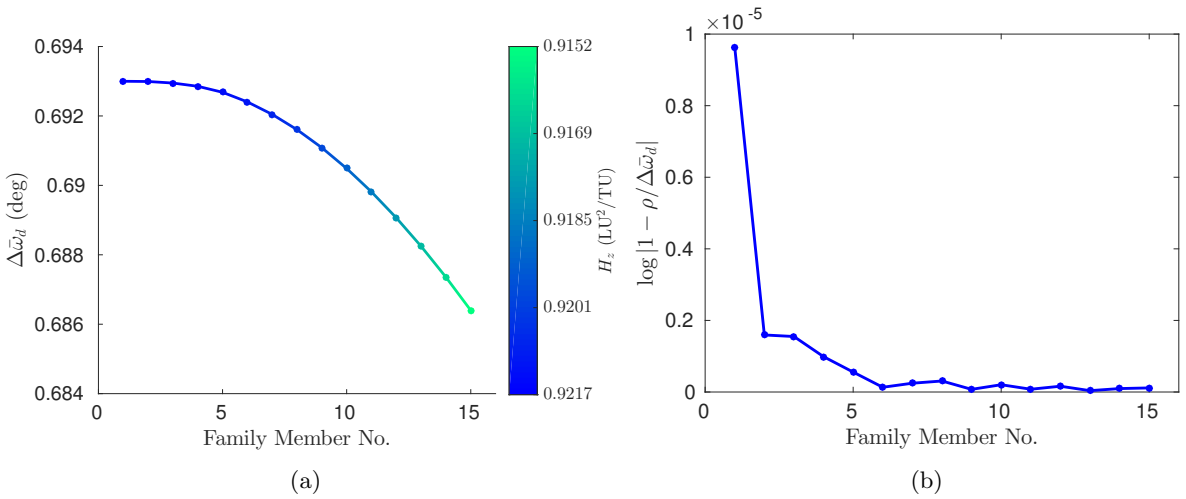

Figure 4.25: Argument of perigee drift per nodal period for all of the HP tori computed with the revised GMOS algorithm. Interestingly, the values of $\Delta\bar{\omega}_d$ are found to match the rotation number of the computed quasi-periodic invariant HP tori within the numerical precision of the revised GMOS algorithm.

trajectory, and evolve with respect to each other as in Fig. 4.22(b). This is still acceptable, however, as many formation flying and cluster flight applications only demands for the inter-satellite distance between the vehicles to remain bounded within some operational threshold [19].

In conclusion, regardless of some long-periodic oscillations, the revised GMOS algorithm succeeds in generating entire families of bounded relative trajectories about axisymmetric bodies once a stable pseudo-circular trajectory of the RRS system is found. This is further demonstrated with the numerical simulations of Fig. 4.26 and 4.27, which demonstrate the validity of our numerical procedure at a range of altitude and inclination values. Specifically, Fig. 4.26 shows a bounded relative trajectory in MEO, whereas Fig. 4.27 exhibits the relative motion between a chief and a deputy in GEO. The initial conditions of the satellites for these simulations are summarized in Table 4.4 & 4.5.

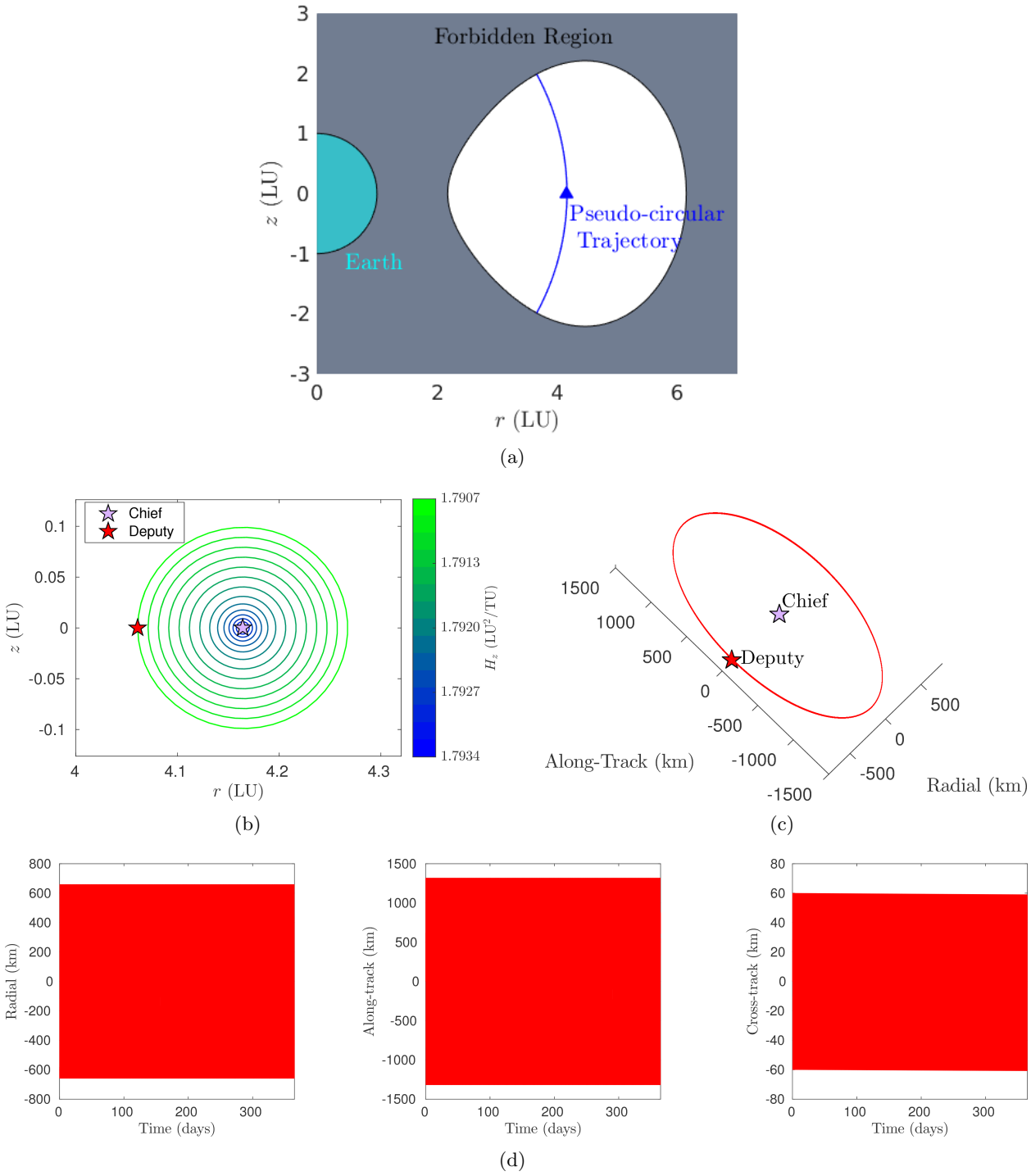

Figure 4.26: Relative motion between a satellite on the surface of a HP torus and a pseudo-circular chief in MEO. a) Pseudo-circular trajectory in rectangular coordinates. b) Initial conditions of the chief and deputy spacecraft in configuration space. c) Relative trajectory in the LVLH frame of the chief. d) Inter-satellite distance over one year.

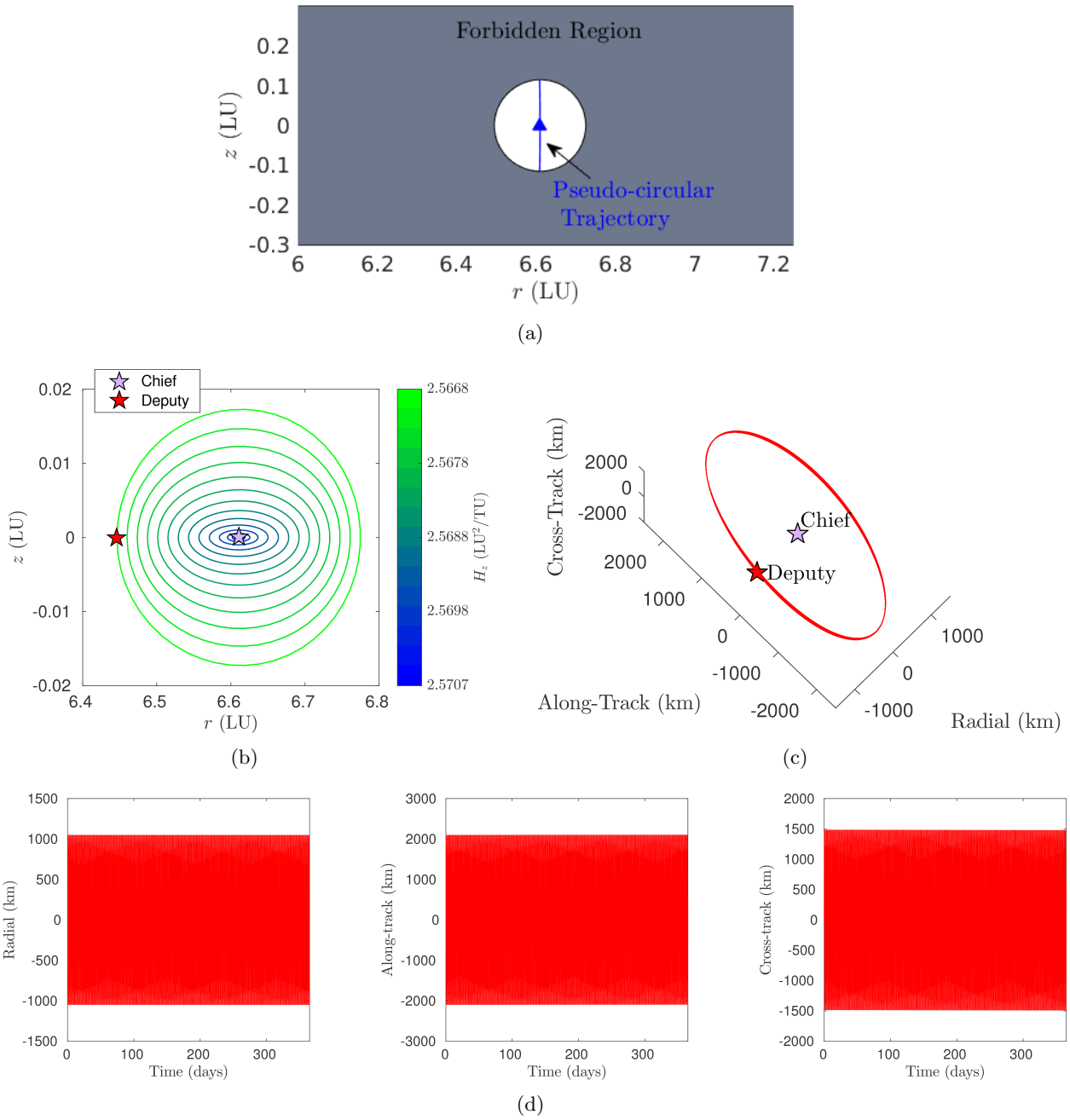

Figure 4.27: Relative motion between a satellite on the surface of a HP torus and a pseudo-circular chief in GEO. a) Pseudo-circular trajectory in rectangular coordinates. b) Initial conditions of the chief and deputy spacecraft in configuration space. c) Relative trajectory in the LVLH frame of the chief. d) Inter-satellite distance over one year.

Table 4.4: Chief and deputy initial conditions for bounded relative motion in MEO

Chief		Units	**Deputy**		Units
r_c	4.16416789734246	(LU)	r_d	4.06089015784987	(LU)
z_c	0.0000	(LU)	z_d	$-3.0735978332768 \times 10^{-6}$	(LU)
$\dot{r}_c$	$-6.52508565223192 \times 10^{-5}$	(LU/TU)	$\dot{r}_d$	$-6.52934204408809 \times 10^{-5}$	(LU/TU)
$\dot{z}_c$	0.233838507959416	(LU/TU)	$\dot{z}_d$	0.240708173039751	(LU/TU)

Table 4.5: Chief and deputy initial conditions for bounded relative motion in GEO

Chief		Units	**Deputy**		Units
r_c	6.61048408889448	(LU)	r_d	6.44619132908859	(LU)
z_c	0.0000	(LU)	z_d	$-2.88103715743783 \times 10^{-5}$	(LU)
$\dot{r}_c$	$-1.194226726868 \times 10^{-6}$	(LU/TU)	$\dot{r}_d$	$-3.6293650524379 \times 10^{-6}$	(LU/TU)
$\dot{z}_c$	0.00678809221761716	(LU/TU)	$\dot{z}_d$	0.0209829766592374	(LU/TU)

4.5 1999 KW4α formations

Due to the success of the revised GMOS algorithm, we now investigate the problem of establishing bounded relative motion in a 5×0 gravity field about the primary of the binary asteroid (66391) 1999 KW4 [89]. Table 4.6 summarizes the value of the zonal coefficients used for the simulations, whereas Fig. 4.28–4.30 display the output of the numerical procedures introduced in Sec. 4.4.

Table 4.6: Zonal coefficients and Legendre polynomials used for the simulations in the proximity of (66391) 1999 KW4α.

Zonal Coefficients	
J_2	4.609160×10^{-2}
J_3	0.517254×10^{-2}
J_4	-2.355357×10^{-2}
J_5	-0.582910×10^{-2}

Specifically, Fig. 4.28 illustrates the pseudo-circular orbit obtained as in Sec. 4.2.1 with $E = -0.4$, $H_z^2 = 0.5$. It turns out that the periodic orbit is still stable and surrounded by a family of two-dimensional quasi-periodic invariant tori. These tori are computed by means of the revised GMOS algorithm to ensure that the nodal and sidereal periods of any deputy on the surface of these

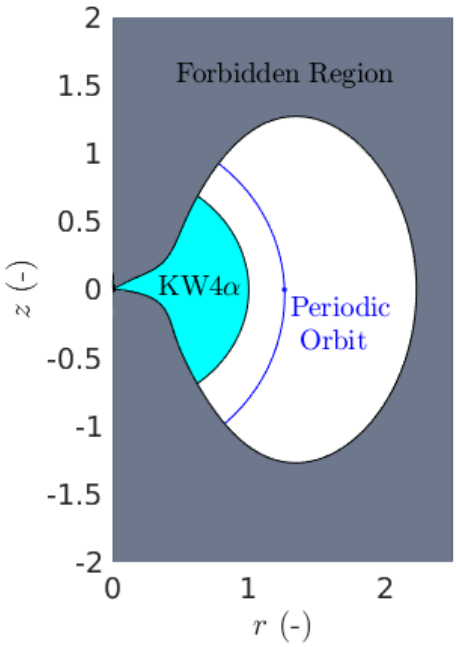

Figure 4.28: Pseudo-circular orbit in a 5×0 gravity field about KW4α. $E = -0.4$, $H_z^2 = 0.5$. The orbital period is 8.6871 TU.

manifolds would match, on average, the values of the chief. As a consequence of this requirement, a deputy being initialized on the greenest invariant curve of Fig. 4.29 ($H_z^2 = 0.5044$) remains in the vicinity of a pseudo-circular chief for more than one year. The computed relative trajectory is shown in Fig. 4.30) with respect to the Local Vertical, Local Horizontal (LVLH) frame of the reference spacecraft. The ICs of the chief and deputy satellites are given by $r_c = 1.26262389714496$, $z_c = 0$, $\dot{r}_c = -0.0245993331834527$, $\dot{z}_c = 0.705809935382072$, and $r_d = 1.25989761907113$, $z_d = 0.0207767003772756$, $\dot{r}_d = -0.00974737945454383$, $\dot{z}_d = 0.705900859223141$ respectively, with $LU = 765.70$ m and $TU = 5346.68$ s as the new length and time scale factors. Also notice that the chief has been initialized with two different initial longitude values to highlight the strong non-linear effects of the zonal harmonics and increase the minimum inter-satellite distance above 100 m (Fig. 4.31. These and other design considerations are further discussed in the conclusive section.

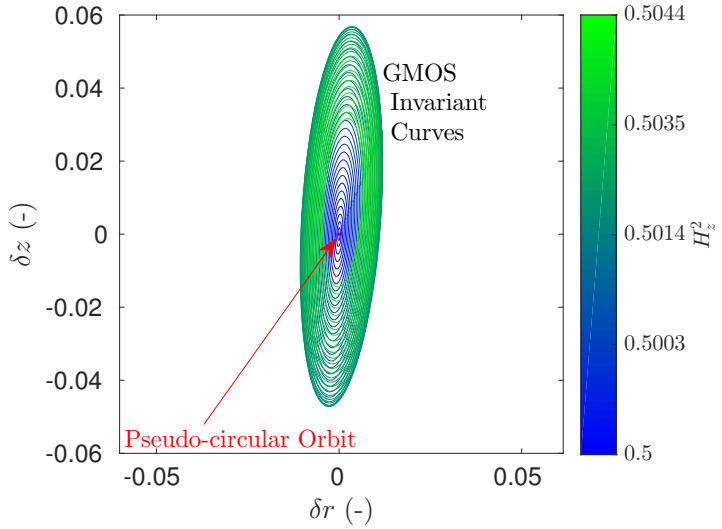

Figure 4.29: Revised GMOS invariant curves in configuration space for the 5×0 gravity field case. Note the non-linear effects of the symmetric gravity field, which cause significant distorsions and drifting in the distribution of the curves.

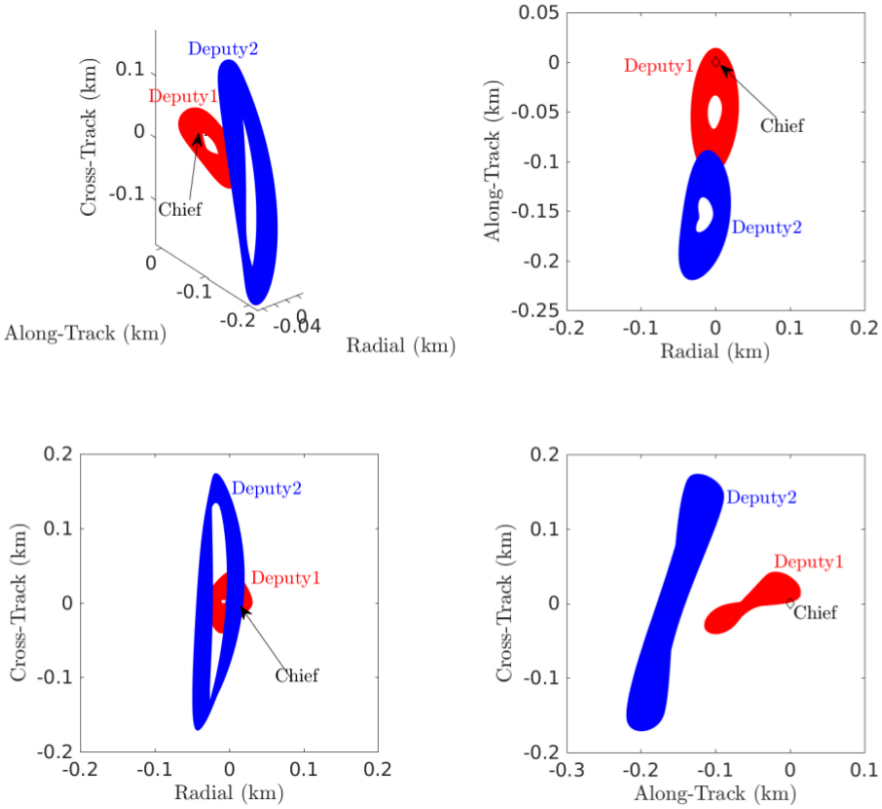

Figure 4.30: Relative motion between a pseudo-circular chief and a deputy on the surface of a HP torus in a 5×0 gravity field about KW4α. The difference between the red and blue trajectories lies in the initial value of the chief longitude ($\phi_0 = 0$ deg and $\phi_0 = 10$ deg, respectively).

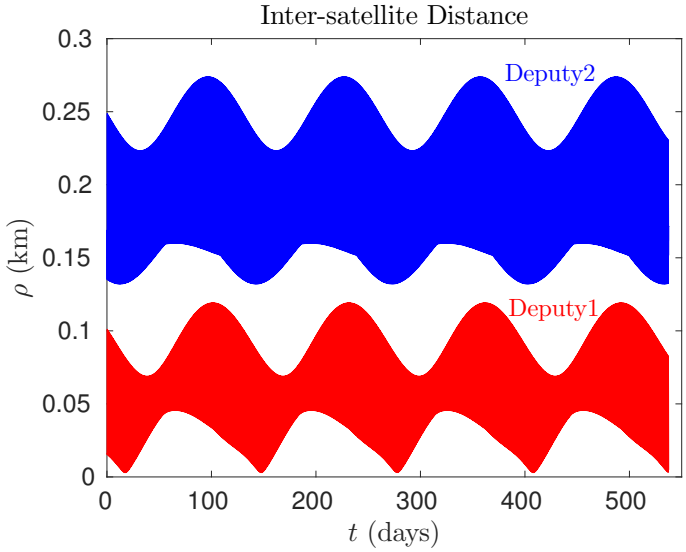

Figure 4.31: Inter-satellite distance between a pseudo-circular chief and a deputy on the surface of a HP torus in a 5×0 gravity field about KW4α. The difference between the red and blue trajectories lies in the initial value of the chief longitude ($\phi_0 = 0$ deg and $\phi_0 = 10$ deg, respectively).

4.6 Conclusions

The numerical simulations of this chapter demonstrate the validity of the revised GMOS algorithm at a range of altitudes and inclination values, as well as beyond Earth's orbit. Whether the spacecraft formation is in LEO, MEO, GEO, or close to a small irregular axisymmetric body, the proposed strategy successfully manages to generate families of quasi-periodic invariant tori that share, on average, the values of the nodal and sidereal periods. Because of this, groups of satellites being initialized on the invariant curves of the stroboscopic mapping displayed in Fig. 4.21, 4.26, 4.27, and 4.29 are guaranteed to never drift apart despite the zonal harmonics perturbations considered in the dynamical model.

It is worth recalling that such a procedure is applicable to any cluster flight and formation flying mission except at critical inclinations. Here, pseudo-circular orbits become unstable and lack center manifolds to be exploited by the algorithm [17]. Consequently, future research should be aimed in characterizing the phase space in the neighbourhood of these very peculiar trajectories and fill the last gap of our design space.

Also notice that less attention has been given to the geometry of the formation in spite of the practical implications that this may have on the success of the mission. Future research should be also looking at ways to establish which of the invariant curves generated with the revised GMOS algorithm satisfy given input geometrical constraints, including finding the optimal initial longitudes of the satellites ϕ_0 for collision avoidance.

Chapter 5

Spacecraft Formation Flight about Small Bodies

The results of the previous Chapter have demonstrated that quasi-periodic invariant tori can establish bounded relative motion in complex dynamical environments. Continuing along this line of work, we now explore the same approach in even more extreme dynamical systems and investigate whether it is possible to design spacecraft formations about small bodies such as asteroids, comets, and small planetary satellites. It is worth noting that this concept has already been proposed as a potential benefit for several asteroid mitigation strategies, including gravity tractors and asteroid ablation [45, 69]. In many of these papers, however, the gravitational attraction of the central body is typically neglected or oversimplified, meaning that passive relative orbits about strongly irregular and asymmetric gravity fields are yet to be found and described.

For all these reasons, Chapter 5 of this thesis is dedicated to the numerical computation of quasi-periodic invariant tori in dynamical systems that are representative of the dynamics near asteroids and small planetary satellites. As a first example, we explore the existence of invariant sets about slowly rotating tri-axial ellipsoids and leverage analytical techniques to compute a family of stable periodic orbits about an asteroid shaped as (4179) Toutatis. Then, we demonstrate that bounded relative motion can indeed be established via dynamical systems techniques by selecting initial conditions in the center manifold of these periodic solutions. Based on this result, we switch to a constant density polyhedron gravity model and witness how the irregular shape of an asteroid manages to complicate the relative motion dynamics. Next, we move to a higher-fidelity model of (4179) Toutatis, and include its complex rotational state in the equations of motion. This higher-

fidelity model gives us the opportunity to practice with three-dimensional quasi-periodic invariant tori and demonstrate the validity of the GMOS algorithm in time-periodic systems. Finally, we move to Mars and study the deployment of spacecraft formations near Phobos. Considering all of the dynamical perturbations acting on a satellite in the vicinity of the Martian moon, this is probably one of the most challenging dynamical problems up to date, and yet, we are still able to compute quasi-periodic trajectories that can serve as nominal orbits for formation flying applications. This capability is illustrated with numerical simulations that account for the irregular shape of the planetary satellite, the gravitational attraction of Mars, as well as kinematic spin-orbit coupling effects due to the eccentricity of the moon's orbit.

5.1 Slowly Rotating Tri-axial Ellipsoids

To start off, consider the motion of a mass particle subject to the gravitational attraction of a slowly rotating tri-axial ellipsoid with principal axes given by $\bar{\alpha} = 2250$ m, $\bar{\beta} = 1200$ m, $\bar{\gamma} = 950$ m. The values are derived from the actual shape of the complex rotator (4179) Toutatis since the same asteroid is further throughout the remainder of this Chapter. However, differently from Sec. 5.3, it is currently assumed that the central body is uniformly spinning about its maximum axis of inertia with $w_b = 1.34 \times 10^{-5}$ rad/s. In this case, the equations of motion in the body-centered body-fixed frame (BCF) of the asteroid are given by [96]

$$\begin{cases} \ddot{x} &= \omega_b^2\, x + 2\,\omega_b\,\dot{y} + U_x, \\ \ddot{y} &= \omega_b^2\, y - 2\,\omega_b\,\dot{x} + U_y, \\ \ddot{z} &= U_z, \end{cases} \tag{5.1}$$

where $\boldsymbol{X} = \begin{bmatrix} x, & y, & z, & \dot{x}, & \dot{y}, & \dot{z} \end{bmatrix}^T$ denotes the state of the spacecraft in BCF, and

$$U_x = \frac{\partial U}{\partial x} = -\frac{3}{2}\,\mu_b\, x \int_0^\infty \left(\frac{1}{\bar{\alpha}^2 + \Lambda + v} \right) \frac{dv}{\Delta(v+\Lambda)}, \tag{5.2a}$$

$$U_y = \frac{\partial U}{\partial y} = -\frac{3}{2}\,\mu_b\, y \int_0^\infty \left(\frac{1}{\bar{\beta}^2 + \Lambda + v} \right) \frac{dv}{\Delta(v+\Lambda)}, \tag{5.2b}$$

$$U_z = \frac{\partial U}{\partial z} = -\frac{3}{2}\,\mu_b\, z \int_0^\infty \left(\frac{1}{\bar{\gamma}^2 + \Lambda + v} \right) \frac{dv}{\Delta(v+\Lambda)}, \tag{5.2c}$$

are the partial derivatives of the gravitational potential

$$U = -\mu_b \frac{3}{4} \int_0^\infty \phi(x, y, z, v + \Lambda) \frac{dv}{\Delta(v + \Lambda)}, \tag{5.3}$$

with

$$\Delta(v + \Lambda) = \sqrt{(\bar{\alpha}^2 + \Lambda + v)(\bar{\beta}^2 + \Lambda + v)(\bar{\gamma}^2 + \Lambda + v)}, \tag{5.4a}$$

$$\phi(x, y, z, v + \Lambda) = \frac{x^2}{\bar{\alpha}^2 + \Lambda + v} + \frac{y^2}{\bar{\beta}^2 + \Lambda + v} + \frac{z^2}{\bar{\gamma}^2 + \Lambda + v} - 1. \tag{5.4b}$$

Observe that $\mu_b = 1792.60$ m^3/s^2 is the gravitational parameter of the simulated ellipsoid, whereas Λ is defined to be either zero or the positive root of $\phi(x, y, z, \Lambda) = 0$ depending on whether U is computed inside or outside of the target asteroid. Also notice that both of (5.2) and (5.3) can be evaluated via the Carlson elliptic integrals described in Ref. [91], which provides an elegant and computationally efficient way of estimating the potential, acceleration, and gravity gradient derived from this gravity model.

The knowledge of the gravitational acceleration allows us to integrate the equations of motion (5.1) and obtain trajectories such as the one of Figure 5.1(a), which results from the implementation of the partially frozen orbit initial conditions derived by Hu and Scheeres for slowly rotating asteroids [52]. As it can be seen, the sample trajectory is very close to be periodic and can be successfully refined via the predictor-corrector scheme of Sec. 2.3 to obtain a fully periodic solution. Fig. 5.1(b) displays the result of Newton's algorithm along with several family members obtained through numerical continuation (Fig. 5.2).

As it can be seen from the root locus of the monodromy matrix eigenvalues shown in Fig. 5.2(b), all of the periodic orbits computed about this uniformly rotating tri-axial ellipsoid turn out to be stable and surrounded by a family of three-dimensional quasi-periodic invariant tori. Although it is possible to apply the numerical procedure of Sec. 3.7 and compute three-dimensional manifolds, it is actually instructive to numerically calculate the two families of two-dimensional subtori that exist in the center manifold of each periodic orbit (Figure 5.3). Our motivation for this reasoning is that two very distinctive relative motion behaviors arise.

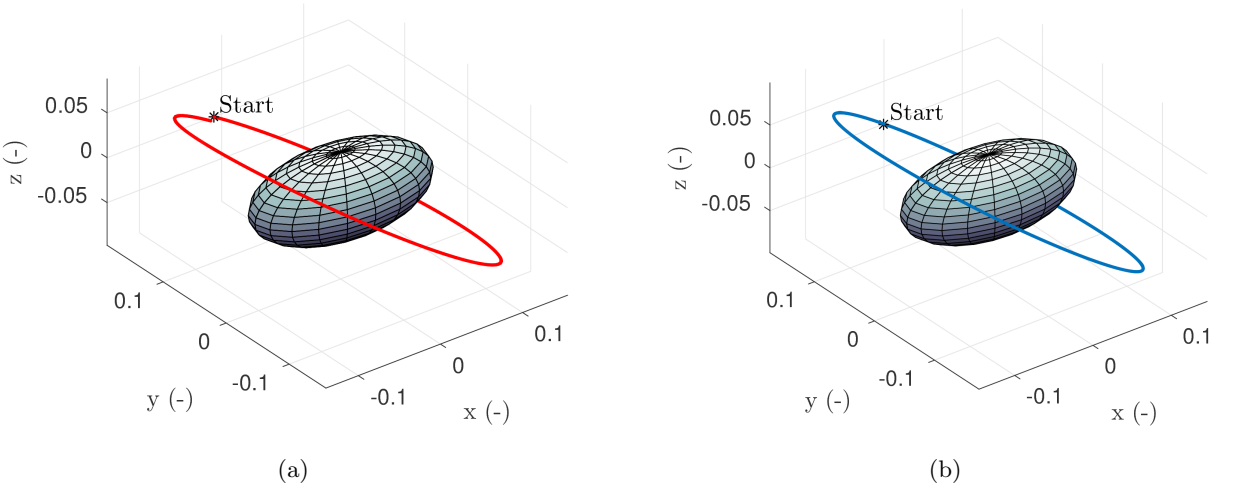

Figure 5.1: First periodic orbit about a slowly rotating tri-axial ellipsoid. a) Initial guess obtained via the numerical integration of partially frozen orbit initial conditions. b) First periodic solution computed via Newton's method. All plots are shown in normalized units with $LU = 21.532$ km.

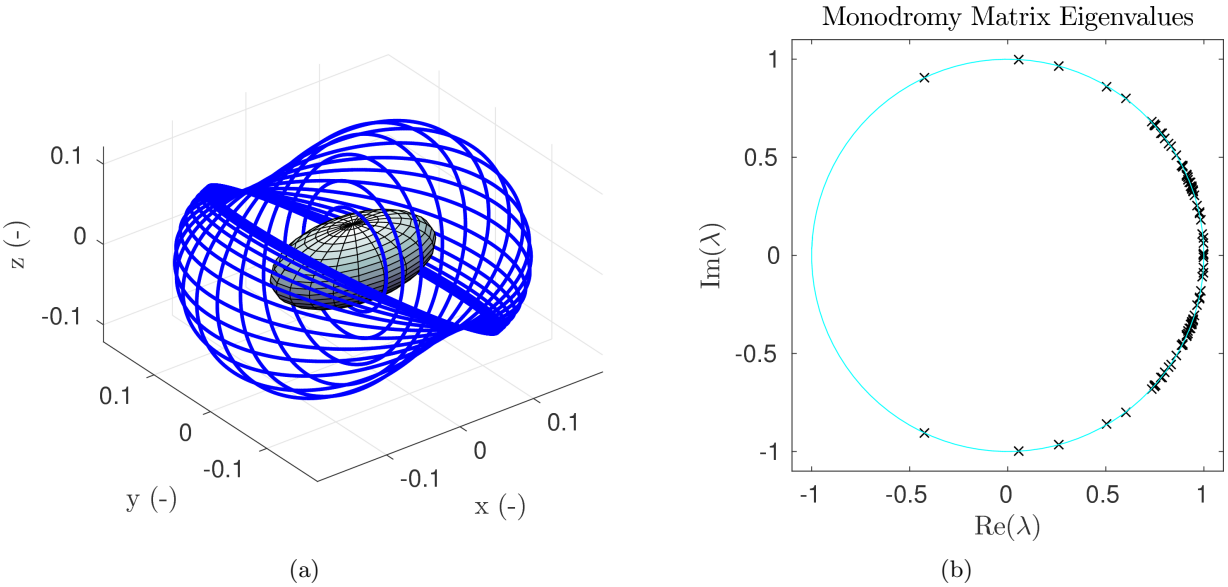

Figure 5.2: a) Family of periodic orbits about a slowly rotating tri-axial ellipsoid. b) Eigenvalues of the monodromy matrices calculated for the different family members.

In the case of Fig. 5.3(a), selecting initial conditions on the surface of this two-dimensional quasi-periodic invariant subtorus yields in-plane relative orbits that resemble the standard $2:1$ ellipse observed for circular formations about spherically symmetric bodies [95]. Differences in the

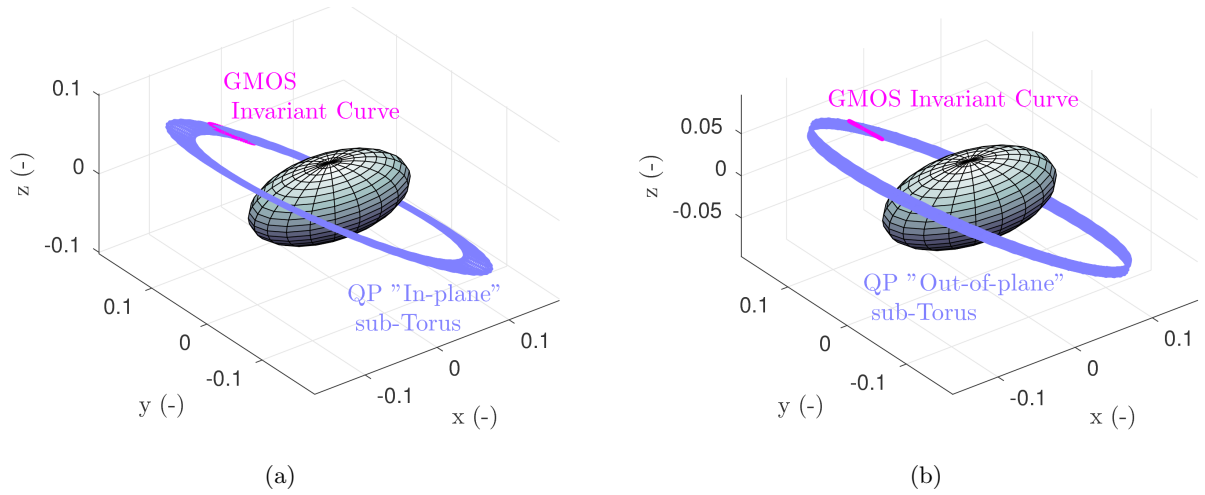

(a) (b)

Figure 5.3: Two-dimensional subtori projected onto the configuration space. a) "In-plane" quasi-periodic trajectories. b) "Out-of-plane" quasi-periodic trajectories.

relative orbit shape are caused by the irregularities of the ellipsoidal gravity field, which also induces out-of-plane oscillations on the order of several meters (Fig. 5.4).

Differently from the previous case, spacecraft formations initialized on the surface of the second family of two-dimensional subtori show large oscillations in both the along-track and cross-track directions (Fig. 5.5). These "out-of-plane" relative orbits are indeed more complicated than the previous ones and certainly less predictable. However, the inter-satellite distance between a chief and a deputy spacecraft being initialized on this manifold never exceeds the upper bound of 1 km circa, thus proving that passive relative orbits can be also found in this second scenario.

Based on this result, we now switch our equations of motion to account for the irregular shape of the central asteroid. This is further discussed in the next section, along with a brief overview of the constant density polyhedron gravity model that is constantly adopted for the remainder of this Chapter.

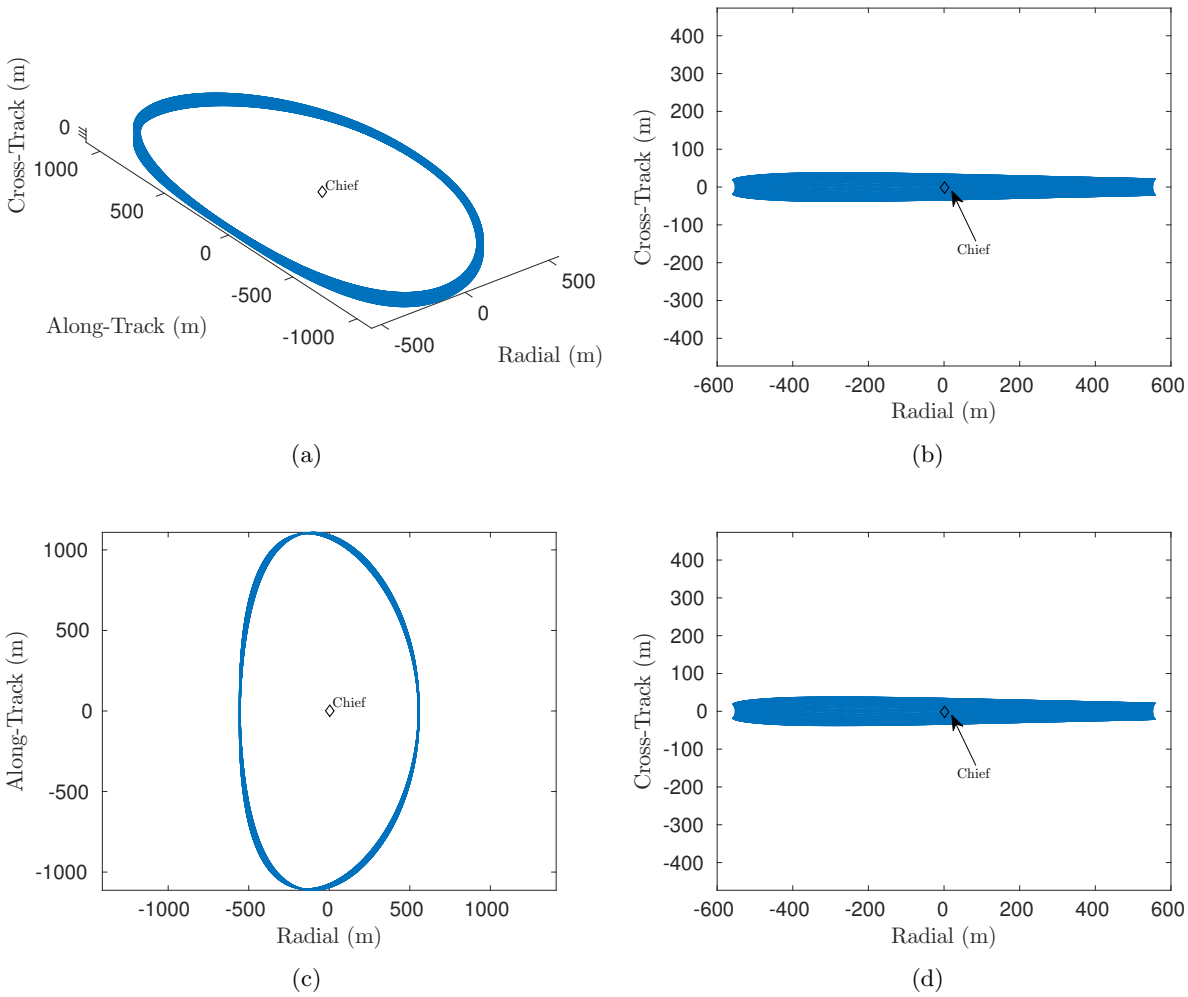

Figure 5.4: In-plane relative orbit obtained for a constant density ellipsoidal gravity field.

5.2 Slowly Rotating Constant Density Polyhedra

According to Werner [111], the gravity field of a constant density polyhedron with v vertices, $f = 2\,v - 4$ facets, and $e = 3\,(v - 2)$ edges can be approximated by two summations: one over the number of edges, and one over the number of facets. This gives the expression of the gravitational potential reported in [98], i.e.,

$$U(\boldsymbol{r}) = \frac{\mathcal{G}\,\sigma}{2}\left[\sum_{e\,\in\,\text{edges}} \boldsymbol{r}_e\,[E_e]\,\boldsymbol{r}_e - \sum_{f\,\in\,\text{facets}} \boldsymbol{r}_f\,[F_f]\,\boldsymbol{r}_f\,\omega_f\right], \tag{5.5}$$

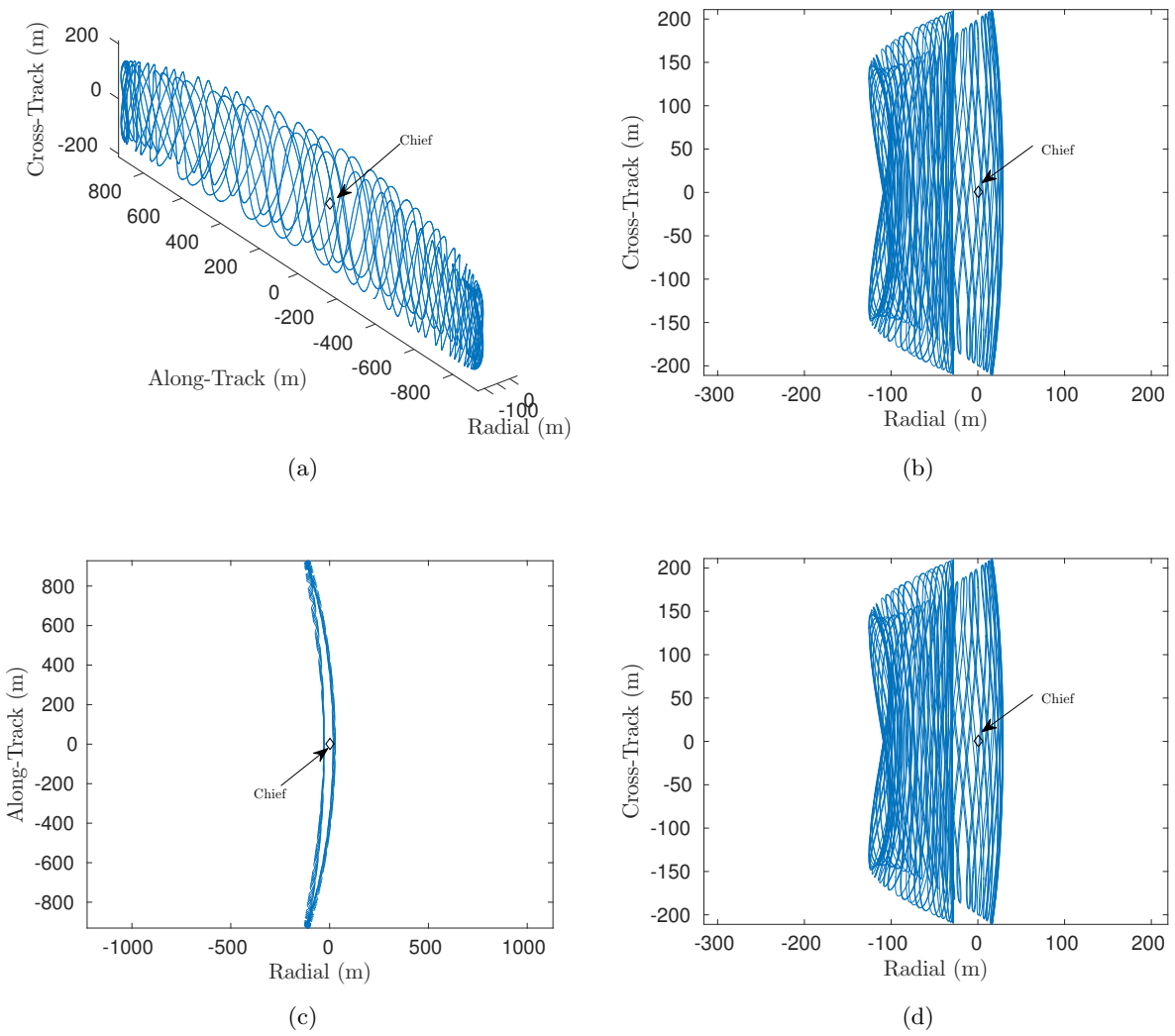

Figure 5.5: Out-of-plane relative orbit obtained for a constant density ellipsoidal gravity field.

from which the formulae for the gravity acceleration and gradient gradient immediately follow:

$$\boldsymbol{a}_g = \frac{\partial U}{\partial \boldsymbol{r}} = -\mathcal{G}\,\sigma \left[\sum_{e \,\in\, \text{edges}} [E_e]\, \boldsymbol{r}_e\, L_e - \sum_{f \,\in\, \text{facets}} [F_f]\, \boldsymbol{r}_f\, \omega_f \right], \tag{5.6}$$

$$[G] = \frac{\partial^2 U}{\partial \boldsymbol{r}^2} = \mathcal{G}\,\sigma \left[\sum_{e \,\in\, \text{edges}} [E_e]\, L_e - \sum_{f \,\in\, \text{facets}} [F_f]\, \omega_f \right]. \tag{5.7}$$

In Eq. (5.5)–(5.7), $\mathcal{G}$ is the gravitational constant, whereas σ is the constant density of the central body. Furthermore, $\boldsymbol{r}$ denotes the position vector of a mass particle subject to the gravitational attraction of the polyhedron, $\boldsymbol{r}_e$ is the relative position vector of the spacecraft with respect to any

point along the e-th edge, and $\boldsymbol{r}_f$ is the relative position vector of $\boldsymbol{r}$ with respect to an arbitrary point on the f-th facet. Finally, $[E_e]$, L_e, $[F_f]$, and ω_f are defined as

$$[E_e] = \hat{\boldsymbol{n}}_f \, (\hat{\boldsymbol{n}}_e^f)^T + \hat{\boldsymbol{n}}_{f'} \, (\hat{\boldsymbol{n}}_e^{f'})^T, \tag{5.8}$$

$$L_e = \ln \frac{r_1^e + r_2^e + |r_2^e - r_1^e|}{r_1^e + r_2^e - |r_2^e - r_1^e|}, \tag{5.9}$$

$$[F_f] = \hat{\boldsymbol{n}}_f \, \hat{\boldsymbol{n}}_f^T, \tag{5.10}$$

$$\omega_f = 2 \arctan \frac{\boldsymbol{r}_1^f \cdot (\boldsymbol{r}_2^f \times \boldsymbol{r}_3^f)}{r_1^f \, r_2^f \, r_3^f + (\boldsymbol{r}_2^f \cdot \boldsymbol{r}_3^f) \, r_1^f + (\boldsymbol{r}_1^f \cdot \boldsymbol{r}_3^f) \, r_2^f + (\boldsymbol{r}_1^f \cdot \boldsymbol{r}_2^f) \, r_3^f} \tag{5.11}$$

where $\hat{\boldsymbol{n}}_f$ denotes the unit vector perpendicular to the f-th facet and pointing away from the central body, $\hat{\boldsymbol{n}}_e^f$ is the unit vector perpendicular to both the edge e and $\hat{\boldsymbol{n}}_f$, $\boldsymbol{r}_1^e$, $\boldsymbol{r}_2^e$ are the position vector of the first and second vertices defining the edge e, and $\boldsymbol{r}_1^f$, $\boldsymbol{r}_2^f$, $\boldsymbol{r}_3^f$ are the first, second, and third vertices defining the facet f (Fig. 5.6).

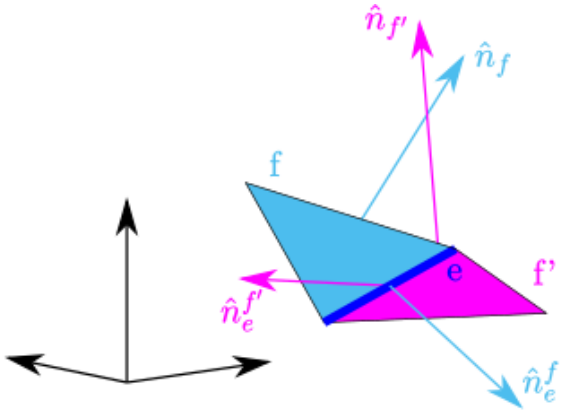

Figure 5.6: Unit vectors for Polyhedron gravity model

By summing over the edges and triangular facets, one has a better representation of the gravity field of a target asteroid. This is especially true when the resolution of *shape model* is high enough to account for the irregularities in the mass distribution of the central body. As an example, consider the plot of Fig. 5.7, which shows a 1600-vertex shape model of (4179) Toutatis along with the relative differences of its gravitational potential with respect to the ellipsoidal case [53, 81].

Considering that these differences can be as large as 12%, it is not surprising that periodic

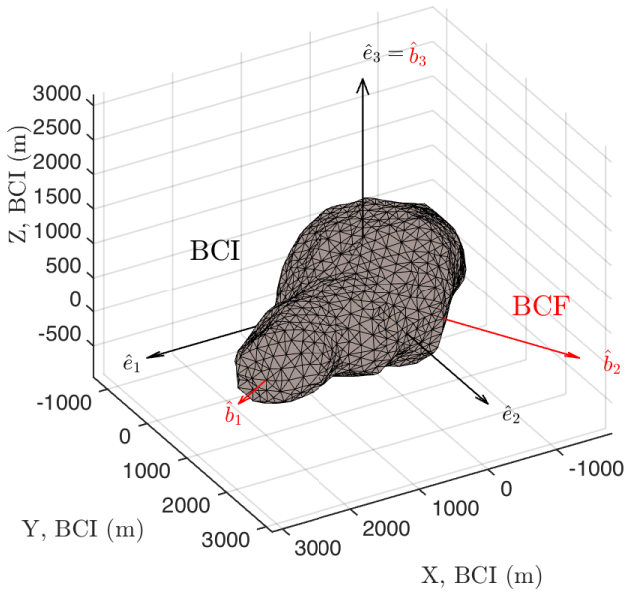

Figure 5.7: (4179) Toutatis shape model and reference frames.

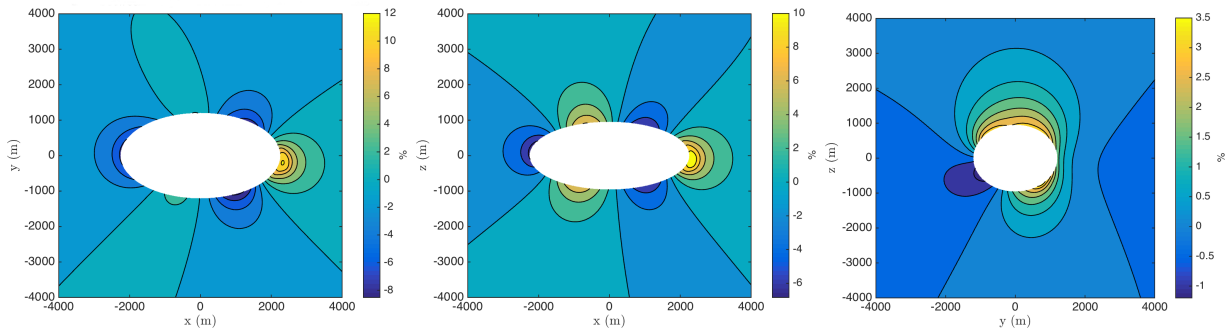

(a) (b) (c)

Figure 5.8: Relative differences between the constant density polyhedron and ellipsoid gravity potentials

and quasi-periodic trajectories behave quite differently from Sec.5.1. For instance, it is found that the family of periodic orbits arising from partially frozen orbit initial conditions eventually change in stability and become unstable as observed in Fig. 5.9. This occurs as soon as the periapsis of the orbits become small enough to place the spacecraft in a region where the difference between the gravitational attractions of the larger and smaller lobes of (4179) Toutatis becomes appreciable.

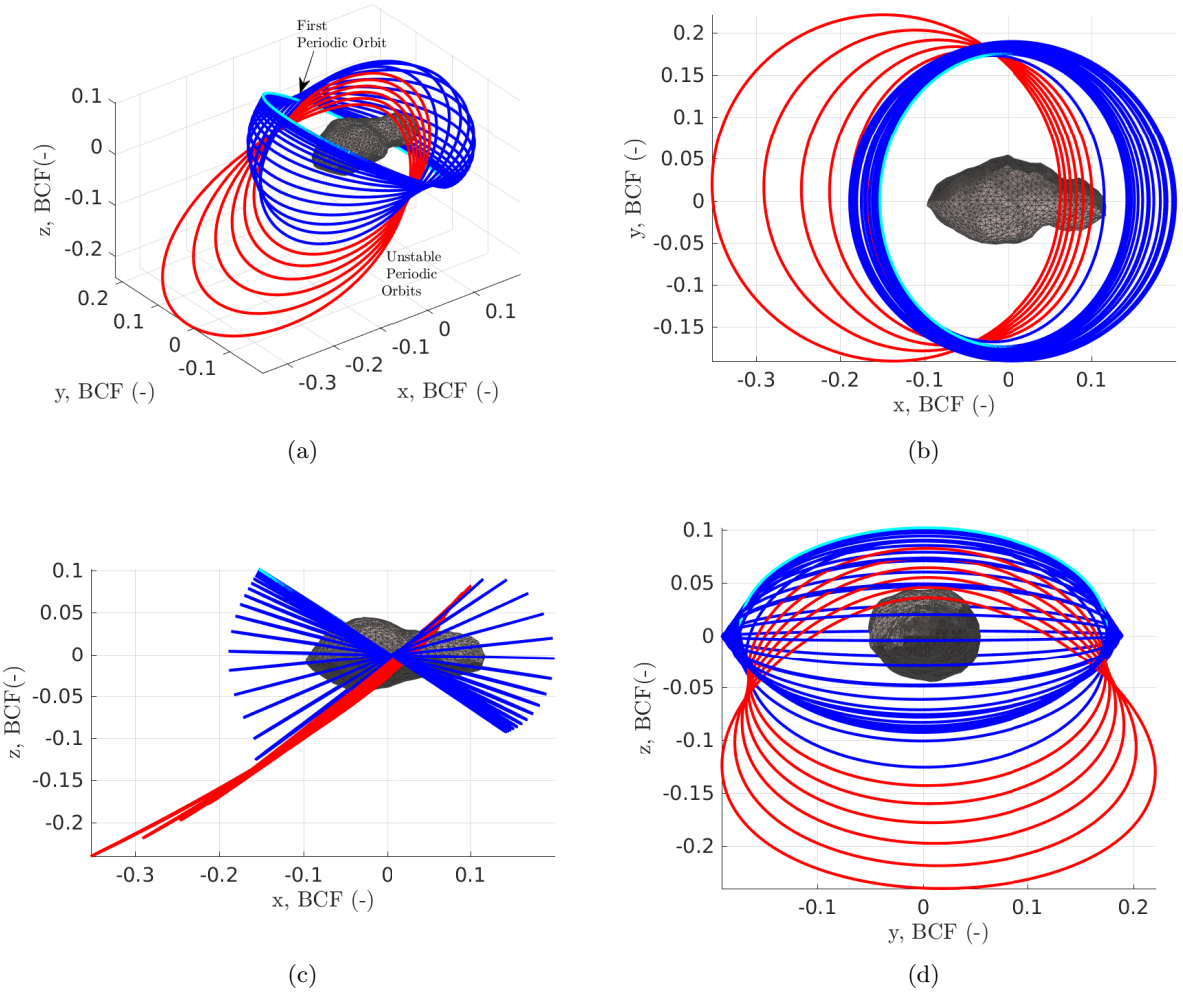

Figure 5.9: Family of periodic orbits about a slowly rotating constant density polyhedron. The blue orbits are stable, whereas the red ones are unstable.

Nevertheless, there is still a number of periodic orbits that remain stable and surrounded by a family of three-dimensional tori in spite of the asymmetries in the gravitational field of the asteroid. For these periodic orbits, we can proceed as in Sec. 5.1 and calculate the two-dimensional subtori that populate their center manifold. In this case, the relative trajectories are much more complicated than before and certainly more similar with respect to each other. Regardless of this complexity, however, bounded relative motion is still maintained for more than a month and without signs of divergence over the long term (Fig. 5.10–5.11). This encouraging result provides the motivation to further improve the realism of our simulations. In fact, as observed by the Chinese

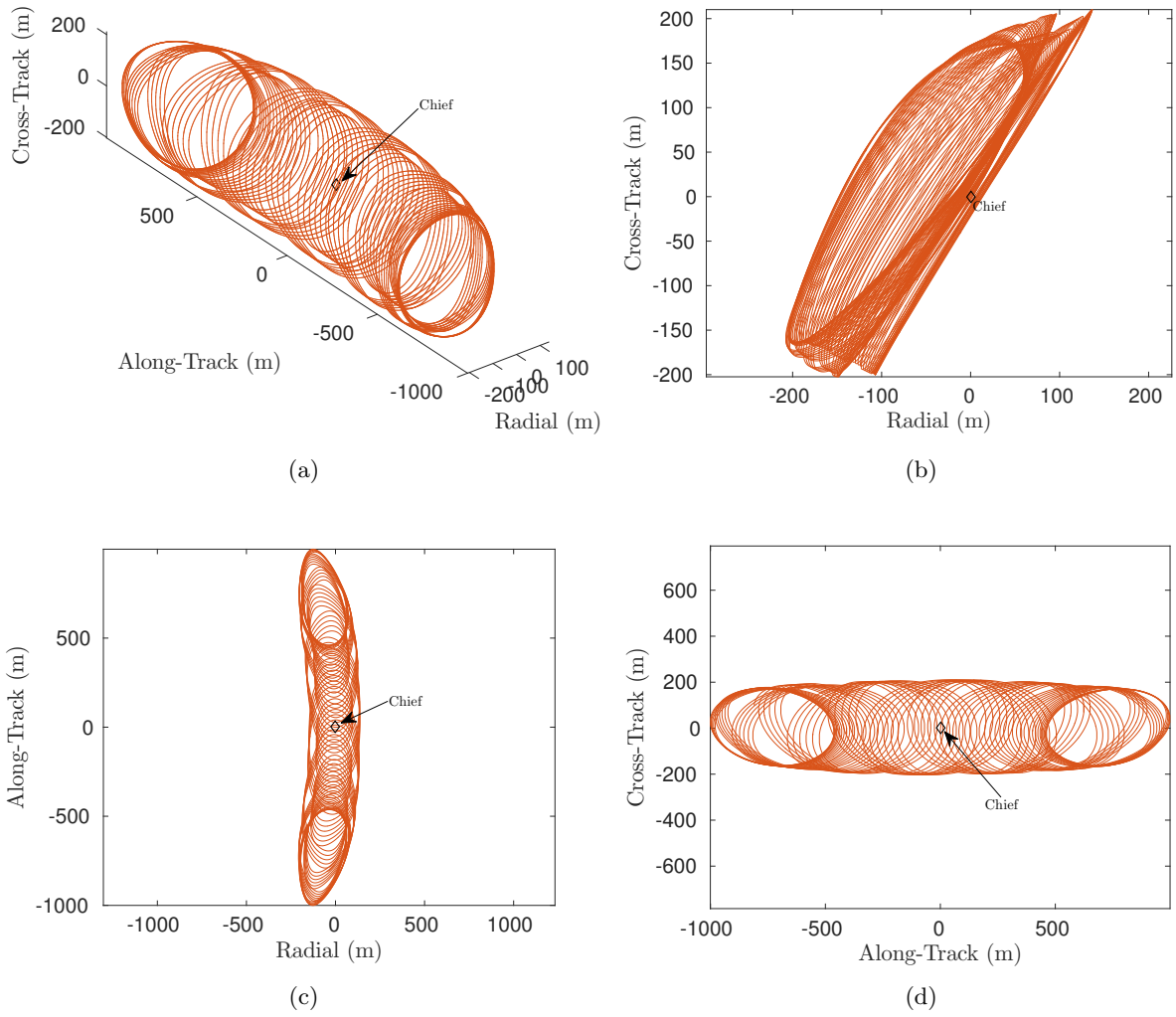

Figure 5.10: In-plane relative orbit obtained for a constant density polyhedron gravity field.

spacecraft Chang'E-2 and radar measurements from Earth [53, 117, 118], it turns out that (4179) Toutatis is actually a complex rotator, spinning about its minimum axis of inertia. Because of this, the equations of motion (5.1) are no longer autonomous and prompt small changes in the GMOS algorithm as described in the following section.

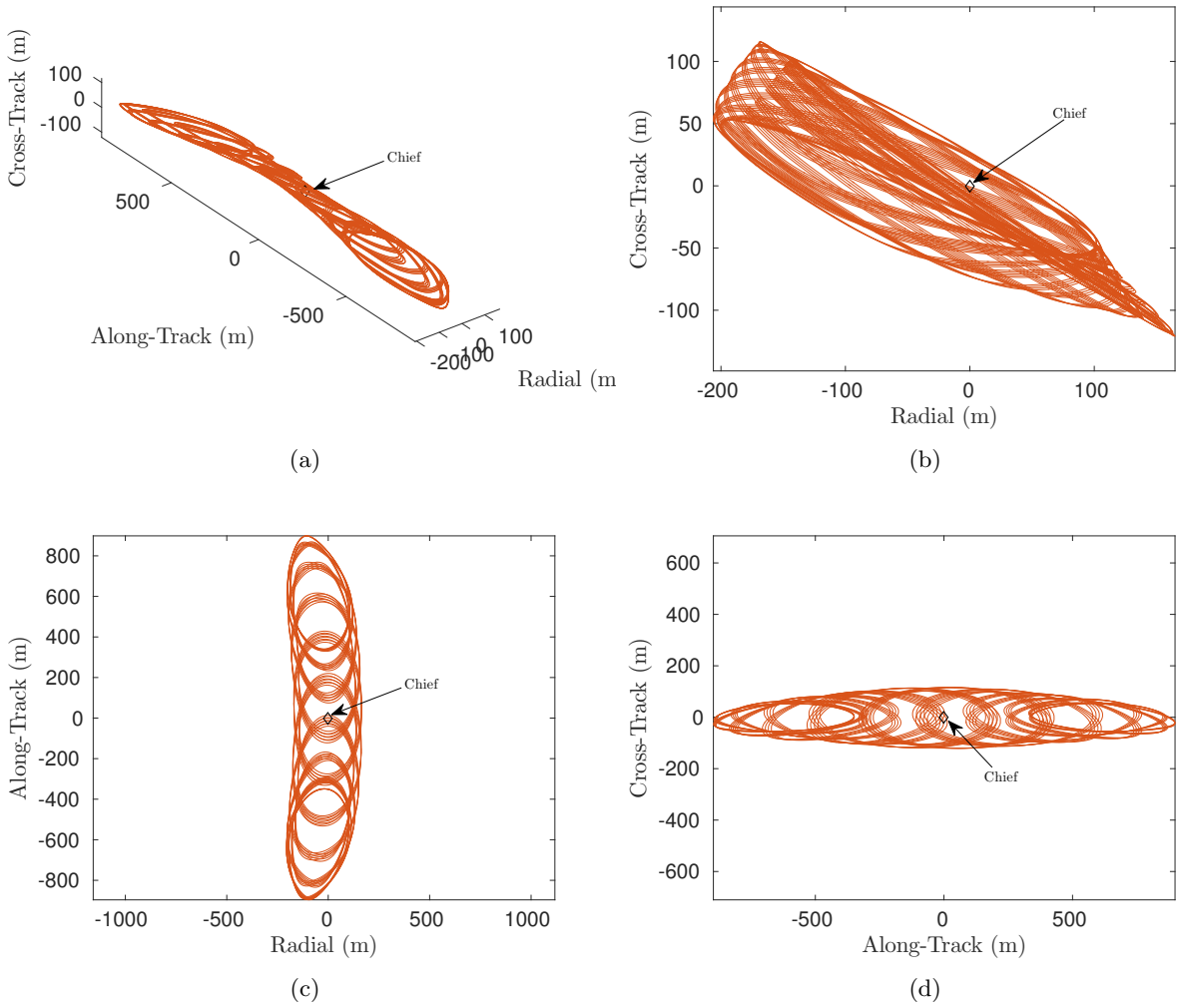

Figure 5.11: Out-of-plane relative orbit obtained for a constant density polyhedron gravity field.

5.3 Complex Rotators

Since Toutatis is a complex rotator, its angular velocity changes periodically over time as described by Euler's equations:

$$\boldsymbol{I}\,\dot{\boldsymbol{\Omega}} = -\boldsymbol{\Omega} \times [\boldsymbol{I}\,\boldsymbol{\Omega}], \tag{5.12}$$

where $\boldsymbol{I} = \mathrm{diag}(I_x, I_y, I_z)$ is the inertia tensor in the principal axis frame of the asteroid, and $\boldsymbol{\Omega}$ is its angular velocity vector.

Assuming that no external torques are acting on the system, Eq. (5.12) admits an analytical

solution in terms of the Jacobi elliptic functions $\mathrm{sn}(\tau)$, $\mathrm{cn}(\tau)$, $\mathrm{dn}(\tau)$ as described in [68]. Specifically, let $\mathcal{B} = \{\mathcal{O}, \hat{\boldsymbol{b}}_1, \hat{\boldsymbol{b}}_2, \hat{\boldsymbol{b}}_3\}$ be the BCF shown in Fig. 5.7 and such that $\hat{\boldsymbol{b}}_1$ is always aligned with Toutatis' longest axis, $\hat{\boldsymbol{b}}_3$ is parallel to the shortest axis, and $\hat{\boldsymbol{b}}_2 = \hat{\boldsymbol{b}}_3 \times \hat{\boldsymbol{b}}_1$ completes the right-handed triad. In this frame,

$$\boldsymbol{\Omega}(\tau) = \omega_l \begin{bmatrix} \sqrt{\dfrac{I_D\,(I_z - I_D)}{I_x\,(I_z - I_x)}}\,\mathrm{dn}(\tau - \tau_0) \\ \sqrt{\dfrac{I_D\,(I_D - I_x)}{I_y\,(I_y - I_x)}}\,\mathrm{sn}(\tau - \tau_0) \\ \sqrt{\dfrac{I_D\,(I_D - I_x)}{I_z\,(I_z - I_x)}}\,\mathrm{cn}(\tau - \tau_0) \end{bmatrix}, \tag{5.13}$$

where

$$\tau - \tau_0 = \sqrt{\frac{I_D\,(I_z - I_D)\,(I_y - I_x)}{I_x\,I_y\,I_z}}\,\omega_l\,(t - t_0), \tag{5.14}$$

I_x, I_y, and I_z are the principal moments of inertia, $I_D = \boldsymbol{\Omega}\,\boldsymbol{I}\,\boldsymbol{I}\,\boldsymbol{\Omega}/(\boldsymbol{\Omega}\,\boldsymbol{I}\,\boldsymbol{\Omega}) = \text{const}$, and $\omega_l = \boldsymbol{\Omega}\,\boldsymbol{I}\,\boldsymbol{\Omega}/|\boldsymbol{I}\,\boldsymbol{\Omega}| = \text{const}$. For Toutatis, $I_x/I_z = 0.31335$, $I_y/I_z = 0.94471$, $I_D/I_z = 0.51983$, and $\omega_l = 1.8548 \times 10^{-5}$ rad/s [97].

Next, observe that the equations of motion of a mass particle subject to the gravitational attraction of a tumbling asteroid, namely

$$\dot{\boldsymbol{x}} = \boldsymbol{f}(t, \boldsymbol{x}) = \begin{cases} \boldsymbol{v}, \\ \\ \boldsymbol{a}_g - \dot{\boldsymbol{\Omega}} \times \boldsymbol{r} - 2\,\boldsymbol{\Omega} \times \boldsymbol{v} - \boldsymbol{\Omega} \times (\boldsymbol{\Omega} \times \boldsymbol{r}), \end{cases} \tag{5.15}$$

also change periodically over time with period $\mathcal{P} = 4\,K_k\,\omega_l\,\sqrt{I_x\,I_y\,I_z/[I_D\,(I_z - I_D)\,(I_y - I_x)]} = 5.42$ days. K_k is the complete Jacobi integral of the first kind [91], whereas $\boldsymbol{a}_g$ represents the gravity of the small body and is obtained via the constant density polyhedron model of Sec. 5.2. Furthermore, $\boldsymbol{r} = \begin{bmatrix} x, & y, & z \end{bmatrix}^T$ and $\boldsymbol{v} = \begin{bmatrix} \dot{x}, & \dot{y}, & \dot{z} \end{bmatrix}^T$ are the position and velocity vectors of the spacecraft expressed in BCF components.

Due to the explicit dependence on time, periodic orbits of (5.15) must have periodicity $k\,P$, where $k \in \mathbb{N}^+$ is an integer multiple. For instance, consider the 1:1 direct orbit displayed in Figure 5.12 and computed via Newton's method while following the analytical derivations of Ref. [97]. Table 5.1 shows the eigenvalues of the monodromy matrix M, thereby illustrating that the

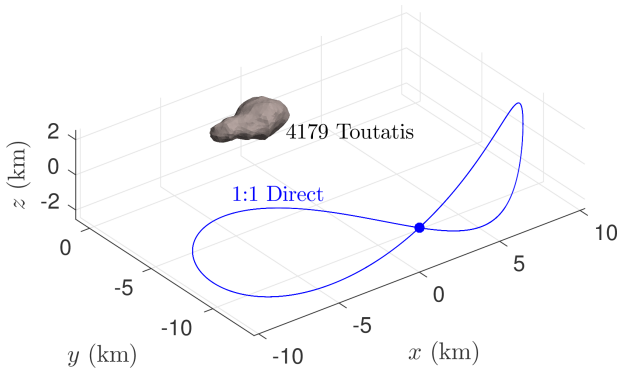

Figure 5.12: 1:1 direct periodic orbit as seen from Toutatis' body-fixed frame.

displayed periodic orbit is actually unstable. Also notice that no unitary eigenvalues pairs are obtained as the system is no longer autonomous. Instead, two complex conjugate eigenvalues pair are found, meaning that the periodic orbit still has a center component populated by a family of three-dimensional quasi-periodic invariant tori.

Table 5.1: Monodromy matrix eigenvalues for the 1:1 direct orbit about (4179) Toutatis.

Eigenvalue	**Value**
λ_1	$-0.0667 + \mathrm{i}\,0.9978$
$\lambda_2 = \bar{\lambda}_1$	$-0.0667 - \mathrm{i}\,0.9978$
λ_3	$-0.0382 + \mathrm{i}\,0.9993$
$\lambda_4 = \bar{\lambda}_3$	$-0.0382 - \mathrm{i}\,0.9993$
λ_5	1.7388
$\lambda_6 = 1/\lambda_5$	0.5751

In this case, one can initialize the GMOS algorithm of Sec. 3.7 via the invariant torus of the monodromy map (3.85) and select $N_1 \times N_2$ points along this two-dimensional surface, i.e., $\boldsymbol{v}(\boldsymbol{\psi}_{j,k})$. Also recall that the period of the underlying periodic orbit as well as the phases of the two complex conjugate eigenvalue pairs may be used to approximate the initial values of the stroboscopic time T and the rotation vector $\boldsymbol{\rho}$. Furthermore, the points $\boldsymbol{X}_0 = \left[\boldsymbol{v}(\boldsymbol{\psi}_{j,k})\right]^T$, $j = 0, \cdots, N_1$, $k = 0, \ldots, N_2$ can be integrated and rotated to generate a reliable approximation of the family tangents $\tilde{\boldsymbol{z}}_r'$ and $\tilde{\boldsymbol{z}}_s'$ as proposed in Sec.3.7.

The latter completes all of the pieces of information required to run the GMOS algorithm

and converge on the invariant torus of the stroboscopic mapping $\boldsymbol{\varphi}_T(\boldsymbol{x}_0, t_0) : \mathbb{R}^n \times \mathbb{R} \to \mathbb{R}^n$. The only difference with respect to previous BVPs is that time now appears explicitly in the equations of motion (5.15). Assuming that $\theta_0 = \tau$, the vector field would depend explicitly on one of the angle variable of the torus θ_0. Because of this, the indeterminacy in the θ_0 angular value observed in Chapter 3 is effectively removed, meaning that the phase condition for the θ_0 angle is no longer necessary. Also recall that three-dimensional quasi-periodic invariant tori of time-periodic systems live in two-parameter families (Section 2.6, [58]). This follows from the fact that $\omega_0 = 2\,\pi/T$ must be resonant with the periodicity of the time-periodic term $\boldsymbol{\Omega}(t)$ appearing in (5.15). Accordingly, the stroboscopic time T is already specified as a multiple integer of $\mathcal{P}$ and does not need to be solved for by our numerical procedure. This reduces the number of parametrizing equations to two, yielding the final list of boundary constraints

$$\boldsymbol{F}(\boldsymbol{z}) = \begin{bmatrix} \boldsymbol{g}(\boldsymbol{X}_0, \boldsymbol{X}_1) \\ p_1(\boldsymbol{X}_0) \\ p_2(\boldsymbol{X}_0) \\ s_1(\boldsymbol{X}_0, \boldsymbol{\rho}) \\ s_2(\boldsymbol{X}_0, \boldsymbol{\rho}) \end{bmatrix} = \boldsymbol{0}, \tag{5.16}$$

where $\boldsymbol{z} = \begin{bmatrix} \boldsymbol{X}_0, & \boldsymbol{\rho} \end{bmatrix}^T$, and $p_1(\boldsymbol{X}_0)$, $p_2(\boldsymbol{X}_0)$, $s_1(\boldsymbol{X}_0, \boldsymbol{\rho})$, $s_1(\boldsymbol{X}_0, \boldsymbol{\rho})$ are specified as in Sec. 3.7.

Fig. 5.13 illustrate the convergence of Newton's method for the first member of the 3D quasi-periodic invariant tori family with $N_1 = 31$, $N_2 = 21$. As it can be seen, the $N_1 \times N_2$ solution points $\boldsymbol{v}(\boldsymbol{\psi}_{j,k})$ overlap with the images of the stroboscopic mapping $\boldsymbol{\varphi}_T$ obtained after the integration of (5.15), followed by a rotation via the two-dimensional rotational operator defined in Eq. (3.69).

As soon as the norm of $\boldsymbol{F}(\boldsymbol{z})$ is below some user-defined tolerance, the singular value decomposition of $D\mathbb{F}(\boldsymbol{z})$ can be applied to update the family tangents and produce a new initial guess for the next member of the family. The process can be iterated multiple times to generate three-dimensional invariant tori of increasing size as prescribed by the predictor-corrector approach of Sec. 2.3. As an example, consider the plot of Fig. 5.14, which illustrates the 25th member of

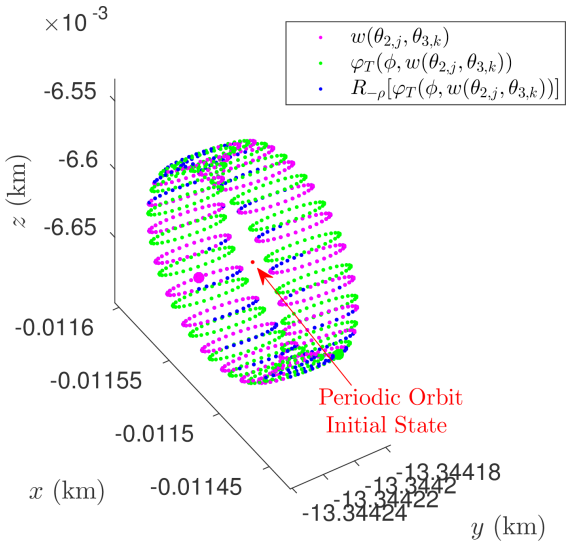

Figure 5.13: GMOS solution points for the first 3D quasi-periodic invariant torus.

the three-dimensional QP tori family obtained with the algorithm.

The manifold of Fig. 5.14 gives plenty of initial conditions to establish bounded relative motion over long intervals of time. For instance, we can place a chief on the 1:1 direct periodic orbit and a deputy on one of the GMOS solution points output by the three-dimensional version of the algorithm to obtain the bounded relative trajectory of Fig. 5.15. Alternatively, we can also place both of the chief and deputy satellites on the surface of the same torus and obtain the relative motion of Fig. 5.16. Once again, no secular drifts in both the along-track and cross-track

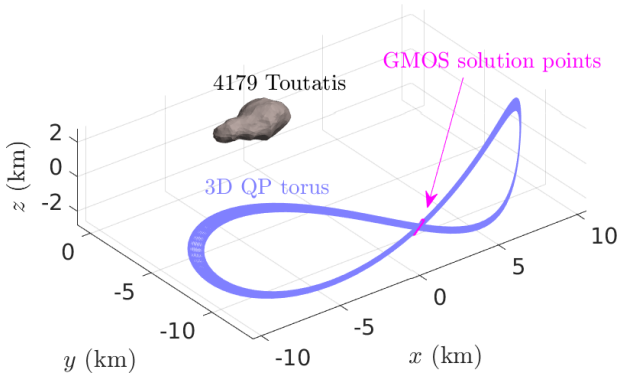

Figure 5.14: 25th member of the three-dimensional quasi-periodic invariant tori family computed with the GMOS algorithm.

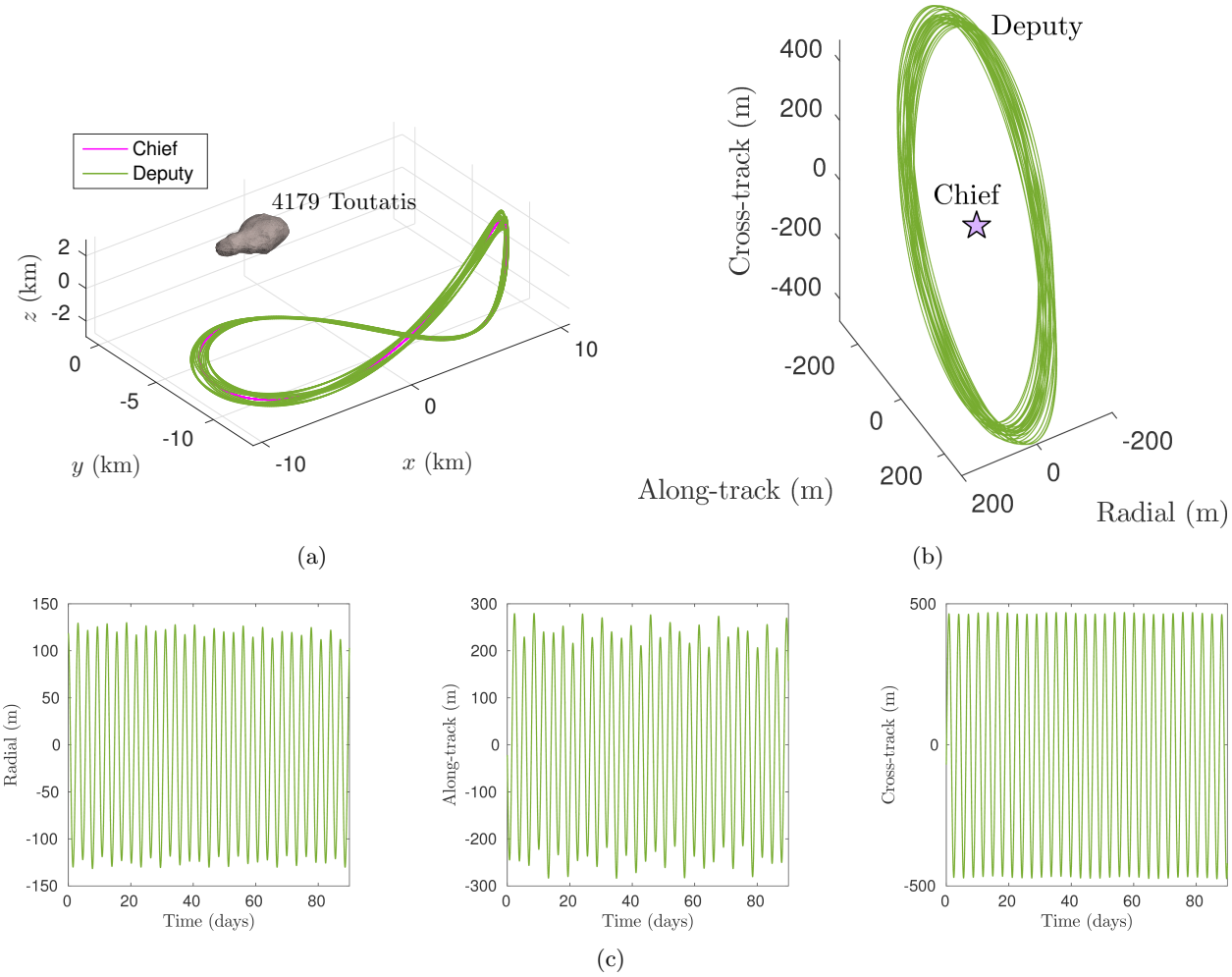

Figure 5.15: Relative motion between a chief on a 1:1 direct periodic orbit and a deputy on the surface of a three-dimensional torus about the complex rotator (4179) Toutatis. a) Satellite orbits in the BCF frame. b) Relative trajectory in the LVLH frame of the chief. c) Inter-satellite distance over three months.

directions are observed, meaning that bounded spacecraft formations can indeed be initialized with the proposed methodology.

5.4 Formation Flight near Phobos

As a final example of a challenging dynamical problem where spacecraft formations can be deployed through quasi-periodic invariant tori, consider the motion of two satellites in the vicinity of the Martian moon Phobos [31, 37]. The small planetary satellite is modeled as a constant density

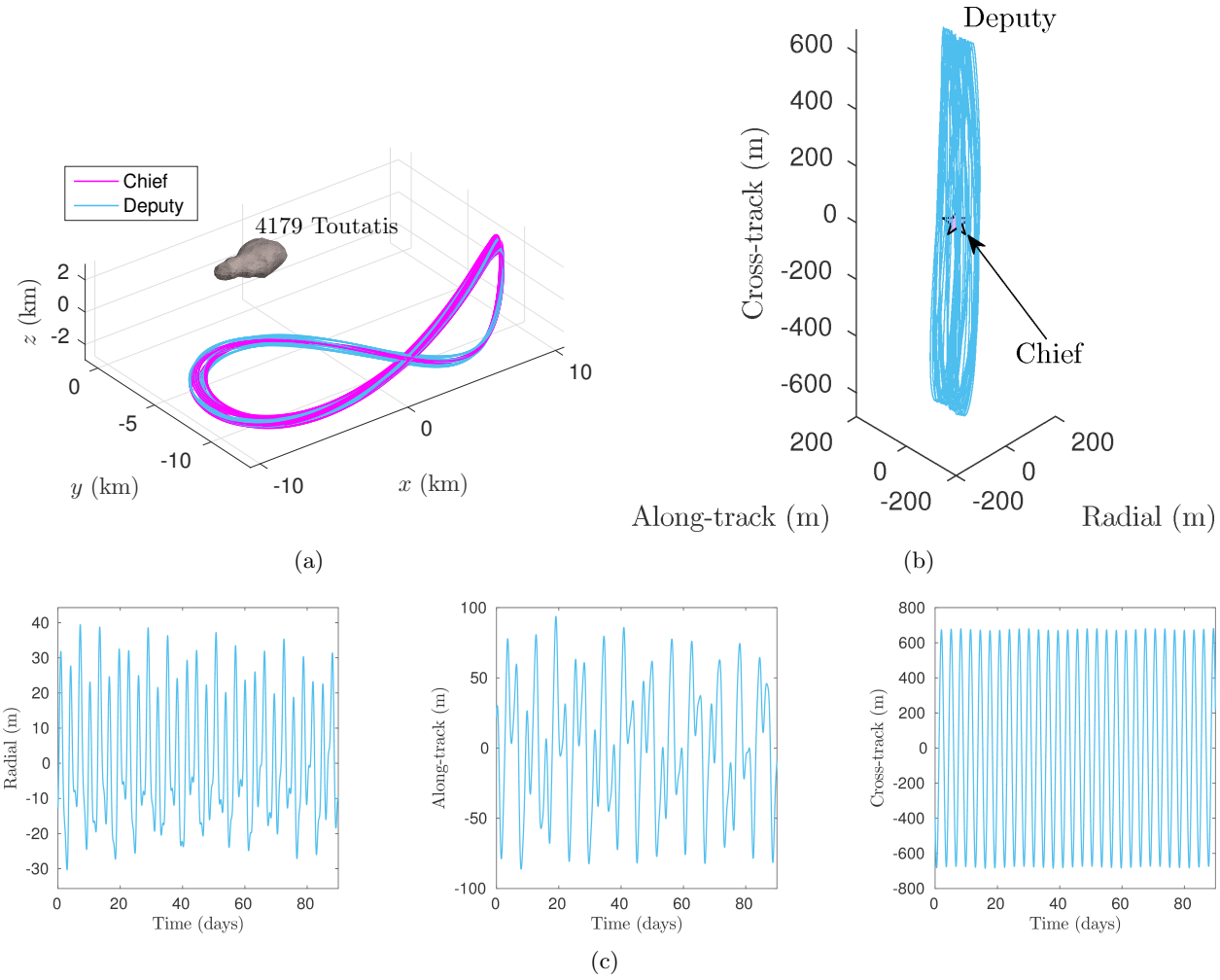

Figure 5.16: Relative motion between a chief and a deputy spacecraft on the surface of the same three-dimensional torus about the complex rotator (4179) Toutatis. a) Satellite orbits in the BCF frame. b) Relative trajectory in the LVLH frame of the chief. c) Inter-satellite distance over three moths.

polyhedron with 2456 triangular facets and follows an ellipse around Mars with $e_P = 0.01515$ [41]. Knowing that the gravitational attraction exerted by the planetary satellite is considerably smaller than the tidal forces generated by Mars, it is safe to assume that the equations of motion of the

spacecraft can be well approximated by the EHP [40, 109]:

$$\boldsymbol{x}' = \boldsymbol{f}(\nu, \boldsymbol{x}) = \begin{cases} u, \\ v, \\ w, \\ \dfrac{1}{1 + e_P \cos\nu} \left(g_x + 3\, x\right) + 2\, v, \\ \dfrac{1}{1 + e_P \cos\nu}\, g_y - 2\, u, \\ \dfrac{1}{1 + e_P \cos\nu}\, g_z - z, \end{cases} \tag{5.17}$$

where $\boldsymbol{x} = \begin{bmatrix} x, & y, & z, & u, & v, & w \end{bmatrix}^T$ represents the state of any massless particle in a pulsating reference frame $\mathcal{S}$ centered on Phobos and such that $\hat{\boldsymbol{x}}$ is constantly aligned with the separatrix between the two barycenters of the primaries, $\hat{\boldsymbol{z}}$ is parallel to the orbital angular momentum of Phobos, and $\hat{\boldsymbol{y}} = \hat{\boldsymbol{z}} \times \hat{\boldsymbol{x}}$ complets the right-handed triad.

Note that the time and length units of Eq. (5.17) are normalized such that one orbital revolution of Phobos around Mars corresponds to $2\,\pi$ and such that the *resonance radius* $a_P \left(\mu_P / \mu_{\sigma^{\prime}}\right)^{(1/3)}$ is equal to 1 with μ_P as the gravitational parameter of Phobos, $\mu_{\sigma^{\prime}}$ as the gravitational parameter of Mars, and $a_P = 9377.2$ km as the semi-major axis of the planetary satellite [98]. It is also assumed that the effects of Mars' oblateness are negligible, so that the trajectory of Phobos around Mars can be simply described by its two-body dynamics. Furthermore, ν is the true anomaly of the planetary satellite as well as the independent variable of (5.17), whereas $\begin{bmatrix} g_x, & g_y, & g_z \end{bmatrix}^T$ are the components of Phobos' gravity in the $\mathcal{S}$ frame, obtained from the rotation of the gravitational acceleration $\boldsymbol{a}_g$ computed in the principal axes frame of the small body. This rotation accounts for kinematic librations due to the eccentricity of Phobos' orbit. In particular, knowing that Phobos is in a synchronous state and assuming that the principal axes of the small body are oriented such that $\hat{\boldsymbol{x}}_P$ is pointing towards the anti-Mars direction, $\hat{\boldsymbol{z}}_P$ is aligned with $\hat{\boldsymbol{z}}$, and $\hat{\boldsymbol{y}}_P = \hat{\boldsymbol{z}}_P \times \hat{\boldsymbol{x}}_P$, the

direction cosine matrix that maps vectors in $\mathcal{B}$ to vectors in $\mathcal{S}$ can be simply given by

$$[\mathcal{S}\,\mathcal{B}] = \begin{bmatrix} \cos\phi_P, & \sin\phi_P, & 0 \\ -\sin\phi_P, & \cos\phi_P, & 0 \\ 0, & 0, & 1 \end{bmatrix} \tag{5.18}$$

where ϕ_P is the libration angle corresponding to the instantaneous difference between ν and Phobos' mean anomaly. An illustration of the reference frames as seen from the leading edge of the planetary satellite is disclosed in Fig. 5.17.

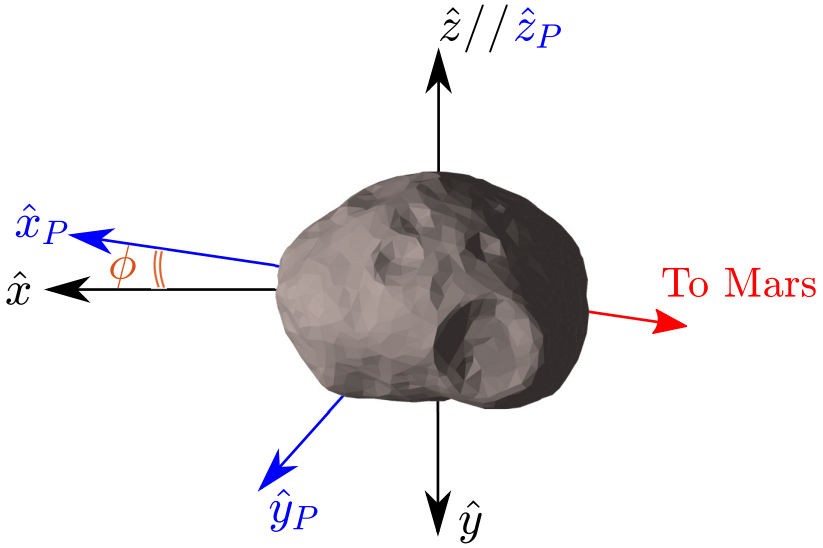

Figure 5.17: $\mathcal{S}$ and $\mathcal{B}$ reference frames as seen from the leading edge of Phobos.

Since $\begin{bmatrix} g_x, & g_y, & g_z \end{bmatrix}^T = [\mathcal{S}\,\mathcal{B}]\,\boldsymbol{a}_g$, the equations of motion (5.17) depends explicitly on the independent variable ν, meaning that the EHP is a non-autonomous system of ordinary differential equations that change periodically with the true anomaly of the planetary satellite. Following Broucke [16], periodic orbits are expected to be isolated at best and must be resonant with the orbital period of Phobos around Mars. As an example, consider the family of Quasi-Satellite Orbits (QSO) obtained in the circular case when $e_P = 0$ and $[\mathcal{S}\,\mathcal{B}]$ is also equal to the identity matrix I_3. Fig. 5.18 displays the chart of the periodic orbit period versus the x-axis crossing with $v < 0$, illustrating that only those solutions whose period is resonant with $2\,\pi$ actually survive when the eccentricity of Phobos is taken into account [112].

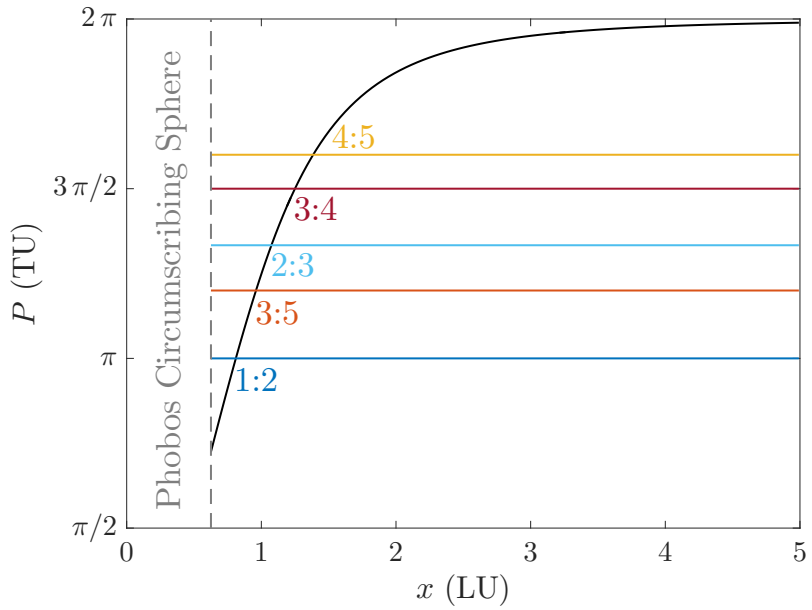

Figure 5.18: Period vs positive x-crossing for the family of quasi-satellite orbits with $e = 0$. Only the periodic orbits whose period is resonant with $2\,\pi$ survive when $e \neq 0$.

Different from periodic orbits, quasi-periodic invariant tori of a six-dimensional non-autonomous Hamiltonian system like (5.17) are still organized in one-parameter families [57]. Accordingly, entire families of solutions are available to help us understand and organize the system dynamics. This is better illustrated with the plots of Fig. 5.19, which displays a sample of QSO orbits along with their corresponding two-dimensional tori in the $e_P \neq 0$ case. It is worth noting that these manifolds have been computed through the collocation algorithm of Sec. 3.5 after setting the stroboscopic time T to match the orbital period of Phobos around Mars, i.e., $2\,\pi$. The reason for this being that one of the torus frequencies, namely ω_0, must be resonant with the periodicity of the equations of motion (5.17) in order to ensure that the computed manifolds are indeed invariant for the time-varying field $\boldsymbol{f}(\nu, \boldsymbol{x})$.

As for the initial guesses of the invariant curves of the stroboscopic mapping, observe that the only periodic orbits available to initialize the algorithm are the ones computed in the circular case. Accordingly, all of the $N_1 = 51$ GMOS solutions points have been initialized along a predetermined QSO orbit obtained in the $e_P = 0$ case. This initial guess is quite far from the true form of the

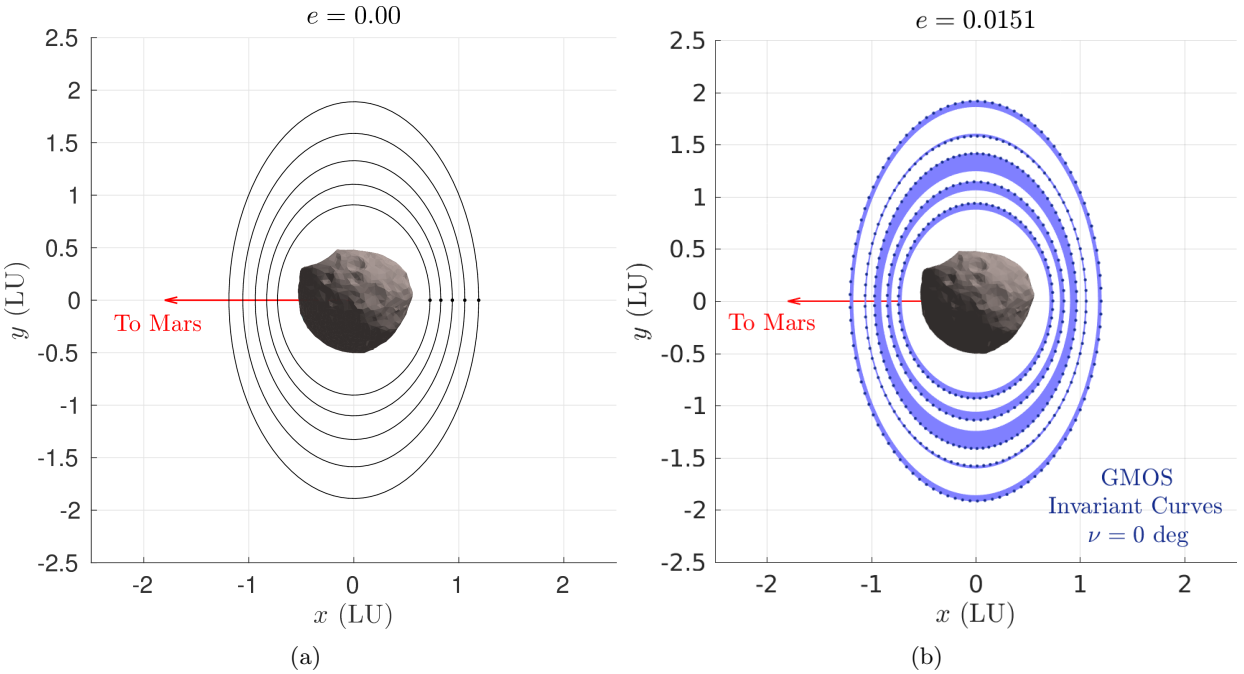

Figure 5.19: a) Family of QSO periodic orbits in the circular Hill problem. b) Family of quasi-QSO invariant tori in the elliptic Hill problem.

invariant curve and definitely less reliable than the invariant circle of the monodromy map used for autonomous systems. For this reason, collocation is actually mandatory to ensure convergence.

The boundary value problem that needs to be solved for generating the two-dimensional tori of Fig. 5.19(b) reads as

$$\begin{cases} \boldsymbol{X}' &= T\,\mathbb{F}(\boldsymbol{\Theta}_0, \boldsymbol{X}), \\ T' &= 0, \\ \rho' &= 0, \end{cases} \tag{5.19}$$

and is subject to the boundary constraints

$$\boldsymbol{F}(\boldsymbol{z}) = \begin{bmatrix} g(\boldsymbol{X}_0, \boldsymbol{X}_1) \\ c_c(\boldsymbol{X}_0) \\ c_d(\boldsymbol{X}_0, \rho) \\ p_1(\boldsymbol{X}_0) \\ s_1(\rho) \end{bmatrix} = \boldsymbol{0}, \tag{5.20}$$

Once again, one of the phase condition is dropped because of the time-dependency appearing in the equations of motion (5.17). Specifically, it is assumed that $\nu = \theta_0$, meaning that a phase condition for the θ_0 angle is no longer required. Moreover, since the stroboscopic time is already specified as $T = 2\,\pi$, only one of the two parametrizing equations is needed. We choose to constrain the rotation number ρ via $s_1(\rho) := \rho - \omega_1\,T = \rho - \omega_1\,2\,\pi = \rho - 4\,\pi^2/\mathcal{P} = 0$ and search for the quasi-periodic invariant torus that emerges from the QSO orbit with period $\mathcal{P}$ when the eccentricity of the moon's orbit is considered. Also notice that the quantity Θ_0 introduced in Eq. (5.19) is defined as $\Theta_0 = \begin{bmatrix}\nu_0, & \cdots, & \nu_{N_1-1}\end{bmatrix}^T$, with $\nu_i = 2\,\pi\,i/N_1$, $i = 0, \ldots, N_1 - 1$, whereas $\mathbb{F}(\boldsymbol{\Theta}_0, \boldsymbol{X})$ reads as

$$\mathbb{F}(\boldsymbol{\Theta}_0, \boldsymbol{X}) = \begin{bmatrix} \boldsymbol{f}(\nu_0, \boldsymbol{x}_0) \\ \cdots \\ \boldsymbol{f}(\nu_{N_1-1}, \boldsymbol{x}_{N_1-1}) \end{bmatrix} \tag{5.21}$$

with $\boldsymbol{f}(\nu, \boldsymbol{x})$ as in (5.17). This gives a well-posed BVP that can be solved with Newton's method as described in Chapter 3.

Following the convergence of the GMOS algorithm, bounded relative orbits about Phobos can be found by selecting arbitrary initial conditions on the surface of the same quasi-periodic torus. Differently from previous cases, care must be taken in specifying initial states with the same value of true anomaly. This condition is satisfied by placing both of the chief and deputy spacecraft on the same invariant curve of the stroboscopic mapping $\boldsymbol{\varphi}_{2\,\pi}$. An example of this is shown in Fig. 5.20, where a chief and a deputy spacecraft are placed on the surface of a quasi-periodic invariant

Table 5.2: Chief and deputy initial conditions for bounded relative motion about M1 Phobos. The initial conditions are expressed in the pulsating synodic reference frame $\mathcal{S}$ with LU = 23.9257 km and TU = 4387.77 s.

	Chief	Units		**Deputy**	Units
x_c	0.740495878892368	(LU)	x_d	0.7372237734449	(LU)
y_c	0.00184411657803554	(LU)	y_d	−0.0800684058209446	(LU)
z_c	−0.00631901696767579	(LU)	z_d	−0.0063644451885002	(LU)
u_c	−0.00801860969426209	(LU/TU)	u_d	−0.163735093218928	(LU/TU)
v_c	−2.16560744054813	(LU/TU)	v_d	−2.15290345625889	(LU/TU)
w_c	−0.00155739474288585	(LU/TU)	w_d	−0.00077243779717515	(LU/TU)

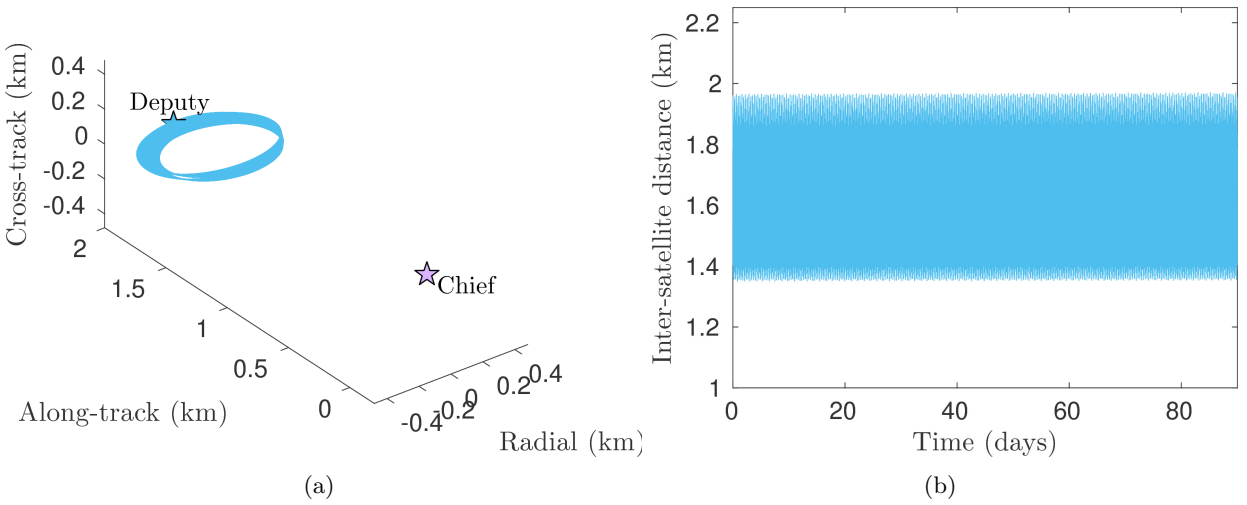

Figure 5.20: Bounded relative trajectory about Phobos. a) Relative trajectory in the LVLH frame of the chief. b) Inter-satellite distance over 90 days.

torus with $\mathcal{P} = 2.7524$ TU when Phobos is at perimartem. This yields the relative trajectory of Fig. 5.20(a), as well as the bounded inter-satellite distance of Fig. 5.20(b). The initial conditions of the two satellites are reported in Table 5.2.

5.5 Conclusions

In this Chapter, several dynamical systems involving the dynamics of mass particles near small bodies have been investigated. Starting from the simple case of a slowly rotating tri-axial ellipsoid, we demonstrated that bounded relative motion can be achieved in spite of the complex shape of the central body. To that end, we computed the two families of two-dimensional subtori that populate the center manifold of "partially frozen orbits" and placed multiple-satellites on their surface. It turns out that two very distinctive relative motion behaviors arise, leading to in-plane and out-of-plane formations that could be useful for scientific investigations of slowly rotating elongated asteroids.

Differently from the ellipsoidal case, two-dimensional subtori about a constant density polyhedron shaped as the (4179) Toutatis do not lead to particularly distinct relative trajectories, but still succeed in ensuring boundedness over long intervals of time. Consequently, we investigated a

more realistic representation of the dynamics near the target asteroid, and included its complex rotational state in the equations of motion. This brought us to computing three-dimensional quasi-periodic invariant tori about unstable 1:1 direct periodic orbits by means of the 3D version of the GMOS algorithm described in Sec. 3.7. To the author's knowledge, this was the first attempt of computing higher dimensional objects with the GMOS algorithm and while testing the generalized pseudo-arclength continuation algorithm of Chapter 3.

Lastly, we considered the equations of motion of the elliptical Hill problem and discussed about the numerical computation of quasi-periodic invariant tori in time-periodic systems. As a case study, we considered the dynamics of satellites near the Martian moon Phobos and tried to deploy spacecraft formations in the vicinity of its surface. Eventually, we were able to numerically converge on the two-dimensional quasi-periodic invariant tori that exist in the phase space when the eccentricity of the moon is modeled, and used these manifolds to establish bounded relative motion regardless of the strong nonlinear forces acting on the satellites within the formation. This proved the utility of quasi-periodic invariant tori not only for formation flying applications, but also for developing a better understanding of the system dynamics in the vicinity of the small planetary satellite.

Chapter 6

Robustness Analysis

In the final Chapter of this thesis, we propose a robustness analysis to validate the numerical results presented throughout this manuscript. We begin by reviewing the different sources of perturbation that may affect the relative motion between two or more satellites in the vicinity of one of the target bodies considered in this research. For example, Section 6.2 of this chapter deals with spacecraft formations in LEO and assess the impact of atmospheric drag, solar radiation pressure, luni-solar perturbations, and non-zonal spherical harmonics gravity terms on the relative trajectories of Chapter 4. A similar investigation is performed for satellite clusters in MEO & GEO, where luni-solar perturbations tend to dominate over radiation pressure and non-zonal coefficients. Next, we move beyond Earth's orbit and assess the robustness of the initial conditions found in Chapter 5 to design bounded relative trajectories about (4179) Toutatis and Phobos (Sections 6.4 & 6.5). In the first case, we find that Solar Radiation Pressure (SRP) has devastating effect on the satellites' orbits, thereby suggesting that its effects should be modeled in the equations of motion for practical realizations of this mission scenario. Conversely, the gravitational effects due to Mars' asymmetric shape are found to be more indulgent on the relative dynamics around Phobos, making it possible to envision distributed space systems for future explorations of the Martian moon.

6.1 Dynamical Perturbations

Consider a spacecraft formation in orbit about one of the target bodies considered in this thesis, i.e., either the Earth, (4179) Toutatis, or Phobos. Let us also recall the definition of the BCI

frame as the pseudo-inertial coordinate system $\mathcal{N}$ centered on one of these objects and described by the triad $\{\hat{\boldsymbol{e}}_1, \hat{\boldsymbol{e}}_2, \hat{\boldsymbol{e}}_3\}$, where $\hat{\boldsymbol{e}}_3$ is constantly aligned with the body's angular momentum vector, $\hat{\boldsymbol{e}}_1$ is pointing towards the vernal equinox, and $\hat{\boldsymbol{e}}_2 = \hat{\boldsymbol{e}}_3 \times \hat{\boldsymbol{e}}_1$.

In BCI, the equations of motion for each satellite in the formation are given by

$$\begin{cases} \ddot{x}_i &= a_x, \\ \ddot{y}_i &= a_y, \\ \ddot{z}_i &= a_z, \end{cases} \tag{6.1}$$

where x_i, y_i, z_i, $\dot{x}_i$, $\dot{y}_i$, $\dot{z}_i$ are the components of the position and velocity vectors of the i-th satellite in the $\mathcal{N}$ frame, and a_x, a_y, a_z are the components of its inertial acceleration. Such an acceleration is given by the sum of the different forces acting on each satellite and its formulation changes depending on the target body being considered. For this reason, we first proceed with a brief overview of the dynamical perturbations that may have significant effects on the relative trajectories presented in this thesis. After that, we continue with our numerical investigations and show how unmodeled dynamics affects the long-term evolution of spacecraft formations on quasi-periodic invariant tori.

6.1.1 Tesseral and Sectorial Harmonics

As a first source of perturbation, recall that the asymmetric part of the geopotential was entirely neglected for all of the numerical simulations about axisymmetric bodies. This assumption enabled Routh reduction and allowed us to focus on the four-dimensional system derived from the Lagrangian of the Earth's zonal problem. However, the non-zonal part of the geopotential still plays an important role on the orbital mechanics of spacecraft about the Earth and explain dynamical effects such as the geostationary equilibrium points or the equilibrium longitude of semisynchronous circular and Molniya orbits [21]. Accordingly, it is interesting to estimate the impact of these additional accelerations on the relative dynamics between two or more satellites and verify whether these terms manage to destroy the relative motion within reasonable time. To that end, observe that the gravitational potential of the Earth up to a certain order, e.g., the fifth,

reads as

$$U(R,\Theta,\phi) = \frac{\mu_\oplus}{R}\left\{1 - \sum_{l=2}^{\infty} J_l \left(\frac{R_\oplus}{R}\right)^l P_l(\sin\Theta) + \ldots \right. \tag{6.2}$$

$$\left. \sum_{l=2}^{\infty}\sum_{m=1}^{l}\left(\frac{R_\oplus}{R}\right)^l P_{lm}(\sin\Theta)\,\left[C_{lm}\cos(m\,\phi) - S_{lm}\sin(m\,\phi)\right]\right\}, \tag{6.3}$$

where P_{lm} are the associated Legendre functions satisfying the differential equation

$$P_{lm}(\sin\Theta) = (1-\sin^2\Theta)^{m/2}\,\frac{\mathrm{d}^m}{\mathrm{d}(\sin\Theta)^m}\,P_l(\sin\Theta). \tag{6.4}$$

C_{lm} and S_{lm} are the Stokes' coefficient and determine the strength of both tesseral ($l \neq m$) and sectorial ($l = m$) harmonics [38, 55, 108]. The values of the unnormalized Earth's coefficients used for the simulations are summarized in Table 6.1. We also note here that the acceleration and gravity gradient derived from the full 5×5 gravitational potential are obtained by means of the recursive formulae described by Cunningham in Ref. [25]. The advantage of this approach is that the acceleration is immediately expressed in Cartesian coordinates and only needs to be rotated in the reference frame of choice.

Table 6.1: Unormalized Earth coefficients used for the simulations. More values can be found in Ref. [80]

Coefficient	**Value**	$\times 10^x$	**Coefficient**	**Value**	$\times 10^x$
C_{21}	-2.414	-10	S_{21}	1.5431	-9
C_{22}	1.57446037456	-6	S_{22}	-9.03803806639	-7
C_{31}	2.19263852917	-6	S_{31}	2.68424890297	-7
C_{32}	3.08989206881	-7	S_{32}	-2.11437612437	-7
C_{33}	1.00548778064	-7	S_{33}	1.97222559006	-7
C_{41}	-5.08799360404	-7	S_{41}	-4.49144872839	-7
C_{42}	7.84175859844	-8	S_{42}	1.48177868296	-7
C_{43}	5.92099402629	-8	S_{43}	-1.20077667634	-8
C_{44}	-3.98407411766	-9	S_{44}	6.5257142537	-9
C_{51}	-5.31803015007603	-8	S_{51}	-8.0858694766073	-8
C_{52}	1.05587168390898	-7	S_{52}	-5.23291936216342	-8
C_{53}	-1.49300637492288	-8	S_{53}	-7.09734236889537	-9
C_{54}	-2.29930029012696	-9	S_{54}	3.86712335850938	-10
C_{55}	4.3082246205179	-10	S_{55}	-1.64818262628074	-9

6.1.2 Third-body Attraction

The gravitational perturbation due to a third attracting mass is given by

$$\boldsymbol{a}_{3rd} = \mu_3 \left(\frac{\boldsymbol{r}_{3,s}}{r_{3,s}^3} - \frac{\boldsymbol{r}_{3,b}}{r_{3,b}^3} \right), \tag{6.5}$$

where μ_3 is the gravitational parameter of the third body, $\boldsymbol{r}_{3,s}$ is its position vector with respect to the i-th spacecraft, and $\boldsymbol{r}_{3,b}$ is the position vector of the perturbing object with respect to the center of the primary body, i.e., either the Earth, (4179) Toutatis, or Phobos.

Since $\boldsymbol{r}_{3,s}$ can be rewritten as the difference $\boldsymbol{r}_{3,b} - \boldsymbol{r}$, where $\boldsymbol{r}$ is the position vector of the spacecraft with respect to the central body, only $\boldsymbol{r}_{3,b}$ needs to be computed. However, depending on the simulation scenario, two different approaches are adopted in this thesis. In the case of Earth formations, we consider the third-body acceleration due to the gravity of the Sun and the Moon, and model their position vectors in the geocentric inertial frame with a 0.1% - 1% level of accuracy using the fast approximations discussed in Section 3.3.2 of Ref. [78]. For the numerical simulations about (4179) Toutatis and Phobos, instead, the heliocentric orbit of the target body is calculated via two-body dynamics. Thus, if $\mathcal{H} = \{\odot, \hat{\boldsymbol{e}}_e, \hat{\boldsymbol{e}}_p, \hat{\boldsymbol{e}}_h\}$ is the perifocal frame of either (4179) Toutatis or Mars such that $\hat{\boldsymbol{e}}_e$ is constantly pointing towards perihelion, $\hat{\boldsymbol{e}}_h$ is aligned with the orbital angular momentum vector, and $\hat{\boldsymbol{e}}_p = \hat{\boldsymbol{e}}_h \times \hat{\boldsymbol{e}}_e$, then the coordinates of the central body with respect to the Sun can be simply expressed by

$$\boldsymbol{r}_{b,3} = -\boldsymbol{r}_{3,b} = \begin{bmatrix} R_b \cos\nu_b & R_b \sin\nu_b & 0 \end{bmatrix}^T, \tag{6.6}$$

where $R_b = a_b\,(1 - e_b^2)/(1 + e_b \cos\nu_b)$, and a_b, e_b, ν_b are the semi-major axis, eccentricity, and true anomaly of the target body, respectively.

6.1.3 Solar Radiation Pressure

Whenever illuminated by the Sun, any satellite in the formation is affected by SRP. Although high-fidelity models exist [74], the acceleration due to solar radiation pressure can be roughly

approximated via the *cannonball* model:

$$\boldsymbol{a}_{SRP} = -\frac{K_r}{r_{\odot,s}^3}\,\boldsymbol{r}_{\odot,s}, \qquad \text{with} \qquad K_r = \left(\frac{\Phi_\odot}{c}\right)\frac{C_{r,S/C}\,R_{AU}^2}{B_{S/C}}. \tag{6.7}$$

$\boldsymbol{r}_{\odot,s}$ is the relative position vector of the Sun with respect to the considered satellite, $R_{AU} = 149\,597\,871\,000$ m is the value of the astronomical unit, $\Phi_\odot = 1367$ W/m^2 is the solar irradiance, $c = 299\,792\,458$ m/s is the value of the speed of light, $C_{r,S/C}$ is the reflectivity coefficient, and $B_{S/C}$ is the mass to area ratio of the spacecraft. For the numerical simulations of this Chapter, it is assumed that all of the satellites in the formation share the same values of $C_{r,S/C} = 1.3$ and $B_{S/C} = 50$ kg/m^2. Also notice that $\boldsymbol{a}_{SRP}$ is always directed in the opposite direction of $\boldsymbol{r}_{\odot,s}$, whereas the magnitude a_{SRP} always scales as the inverse of the distance between the spacecraft and the Sun squared.

6.1.4 Atmospheric Drag

As a final source of perturbation, atmospheric drag is included in the robustness analysis for spacecraft formations in LEO so as to study the effects of the Earth's atmosphere on the relative dynamics. The classical formulation of the drag acceleration is described by many authors as

$$\boldsymbol{a}_{drag} = -\frac{1}{2}\,C_{d,S/C}\,\rho_{atm}\,\frac{v_{rel}}{B_{S/C}}\,\boldsymbol{v}_{rel} \tag{6.8}$$

where $BC = B_{S/C}/C_{d,S/C}$ is the ballistic coefficient of a satellite and depends on both its mass-to-cross sectional area ratio, $B_{S/C}$, and drag coefficient, $C_{d,S/C} = 2.1$. Furthermore, if $\boldsymbol{\omega}_\oplus = \omega_\oplus\,\hat{\boldsymbol{e}}_3 = 7.292115 \times 10^{-5}\,\hat{\boldsymbol{e}}_3$ (rad/s) is the Earth's spin rate, one finds that the velocity of a satellite relative to the Earth's atmosphere is

$$\boldsymbol{v}_{rel} = \boldsymbol{v} - \boldsymbol{w}_\oplus \times \boldsymbol{r}, \tag{6.9}$$

where $\boldsymbol{r}$ and $\boldsymbol{v}$ are the position and velocity vector of the spacecraft, respectively. Lastly, ρ_{atm} is the atmospheric density, which can be assumed to change exponentially with the altitude h as according to

$$\rho_{atm} \simeq \rho_{atm,0}\,e^{-\dfrac{h-h_0}{H}}. \tag{6.10}$$

In this thesis, $\rho_{atm,0} = 6.967 \times 10^{-13}$ kg/m^3 and $h_0 = 500$ km are the reference values for the density and altitude of the spacecraft, respectively, whereas the scale factor H is specified by $H = 63.822$ km as suggested in Ref. [108].

6.2 LEO Formations

We now start our analysis by investigating the robustness of the spacecraft formations in LEO generated with the revised GMOS algorithm. The unperturbed case was shown in Fig. 4.21 – 4.22 and proved that bounded relative motion can indeed be established about the Earth while placing multiple satellites on the surface of quasi-periodic invariant HP tori (Fig. 4.17(b)). Differently from Section 4.4, we now integrate the initial conditions of the satellites after including atmospheric drag, solar radiation pressure, luni-solar third body attraction, and sectorial/tesseral harmonics to the equations of motion (6.1).

As shown in Fig. 6.1, the inclusion of these additional forces results in secular drifts that tend to destroy spacecraft formations in LEO very quickly. Specifically, it is found that atmospheric drag has the most significant impact on the relative dynamics of spacecraft at these altitudes due to the large differences in the nodal and sidereal periods of the vehicles introduced by this perturbation (Fig. 6.2). It is also worth noting that all of the other perturbations have minor effects on the relative trajectory, with luni-solar attraction, solar radiation pressure, and C_{22} effects causing deviations of only a few kilometers per month in the radial and along-track directions. This result suggests that spacecraft formations being initialized with the revised GMOS algorithm may actually survive at higher altitudes where the effects of atmospheric drag become negligible.

6.3 MEO & GEO Formations

We now consider the case of a chief and a deputy satellite being initialized in MEO and GEO as in Fig. 4.26 and 4.27. Fig. 6.3 and 6.4 display the relative motion and periods of a MEO formation under the effects of an asymmetric gravity field, SRP, and luni-solar attraction. Similarly, Fig. 6.5 and 6.6 illustrate the same quantities at geostationary altitudes.

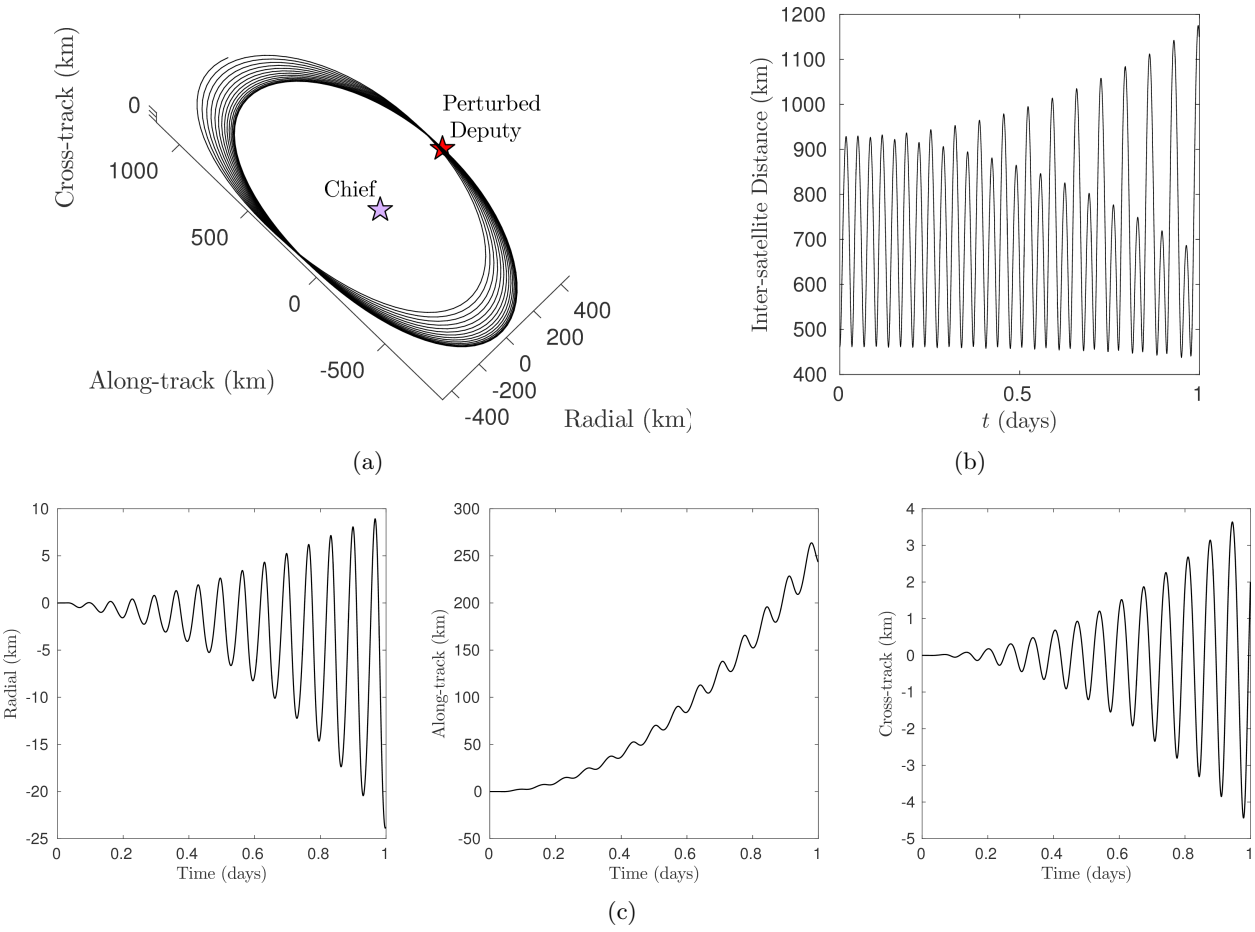

Figure 6.1: LEO formations under luni-solar, atmospheric drag, SRP, and asymmetric gravitational perturbations over one day. a) Relative trajectory in the LHLV frame of the chief. b) Inter-satellite distance over one day. c) Differences in radial, along-track, and cross-track directions with respect to the unperturbed case.

It is observed that the gravitational attractions of the Sun and the Moon are the dominant forces at these orbital regimes. Most notably, these sources of perturbations create a relative difference between the nodal periods of the two satellites that cause them to slowly drift apart in the radial and along-track directions. After one month, the total drift from the unperturbed case can be quantified in tens and hundreds of kilometers for the MEO and GEO cases, respectively. Therefore, it seems reasonable to maintain the spacecraft in the formation with only a few burns per month and without a significant amount of fuel.

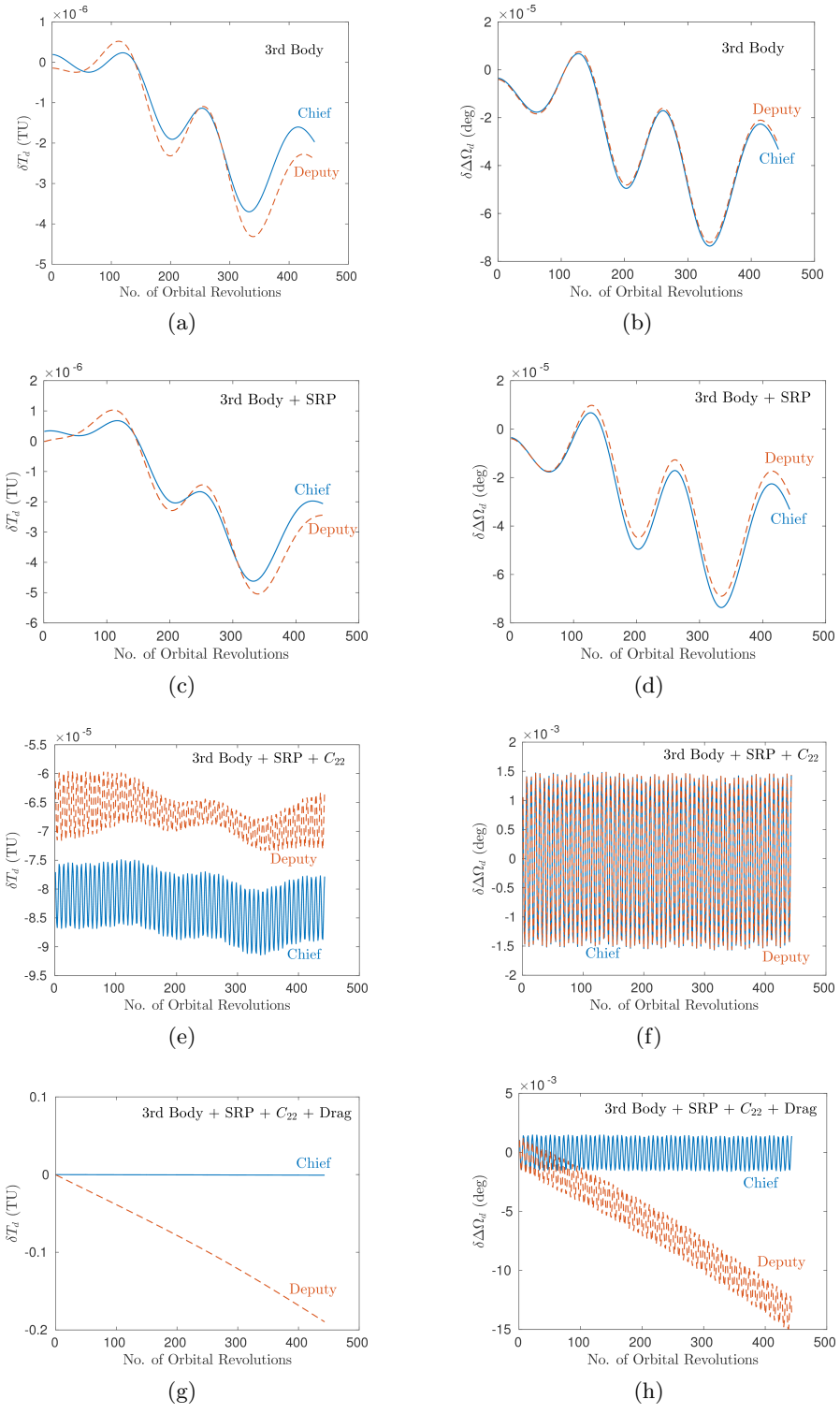

Figure 6.2: Monthly changes in the nodal and sideresiderealal periods of two satellite in a LEO formation due to external perturbations. a) - b) luni-solar third body attraction. c) - d) luni-solar plus SRP. e) - f) luni-solar plus SRP and spherical harmonics coefficients. g) - h) drag included.

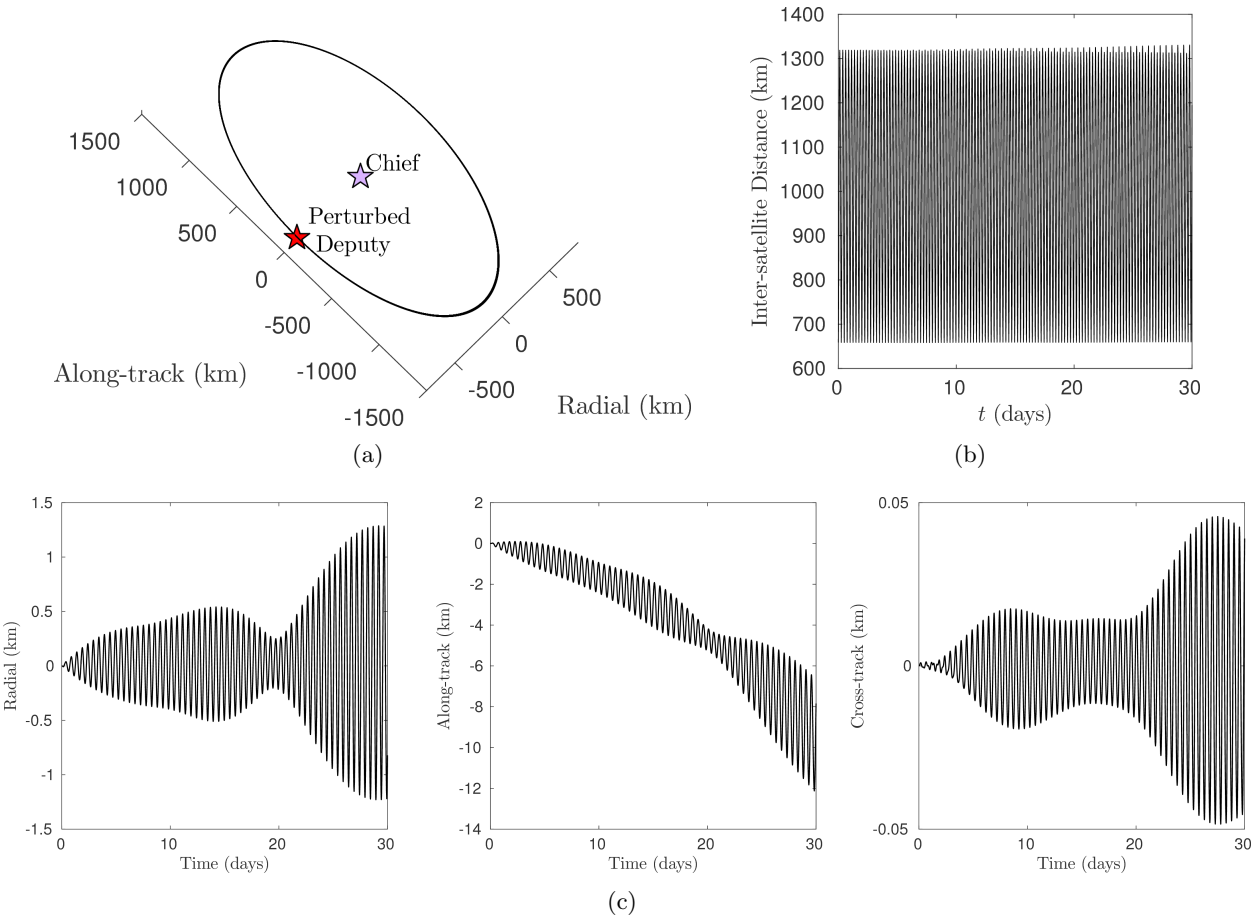

Figure 6.3: MEO formations under luni-solar attraction, SRP, and asymmetric gravitational perturbations over one month. a) Relative trajectory in the LHLV frame of the chief. b) Inter-satellite distance over one month. c) Differences in radial, along-track, and cross-track directions with respect to the unperturbed case.

6.4 (4179) Toutatis Formations

Moving beyond Earth's orbit, let us now consider a formation of two satellites being deployed on the three-dimensional quasi-periodic invariant torus of Fig. 5.14. Recall that the three-dimensional manifold has been computed in the principal axes frame of (4179) Toutatis while using a constant density polyhedron model to simulate its gravitational attraction. Meanwhile, Jacobi's elliptic functions have been used to evaluate the analytical solutions of Euler's equations and account for the complex rotational state of the small body. This leaves us with external perturbations that mostly depends on the presence of the Sun and its activity.

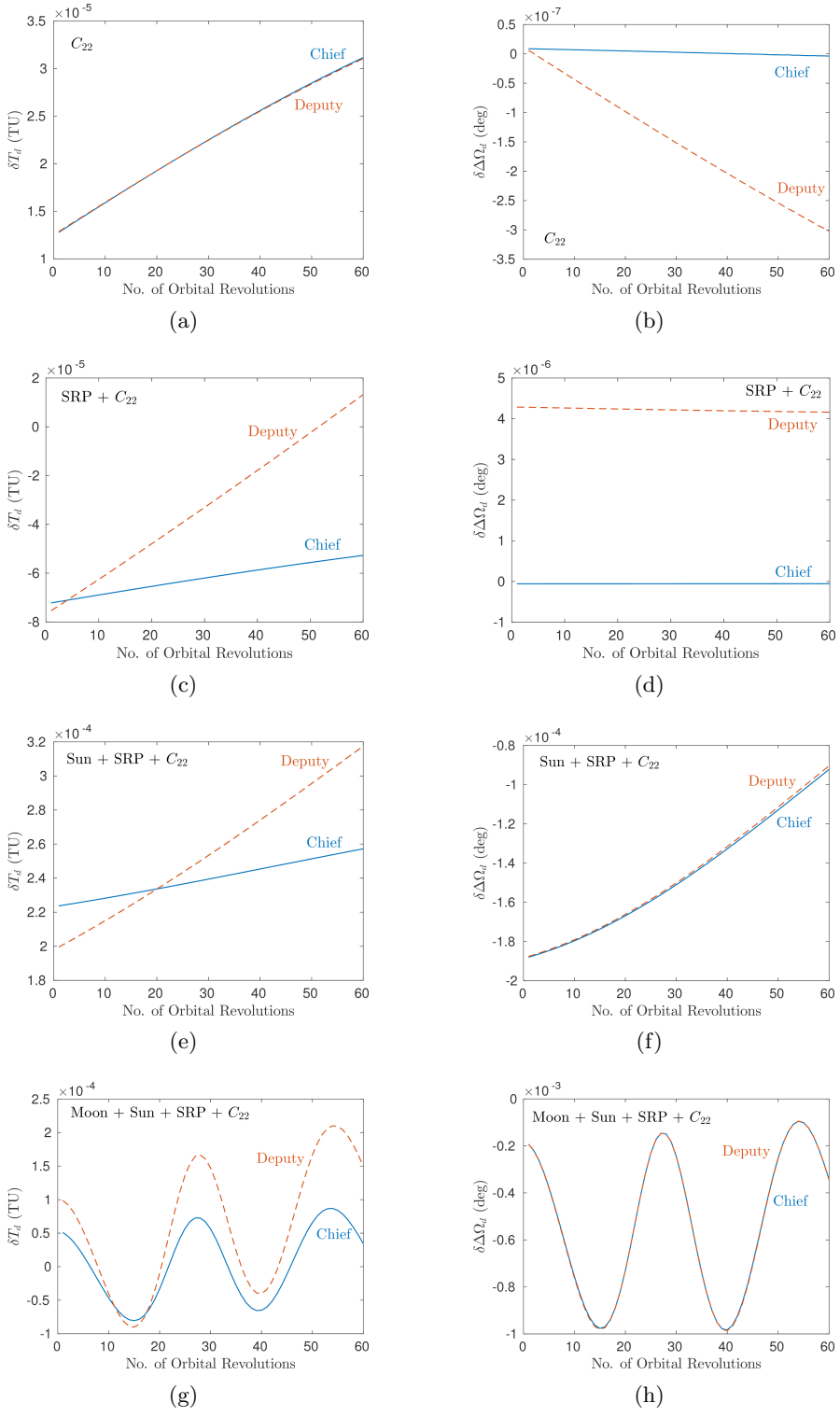

Figure 6.4: Monthly changes in the nodal and sidereal periods of two satellite in a MEO formation due to external perturbations. a) - b) spherical harmonics coefficients. c) - d) spherical harmonics plus SRP. e) - f) spherical harmonics plus SRP and solar gravity. g) - h) Moon gravity included.

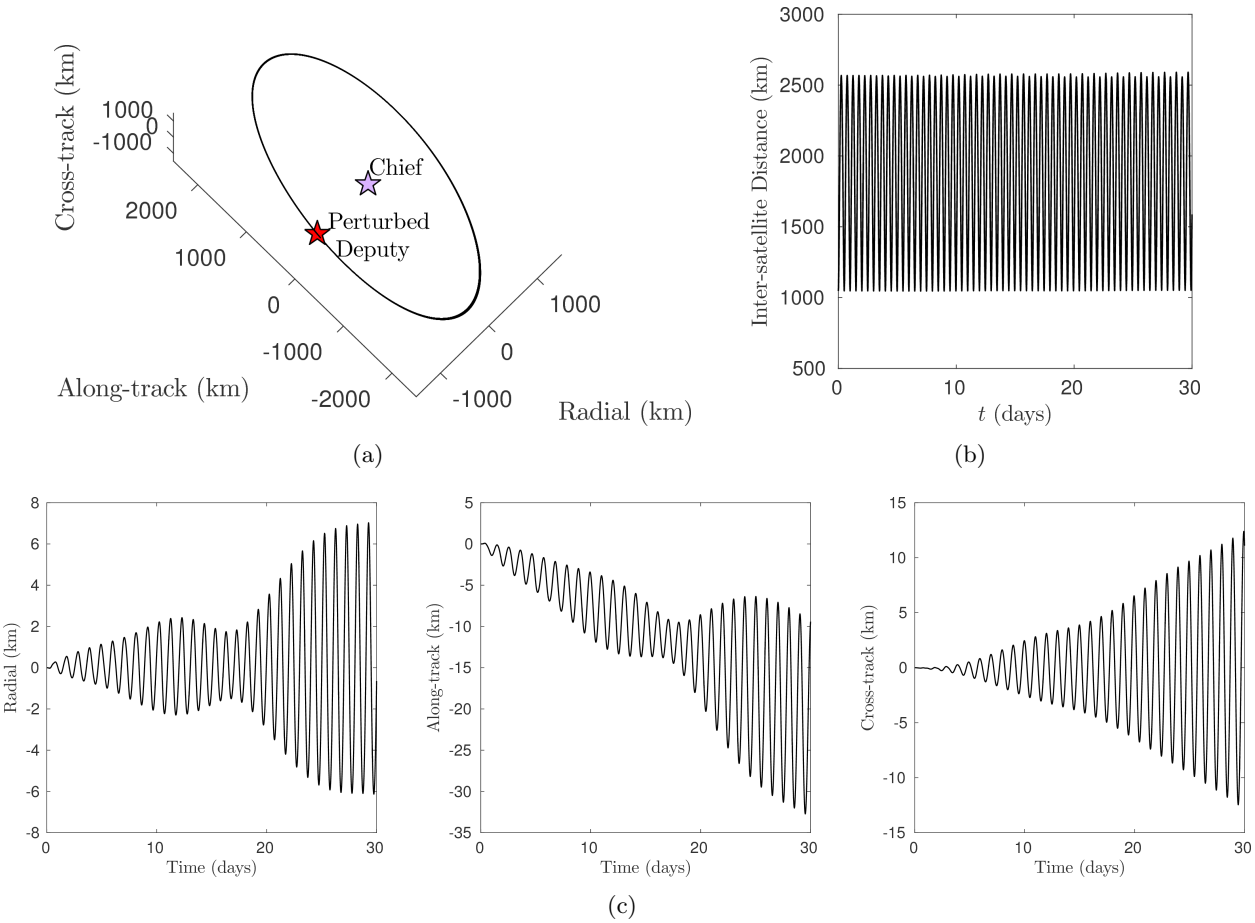

Figure 6.5: GEO formations under luni-solar attraction, SRP, and asymmetric gravitational perturbations over one month. a) Relative trajectory in the LHLV frame of the chief. b) Inter-satellite distance over one month. c) Differences in radial, along-track, and cross-track directions with respect to the unperturbed case.

For example, Fig. 6.7 shows the equivalent of the bounded relative trajectory illustrated in Fig. 5.15 after including the Sun's third body attraction and solar radiation pressure to the equations of motion (5.15). The relative position vector of the Sun as seen from the center of the asteroid is found via (6.6) with $a_b = 2.5445$ AU and $e_b = 0.6241$ as the semi-major axis and eccentricity values produced by NASA JPL's HORIZON on Nov, 10th, 1992 at 1:42:05 UTC [79]. It is also found that the asteroid's inclination, RAAN, argument of perihelion, and mean anomaly at this epoch correspond to $i_b = 0.4481$ deg, $\Omega_b = 125.1982$ deg, $\omega_b = 277.9992$ deg, and $M_b = 359.1509$ deg, respectively. This information allows to correctly build the direction cosine

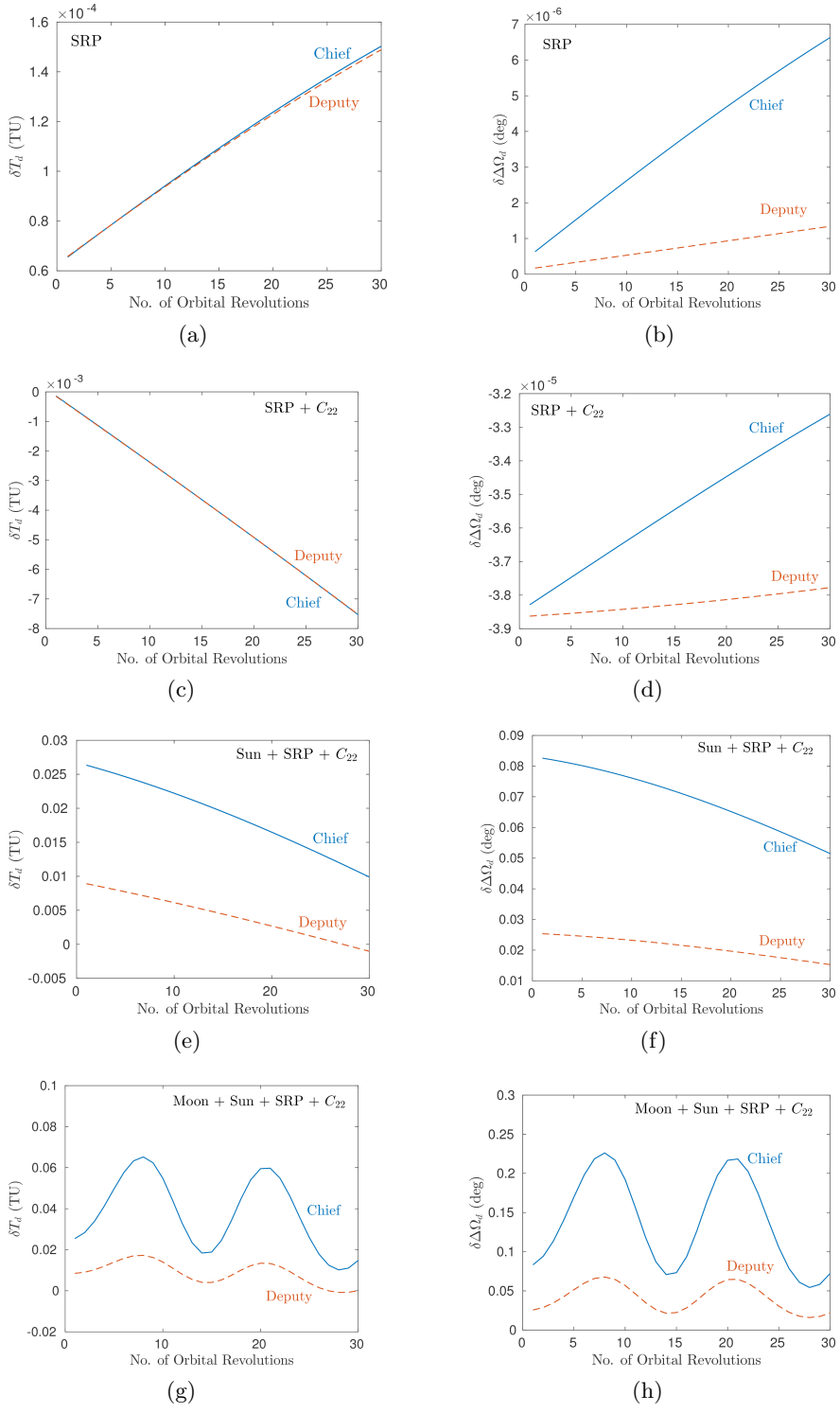

Figure 6.6: Monthly changes in the nodal and sidereal periods of two satellite in a GEO formation due to external perturbations. a) - b) spherical harmonics coefficients. c) - d) spherical harmonics plus SRP. e) - f) spherical harmonics plus SRP and solar gravity. g) - h) Moon gravity included.

matrix that rotates from the perifocal frame to the BCI frame of (4179) Toutatis. From there, the position of the vector of the Sun can be expressed in BCF frame components via $\boldsymbol{r}^{\mathcal{B}}_{\odot,c} = [\mathcal{B}\mathcal{N}]\,\boldsymbol{r}^{\mathcal{N}}_{\odot,c}$, where $\mathcal{B}$ is the body-fixed frame of the asteroid defined in Sec. 5.3 and

$$\begin{aligned}[\mathcal{B}\mathcal{N}] &= R_3(\gamma)\,R_1(\beta)\,R_3(\alpha), \\ &= \begin{bmatrix} \cos\gamma & \sin\gamma & 0 \\ -\sin\gamma & \cos\gamma & 0 \\ 0 & 0 & 1 \end{bmatrix} \begin{bmatrix} 1 & 0 & 0 \\ 0 & \cos\beta & \sin\beta \\ 0 & -\sin\beta & \cos\beta \end{bmatrix} \begin{bmatrix} \cos\alpha & \sin\alpha & 0 \\ -\sin\alpha & \cos\alpha & 0 \\ 0 & 0 & 1 \end{bmatrix}\end{aligned} \tag{6.11}$$

is the rotation matrix obtained from the 3-1-3 sequence of Euler's angles $\boldsymbol{\alpha} = \begin{bmatrix} \alpha, & \beta, & \gamma \end{bmatrix}^T$ adopted in Ref. [105] & [117]. Following the same references, the values of the Euler's angles $\boldsymbol{\alpha}$ and the body's angular momentum vector $\boldsymbol{\Omega}$ are generated through the numerical integration of

$$\dot{\boldsymbol{\alpha}} = \frac{1}{\sin\beta} \begin{bmatrix} \sin\gamma & \cos\gamma & 0 \\ \cos\gamma\,\sin\beta & -\sin\gamma\,\sin\beta & 0 \\ -\sin\gamma\,\cos\beta & -\cos\gamma\,\cos\beta & \sin\beta \end{bmatrix} \boldsymbol{\Omega}, \tag{6.12}$$

and

$$\dot{\boldsymbol{\Omega}} = \boldsymbol{I}^{-1}\left(-\boldsymbol{\Omega} \times \boldsymbol{I}\,\boldsymbol{\Omega} + \boldsymbol{L}_{\odot}\right) \tag{6.13}$$

with $\alpha = -160.3761$ (deg), $\beta = 143.0380$ (deg), $\gamma = -30.1492$ (deg), $\Omega_x = 98.9717$ (deg/day), $\Omega_y = 0.0$ (deg/day), and $\Omega_z = 36.1577$ (deg/day) as the initial conditions. $\boldsymbol{I}$ is the inertia matrix defined in Chapter 5, whereas $\boldsymbol{L} = \dfrac{\mu_{\odot}}{r^5_{\odot,c}}\,\boldsymbol{r}_{\odot,c} \times \boldsymbol{I}\,\boldsymbol{r}_{\odot,c}$ is the solar torque acting on Toutatis. We do not model the gravitational force and torque generated by the Earth, even though the selected epoch is close to the Earth flyby occurred in December 1992. The interested reader may find detailed discussions of these and subsequent close encounters with the Earth in Ref. [87, 88].

Differently from those papers, our goal is to assess the impact of solar radiation pressure and Sun third body attraction on the relative dynamics between a chief and a deputy spacecraft. It is found that SRP is the major source of perturbation as its magnitude is 1% circa of the gravitational attraction exerted by the small body. Because of this, both of the satellites tend

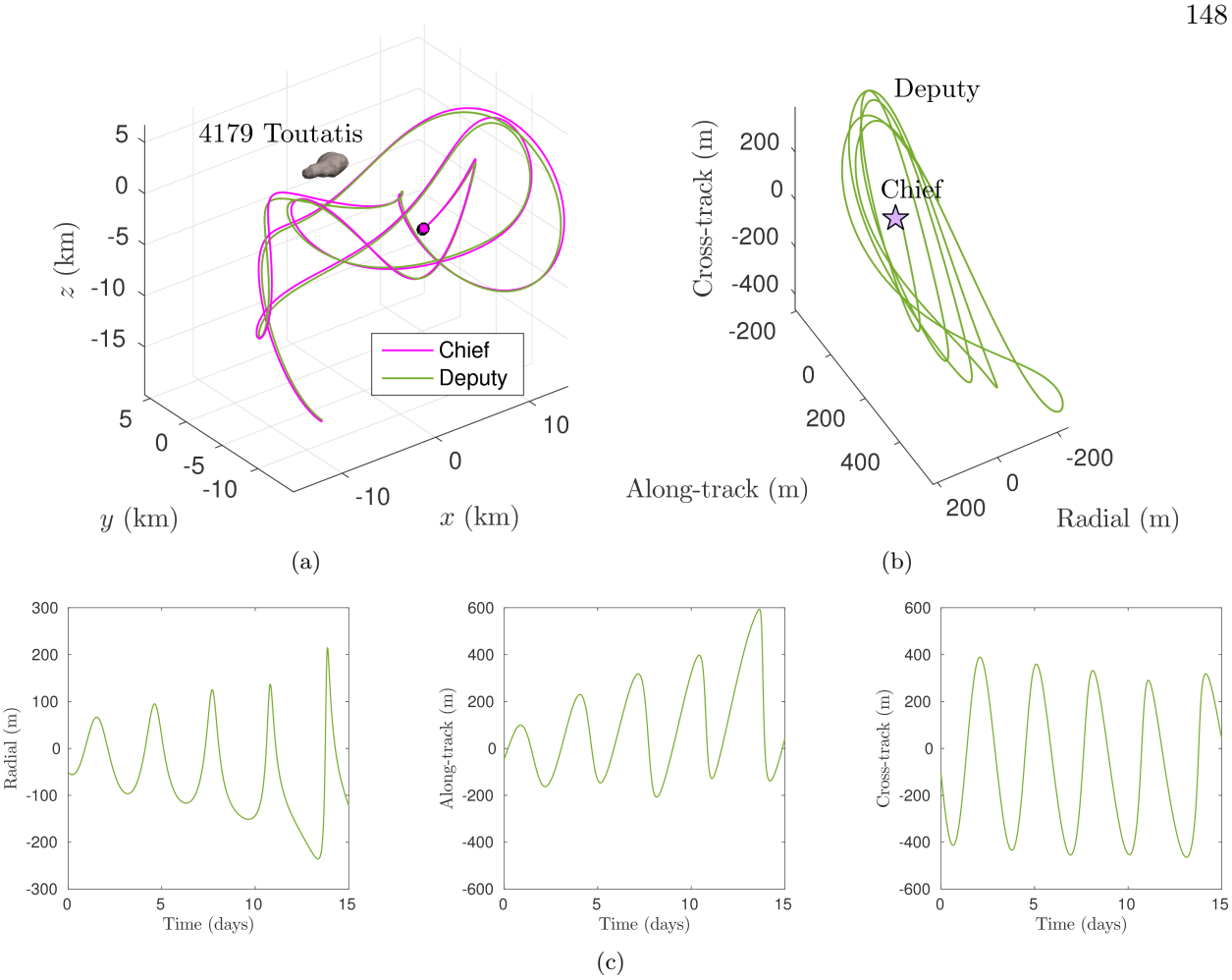

Figure 6.7: Perturbed relative motion between a chief on a 1:1 direct periodic orbit and a deputy on the surface of a three-dimensional torus about the complex rotator (4179) Toutatis. a) Satellite orbits in the body-fixed frame. b) Relative trajectory in the LVLH frame of the chief. c) Inter-satellite distance over two weeks.

to quickly deviate from their unperturbed trajectories and separate from each other in less than a month. Conversely, only a tiny fraction of this drift seems to be caused by solar gravity as the magnitude of this perturbation turns out to be two-to-three orders of magnitude smaller than (6.7). Numerical simulations prove that, with the gravity of the Sun as the only perturbation, the two satellites would remain within reasonable distances from each other for more than a month. Accordingly, future designs of spacecraft formations about (4179) Toutatis should focus on adding SRP to the equations of motion and potentially leverage the attitude of the spacecraft to control the relative positioning of the satellites within the cluster.

6.5 Phobos Formations

As a final example, let us consider the relative motion between a chief and a deputy spacecraft being initialized on the surface of the quasi-periodic invariant torus computed in the synodic frame of an eccentric Phobos around Mars (Sec. 5.4). According to previous research [116], the main perturbations in the vicinity of the small planetary satellite are caused by the non-spherical shape of Mars. Specifically, the gravitational accelerations due to the oblateness and ellipticity of the planet seem to impact the most on the relative dynamics of artificial satellites near the Martian moon. Including these terms, the equations of motion for a massless spacecraft near Phobos can be rewritten in the synodic reference frame of Chapter 5 as

$$\ddot{\boldsymbol{r}} + \dot{\boldsymbol{\Omega}} \times \boldsymbol{r} + 2\,\boldsymbol{\Omega} \times \boldsymbol{v} + \boldsymbol{\Omega} \times (\boldsymbol{\Omega} \times \boldsymbol{r}) = \nabla \mathcal{U} - \boldsymbol{a}_{P,\sigma'}, \tag{6.14}$$

where $\boldsymbol{r}$ and $\boldsymbol{v}$ are the position and velocity vectors of a satellite with respect to Phobos, respectively, $\boldsymbol{\Omega}$ is the angular velocity vector of the $\mathcal{S}$ frame as seen from an inertial coordinate system, and $\boldsymbol{a}_{P,\sigma'}$ is the gravitational acceleration of Phobos due to Mars. Furthermore, $\mathcal{U}$ is the gravitational potential of a massless spacecraft and is given by

$$\mathcal{U} = \frac{\mu_{\sigma'}}{R}\left[1 - J_2\left(\frac{R_{\sigma'}}{R}\right)^2 P_2(\sin\Theta) + \left(\frac{R_{\sigma'}}{R}\right)^2 P_{22}(\sin\Theta)\,\left(C_{22}\cos(2\,\phi) - S_{22}\sin(2\,\phi)\right)\right] + U(\boldsymbol{r}), \tag{6.15}$$

where $U(\boldsymbol{r})$ is the same as (5.5), $\mu_{\sigma'} = 4.282837 \times 10^4$ (km^3/s^2) is the gravitational parameter of Mars, R, Θ, ϕ are the spherical coordinates of the satellite with respect to Mars' body-fixed frame, and $J_2 = 1.960450 \times 10^{-3}$, $C_{22} = -5.463228 \times 10^{-5}$, $S_{22} = 3.158708 \times 10^{-5}$ as specified in Ref. [63]. It is also assumed that the position of Phobos with respect to Mars can be identified via its two-body dynamics. This enables some useful simplifications that do not degrade the accuracy of the numerical simulations over short intervals of time because of the small inclination and eccentricity of the Martian moon. For example, we assume that the angular velocity vector $\boldsymbol{\Omega}$ can be simply expressed as $\dot{\nu}_P\,\hat{\boldsymbol{z}}$, where $\dot{\nu}_P = h_P/r_P^2$, $h_P = \sqrt{\mu_{\sigma'}\,a_P\,(1-e_P^2)}$, and $r_P = a_P\,(1-e_P^2)/(1+e_P\,\cos\nu_P)$. $a_P = 9377.2$ km and $e_P = 0.0151$ are the semi-major axis and eccentricity of Phobos, respectively.

Lastly, we neglect second-order spin-orbit coupling effects that affect the libration angle of the planetary satellite as discussed in Ref. [30, 75].

Regardless of these assumptions, we find that the spacecraft of Fig. 6.8 are still bounded for more than a week in spite of the secular component appearing in the along-track separation between the two vehicles. Such a time frame would satisfy the operational requirements of past and future missions to Phobos [70, 82], and enable future investigations of the Martian moon based on distributed space systems.

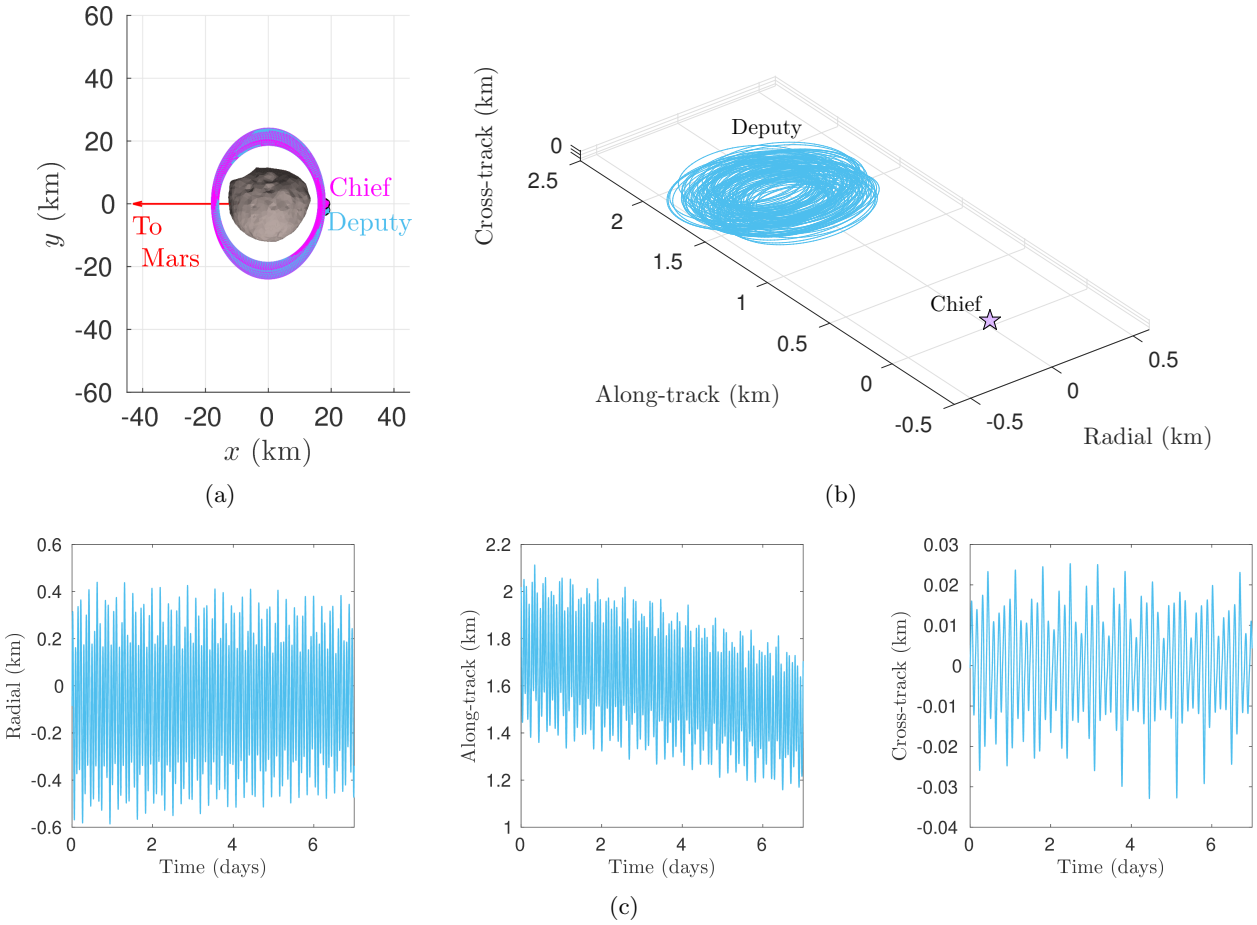

Figure 6.8: Perturbed relative dynamics between a chief and a deputy spacecraft near M1 Phobos. a) Satellite orbits in the sinodic reference frame $\mathcal{S}$. b) Relative trajectory in the LVLH frame of the chief. c) Inter-satellite distance over one weeks.

6.6 Conclusions

This Chapter presented a robustness analysis of the different initial conditions identified throughout this thesis to establish bounded relative motion at a variety of celestial bodies. Starting from spacecraft formations about an axisymmetric Earth, we simulated the effects of atmospheric drag, SRP, luni-solar perturbations, and tesseral plus sectorial harmonics up to the fifth order to quantify the error in the relative motion introduced by unmodeled dynamics. As it turns out, atmospheric drag seems to utterly degrade the quality of our initial conditions by causing a secular drift in the nodal period of the deputy spacecraft that destroys the formation within a few orbital revolutions. Such a behavior is not observed at higher altitudes, where luni-solar perturbations seem to have only minor effects on the relative distance between satellites in MEO and GEO formations.

Differently from these orbital regimes, it was found that SRP plays a major role in disturbing the orbital mechanics of vehicles near (4179) Toutatis. Specifically, solar radiation pressure causes the chief and deputy spacecraft to quickly deviate from the surface of the three-dimensional quasi-periodic invariant torus that was found to guarantee bounded relative motion in the unperturbed case. Because of that, the satellites in the formation tend to slowly drift apart from each other in the along-track direction and eventually separate in less than a month.

Lastly, the robustness of initial conditions yielding bounded relative motion about Phobos was tested under the effects of J_2, C_{22}, and S_{22} spherical harmonics coefficients derived from the non-spherical shape of Mars. A simplified model was implemented to include these additional perturbations in the equations of motion and assess their impact on the relative dynamics between the chief and deputy spacecraft of Fig. 5.20. Despite the limitations of the model, it was found that the two satellites remain in the close proximity of the Martian moon for more than a week and without significant deviations from the unperturbed relative orbit.

Chapter 7

Conclusions and Future Work

This dissertation investigates the benefits of using quasi-periodic invariant tori for formation flying applications. By explicitly calculating these manifolds, sets of initial conditions that naturally yield bounded relative motion are found and used to design bounded relative trajectories in a variety of astrodynamics problems such as the dynamics of satellites about axisymmetric bodies and the motion of mass particles near asteroids and small planetary satellites.

In preparation for our numerical investigations, we started our discussion by reviewing some of the tools available in DST for computing fixed points and periodic orbits. This helped us introduce some of the terminology that recurred throughout this thesis, and lay out the foundation for the numerical procedures of Chapter 3. For example, we introduced the predictor-corrector scheme that was later applied for numerical continuation, and formally defined quasi-periodic tori as the images of diffeomorphisms that satisfy the non-resonant conditions discussed in Sec. 2.6.

Chapter 3 of this thesis dealt with the numerical computation of quasi-periodic invariant tori and outlined some of the modern methodologies available in the literature for calculating these dynamical structures. Specifically, we distinguished between PDE and TPBVP approaches and proposed a simple numerical test for assessing the accuracy of the reviewed methodologies. By studying quasi-periodic motion in the body-fixed frame of the Earth, we identified GMOS as our method of investigation for future analysis. This conclusion was drawn not only from accuracy and runtime considerations, but also because the algorithm provides easy accessibility to the stability of quasi-periodic trajectories, can be recast into multiple-shooting or collocation form, and can be

successfully adapted to handle the numerical computation of three-dimensional tori.

Another important feature of GMOS is that it can be conveniently modified to incorporate additional constraints for fixing the external parameters of a dynamical system. This turned out to be a crucial aspect for the design of bounded relative orbits about axisymmetric bodies, where the dynamics of spacecraft can be fundamentally described by three periods. First is the nodal period, which is commonly defined as the time elapsed between two consecutive equatorial plane crossings at the ascending node. Second is the sidereal period, which depends on the drift in the right ascension of the ascending node per nodal period. Lastly, there is the anomalistic period, which is a function of the difference between the argument of pericenter of a satellite at consecutive equatorial plane crossings. In order to ensure bounded relative motion between a chief and a deputy spacecraft, at least two of their fundamental periods need to be matched on averaged. This condition was enforced by adding extra constraints to the GMOS algorithm and fix the averaged values of the nodal and sidereal periods of a torus. The resulting procedure, hereby referred to as the revised GMOS algorithm, manages to produce entire families of bounded relative orbits at a range of altitude and inclination values such as LEO, MEO, and GEO orbital regimes.

Moving beyond Earth's orbit, the fifth Chapter of this dissertation investigated the problem of establishing bounded relative motion about small irregular bodies. As a first example, we considered the asteroid (4179) Toutatis and build from 1:1 direct periodic orbits found in the literature to identify a whole family of three-dimensional quasi-periodic invariant tori. To the best of the author's knowledge, this was the first attempt to compute higher-dimensional tori about asteroids and the manifolds successfully gave initial conditions for bounded relative motion in spite of the irregular shape and complex rotational state of the target asteroid. Next, we considered the case of the Martian moon Phobos and applied GMOS to calculate the quasi-periodic invariant tori that populate the phase space when the eccentricity of the planetary satellite is taken into account. Once again, bounded relative trajectories were obtained by placing a chief and a deputy satellite on the surface of a quasi-periodic invariant torus found in a high-fidelity model of the orbital environment near Phobos. Specifically, we modeled the moon as a constant density polyhedron

with 2456 triangular facets and included the libration of the planetary satellite around Mars to simulate first-order spin-orbit coupling effects and improve the realism of our simulations.

The last Chapter of this dissertation covered the main sources of perturbation that have the potential to significantly impact on the relative dynamics of spacecraft near the Earth, (4179) Toutatis, and Phobos. Although atmospheric drag and solar radiation pressure were found to quickly destroy the formations in LEO and near Toutatis, luni-solar perturbations and SRP seem to have less of an impact on the relative dynamics in MEO and GEO. The same can be said for the J_2, C_{22}, and S_{22} harmonics of Mars near Phobos, giving us hope that quasi-periodic invariant tori could represent a robust design option for flying multiple vehicles around this object.

Moving forward, it is worth noting that all of the numerical simulations of Chapter 6 assumed perfect knowledge of the initial conditions of the chief and deputy spacecraft. Unfortunately, such an assumption is usually too optimistic due to navigation errors and the introduction of stochastic components in the states of the satellites. Accordingly, future research should be dealing with the development of guidance and control laws that mitigate the effects of navigation and perturbation errors. This topic seems particularly attractive for spacecraft formations near the Earth and Toutatis, where atmospheric drag and solar radiation pressure can be effectively leveraged to propellentless maneuver the satellites in the formation [29, 67, 9].

Another interesting idea to pursue would be the design of quasi-periodic invariant tori about asteroids with SRP in the equations of motion. Current research has already identified dynamical substitutes that replace certain equilibrium points with periodic orbits, and it seems feasible to further expand on this result by calculating the quasi-periodic trajectories that populate the center manifold around these periodic solutions [113].

Lastly, the design of bounded relative trajectories about axisymmetric bodies warrants further investigation. In addition to trajectories at critical inclinations, we did not discuss the case of other periodic orbits that bifurcate from the pseudo-circular trajectories of Chapter 4. Yet, the study of other periodic and quasi-periodic solutions could open the door to new formation geometries and help us better organize the system dynamics. It would also be interesting to further explore the

limits of the revised GMOS algorithm by trying to design bounded relative orbits about arbitrary trajectories. While this poses some numerical challenges, ongoing research seems to suggest the validity of our technique even for highly eccentric orbits. If that is the case, a ubiquitous design strategy for spacecraft formations about the Earth would be possible and not far from reality.

Bibliography

[1] K. T. Alfriend, S. Vadali, P. Gurfil, J. P. How, and L. S. Breger. Spacecraft Formation Flying: Dynamics, Control, and Navigation. Butterworth-Heinemamn Oxford, 2009.

[2] V. I. Arnol'd and A. Avez. Ergodic Problems of Classical Mechancis. Princeton University Press, 1968.

[3] V. I. Arnold, V. V. Kozlov, and A. I. Neishtadt. Mathematical Aspects of Classical and Celestial Mechanics. Springer-Verlag Berlin, 3rd edition, 2006.

[4] U. M. Ascher, R. M. Mattheij, and R. D. Russell. Numerical Solution of Boundary Value Problems for Ordinary Differential Equations. SIAM Philadelphia, 1995.

[5] B. T. Barden and K. C. Howell. Formation flying in the vicinity of libration point orbits. paper AAS 98-169 presented at the AAS/AIAA Space Flight Mechanics Meeting, Monterey, CA, 1998.

[6] N. Baresi and D. J. Scheeres. Bounded relative motion under zonal harmonics perturbations. Celestial Mechanics and Dynamical Astronomy, 127(4):527–548, 2016.

[7] N. Baresi and D. J. Scheeres. Quasi-periodic invariant tori of time-periodic dynamical systems: Applications to small body exploration. paper IAC-16.C1.7.4x32824 presented at the 67th International Astronautical Congress, Guadalajara, Mexico, 2016.

[8] N. Baresi, D. J. Scheeres, and H. Schaub. Bounded relative orbits about asteroids for formation flying and applications. Acta Astronautica, 123:364–375, June–July 2016.

[9] O. Ben-Yaacov and P. Gurfil. Long-term cluster flight of multiple satellites using differential drag. Journal of Guidance, Control, and Dynamics, 36(6):1731–1740, 2013.

[10] P. Binetruy, P. Bouyer, M. Cruise, R. Genzel, M. Kasevich, B. Klipstein, G. Muller, M. Perryman, B. Schutz, and S. Vitale. The esa-l3 gravitational wave mission. Technical report, ESA, 2016.

[11] L. Blitzer. Nodal period of an earth satellite. AIAA Journal, 2(8):1459–1460, 1964.

[12] T. A. Bray and C.L. Gouclas. Doubly symmetric orbits about the collinear lagrangian points. The Astronomical Journal, 72, 1967.

[13] L. Breger, J. P. How, and K. T. Alfriend. Partial j2-invariance for spacecraft formations. paper AIAA 2006-6585 presented at the AIAA Guidance, Navigation, and Control Conference, Keystone, CO, 2006.

[14] H. W. Broer, G. B. Huitema, and M. B. Sevryuk. Quasi-periodic Motions in Families of Dynamical Systems. Springer-Verlag Berlin, 1996.

[15] S. B. Broschart, G. Lantoine, and D. J. Grebow. Quasi-terminator orbits near primitive bodies. Celestial Mechanics and Dynamical Astronomy, 120(2):195–215, oct 2014.

[16] R. A. Broucke. Stability of periodic orbits in the elliptic, restricted three-body problem. AIAA Journal, 7(6):1003–1009, 1969.

[17] R. A. Broucke. Numerical integration of periodic orbits in the main problem of artificial satellite theory. Celestial Mechanics and Dynamical Astronomy, 58:99–123, 1994.

[18] D. Brouwer. Solution of the problem of artificial satellite theory without drag. The Astronomical Journal, 64:378, 1959.

[19] O. Brown, P. Eremenko, and B. A. Hamilton. Fractionated space architectures: A vision for responsive space. presented at the 4th Responsive Space Conference, Los Angeles, CA, 2006.

[20] E. Castella and À. Jorba. On the vertical families of two-dimensional tori near the triangular points of the bicircular problem. Celestial Mechanics and Dynamical Astronomy, 76(1):35—-54, 2000.

[21] C. Chao. Applied Orbit Perturbation and Maintenance. American Institute of Aeronautics and Astronautics, Reston, VA, 2005.

[22] J. Chu, J. Guo, and E. Gill. Long-term passive distance-bounded relative motion in the presence of j2 perturbations. Celestial Mechanics and Dynamical Astronomy, 121(4):385–413, 2015.

[23] W. H. Clohessy and R. S. Wiltshire. Terminal guidance system for satellite rendezvous. Journal of Aerospace Sciences, 27(9):653–658, 1960.

[24] J. Cronin. Some periodic solutions of a four-body problem. Icarus, 3:423–428, 1964.

[25] L. Cunningham. On the computation of the spherical harmonic terms needed during the numerical integration of the orbital notion of an artificial satellite. Celestial Mechanics, 2:207—-216, 1970.

[26] S. D' Amico, J. Ardaens, and R. Larsson. Spaceborne autonomous formation-flying experiment on the prisma mission. Journal of Guidance, Control, and Dynamics, 35(3):834–850, 2012.

[27] T. A. Davis. Direct Methods for Sparse Linear Systems. SIAM Philadelphia, 2006.

[28] R. De la Llave. A tutorial on kam theory. Proceedings of Symposia in Pure Mathematics, 69:175–296, 1998.

[29] L. Dell'Elce. Satellite orbits in the atmosphere: Uncertainty quantification, propagation, and optimal control. PhD thesis, University of Liege, 2015.

[30] L. Dell'Elce, N. Baresi, S. P. Naidu, L. A. M. Benner, and D. J. Scheeres. Numerical investigation of the dynamical environment of 65803 didymos. Advances in Space Research, 59:1304–1320, 2017.

[31] A. Dobrovolskis and J. A Burns. Life near the roche limit : Behavior of ejecta from satellites close to planets. Icarus, 42:422–441, 1980.

[32] E. J. Doedel. Auto: A program for the automatic bifurcation analysis of autonomous systems. Congressus Numerantium, 30:265–284, 1981.

[33] E. J. Doedel, H. B. Keller, and J. Kernevez. Numerical analysis and control of bifurcation problems (ii): Bifurcation in infinite dimensions. International Journal of Bifurcation and Chaos, 01(04):745, 1991.

[34] E. J. Doedel, V. A. Romanov, R. C. Paffenroth, H. B. Keller, D. J. Dichmann, J. Galán-Vioque, and A. Vanderbauwhede. Elemental periodic orbits associated with the libration points in the circular restricted 3-body problem. International Journal of Bifurcation and Chaos, 17(8):2625–2677, 2007.

[35] X. Duan and P. M. Bainum. Design of Spacecraft Formation Flying Orbits. Advances in Astronautical Sciences, 116:1379–1399, 2004.

[36] M. Duering, M. Vasile, and M. Landgraf. Uncontrolled spacecraft formations on two-dimensional invariant tori. Pasadena, CA, 2012. presented at the 23rd International Symposium on Spaceflight Dynamics, Pasadena, CA.

[37] T. C. Duxbury, A. V. Zakharov, H. Hoffmann, and E. A. Guinness. Spacecraft exploration of phobos and deimos. Planetary and Space Science, 102:9–17, 2014.

[38] E. Fantino and S. Casotto. Methods of harmonic synthesis for global geopotential models and their first-, second- and third-order gradients. Journal of Geodesy, 83(7):595–619, 2009.

[39] R. Farquhar and A. A. Kamel. Quasi-periodic orbits about the translunar libration point. Celestial Mechanics, 7(4):458–473, 1973.

[40] A. Farres and Á. Jorba. Orbital dynamics of a solar sail near l1 and l2 in the elliptic hill problem. Naples, Italy, 2012. paper IAC-12.C1.6.4 presented at the 63rd International Astronautical Congress, Naples, Italy.

[41] R.W. Gaskell. Gaskell phobos shape model v1.0. v01-sa-visa/visb-5-phobosshape-v1.0, 2011.

[42] G. Gómez, J. Llibre, R. Martinez, and C. Simó. Dynamics and Mission Design near Libration Points, Vol. 1. Fundamentals: the Case of Collinear Libration Points. World Scientific, 2001.

[43] G. Gómez, J. Masdemont, and C. Simó. Quasi-halo orbits associated with libration points. Journal of the Astronautical Sciences, 46(2):135–176, 1998.

[44] G. Gómez and J. Mondelo. The dynamics around the collinear equilibrium points of the rtbp. Physica D: Nonlinear Phenomena, 157(4):283–321, 2001.

[45] S. Gong, J. Li, and H. BaoYin. Formation flying solar-sail gravity tractors in displaced orbit for towing near-earth asteroids. Celestial Mechanics and Dynamical Astronomy, 105(1-3):159–177, nov 2009.

[46] P. Gurfil. Relative motion between elliptic orbits: Generalized boundedness conditions and optimal formationkeeping. Journal of Guidance, Control, and Dynamics, 28(4):761–767, 2005.

[47] A. Haro and R. de la Llave. A parameterization method for the computation of invariant tori and their whiskers in quasi-periodic maps: Explorations and mechanisms for the breakdown of hyperbolicity. SIAM Journal on Applied Dynamical Systems, 6(1):142–207, 2007.

[48] M. E. Henderson. Multiple parameter continuation: Computing implicitly defined k-manifolds. International Journal of Bifurcation and Chaos, 12(03):451–476, 2002.

[49] M. Henon. Numerical exploration of the restricted problem, v. Astronomy and Astrophysics, 1:223–238, 1969.

[50] M. Henon. Generating families in the restricted three-body problem. Springer-Verlag Berlin, 1997.

[51] K. C. Howell. Three-dimensional periodic halo orbits. Celestial Mechanics, 32(1):53–71, 1984.

[52] W. Hu and D. J. Scheeres. Spacecraft motion about slowly rotating asteroids. Journal of Guidance, Control, and Dynamics, 25(4):765–775, jul 2002.

[53] R. S. Hudson and S. J. Ostro. Shape and non-principal axis spin state of asteroid 4179 toutatis. Science, 270(5233):84–86, 1995.

[54] S. P. Huges. Formation tetrahedron design for phase i of the magnetospheric multiscale mission. Technical report, NASA Technical Reports Server, 2003.

[55] B. Jones. Efficient Models for the Evaluation and Estimation of the Gravity Field. PhD thesis, University of Colorado Boulder, 2010.

[56] Á. Jorba. Numerical computation of the normal behaviour of invariant curves of n-dimensional maps. Nonlinearity, 14:943–976, 2001.

[57] À. Jorba and J. Masdemont. Dynamics in the center manifold of the collinear points of the restricted three-body problem. Physica D: Nonlinear Phenomena, 132:189–213, 1999.

[58] A. Jorba and E. Olmedo. On the computation of reducible invarint tori on a parallel computer. SIAM Journal on Applied Dynamical Systems, 8(4):1382—-1404, 2009.

[59] À. Jorba and J. Villanueva. On the persistence of lower dimensional invariant tori under quasi-periodic perturbaitons. Journal of Nonlinear Science, 7(5):427—-473, 1997.

[60] A. Katok and B. Hasselblatt. Modern Theory of Dynamical Systems. Cambridge University Press, 1996.

[61] H. B. Keller. Numerical solution of bifurcation and nonlinear eigenvalue problems. Applications of Bifurcation Theory, pages 359–384, 1977.

[62] E. Kolemen, N. J. Kasdin, and P. Gurfil. Multiple poincaré sections method for finding the quasi-periodic orbits of the restricted three-body problem. Celestial Mechanics and Dynamical Astronomy, 112(1):47–74, jan 2012.

[63] A. S. Konopliv, S. W. Asmar, W. M. Folkner, Ö. Karatekin, D. C. Nunes, S. E. Smrekar, C. F. Yoder, and M. T. Zuber. Mars high resolution gravity fields from mro, mars seasonal gravity, and other dynamical parameters. Icarus, 211:401–428, 2011.

[64] W. S. Koon, J. E. Marsden, J. Masdemont, and R. M. Murray. J2 dynamics and formation flight. paper AIAA 2001-4090 presented at the AIAA Guidance, Navigation, and Control Conference and Exhibit, Montreal, Canada, 2001.

[65] Y. Kozai. Motion of a particle with critical inclination in the gravitational field of a spheroid. Smithsonian Contribution to Astrophysics, 5:53, 1961.

[66] G. Krieger, M. Zink, M. Bachmann, B. Brautigam, D. Schulze, M. Martone, P. Rizzoli, U. Steinbrecher, J. Walter Antony, F. De Zan, I. Hajnsek, K. Papathanassiou, F. Kugler, M. Rodriguez Cassola, M. Younis, S. Baumgartner, P. Lopez-Dekker, P. Prats, and A. Moreira. Tandem-x: A radar interferometer with two formation-flying satellites. Acta Astronautica, 89:83–98, 2013.

[67] H. Li and T. Williams. Reconfiguration of sun-earth libration point formations using solar radiation pressure. Journal of Spacecraft and Rockets, 43(6):1328–1339, nov 2006.

[68] W. D. MacMillan. Dynamics of Rigid Bodies. Dover New York, 1960.

[69] C. Maddock, J. P. Sanchez Cuartielles, M. Vasile, and G. Radice. Comparison of single and multi-spacecraft configurations for nea deflection by solar sublimation. volume 886, pages 303–316. AIP Conference Proceedings, 2007.

[70] M. Y. Marov, V. S. Avduevsky, E. L. Akim, T. M. Eneev, R. S. Kremnev, S. D. Kulikov, K. M. Pichkhadze, G. A. Popov, and G. N. Rogovsky. Phobos-grunt : Russian sample return mission. Advances in Space Research, 33(12):2276–2280, 2004.

[71] V. Martinusi and P. Gurfil. Solutions and periodicity of satellite relative motion under even zonal harmonics perturbations. Celestial Mechanics and Dynamical Astronomy, 111(4):387–414, 2011.

[72] J. M. Maruskin. Introduction to Dynamical Systems and Geometric Mechanics. Solar Crest, 2012.

[73] J. H. Mathews and K. D. Fink. Numerical Methods using MATLAB. Pearson, Prentice Hall, Upper Saddle River, N. J., 4th edition, 2004.

[74] J. W. McMahon. An Analytical Theory for the Perturbative Effect of Solar Radiation Pressure on Natural and Artificial Satellites. PhD thesis, University of Colorado Boulder, 2011.

[75] J. W. McMahon and D. J Scheeres. Dynamic limits on planar libration-orbit coupling around an oblate primary. Celestial Mechanics and Dynamical Astronomy, 115(4):365–396, 2013.

[76] J. D. Meiss. Differential Dynamical Systems. SIAM, 2007.

[77] K. Meyer, G. Hall, and D. Offin. Introduction to Hamiltonian Dynamical Systems and the N-Body Problem. Springer, 2nd edition, 2010.

[78] O. Montenbruck and E. Gill. Satellite Orbits. Springer-Verlag Berlin, 2000.

[79] NASA. Nasa jpl's horizons.

[80] NASA. Nga/nasa egm96.

[81] C Neese. Ed. small body radar shape models v2.0. ear-a-5-ddr-radarshape-models-v2.0, 2004.

[82] Institute of Space and Astronautical Science. JAXA's Martian Moon eXplorer (MMX), 2017.

[83] Z. P. Olikara. Computation of Quasi-periodic Tori and Heteroclinic Connections in Astrodynamics using Collocation Techniques. PhD thesis, University of Colorado Boulder, 2016.

[84] Z. P. Olikara. Mapping connections between planar sun-earth-moon libration point orbits. paper AAS 17-516 presented at the 27th AAS/AIAA Space Flight Mechanics Meeting, San Antonio, TX, 2017.

[85] Z. P. Olikara and K. C. Howell. Computation of quasi-periodic invariant tori in the restricted three-body problem. paper AAS 10-120 presented at the 20th AAS/AIAA Space Flight Mechanics Meeting, San Diego, CA, 2010.

[86] Z. P. Olikara and D. J. Scheeres. Numerical method for computing quasi-periodic orbits and their stability in the restricted three-body problem. paper AAS 12-361 presented at the 2012 AIAA/AAS Astrodynamics Specialist Conference, Minneapolis, MN, 2012.

[87] S. J. Ostro, R. S. Hudson, R. F. Jurgens, K. D. Rosema, D. B. Campbell, D. K. Yeomans, J. F. Chandler, J. D. Giorgini, R. Winkler, R. Rose, S. D. Howard, M. A. Slade, P. Perillat, and I. I. Shapiro. Radar images of asteroid 4179 toutatis. Science, 270(5233):80–83, oct 1995.

[88] S. J. Ostro, R. S. Hudson, K. D. Rosema, J. D. Giorgini, R. F. Jurgens, D. K. Yeomans, P. W. Chodas, R. Winkler, R. Rose, D. Choate, R. A. Cormier, D. Kelley, R. Littlefair, L. A. M. Benner, M. L. Thomas, and M. A. Slade. Asteroid 4179 toutatis : 1996 radar observations. Icarus, 139:122–139, 1999.

[89] S. J. Ostro, J. Margot, L. A. M Benner, J. D. Giorgini, D. J. Scheeres, E. G. Fahnestock, S. B. Broschart, J. Bellerose, R. F. Jurgens, E. Jong, and S. Suzuki. Radar imaging of binary near-earth asteroid (66391) 1999 kw4. Science, 314(November):1276–1280, 2006.

[90] J. S. Parker. Low-energy ballistic lunar transfers. PhD thesis, University of Colorado Boulder, 2007.

[91] W. H. Press, S. A. Teukolsky, W. T. Vetterling, and B. P. Flannery. Numerical Recipes: The Art of Scientific Computing. Cambridge University Press, 3rd edition, sep 2007.

[92] D. L. Richardson and N. D. Cary. A uniformly valid solution for motion about the interior libration point of the perturbed elliptic-restricted problem. presented at the AAS/AIAA Astrodynamics Specialist Conference, Nassau, Bahamas, 1975.

[93] M. Sabatini, D. Izzo, and R. Bevilacqua. Special inclinations allowing minimal drift orbits for formation flying satellites. Journal of Guidance, Control, and Dynamics, 31(1):94–100, 2008.

[94] H. Schaub and K. T. Alfriend. J2 invariant relative orbits for spacecraft formations. Celestial Mechanics and Dynamical Astronomy, 79(2):77–95, 2001.

[95] H. Schaub and J. L. Junkins. Analytical Mechanics of Space Systems. American Institute of Aeronautics and Astronautics, Reston, VA, 3rd edition, 2014.

[96] D. J Scheeres. Dynamics about uniformly rotating triaxial ellipsoids: Applications to asteroids. Icarus, 110(2):225–238, 1994.

[97] D. J. Scheeres. Dynamics of orbits close to asteroid 4179 toutatis. Icarus, 132:53–79, 1998.

[98] D. J. Scheeres. Orbital Motion in Strongly Perturbed Environments. Springer-Verlag Berlin, 2012.

[99] F. Schilder, H. M. Osinga, and W. Vogt. Continuation of quasi-periodic invariant tori. SIAM Journal on Applied Dynamical Systems, 4(3):459–488, jan 2005.

[100] R. Seydel. Practical Bifurcation and Stability Analysis. Springer Science & Business Media, 2009.

[101] M. Shibata and A. Ichikawa. Orbital rendezvous and flyaround based on null controllability with vanishing energy. Journal of Guidance, Control, and Dynamics, 30(4):934–945, jul 2007.

[102] C. Simo, G. Gómez, À. Jorba, and J. Masdemont. The bicircular model near the triangular libration points of the rtbp. In From Newton to Chaos, pages 343—-370. Plenum Press, New York, 1995.

[103] V. Szebehely. Theory of Orbit. Elsevier, 1967.

[104] V. Szebehely and G. Giacaglia. On the elliptic restricted problem of three bodies. The Astronomical Journal, 69(3):230–235, 1964.

[105] Y. Takahashi, M. W. Busch, and D. J. Scheeres. Spin state and moment of inertia characterization of 4179 toutatis. The Astronomical Journal, 146(95), 2013.

[106] B. D. Tapley, S. Bettadpur, M. Watkins, and C. Reigber. The gravity recovery and climate experiment: Mission overview and early results. Geophysical Research Letters, 31(9):1–4, 2004.

[107] S. Vadali, H. Schaub, and K. Alfriend. Initial conditions and fuel-optimal control for formation flying of satellites. presented at the AIAA Guidance, Navigation, and Control Conference and Exhibit, Portland, OR, 1999.

[108] D. A. Vallado. Fundamentals of Astrodynamics and Applications. Microcosm Press, 4th edition, mar 2013.

[109] G. Voyatzis, I. Gkolias, and H. Varvoglis. The dynamics of the elliptic hill problem: Periodic orbits and stability regions. Celestial Mechanics and Dynamical Astronomy, 113(1):125–139, 2012.

[110] R. Walker, D. Binns, I. Carnelli, M. Kueppers, and A. Galvez. Cubesat opportunity payload inter-satellite network sensors (copins) on the esa asteroid impact mission (aim). 6th Interplanetary CubeSat Workshop, Cambridge, UK, 2017.

[111] R. A. Werner and D. J Scheeres. Exterior gravitation of a polyhedron derived and compared with harmonic and mascon gravitation representations of asteroid 4769 castalia. Celestial Mechanics and Dynamical Astronomy, 65(3):313–344, 1996.

[112] W. E. Wiesel. Stable orbits about the martian moons. Journal of Guidance, Control, and Dynamics, 16(3), 1993.

[113] X. Xin, D. J. Scheeres, and X. Hou. Forced periodic motions by solar radiation pressure around uniformly rotating asteroids. Celestial Mechanics and Dynamical Astronomy, 126(4):405–432, nov 2016.

[114] M. Xu, Y. Wang, and S. Xu. On the existence of j2 invariant relative orbits from the dynamical system point of view. Celestial Mechanics and Dynamical Astronomy, 112(4):427–444, 2012.

[115] M. Xu and S. Xu. J2 invariant relative orbits via differential correction algorithm. Acta Mechanica Sinica, 23(5):585–595, 2007.

[116] M. Zamaro. Natural and Artificial Orbits around the Martian Moon Phobos. PhD thesis, University of Strathclyde, 2015.

[117] Y. Zhao, J. Ji, J. Huang, S. Hu, X. Hou, Y. Li, and W. Ip. Orientation and rotational parameters of asteroid 4179 toutatis : New insights from chang'e-2' s close flyby. Monthly Notices of the Royal Astronomical Society, 450(4):3620–3632, 2015.

[118] X. Zou, C. Li, J. Liu, W. Wang, H. Li, and J. Ping. The preliminary analysis of the 4179 toutatis snapshots of the chang'e-2 flyby. Icarus, pages 348–354, 2014.

[119] M. T. Zuber, D. E. Smith, M. M. Watkins, S. W. Asmar, A. S. Konopliv, F. G. Lemoine, H. J. Melosh, G. A. Neumann, R. J. Phillips, S. C. Solomon, M. A. Wieczorek, J. G. Williams, S. J. Goossens, G. Kruizinga, E. Mazarico, R. S. Park, and D. Yuan. Gravity field of the moon from the gravity recovery and interior laboratory (grail) mission. Science, dec 2012.

List of Acronyms

- body-centered inertial frame (BCI)
- body-centered body-fixed frame (BCF)
- Boundary Value Problem (BVP)
- Central Differences (CD)
- Circular Restricted Three-Body Problem (CRTBP)
- Discrete Fourier Transform (DFT)
- Distributed Space Systems (DSS)
- Dynamical Systems Theory (DST)
- Elliptical Restricted Three-Body Problem (ERTBP)
- co-rotating frame of the Earth (ECEF)
- Elliptical Hill Problem (EHP)
- Highly Elliptical Orbit (HEO)
- Hill Problem (HP)
- Initial Value Problems (IVP)
- Local Vertical, Local Horizontal (LVLH)

- Medium Earth Orbit (MEO)
- Planar Circular Orbit (PCO)
- Planar Circular Restricted Three-Body Problem (PCRTBP)
- Partial Differential Equations (PDE)
- Quasi-Satellite Orbits (QSO)
- Right Ascension of the Ascending Node (RAAN)
- Routh Reduced System (RRS)
- Spacecraft Formation Flying (SFF)
- Solar Radiation Pressure (SRP)
- State Transition Matrix (STM)
- Two-Body Problem (TBP)
- Two-Point Boundary Value Problems (TPBVP)